



**HAL**  
open science

# Implementation of anti-corrosion nano-containers in the processes of surface treatment

Ioannis Gergianakis

► **To cite this version:**

Ioannis Gergianakis. Implementation of anti-corrosion nano-containers in the processes of surface treatment. Chemical and Process Engineering. Université Paul Sabatier - Toulouse III, 2016. English. NNT : 2016TOU30045 . tel-01473870

**HAL Id: tel-01473870**

**<https://theses.hal.science/tel-01473870>**

Submitted on 22 Feb 2017

**HAL** is a multi-disciplinary open access archive for the deposit and dissemination of scientific research documents, whether they are published or not. The documents may come from teaching and research institutions in France or abroad, or from public or private research centers.

L'archive ouverte pluridisciplinaire **HAL**, est destinée au dépôt et à la diffusion de documents scientifiques de niveau recherche, publiés ou non, émanant des établissements d'enseignement et de recherche français ou étrangers, des laboratoires publics ou privés.



Université  
de Toulouse

# THÈSE

En vue de l'obtention du

## DOCTORAT DE L'UNIVERSITÉ DE TOULOUSE

Délivré par : *l'Université Toulouse 3 Paul Sabatier (UT3 Paul Sabatier)*

---

---

Présentée et soutenue le *24/03/2016* par :

**GERGIANAKIS IOANNIS**

Mise en oeuvre de nano-réservoirs anti-corrosion dans des procédés de  
traitement de surface

---

---

### JURY

PAUCHARD LUDOVIC	DR CNRS, FAST, Université d'Orsay	Rapporteur
PRELOT BÉNÉDICTE	CR CNRS, ICGM, Université de Montpellier	Rapporteur
FORI BENOIT	Docteur, MECAPROTEC Industries	Membre du jury
LETTINGA MINNE PAUL	Professeur, ICS-3, Forschungszentrum Jülich	Membre du jury
MORRIS JEFFREY	Professeur, Levich Institute, CUNY	Membre du jury
BACCHIN PATRICE	Professeur, LGC Université de Toulouse	Directeur de thèse
HALLEZ YANNICK	MdC, LGC, Université de Toulouse	Directeur de thèse
MEIRELES MARTINE	DR CNRS, LGC, Université de Toulouse	Directrice de thèse

---

**École doctorale et spécialité :**

*MEGEP : Génie des procédés et de l'Environnement*

**Unité de Recherche :**

*Laboratoire de Génie Chimique de Toulouse*

**Directeur(s) de Thèse :**

*BACCHIN Patrice, HALLEZ Yannick et MEIRELES Martine*

**Rapporteurs :**

*PAUCHARD Ludovic et PRELOT Bénédicte*



## Acknowledgements

Firstly I would like to thank the region of Midi-Pyrénées and MECAPROTEC Industries for their financial support which enabled me to realise this thesis in the Laboratoire de Génie Chimique.

My sincerest gratitude goes to the members of the jury that had to travel from different parts of the world (and within France) to participate in the evaluation of this work. I would like to thank professor Jeffrey Morris for accepting the presidency of the jury, professor Minne Paul Lettinga for adding a “Greek touch” during the defence and Benoit Fori for agreeing to participate in the jury. I express my great appreciation to the reviewers of my thesis, Bénédicte Prelot and Ludovic Pauchard for accepting the mind-numbing task of reviewing this work. Thank you all, for the very interesting discussion that followed my presentation and your constructive comments. I am looking forward meeting you again, perhaps in a conference, with new problems and ideas to discuss.

I thank the Laboratoire de Génie Chimique and the two different directors that succeeded during my stay, for hosting me for the past three years and giving me the opportunity to “play” with almost all the instruments they have in the lab, and above everything for giving me the liberty to move around and arrange my working space-time without restrictions. Amongst the permanent staff of the lab I would like to thank Sandrine and Laure for their patience in teaching me how to use some of the instruments, answering my newbie questions, for their help to set-up my experiments and in some cases doing some measurements for me.

A big thank you goes to all the friends I made in Toulouse; Alessio, Alexandra, Alike, Arthur, Aurelie, Ayushi, Christian, Dmitro, Emelyne, Han, Izabella, Johanne, Joseph, Lucia, Meredith, Nayan, Nhat, Yandi, Zena (alphabetically to avoid conflicts of affection) thank you for the moments we shared. Thank you for supporting me in many days of despair during my writing, for bearing with me in many days of grumpiness (apparently every day from what you told me - lies) and of course thank you for sharing with me my “few” (that is not true) days of joy. I hope you will miss me and you can not live without me.

“Unfortunately” I was not able to continue my thesis for an eternity. Even though my stay was prolonged for a few months, some people wanted me to finish the job. Concerning the three most important people for my project I want to first thank you all for your availability and your readiness whenever something came up. This is something that might be overseen by some people, but I think it is crucial for the health of a project as well as for the sanity and performance of a PhD student. You

were almost always in the lab and always available for questions and discussion. Martine, thank you very much for always being in a great mood and seeing the bright side side of things, trying to motivate me and almost never saying no if an interesting idea came up. Thank you for trusting me with this project. Yannick, thank you for your critical thinking, for not accepting an answer that did not make sense to you, always questioning and telling me to look deeper. Even though sometimes I despaired with your corrections and suggestions, I know that from your side you “despaired” with what I was writing or not writing. Patrice, thank you for your critical comments from your multidisciplinary point of view and your motivating and curious character. I believe that the three of you comprise a very strong team and even though sometimes having three supervisors was difficult when decisions or compromises were needed, it was in the best interests of both the project and myself. Finally, after this project I was able to connect the two different paths I followed during my undergraduate and graduate studies (material science and fluid mechanics), a connection that was not at all obvious for me all these years.

To close, I wish to thank my family for acting as a “buffer solution” and keeping me in equilibrium throughout the ups and downs of a PhD. Even though they were not physically in Toulouse, our telephone discussions helped me through some challenging times. A big thank you goes to Elaine that managed to proofread my thesis on such a short notice.

*Do not pray for an easy life, pray for the strength to endure a difficult one.*

**Bruce Lee**

---

## Résumé

---

L'utilisation de chrome hexavalent comme inhibiteur de corrosion dans les revêtements protecteurs de pièces métalliques sera bientôt interdit car cet élément est considéré comme cancérigène et mutagène. L'une des stratégies proposées pour remédier à ce problème est l'incorporation de nano-réservoirs contenant des inhibiteurs de corrosion, autres que le chrome, dans une matrice de revêtement. L'approche utilisée dans ce travail est basée sur la physisorption de l'inhibiteur de corrosion sur des nano-particules chargées. C'est une approche électrochimique où un sel, l'inhibiteur de corrosion, est adsorbé sur la surface des nano-particules chargées. Après l'incorporation de nano-réservoirs chargés dans la matrice de revêtement et le dépôt du film sur le substrat, la morphologie finale, et donc l'homogénéité, du film dépend de plusieurs paramètres tels que la vitesse d'évaporation du film et les interactions entre particules. Par conséquent, il faut s'assurer que les nano-réservoirs sont dispersés de manière homogène à l'intérieur du revêtement ou être en mesure de prédire où les inhomogénéités vont se développer. Ainsi, le premier objectif de ce travail est de développer une stratégie de modélisation pour étudier l'écoulement de suspensions contenant des nano-particules dans des solutions électrolytiques. Les interactions prises en compte ici sont d'origine hydrodynamique, thermique et électrostatique. Nous montrons que dans le cas du séchage d'un film contenant des nano-particules, les interactions pertinentes sont celles d'origine thermique et électrostatique seulement. Sur la base de ce résultat, l'exemple d'un micro-évaporateur est présenté dans lequel des expériences numériques du séchage d'une suspension de nano-particules avec différentes charges de surface ont été réalisées. Sachant que les interactions entre particules sont influencées surtout par la charge et la concentration de l'électrolyte dans la suspension, il existe une réelle motivation pour étudier ces interactions dans les systèmes de nano-particules synthétisées en vue de la conception de nano-réservoirs. Par conséquent, le deuxième objectif de ce travail est de synthétiser des nano-réservoirs de boehmite, d'étudier leur stabilité dans une gamme de concentration d'inhibiteur de corrosion, et finalement de valider ce type de nano-réservoirs pour des applications de revêtements anti-corrosion.

---

## Abstract

---

The use of hexavalent Chromium as a corrosion inhibitor in protective coatings of metal parts will soon be prohibited because this element is considered carcinogenic and mutagenic. One of the strategies suggested to overcome this problem is the incorporation of nano-containers containing corrosion inhibitors, other than Chromium, inside a coating matrix. The nano-containers approach used in this work is based on the physisorption of the corrosion inhibitor on charged nano-particles. It is an electrochemical approach where a salt, the corrosion inhibitor, is adsorbed on the surface of the charged nano-particles. After the incorporation of the charged nano-containers in the coating matrix and the deposition of the film on the substrate, the final morphology and therefore the homogeneity of the film will depend on several parameters such as the evaporation rate and the interactions between particles. Consequently, one has to insure that the nano-containers are homogeneously dispersed inside the coating matrix after the deposition, or be able to predict where inhomogeneities will develop. Hence, the first aim of this work is to develop a modeling strategy to study the flow of suspensions containing interacting nano-particles in electrolyte solutions. The interactions taken into account here are of hydrodynamic, thermal, and electrostatic origin and it is argued that in the application of film drying of nano-particles the interactions relevant are those of thermal and electrostatic origin only. Based on this idea, the simulation of the drying of a suspension with nano-particles of different charges has been realized in a micro-evaporator. Considering that particle interactions are influenced by the charge and the electrolyte concentration of the suspension, there is a clear motivation to study these interactions in a synthesized system of nano-particles, candidate in the design of nano-containers. Therefore, the second aim of this work is to synthesize boehmite nano-containers, study their stability in a range of corrosion inhibitor concentration, and finally qualify them as candidates for the application of anti-corrosion coatings.

---

# Contents

<b>Introduction</b>	<b>1</b>
1 Introduction . . . . .	1
1.1 How can corrosion be prevented? . . . . .	2
1.2 Thin films containing nano-containers . . . . .	5
1.3 Summary . . . . .	9
2 References . . . . .	11
<b>1 Transport of nano-containers</b>	<b>13</b>
1 How to model a mixture of particles and fluid macroscopically? . . .	15
1.1 Development of a mixture model . . . . .	16
1.1.1 Averaging procedure . . . . .	17
1.1.2 Equations of continuity and momentum . . . . .	19
1.1.3 Remarks . . . . .	25
1.2 The Suspension Balance Model closure . . . . .	27
1.2.1 Particle phase transport equation . . . . .	27
1.2.2 Suspension momentum balance . . . . .	29
1.3 Code validation case . . . . .	30
1.4 Discussion and Summary . . . . .	32
2 When do we have to include thermodynamic and hydrodynamic ef- fects in continuous models of flowing colloidal suspensions? . . . .	34
3 Suspension drying in a micro-evaporator . . . . .	51
3.1 Numerical implementation . . . . .	53
3.2 Simulation of drying . . . . .	58
3.2.1 Comparison between 2-D and 1-D approach . . . .	58

---

3.2.2	Effect of viscosity in the solution . . . . .	61
3.2.3	Comparison of cases with different Péclet numbers	64
3.2.4	Comparison of cases with different particle charges	66
3.3	Summary and Conclusions . . . . .	68
4	References . . . . .	71
<b>2</b>	<b>Let there be nano-containers</b>	<b>75</b>
1	How are they made and what do they look like? . . . . .	77
1.1	Nano-container development . . . . .	79
1.1.1	Particle synthesis . . . . .	80
1.1.2	Physical characteristics of the particles . . . . .	81
1.1.3	Matrix composition . . . . .	85
1.2	Discussion and Summary . . . . .	87
2	Do they stay suspended? . . . . .	90
2.1	Electrokinetic testing of stability . . . . .	92
2.1.1	Evaluation of interface-solution properties from electrophoretic velocity . . . . .	92
2.1.2	Repulsive electrical potential between rod-like particles . . . . .	98
2.2	Experimental investigation of destabilizing conditions . . .	104
2.2.1	Speciation analysis . . . . .	109
2.2.2	Aggregation of cylinders and CCC . . . . .	112
2.3	Discussion and Summary . . . . .	115
3	Are they actually nano-containers? . . . . .	118
3.1	Experimental study of adsorption . . . . .	119
3.2	How is Cerium adsorbed? . . . . .	123
3.2.1	Surface complexation modeling . . . . .	123
3.2.2	Adsorption of a monovalent cation . . . . .	128
3.3	Summary . . . . .	130
4	References . . . . .	132
<b>3</b>	<b>General conclusions and perspectives</b>	<b>137</b>
<b>A</b>	<b>Appendix</b>	<b>143</b>
1	Proof of relation (1.19) . . . . .	144
2	Proof of relation (1.21) . . . . .	145
3	Proof of relation (1.25) . . . . .	146

---

4	Dialysis procedure . . . . .	148
5	Adsorption protocol . . . . .	149
6	Adsorption time . . . . .	154
7	References . . . . .	156



# List of Figures

1	Degraded airplane piece demonstrating corrosion . . . . .	1
2	Schematic representation of a protective coating . . . . .	2
3	Nano-containers based on adsorption . . . . .	4
4	Dried droplets of $\gamma$ -alumina for different $pH$ . . . . .	5
5	Drying a film of polystyrene particles in water from Routh . . . . .	6
6	Dried latex ESEM images taken from Islam et al. . . . .	7
7	Drying of suspensions with different particles shapes (Yunker et al.)	8
1.1	Schematic representation of volume averaging . . . . .	17
1.2	Traction $\mathbf{n} \cdot \boldsymbol{\sigma}$ on the particle surface . . . . .	22
1.3	Scalar transport validation in sedimentation case . . . . .	32
1.4	Microevaporator design from Salmon and Leng; Merlin et al. . . . .	51
1.5	Particle Peclet number $Pe_p$ as a function of the evaporation rate . . . . .	54
1.6	Effective viscosity $\eta/\eta_0$ as a function of particle volume fraction . . . . .	55
1.7	Osmotic pressure, hindrance factor and effective diffusion coefficient as a function of particle concentration . . . . .	57
1.8	Comparison of 1-D and 2-D concentration profiles . . . . .	58
1.9	Particle concentration $\phi$ contours for different times . . . . .	60
1.10	Comparison of the concentration profiles between cases of constant and variable viscosity . . . . .	61
1.11	Comparison of concentration profiles along the $x$ -axis . . . . .	62
1.12	Particle concentration $\phi$ contours for different times . . . . .	63
1.13	Concentration contours comparison for the same time and different Péclet numbers . . . . .	64

---

1.14	Comparison of suspension streamlines between simulations with constant and variable viscosity . . . . .	65
1.15	Comparison of the concentration contours for particles with different surface charges . . . . .	67
2.1	Types of nano-containers found in literature . . . . .	78
2.2	Type of nano-containers based on the adsorption of the corrosion-inhibitor . . . . .	79
2.3	Cryo-TEM image of boehmite nano-particles and particle size determination by DLS and cryo-TEM . . . . .	82
2.4	Very fine powder of boehmite nano-particles after freeze-drying . . . . .	85
2.5	Coarse-grained particle model used for modelling . . . . .	87
2.6	Schematic representation of the surface of metal oxides from Franks and Gan (2007) . . . . .	89
2.7	Schematic of Electric Double Layer . . . . .	91
2.8	The slip plane . . . . .	93
2.9	Electro-kinetic results for different electrolyte concentration . . . . .	96
2.10	Electrostatic interaction between two charged flat plates in an electrolyte solution. . . . .	99
2.11	Schematic of interaction potential of two charged surfaces . . . . .	100
2.12	Two interacting cylinders in parallel orientation (a) and in crossed orientation (b). . . . .	101
2.13	Calculation of the interaction potential between cylinders . . . . .	103
2.14	DLS measurement of hydrodynamic radius of aggregates as a function of time . . . . .	105
2.15	Phase diagram of stability of boehmite nano-particles and $Ce(NO_3)_3$ . . . . .	107
2.16	Partial concentration of Cerium species in solution . . . . .	111
2.17	Partial concentration of Cerium species in solution estimated by MINTEQ . . . . .	113
2.18	Calculated stability ratio as function of electrolyte concentration . . . . .	114
2.19	Adsorption Q in <i>mol</i> of Cerium per <i>gr</i> of nano-particles . . . . .	121
2.20	Schematic of the Triple Layer Model . . . . .	124
2.21	Representation of the charge and potential distribution . . . . .	125
2.22	Triple Layer Model fit on the adsorption results . . . . .	129
2.23	(a) Concentration of adsorbed cation as a function of <i>pH</i> , (b) Concentration of cations in the bulk. . . . .	130

---

A.1	Traction $\mathbf{n} \cdot \boldsymbol{\sigma}$ on the particle surface . . . . .	146
A.2	Dialysis concept ( <i>left</i> ) at time $t_0$ ( <i>right</i> ) at equilibrium . . . . .	148
A.3	Absorbance of the Xylenol-Cerium complex . . . . .	152
A.4	Calibration curves used with Xylenol-Cerium complex . . . . .	152
A.5	Adsorption $Q$ in <i>mol</i> of Cerium per <i>gr</i> of nano-particles as a function of time of contact . . . . .	154



# List of Tables

2.1	Electro-kinetic data for boehmite ( $\gamma$ -alumina) found in literature . . .	95
2.2	Parameters used for the calculation of the potential of interaction . . .	103
2.3	Summary table of adsorption experiments . . . . .	120
2.4	Electro-kinetic data for boehmite ( $\gamma$ -alumina) found in literature . . .	128



## 1 Introduction

Corrosion of aluminum alloys is a major problem in the aircraft industry (see Figure 1). It arises from the use of aluminum alloys (series 2XXX) containing copper to enhance the mechanical resistance of the material, but this also makes it susceptible to corrosion when exposed to aggressive environments. Many of the surface treatment techniques utilised to prevent corrosion are implemented by the use of Chromium (Cr(VI)) which is a known corrosion inhibitor simple in its usage. However, Cr(VI) was classified by the European regulation REACH (Registration, Evaluation, Authorisation and Restriction of Chemicals) as Carcinogenic, Mutagenic or toxic for Reproduction (CMR). This regulation imposes the complete substitution of components containing Cr(VI) with products that do not contain CMR in the very near future.



**Figure 1:** Degraded airplane piece demonstrating corrosion

This work is part of the project ECOREV aimed at the development of new techniques to replace Chromium in surface treatments. The objective was to develop new treatments, initially by academic partners (LGC, CIRIMAT) at a laboratory scale and then to transfer them to the pilot level and semi-industrial pilot level by MECAPRO-TEC Industries.

The approach undertaken in the ECOREV project was to conduct three parallel scientific studies. Two of them were focused on the development of two new surface treatments and the third one, relevant here, was the study and modelling of the colloidal dispersions used by the other members of the project. In this introduction a very brief report will be given about corrosion prevention by coatings, we will then focus on the main subjects of this work: the anti-corrosion nano-containers and the coatings formed by thin film drying.

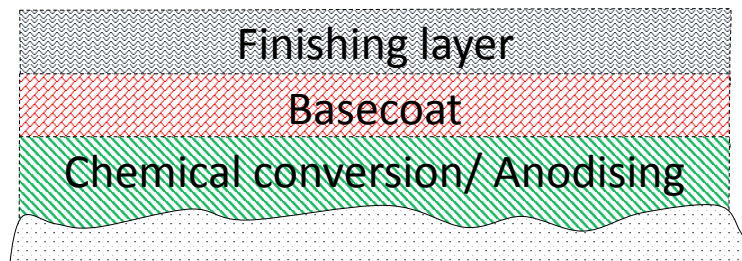


**Figure 2:** Schematic representation of a protective system of coatings used in the aeronautics industry.

### 1.1 How can corrosion be prevented?

Aluminum itself is resistant to corrosion because of a thin layer of oxide ( $\text{Al}_2\text{O}_3$ ) developed when it comes into contact with water. However, when mixed with other elements to create alloys, the final material inherits the corrosion sensitivity of its components. For example, the aluminum alloy series 2XXX, containing copper, is susceptible to corrosion. There is a range of techniques used to prevent corrosion in aluminum alloy pieces, such as chemical conversion, anodizing, and more recently sol-gel coating. The first two techniques are heavily based on the use of Cr(VI) and Cr(III) when used for the protection of aluminum. The third technique is based on the deposition of a thin liquid matrix containing small particles on the substrate, in order to create a rigid coating after drying.

Usually, a protective coating system is composed by the three layers depicted in Figure 2. In contact with the surface, there is a chemical conversion or anodized layer (primer). The new surface is covered with the paint and the final layer is composed of the finishing products. The interest of project ECOREV was to replace the first layer which is in contact with the substrate and the techniques used to coat it depend on Chromium.

Anti-corrosive coatings can be classified according to the mechanisms by which they protect a metal. The three principle protective mechanisms of anti-corrosive coatings are barrier protection, sacrificial protection (galvanic effect) and passivation of the substrate surface (Davis (2000)). Based on these mechanisms the coatings are divided into barrier coatings, sacrificial coatings and inhibitive coatings.

Barrier protection is achieved when coatings completely isolate the substrate from the environment. They are used as primer, intermediate, or finishing coating. The degree of protection offered by a barrier coating system is highly dependent on the thickness of the coating system as well as the type and nature of the binder sys-

tem. A key element for high-performance barrier coatings is a high density of the coating material.

Sacrificial protection is achieved by coating the substrate with a more electrochemically active metal. These coatings rely on the principle of galvanic corrosion for the protection of metals against corrosion. This means that the substrate is protected by a metal or alloy that is more electrochemically active than the material to be protected. Unlike barrier coatings, sacrificial coatings are only applied as primers because they are only effective if the coating is in direct contact with the substrate.

Finally, an inhibitive coating can be realised by the addition of corrosion inhibitors to the corresponding layer. Inhibitors are chemical species, such as Chromium or Cerium, that can delay corrosion. Inhibitors can be incorporated in a protective coating or in a primer for the coating. When a defect appears in the coating, the inhibitor leaches from the coating and reacts with the substrate. The anti-corrosive mechanism of inhibitive coatings relies on the passivation of the substrate and the build-up of a protective layer consisting of insoluble metallic complexes, which impede transport of aggressive species by acting as a barrier.

The coatings relevant to this work are the barrier and inhibitive coatings. In the work of Jaubert (2012) the barrier coating was formed by a sol-gel method using 3-Glycidyloxypropyl)trimethoxysilane (GPTMS) and Aluminum-tri-sec-butoxide (ASB). The corrosion inhibitor that was added to this polymer matrix was Cerium Nitrate ( $\text{Ce}(\text{NO}_3)_3$ ). However, it was found that there was a limitation in the quantity of Cerium that could be added without modifying both the mechanical and barrier properties of the coating. To overcome this problem, the idea was to use nano-containers in order to stock the excessive quantity of Cerium in the coating and when these nano-containers were triggered correctly from the environment they would liberate Cerium. Integration of nano-containers containing a corrosion inhibitor in a coating seems a valid strategy to substitute Chromium in the long term (Shchukin and Möhwald (2007); Tavandashti and Sanjabi (2010)).

The nano-containers proposed in the literature are classified into three principal categories. The Layer-by-Layer nano-containers are composed by alternating layers of the barrier coating and the corrosion inhibitor, creating a coating with the corrosion inhibitor spread between the barrier coating. A second technique consists of distributing permeable capsules loaded with the corrosion inhibitor in the coating matrix. The third one, which is relevant here, is based on the adsorption of the corrosion inhibitor on the surface of metal oxide nano-particles (Zheludkevich et al. (2005); Shchukin and Möhwald (2007); Tavandashti and Sanjabi (2010); Jaubert (2012)) and

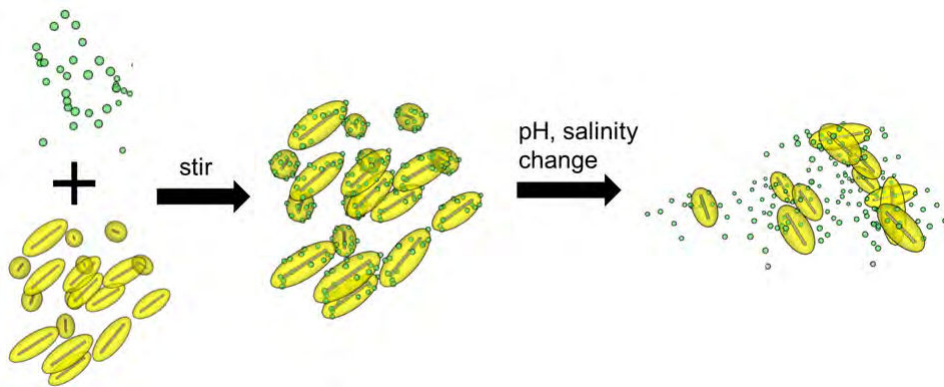


**Figure 3:** Nano-containers concept used in this work. The green spheres are the corrosion inhibitors and the yellow ellipsoids are the nano-containers. The corrosion inhibitor is adsorbed on the surface of the nano-container and if triggered correctly it can be released.

then incorporate these nano-containers into the coating matrix. The concept of this last approach is shown schematically in Figure 3, where the corrosion inhibitor (green spheres) is adsorbed on the surface of the nano-particles (yellow ellipsoids) and it is desorbed if triggered by a change of physico-chemical conditions. The nano-particles used in this work were aluminum oxy-hydroxide, or boehmite, which furthermore have been shown to serve as mechanical reinforcement when incorporated into the coating matrix.

Promising results have been obtained when the corrosion inhibitor is loaded in mesoporous silica, or boehmite  $\gamma$ -AlOOH nano-particles (Esteban (2011); Jaubert (2012)). Nevertheless, a clear understanding of the function as well as the limitations of this type of nano-containers is missing. Thus a correct account of the mechanism of adsorption and desorption of the corrosion inhibitor on the nano-particles is needed.

Finally, another important factor affecting the performance of a coating is the inhomogeneities it might contain. The system of coating matrix, particles, and Cerium described above is principally deposited on the substrates by dip-coating, spray coating or spin coating. After the deposition of a liquid film by dip-coating for example, the coated substrate is left to dry and the film solidifies. The performance of this coating will depend on possible impurities or inhomogeneities that might appear inside the coating mixture, during the deposition step or during drying. Thin liquid films containing particles which undergo drying are known to be prone to inhomogeneities because of the particle transport inside the liquid volume. These inhomogeneities can have an impact on the morphology as well as on the mechanical behaviour of the final



**Figure 4:** Dried droplets of an aqueous  $\gamma$ -alumina suspension for different  $pH$  values. The left deposit is an example of coffee ring formation, while the right one is a homogeneous deposit.

product, and can of course deteriorate the anti-corrosion performance of the coating.

## 1.2 Thin films containing nano-containers

Thin films derived from a sol-gel transition induced by drying, constitute a promising technology for primer coating (Zheludkevich et al. (2005, 2007); Tavandashti and Sanjabi (2010)). A sol is a dispersion of small particles in a liquid, small enough that gravitational forces are negligible and dominated by short-range forces and thermal motion (such as van der Waals and electrostatic surface charges). Particles for which these criteria are true are usually referred to as colloids and their size is below  $1 \mu m$ . This system of liquid and particles is usually referred to as a suspension and in the case of colloids, a colloidal suspension. Gel is a cluster of particles linked together through condensation or aggregation until a unified cluster is formed in the vicinity of the containing vessel.

When a suspension is dried over a substrate, a thin film is formed. The domain of thin film drying has received much attention lately since the transitions observed during drying are found to impact on the final morphology of the film. These transitions depend greatly on the transport of particles inside the film volume. An expression of this particle transport can be observed on coffee stains taking the form of "*coffee rings*". In Figure 4 an example of dried droplets of an aqueous  $\gamma$ -alumina suspension is presented, for different  $pH$  values. The left deposit corresponds to a "coffee-ring" formation. Particles consolidate at the contact line between the substrate and drop, creating a solid region. This movement of particles is due to a fluid flow from the center of the droplet towards the edges of the film. A first explanation for the coffee-ring effect was based on capillary flow, proposed by Deegan et al. (1997). In short,

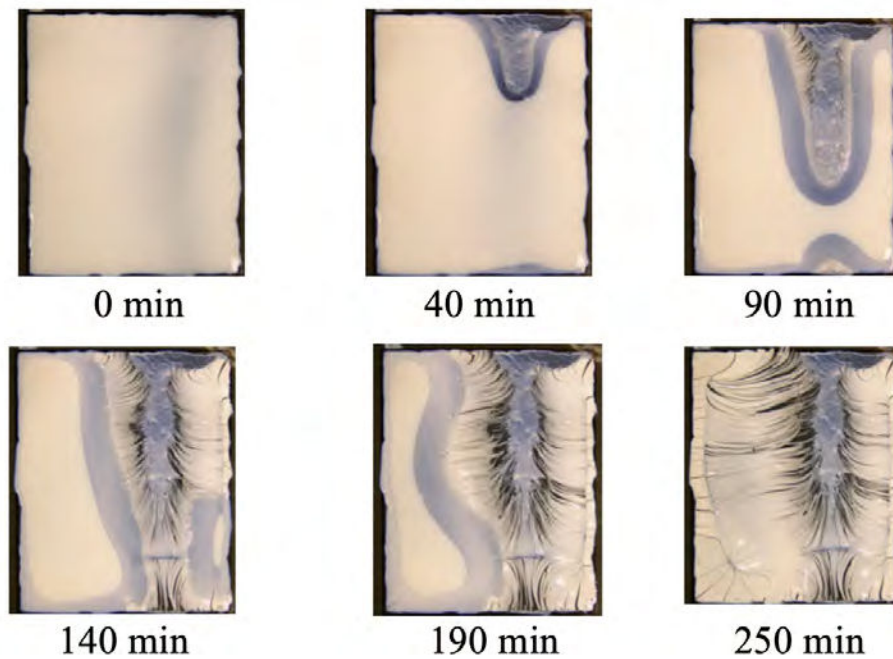


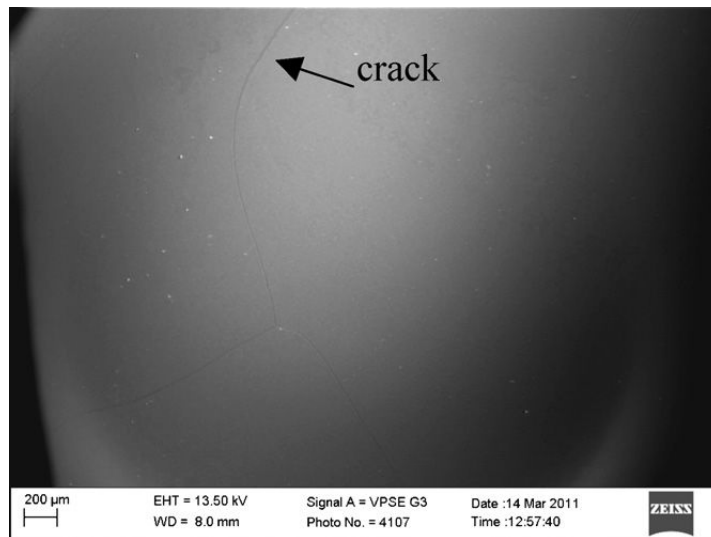
**Figure 5:** Drying a film of 200 *nm* polystyrene particles in water. The film is about 30 cm across and has an initial particle loading of 10 *wt%* (Routh (2013)).

the enhanced evaporation rate near the contact-line “pumps” the suspension from the center of the drop towards the exterior.

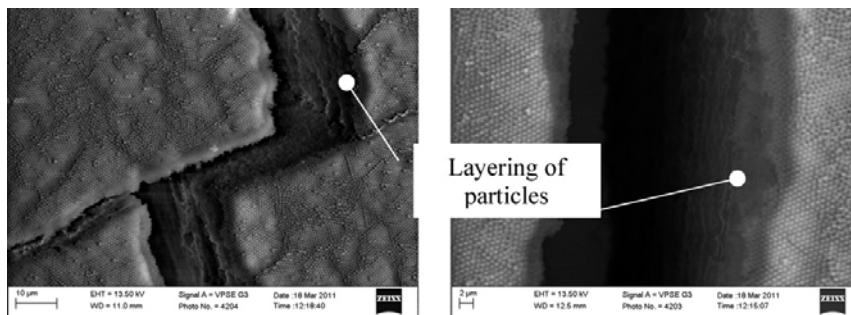
Another manifestation due to similar physics is the horizontal propagation of drying fronts (Routh and Russel (1998)) which is observed in large colloidal films. The drying process for a dispersion of polystyrene particles in water is shown in Figure 5 (Routh (2013)). Initially the film is liquid everywhere but as time advances, drying consolidates the particles creating drying fronts. The drying fronts are defined in the opaque region that lies between the white suspension and the dried zone. For time 90 *min*, cracks have started appearing and they propagate as drying continues. Film cracking is a very active field of research with the ultimate objective to control cracks appearing from particle self-assembly or packing (Pauchard et al. (1999); Goehring et al. (2010); Boulogne et al. (2014)).

It is clear that the drying processes determine the final morphology of the film. After the deposition by coating, there is a substantial volume reduction and an internal stress accumulation due to the large amount of solvents and water evaporation. Cracks are easily formed due to this internal stress if the film formation conditions are not carefully controlled (Wang and Bierwagen (2009)). An example from Islam et al. (2012) is given in Figure 6 where Environmental Scanning Electron Microscope

images show a macroscopic formed crack because of drying. Further magnification of this crack reveals organized layers of latex particles with a crystal like structure. As one can suspect, an anti-corrosion coating containing cracks will allow corrosive species to attack the substrate.



(a)



(b)

**Figure 6:** ESEM images taken from Islam et al. (2012). (a) Low magnification ESEM image of the surface of a dried latex specimen and (b) Higher magnification ESEM images of cracked faces observed in film-formed latex specimen.

Different approaches can be followed to control the morphology and homogeneity of a thin film. An experiment of drying droplets from Yunker et al. (2011) is presented in Figure 7. Two different types of particles were used under the same evaporation conditions. In the upper row of images, drying of a suspension of spherical particles led to a coffee-ring deposit. On the other hand, using ellipsoidal particles suppressed this effect creating a more homogeneous deposit as depicted in the lower

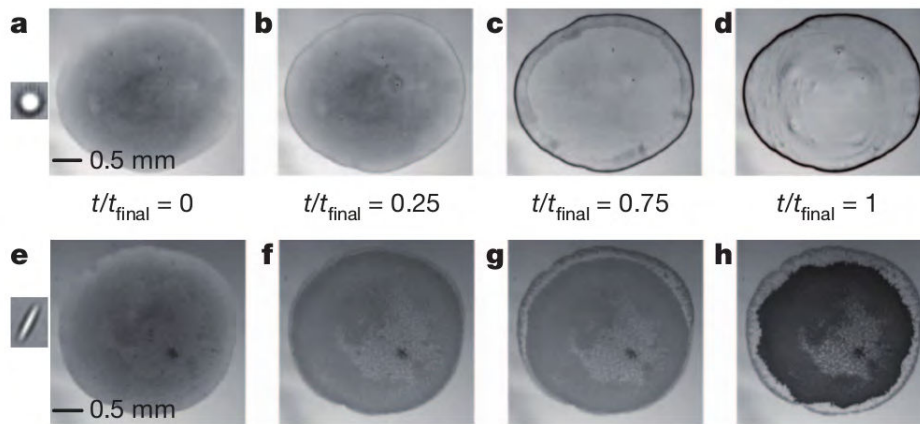


**Figure 7:** Images taken from Yunker et al. (2011). Experimental snapshots at different times  $t/t_{final}$  during the evaporation of a drop of particle suspension; shown are data for spherical particles (left inset:  $a-d$ ) and for ellipsoidal particles with aspect ratio  $a = 3.5$  (left inset:  $e-h$ ).

row of images.

Another way to control or change the morphology of a film is through colloidal interactions. Colloidal particles are usually electrostatically charged. Changing the composition of their solvent, in terms of electrolyte concentration for example, can significantly affect their macroscopic behaviour due to the screening of the interactions between particles (Russel et al. (1992); Hunter (2001)). In Figure 4, simply by changing the  $pH$  from 8.3 (left deposit) to 10.7 (right deposit), a completely different final morphology of the deposit is observed. König et al. (2008) found that a salt concentration increase in a suspension of acrylic latex particles, leads to high concentration inhomogeneities along the thickness of the film and that the effect depends on the particular type of ions used. He observed a high particle concentration at the evaporation surface, while the concentration was much lower close to the substrate. This is a behaviour usually found in the literature as “skinning” or “skin formation” (Russel (2011)). Finally, Pauchard et al. (1999) in a series of desiccation experiments with silica sol droplets, observed that crack patterns tend to differentiate depending on the salt concentration.

From the aforementioned observations, it is clear that there are many parameters influencing thin film drying; from the shape of the particles to the  $pH$  of the solvent and the salt concentration. In order to be able to predict the final morphology of the deposited film in geometries that are relevant in the aeronautic industry, a macroscopic particle transfer model is needed. But since thin film drying is heavily

influenced by the micro-structure and the interactions between the particles, there is a definite need to incorporate them in macroscopic approaches.

### 1.3 Summary

Due to Chromium's classification as a Carcinogenic, Mutagenic or Toxic for Reproduction by the European regulation REACH, intense research is required to replace it with an appropriate candidate that meets the demands of aircraft industries.

In this introduction a brief account of the techniques actually used to prevent corrosion has been given. Most of them are based on the use of hexavalent Chromium. A relatively new approach to creating barrier anti-corrosion coatings is the use of a sol-gel transition and the addition of a corrosion inhibitor other than Chromium. Previous works on this subject have shown that a possible candidate to replace Chromium is Cerium. Unfortunately, when Cerium is added to the sol-gel matrix in excessive quantities, it has been shown to degrade the performance and mechanical properties of the coating. A solution to this problem was found by incorporating nano-containers into the sol to stock excessive quantities of Cerium. They can be released later if triggered correctly. The nano-containers approach used in this work is based on the adsorption of the corrosion inhibitor on the surface of nano-particles. After the nano-particles are loaded, they are mixed with the sol-gel matrix and the dispersion can be deposited using a technique such as dip-coating.

The fact that the deposited liquid film contains nano-particles can be problematic for the final morphology of the coating, and thus for its anti-corrosion performance. Drying of thin films containing particles exhibits a number of interesting phenomena due to the transport of particles in the film volume. Because of this transport, inhomogeneities can be created, such as coffee-rings and a surface skin.

The first objective of this work was to develop a macroscopic model for the transport of interacting nano-particles (nano-containers) in electrolyte solutions. This objective was achieved in Chapter 1. In Section 1 a macroscopic model for particle transport is derived that takes into account hydrodynamic and electrostatic interactions between particles. In Section 2 a study of the interplay between hydrodynamic and electrostatic interactions between particles is presented in the case of a channel flow. This study allowed us to discriminate regimes where colloidal interactions are more relevant than the hydrodynamic ones, and vice-versa. Based on this result, the simulation of the evaporation of a colloidal suspension will be demonstrated in Section 3, for different process conditions such as the evaporation rate and the particle surface charge.

Motivated by the strong dependence of the film morphology on the particle interactions, the second objective, achieved in Chapter 2, was to study a real nano-container system in terms of stability and capacity to adsorb and desorb a corrosion inhibitor. First, a detailed account of the synthesis and characterization of boehmite nano-particles is given. The solvent composition is also investigated. Secondly, the stability of the nano-containers is studied, as a function of added salt concentration in Section 2. Lastly, a study of the adsorption of Cerium Nitrate on boehmite nano-particles is described, in Section 3, to qualify them as nano-containers.

---

## 2 References

- Boulogne, F., Giorgiutti-Dauphiné, F., and Pauchard, L. (2014). Surface patterns in drying films of silica colloidal dispersions. *Soft Matter*, 11(1):102–108.
- Davis, J. R. (2000). *Corrosion: Understanding the Basics*. ASM International.
- Deegan, R. D., Bakajin, O., Dupont, T. F., Huber, G., Nagel, S. R., and Witten, T. A. (1997). Capillary flow as the cause of ring stains from dried liquid drops. *Nature*, 389(6653):827–829.
- Esteban, J. (2011). *Développement par procédé sol-gel de revêtements anti-corrosion d'alliages d'aluminium à usage aéronautique : de l'effet barrière à l'auto-cicatrisation*. Phd thesis, Université de Toulouse, Université Toulouse III - Paul Sabatier.
- Goehring, L., Clegg, W. J., and Routh, A. F. (2010). Solidification and ordering during directional drying of a colloidal dispersion. *Langmuir*, 26(12):9269–9275.
- Hunter, R. J. (2001). *Foundations of Colloid science*. Oxford University Press, Oxford ; New York, 2 edition edition.
- Islam, O., Dragnevski, K. I., and Siviour, C. R. (2012). On some aspects of latex drying – ESEM observations. *Progress in Organic Coatings*, 75(4):444–448.
- Jaubert, O. (2012). *Revêtements hybrides multifonctionnels élaborés par voie sol-gel pour la protection d'alliages d'aluminium pour l'aéronautique*. PhD thesis, Université Toulouse III - Paul Sabatier.
- König, A. M., Weerakkody, T. G., Keddie, J. L., and Johannsmann, D. (2008). Heterogeneous drying of colloidal polymer films: Dependence on added salt. *Langmuir*, 24(14):7580–7589.
- Pauchard, L., Parrisé, F., and Allain, C. (1999). Influence of salt content on crack patterns formed through colloidal suspension desiccation. *Phys. Rev. E*, 59(3):3737–3740.
- Routh, A. F. (2013). Drying of thin colloidal films. *Rep. Prog. Phys.*, 76(4):046603.
- Routh, A. F. and Russel, W. B. (1998). Horizontal drying fronts during solvent evaporation from latex films. *AIChE Journal*, 44(9):2088–2098.

- 
- Russel, W. B. (2011). Mechanics of drying colloidal dispersions: Fluid/solid transitions, skinning, crystallization, cracking, and peeling. *AIChE J.*, 57(6):1378–1385.
- Russel, W. B., Saville, D. A., and Schowalter, W. R. (1992). *Colloidal Dispersions*. Cambridge University Press.
- Shchukin, D. and Möhwald, H. (2007). Self-repairing coatings containing active nanoreservoirs. *Small*, 3(6):926–943.
- Tavandashti, N. P. and Sanjabi, S. (2010). Corrosion study of hybrid sol–gel coatings containing boehmite nanoparticles loaded with cerium nitrate corrosion inhibitor. *Progress in Organic Coatings*, 69(4):384–391.
- Wang, D. and Bierwagen, G. P. (2009). Sol–gel coatings on metals for corrosion protection. *Progress in Organic Coatings*, 64(4):327–338.
- Yunker, P. J., Still, T., Lohr, M. A., and Yodh, A. G. (2011). Suppression of the coffee-ring effect by shape-dependent capillary interactions. *Nature*, 476(7360):308–311.
- Zheludkevich, M. L., Serra, R., Montemor, M. F., Yasakau, K. A., Salvado, I. M. M., and Ferreira, M. G. S. (2005). Nanostructured sol–gel coatings doped with cerium nitrate as pre-treatments for AA2024-T3: Corrosion protection performance. *Electrochimica Acta*, 51(2):208–217.
- Zheludkevich, M. L., Shchukin, D. G., Yasakau, K. A., Möhwald, H., and Ferreira, M. G. S. (2007). Anticorrosion coatings with self-healing effect based on nanocontainers impregnated with corrosion inhibitor. *Chem. Mater.*, 19(3):402–411.

# Transport of nano-containers

1



---

## 1 How to model a mixture of particles and fluid macroscopically?

The modelling of a mixture of different phases is usually approached in two different ways. In the first one, a clear discrimination exists between the two phases (ex. solid and liquid), the principal modelling effort being the interaction between the phases, as well as interactions inside the same phase. In the second approach the mixture is considered to be, as the word suggests, a “mixture” of the phases that composes a single effective phase which of course has the averaged properties of each of its phases. Consequently, the objective is to find the contribution of each phase to the average properties of the mixture. For example in a rotational rheometer the measurement of viscosity refers to the viscosity of the mixture and not the viscosity of the separate phases. The choice between these approaches is usually made, depending on the domain of application, as well as on the scales of interest. Based on this discrimination of the modelling strategies, many simulation techniques have been developed to accommodate such models.

In the case where the phases are treated separately two very well known approaches exist, the Euler-Euler and the Euler-Lagrange approaches. The first one treats each phase of the system as a continuous medium, while the second one treats the fluid phase as continuous medium and the solid phase as an ensemble of dispersed rigid bodies. There are many variations of these methods, some of them being detailed in Prosperetti and Tryggvason (2009).

On the other hand, the mixture models treat all the existing phases as a single Eulerian phase or continuous medium. The challenge in this case is to connect the changes in the microscopic scale that may arise from particle interactions, with the macroscopic scale. From an engineering point of view, the details of the microstructure might be ignored as long as a predictive model can be established as a function of macroscopic quantities only.

In the case of suspensions, when the particles become very small (colloids), Lagrangian methods are limited to simulate small volumes because it is computationally demanding. This problem becomes even more important if the concentration of the solid phase is high. Therefore, Lagrangian methods often cannot be used in processes found in engineering. By averaging physical variables obtained by a Lagrangian method, one can obtain useful results that can further be used to build an Eulerian model. In order to do such a transition from a Lagrangian to an Eulerian model, an averaging method has to be defined. The purpose of averaging is to capture the

macroscopic behaviour of suspensions, which is connected with its micro-structure, by filtering out the microscopic degrees of freedom at the level of particles. One example in which the microstructure affects the macroscopic behaviour of a mixture is the phenomenon of shear-induced migration in flows of particulate systems. It was first recognised by Leighton and Acrivos (1987) to explain anomalies observed in a Couette viscometer, in which a decrease in the suspension viscosity was observed after long periods of shearing. It was demonstrated that this phenomenon is due to the shear-induced migration or, differently put, the migration of particles from regions of high shear rate to regions of low shear rate. To relate this micro structural change to macroscopic quantities, two main types of continuous models have been developed: the phenomenological diffusive flux model of Phillips et al. (1992) and the Suspension Balance Model proposed by Nott and Brady (1994). This second model is the one used in this work. It is based on the averaging of the local mass and momentum conservation equations throughout the suspension.

In what follows an averaging procedure will be detailed based on the work of Anderson and Jackson (1967), Jackson (1997) and with some recent developments from Nott et al. (2011). Even though the derivation of these equations exists in literature, it is included here for completeness. In a first time, the macroscopic, or Eulerian, equations of conservation of mass and momentum will be derived for a mixture of a fluid and colloidal particles. The closure for this set of equations will be provided by the Suspension Balance Model of Nott and Brady (1994); Nott et al. (2011) which was modified for the case of colloidal suspensions. Lastly, a brief validation case will be presented to test the code developed for the solution of the equations.

## 1.1 Development of a mixture model

Consider a mixture of a Newtonian fluid of density  $\rho^f$ , and rigid spherical particles of radius  $a$  and density  $\rho^p$ , as depicted in Figure 1.1. The size of the particles is at the colloidal scale thus  $a < 1 \mu m$  and they are electrostatically charged. The fluid that suspends the particles is an electrolyte solution. Particles will be considered well dispersed throughout this work. Furthermore, the flow conditions considered in this work are in the creeping regime thus the particle Reynolds number  $Re_p$ , defined as the relative strength of the inertial to viscous forces acting on the particles,  $Re_p = \rho^p \dot{\gamma} a^2 / \eta$  is very small compared to unity. Taking into account the Brownian motion of the particles and the hydrodynamic force in the creeping regime another non-dimensional number can be defined, the particulate Péclet number  $Pe_p = 6\pi\eta\dot{\gamma}a^3/k_bT$ .

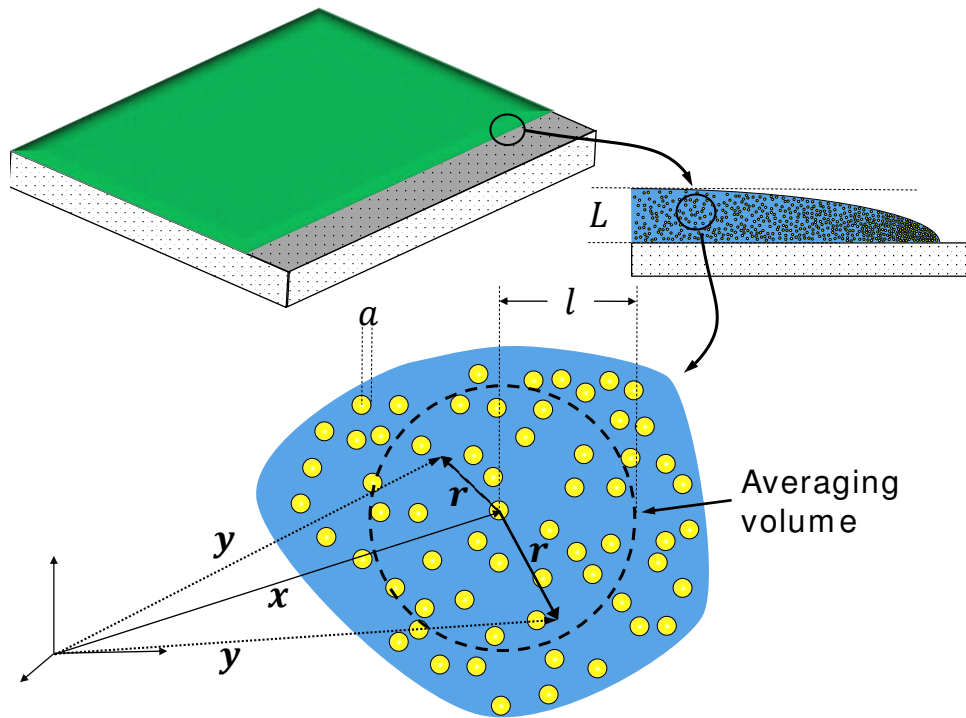


**Figure 1.1:** Schematic representation of volume averaging where the involved length scales, the averaging volume and the system of coordinates are noted.

### 1.1.1 Averaging procedure

In the mixture of fluid and particles described before, the volumes occupied by each phase are respectively  $V^f$  and  $V^p$ . When this mixture flows, the interface between the two phases continuously changes with time. To average these phases into a single effective fluid or mixture, a weighting function  $g(\mathbf{x}, \mathbf{y})$  is introduced. It is given by Anderson and Jackson (1967); Jackson (1997); Nott et al. (2011) and is normalised such that

$$\int g(\mathbf{x}, \mathbf{y}) dV = 1 \quad (1.1)$$

where  $V \equiv V^f + V^p$  and vectors  $\mathbf{x}$  and  $\mathbf{y}$  are expressed on the same frame of reference. A geometrical representation of the vectors is depicted in Figure 1.1, where  $\mathbf{x}$  are the coordinates of the averaged variables and  $\mathbf{y}$  are the coordinates of the vector used for the integration. More specifically, if a radius of integration  $l$  is defined then it means that  $\mathbf{x}$  is the center of an averaging volume with radius  $l$ , and

$|\mathbf{x} - \mathbf{y}| \equiv |\mathbf{r}| < l$ . This statement can be formalised by defining  $l$  of  $g$  as

$$\int_{|\mathbf{r}| < l} g(\mathbf{x}, \mathbf{y}) dV = 1/2. \quad (1.2)$$

Choosing an isotropic form of the smoothing function  $g(|\mathbf{r}|)$  leads to a useful expression

$$\nabla_x g(\mathbf{r}) = -\nabla_y g(\mathbf{r}) \quad (1.3)$$

where the subscripts indicate the variable with respect to which the gradient is taken; for ease of notation hereafter  $\nabla_x$  will be noted as  $\nabla$ . The validity of the volume averaging depends on the separation of scale between the particle radius  $a$ , the averaging radius  $l$  and a macroscopic length  $L$ . More formally, if  $a \ll l \ll L$  then the volume-averaged properties do not depend strongly on the exact form of the smoothing function (Anderson and Jackson (1967); Jackson (1997); Nott et al. (2011)).

If  $\xi(\mathbf{y})$  is a microscopically varying quantity over the entire volume  $V$  of the mixture, then one can define  $\langle \xi \rangle$  as the volume average of this quantity at point  $\mathbf{x}$

$$\langle \xi \rangle(\mathbf{x}) = \int \xi(\mathbf{y}) g(\mathbf{x}, \mathbf{y}) dV \quad (1.4)$$

where  $\langle \rangle$  denotes an averaging procedure over different phases. Here the integral runs over both the solid phase and the fluid phase. Time dependency will not be shown explicitly except in cases that cause ambiguity. The volume fraction of the particle phase  $\phi$  and the volume fraction of the liquid phase  $\epsilon = 1 - \phi$  are given by

$$\phi(\mathbf{x}) = \int \chi(\mathbf{y}) g(\mathbf{x}, \mathbf{y}) dV \quad (1.5)$$

$$\epsilon(\mathbf{x}) = \int [1 - \chi(\mathbf{y})] g(\mathbf{x}, \mathbf{y}) dV \quad (1.6)$$

where  $\chi$  is a phase-indicator function used to simplify the borders of the integrals, and which was introduced by Drew (1983)

$$\chi = \begin{cases} 1 & \text{if } \mathbf{y} \in V^p \\ 0 & \text{if } \mathbf{y} \in V^f. \end{cases} \quad (1.7)$$

In the absence of function  $\chi$  each integral should have been bound by the corresponding phase volume,  $V^p$  for particle phase and  $V^f$  for the fluid phase. When there is no mass transfer between the two phases,  $\chi$  has the properties

$$\frac{D\chi}{Dt} = 0, \quad (1.8)$$

$$\nabla_{\mathbf{y}}\chi = -\mathbf{n}\delta(\mathbf{y} - \mathbf{y}_s) \quad (1.9)$$

where  $D/Dt \equiv \partial/\partial t + \mathbf{u} \cdot \nabla_{\mathbf{y}}$  is the material derivative,  $\mathbf{n}$  is the unit outward normal vector at  $\mathbf{y}_s$  which are points on the surface of the particles, and  $\delta$  is the Dirac delta function.

From here on the volume averages over the solid phase only and over the fluid phase only will be referred to as the solid phase average and the fluid phase average, respectively. The value of  $\xi$  for the solid and fluid phase averages is given by

$$\phi(\mathbf{x})\langle\xi\rangle^s(\mathbf{x}) = \int \chi(\mathbf{y})\xi(\mathbf{y})g(\mathbf{x}, \mathbf{y}) dV \quad (1.10)$$

$$\epsilon(\mathbf{x})\langle\xi\rangle^f(\mathbf{x}) = \int [1 - \chi(\mathbf{y})] \xi(\mathbf{y})g(\mathbf{x}, \mathbf{y}) dV. \quad (1.11)$$

Simple addition of this set of equations leads to the suspension average of the quantity  $\xi$

$$\langle\xi\rangle(\mathbf{x}) = \phi(\mathbf{x})\langle\xi\rangle^s(\mathbf{x}) + (1 - \phi(\mathbf{x}))\langle\xi\rangle^f(\mathbf{x}). \quad (1.12)$$

### 1.1.2 Equations of continuity and momentum

To obtain the volume averaged equations of motion, the integration of the point equations of continuity and momentum for an incompressible medium is needed. They read

$$\nabla_{\mathbf{y}} \cdot \mathbf{u} = 0 \quad (1.13)$$

$$\rho \frac{D_{\mathbf{y}}}{D_{\mathbf{y}}t} \mathbf{u} = \nabla_{\mathbf{y}} \cdot \boldsymbol{\sigma} + \mathbf{b} \quad (1.14)$$

which apply for every point in both phases (fluid and solid). Here,  $\boldsymbol{\sigma}$  is the stress tensor and  $\mathbf{b}$  is the external forces acting on the system. As already discussed in the introduction, it is assumed that the inertial forces are negligibly small. This simplifies the momentum equation to the Stokes equation

$$0 = \nabla_{\mathbf{y}} \cdot \boldsymbol{\sigma} + \mathbf{b}. \quad (1.15)$$

In what follows, the volume averaged equations of motion for the mixture, the solid phase and the fluid phase will be derived, using the averaging procedure discussed previously.

*Mixture*

Starting with the derivation of the volume averaged equation of continuity for the suspension, an average property  $\xi$  of the suspension can be obtained using Equation (1.12) (from hereafter the arguments of the variables are dropped for the sake of compactness)

$$\langle \xi \rangle = \phi \langle \xi \rangle^s + (1 - \phi) \langle \xi \rangle^f \quad (1.16)$$

$$= \int \chi \xi g dV + \int (1 - \chi) \xi g dV. \quad (1.17)$$

Substituting  $\xi$  with the point equation of continuity  $\nabla_{\mathbf{y}} \cdot \mathbf{u}$ , it yields

$$\langle \nabla_{\mathbf{y}} \cdot \mathbf{u} \rangle = \int \chi g \nabla_{\mathbf{y}} \cdot \mathbf{u} dV + \int (1 - \chi) g \nabla_{\mathbf{y}} \cdot \mathbf{u} dV = 0. \quad (1.18)$$

Following Nott et al. (2011), in Appendix 1 it is proven that the above equation can be written as

$$\nabla \cdot [\phi \langle \mathbf{u} \rangle^s] + \nabla \cdot [(1 - \phi) \langle \mathbf{u} \rangle^f] = \nabla \cdot \langle \mathbf{u} \rangle = 0 \quad (1.19)$$

indicating that the suspension is incompressible, as it was intuitively expected for a mixture that is composed from an incompressible fluid and an incompressible particle phase. Nonetheless, it does not mean that the suspension-averaged density  $\langle \rho \rangle = \phi \rho^p + (1 - \phi) \rho^f$  is constant.

The momentum balance equation can be derived for the suspension by substituting  $\nabla_{\mathbf{y}} \cdot \boldsymbol{\sigma}$  in the suspension average property Equation (1.12) in the place of  $\xi$

$$\langle \nabla_{\mathbf{y}} \cdot \boldsymbol{\sigma} \rangle = \int \chi g \nabla_{\mathbf{y}} \cdot \boldsymbol{\sigma} dV + \int (1 - \chi) g \nabla_{\mathbf{y}} \cdot \boldsymbol{\sigma} dV + \int g \mathbf{b} dV = 0 \quad (1.20)$$

where the last term of the equation is the external body forces, like gravity, and they are already averaged for the whole suspension. Again, following Nott et al. (2011), it is proven that (Appendix 2) the above equation can be re-written

$$\nabla \cdot [(1 - \phi) \langle \boldsymbol{\sigma} \rangle^f] + \nabla \cdot [\phi \langle \boldsymbol{\sigma} \rangle^s] + \langle \mathbf{b} \rangle = 0. \quad (1.21)$$

Even though further simplifications can be made, it will be left for discussion later in the text.

*Solid phase*

The same procedure as before can be followed for the derivation of the continuity and momentum equations of the solid phase. Starting with Equation (1.10) and replacing  $\nabla_{\mathbf{y}} \cdot \mathbf{u}$  in the place of  $\xi$  using the same procedure as described in Appendix 1, the continuity equation for the solid phase reads

$$\phi \langle \nabla_{\mathbf{y}} \cdot \mathbf{u} \rangle^s = \int \chi g \nabla_{\mathbf{y}} \cdot \mathbf{u} dV = 0.$$

It can be written as

$$\frac{\partial \phi}{\partial t} + \nabla \cdot [\phi \langle \mathbf{u} \rangle^s] = 0. \quad (1.22)$$

Similarly, the momentum equation for the solid phase following the proof in Appendix 2

$$\int \chi g \nabla_{\mathbf{y}} \cdot \boldsymbol{\sigma} dV + \int \chi g \mathbf{b} dV = 0$$

can be re-written as

$$\nabla \cdot [\phi \langle \boldsymbol{\sigma} \rangle^s] + \int g \boldsymbol{\sigma} \cdot \mathbf{n} \delta(\mathbf{y} - \mathbf{y}_s) dV + \phi \langle \mathbf{b} \rangle^s = 0. \quad (1.23)$$

The term containing the integral can be transformed to a summation over the particles, based on the fact that  $\delta(\mathbf{y} - \mathbf{y}_s)$  is a function that has a non-zero value only on the surface of the particles. It can thus be modified in a summation on all the particles  $p$ , of the surface integral on the surface  $S_p$  of each particle

$$\nabla \cdot [\phi \langle \boldsymbol{\sigma} \rangle^s] + \sum_p \int_{S_p} g \mathbf{n} \cdot \boldsymbol{\sigma} dS + \phi \langle \mathbf{b} \rangle^s = 0 \quad (1.24)$$

The second term of the equation is the volume-averaged traction on the particle surface. In an effort to evaluate this term, Nott et al. (2011) re-wrote it as a sum of stress moments using a Taylor expansion for  $g$ . Going one step further, and using the same technique, he proved that the solid phase momentum balance is equal to the particle phase momentum balance. Previous authors (Anderson and Jackson (1967); Jackson (1997)) had shown that this equality was holding up to  $\mathcal{O}(a^2/L^2)$ . Nott et al.'s development is important since the particle phase averages are more easily accessed by experiments and simulations. For reasons of clarity, the derivation of the particle phase equations are discussed in the next subsection.

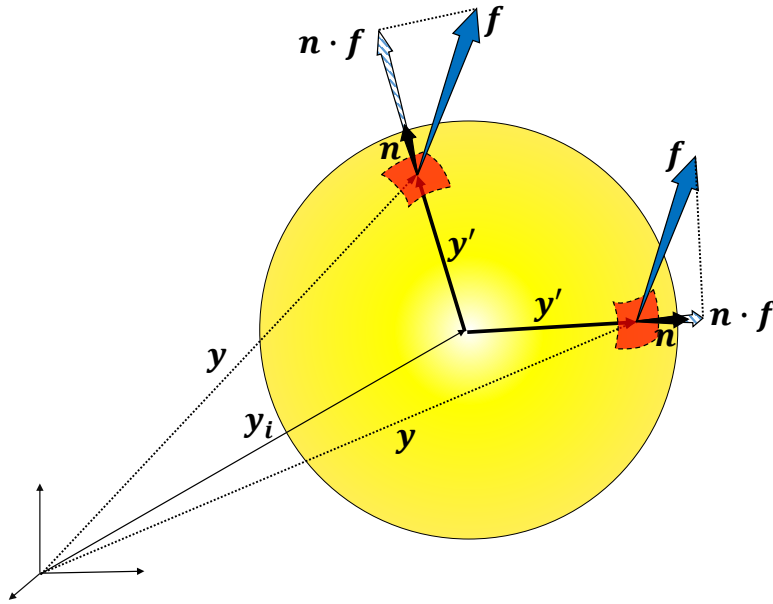


Figure 1.2: Traction  $n \cdot \sigma$  on the particle surface

### Particle phase

Lately, it was proven by Nott et al. (2011) that the momentum equation for the averaged solid phase and averaged particle phase are equal; the latter is just another form of the former. Although the proof is purely mathematical it will be briefly included here, as the sudden change of symbols and expressions may be misleading for the reader. Furthermore, it includes quantities that will be discussed further in the text.

Using the Taylor expansion for  $g(\mathbf{x}, \mathbf{y})$  and the first term of Equation (1.24) (see Appendix 3),  $\phi\langle\sigma\rangle^s$  can be re-written as moments expansion of the surface traction

$$\begin{aligned} \phi\langle\sigma\rangle^s &= n\langle\mathbf{S}\rangle^p - \frac{1}{2}\nabla \cdot n\langle\mathbf{Q}\rangle^p + \dots \\ &+ \sum_p g_i \int_{V_p} \mathbf{y}'\mathbf{b} dV - \frac{1}{2}\nabla \cdot \sum_p g_i \int_{V_p} \mathbf{y}'\mathbf{y}'\mathbf{b} dV + \dots \end{aligned} \quad (1.25)$$

where  $\mathbf{S}$  is the first moment of surface traction,  $\mathbf{Q}$  is the second moment of surface traction on the surface,  $\mathbf{y}' = \mathbf{y} - \mathbf{y}_i$  is the position vector in the frame of reference of particle  $i$  and  $g_i \equiv g(\mathbf{x}, \mathbf{y}_i)$  is the weighting function at the center of particle  $i$ . The moments of traction can be defined starting from the force  $\mathbf{f}$  exerted on the particle which is the zeroth moment of surface traction

$$\begin{aligned}\mathbf{f} &= \int_{S_p} \mathbf{n} \cdot \boldsymbol{\sigma} dS \\ \mathbf{S} &= \int_{S_p} \mathbf{y}' \mathbf{f} dS \\ \mathbf{Q} &= \int_{S_p} \mathbf{y}' \mathbf{y}' \mathbf{f} dS.\end{aligned}$$

Following the same procedure for the second term of the solid momentum equation

$$\sum_p \int_{S_p} \mathbf{n} \cdot \boldsymbol{\sigma} g dS = n \langle \mathbf{f} \rangle^p - \nabla \cdot (n \langle \mathbf{S} \rangle^p) + \nabla \cdot \left( \frac{1}{2} \nabla \cdot n \langle \mathbf{Q} \rangle^p \right) + \dots$$

It is clear that by replacing in Equation (1.24) the developments for  $\phi \langle \boldsymbol{\sigma} \rangle^s$  and  $\sum_p \int_{S_p} \mathbf{n} \cdot \boldsymbol{\sigma} g dS$ , most of the terms are cancelled and the remaining ones concern the particle forces and a sum of moments of the external forces  $\mathbf{b}$ . If the averaged body force  $\phi \langle \mathbf{b} \rangle^s$  is also developed in a sum of moments and substituted in the last development of Equation (1.24), all the remaining terms of the external forces are cancelled and leave behind

$$0 = n v_p \sum_p g_i \mathbf{b}^{ext} + n \sum_p g_i \mathbf{f}_i \quad (1.26)$$

$$= n v_p \langle \mathbf{b}^{ext} \rangle^p + n \langle \mathbf{f} \rangle^p \quad (1.27)$$

where  $\langle \mathbf{f} \rangle^p \equiv \langle \mathbf{f}^h \rangle^p + \langle \mathbf{f}^{ip} \rangle^p + \langle \mathbf{f}^b \rangle^p$  are the averaged forces acting on the particles due to interactions with the fluid, interactions with the particles and contact forces of the particles respectively;  $\langle \mathbf{b}^{ext} \rangle^p$  corresponds to an external force field like gravity.

Recently, Nott et al. (2011) demonstrated that the averaged forces of the particle phase,  $n \langle \mathbf{f} \rangle^p$ , can be written as the sum of the divergence of a stress and an interface drag (the motivation will be discussed in the discussion subsection). This concept can be demonstrated for a pairwise additive force.

Assuming an averaged force,  $\langle \mathbf{f}^X \rangle^p$  is pairwise additive then the force on a particle  $i$  from a particle  $j$  is denoted as  $\mathbf{f}_{ij}^X$

$$n \langle \mathbf{f}^X \rangle^p = \sum_i g_i \sum_{j \neq i} \mathbf{f}_{ij}^X \quad (1.28)$$

which according to Jackson (1997); Nott et al. (2011) can be re-written

$$n \langle \mathbf{f}^X \rangle^p = \sum_i \sum_{j \neq i} g_i \mathbf{f}_{ij}^X - \sum_i \sum_{j \neq i} g_{ij}^X \mathbf{f}_{ij}^X \quad (1.29)$$

where  $g_{ij}^X = g(\mathbf{x}, \mathbf{y}_{ij}^X)$  is the averaging function at the point  $X$ . This point could be one of contact between two particles, or in the case of forces acting from a distance, a point in the middle of the distance between the particles centers. The validity of the above equation lies on the identical vanishing of the second part of the right hand side of the equation, because of Newton's third law,  $\mathbf{f}_{ij}^X = \mathbf{f}_{ji}^X$ . Developing  $g_{ij}^X$  by Taylor expansion about  $g_i$  and substituting in Equation (1.29) yields

$$n\langle \mathbf{f}^X \rangle^p = \nabla \cdot (n\langle \boldsymbol{\sigma}^X \rangle^p) \quad (1.30)$$

where

$$\begin{aligned} n\langle \boldsymbol{\sigma}^X \rangle^p &= \sum_i g_i \sum_{j \neq i} (\mathbf{y}_{ij}^X - \mathbf{y}_i) \mathbf{f}_{ij}^X \\ &\quad - \frac{1}{2} \nabla \cdot \sum_i g_i \sum_{j \neq i} (\mathbf{y}_{ij}^X - \mathbf{y}_i) (\mathbf{y}_{ij}^X - \mathbf{y}_i) \mathbf{f}_{ij}^X \\ &= \sum_i g_i \mathbf{S}_i^X - \frac{1}{2} \nabla \cdot \sum_i g_i \mathbf{Q}_i^X + \dots \end{aligned}$$

The last equality is based on moments of the force acting on the surface of particles. A similar derivation can be devised for the case of non-pairwise additive forces where an arbitrary reference point  $X$  of action has to be defined.

Using the transformation of force to a divergence of stress, for example in the case of particle interactions, yields

$$n\langle \mathbf{f}^{ip} \rangle^p = \nabla \cdot (n\langle \boldsymbol{\sigma}^{ip} \rangle^p). \quad (1.31)$$

In the case of the averaged hydrodynamic force, none of the above assumption holds; it is neither pairwise additive nor does the sum of the force over all particles equals zero. Restricting the particle Reynolds number to be very small, or  $Re_p \ll 1$ , Nott et al. (2011) demonstrated that a decomposition of  $\langle \mathbf{f}^h \rangle^p$  exists

$$n\langle \mathbf{f}^h \rangle^p = n\langle \mathbf{f}^h \rangle_{drag} + \nabla \cdot (n\langle \boldsymbol{\sigma}^h \rangle^p) \quad (1.32)$$

where  $\langle \mathbf{f}^h \rangle_{drag}$  is an interface drag and  $\langle \boldsymbol{\sigma}^h \rangle^p$  a hydrodynamic particle stress. The expressions for the inter-phase drag and the hydrodynamic particle stress are

$$n\langle \mathbf{f}^h \rangle_{drag} = \sum_i g_i \mathbf{f}_i^h + \sum_i \sum_{j \neq i} g_{ij}^m \mathbf{f}_{ij}^h$$

$$n\langle\boldsymbol{\sigma}^h\rangle^p = \sum_i g_i \sum_j (\mathbf{y}_{ij}^m - \mathbf{y}_i) \mathbf{f}_{ij}^h - \frac{1}{2} \nabla \cdot \sum_i g_i \sum_j (\mathbf{y}_{ij}^m - \mathbf{y}_i) \times (\mathbf{y}_{ij}^m - \mathbf{y}_i) \mathbf{f}_{ij}^h + \dots$$

where

$$\mathbf{f}_{ij}^h \equiv \mathbf{R}_{ij}^{FU} \cdot (\mathbf{u}_j - \langle\mathbf{u}\rangle_j) + \mathbf{R}_{ij}^{F\Omega} \cdot (\boldsymbol{\omega}_j - \langle\boldsymbol{\omega}\rangle_j) + \mathbf{R}_{ij}^{FE} : (-\langle\mathbf{e}\rangle_j) + \dots \quad (1.33)$$

where  $\mathbf{R}^{FU}$ ,  $\mathbf{R}^{F\Omega}$  and  $\mathbf{R}^{FE}$  are hydrodynamic resistance tensors.

Combining the above expressions for the averaged particle forces with Equation (1.27) leads to

$$n v_p \langle \mathbf{b}^{ext} \rangle^p + n \langle \mathbf{f}^h \rangle_{drag} + \nabla \cdot \boldsymbol{\Sigma}^p = 0 \quad (1.34)$$

where  $\boldsymbol{\Sigma}^p \equiv n \langle \boldsymbol{\sigma} \rangle^p = n \langle \boldsymbol{\sigma}^h \rangle^p + n \langle \boldsymbol{\sigma}^p \rangle^p + n \langle \boldsymbol{\sigma}^b \rangle^p$ .

### Fluid phase

Lastly, for reasons of completeness, the volume averaged equations for the fluid phase can be derived with the same method used for the suspension. The equation of continuity writes

$$\frac{\partial}{\partial t} (1 - \phi) + \nabla \cdot [(1 - \phi) \langle \mathbf{u} \rangle^f] = 0 \quad (1.35)$$

and the averaged momentum for the fluid phase writes

$$\nabla \cdot [(1 - \phi) \langle \boldsymbol{\sigma} \rangle^f] - \sum_p \int_{S_p} g_p \mathbf{n} \cdot \boldsymbol{\sigma} dS + (1 - \phi) \langle \mathbf{b} \rangle^f = 0. \quad (1.36)$$

### 1.1.3 Remarks

At this point some interesting remarks need to be made. As already discussed from Anderson and Jackson (1967); Jackson (1997); Nott et al. (2011), not all of these equations are needed. A solution to this system can be given by solving two of the above equations, for example the averaged equations for the suspension and the particle phase. All choices are equivalent and it is only a matter of convenience.

In parallel with the development of the volume averaging method, as described above, which is often used in the domain of chemical engineering, there were developments from various communities working on two-phase flows. The *Suspension*

*Balance Model* (SBM) for example, developed by Nott and Brady (1994), is an approach for the study of flowing suspensions (rheological studies), based on the momentum and mass transfer of the particulate phase in a way analogous to a molecular system. Until recently these two approaches were developed and treated separately. A discrepancy of the SBM that was pointed out by Lhuillier (2009) led to a revision of SBM by Nott et al. (2011) using a rigorous volume averaging approach. Therefore, the equations of motion derived above for a general two-phase flow can be used in the framework of the SBM.

The inconsistency in the original suspension balance model by Nott and Brady laid in the assimilation of the solid phase stress (or Batchelor's "particle stress")  $\Sigma^s \equiv \phi \langle \boldsymbol{\sigma} \rangle^s$  (Equation (1.25)) to the particle phase stress  $\Sigma^p$  (Equation (1.34)). Explained differently, the particle phase stress was assimilated to the particles contribution to the suspension stress. While the former is related to the moments of the hydrodynamic interaction forces between particles about their centers, the latter contains the moments of the fluid traction on the surface of the particles. Consequently, since  $\Sigma^p$  was assumed to be identical to  $\Sigma^s$ , conservation equations were closed in a seemingly rigorous and self-consistent way, provided a rheological model was proposed for the solid phase stress  $\Sigma^s$ . Even if the self-consistency of the SBM was not exact, the numerous satisfactory predictions (Morris and Boulay (1999); Frank et al. (2003); Miller et al. (2009); Dbouk et al. (2013)) obtained with the original suspension balance model seem to indicate that the phenomenological forms of the two stress tensors should be close, so that in practice the SBM remains a good approximate model.

Following a common choice made from rheologists, I will focus on the equation for the particle phase (similar with solid phase) and the equation for the mixture. The advantage of this choice is that simulation results for the mixture can be directly compared with the quantities measured experimentally, and particle phase averages are nowadays more and more accessible through particle dynamic simulations. In the remainder of this subsection I will discuss the use of a diffusive flux concept that describes the mass transfer of the particulate phase, as well as the constitutive equations needed for the closure of the following equations

$$0 = \frac{\partial}{\partial t} \phi + \nabla \cdot [\phi \langle \mathbf{u} \rangle^p] \quad (\text{particle}) \quad (1.37a)$$

$$0 = \nabla \cdot \langle \mathbf{u} \rangle \quad (\text{suspension}) \quad (1.37b)$$

$$0 = n v_p \langle \mathbf{b}^{ext} \rangle^p + n \langle \mathbf{f}^h \rangle_{drag} + \nabla \cdot \Sigma^p \quad (\text{particle}) \quad (1.38a)$$

$$0 = \langle \mathbf{b} \rangle + \nabla \cdot \Sigma^f + \nabla \cdot \Sigma^s \quad (\text{suspension}) \quad (1.38b)$$

where  $\Sigma^f = (1 - \phi) \langle \sigma \rangle^f$ .

## 1.2 The Suspension Balance Model closure

In the previous subsection the equations of momentum include terms ( $\Sigma^s$ ,  $\Sigma^p$ ,  $n \langle \mathbf{f}^h \rangle_{drag}$ ) that need further discussion and closure relations. To correctly predict the flow of a suspension, closure relations need to include the most important rheological features. When particles are present inside a liquid, two principal rheological effects can be observed: a non-Newtonian rheology and the appearance of possible normal stress differences (NSD). One expression of this particular behaviour of flowing suspensions is the phenomenon of shear-induced migration.

In the original Suspension Balance Model (Nott and Brady (1994)), the particle-phase stress  $\Sigma^p$  was equal to the solid-phase stress  $\Sigma^s$ . Since it is now clear that the particle and solid phase stresses are in principle different, although probably close, it is possible to use the SBM keeping in mind that some inconsistencies might arise and that there is no strict reason to equate the two tensors. Thus, when used for the particle momentum balance (Equation (1.38a)), since the objective is to provide a mechanism for shear induced migration under the effect of normal stress differences, the particle phase stress ( $\Sigma^p$ ) can be modelled with only the normal stress contribution of  $\Sigma^s$ . On the other hand, when the suspension momentum equation (Equation (1.38b)) is considered, then the solid stress contribution ( $\Sigma^s$ ) can contain both normal and shear contributions. This approach was followed by Frank et al. (2003); Semwogerere et al. (2007); Clausen (2013) and leads to results in very good agreement with experimental data in fully-developed flows.

Thus, taking into account that  $\Sigma^p = \Sigma^s$  and that only the normal part of  $\Sigma^p$  is relevant in the particle phase equation, the system of Equations (1.37a), (1.37b), (1.38a) and (1.38b) will be detailed below.

### 1.2.1 Particle phase transport equation

In an attempt to decrease the number of unknowns and express the equations in quantities that are known (or about to be solved), by combining Equations (1.37a)

and (1.37b) the mass conservation of the particle phase can be written as

$$\frac{\partial \phi}{\partial t} + \langle \mathbf{u} \rangle \cdot \nabla \phi = -\nabla \cdot \mathbf{j} \quad (1.39)$$

where  $\mathbf{j} = \phi \langle \mathbf{u} \rangle^p - \langle \mathbf{u} \rangle$  is the mass flux taking place in the “effective fluid” (the suspension) and is a function of the slip velocity between particles and suspension. The slip velocity can be given as a function of the drag force between the particle and the suspension phases by

$$\phi \langle \mathbf{u} \rangle^p - \langle \mathbf{u} \rangle = -\frac{2a^2}{9\eta} n f(\phi) \langle \mathbf{f}^h \rangle_{drag}. \quad (1.40)$$

Combining Equations (1.39) and (1.40)

$$\frac{\partial \phi}{\partial t} + \langle \mathbf{u} \rangle \cdot \nabla \phi = \nabla \cdot \left[ \frac{2a^2}{9\eta} n f(\phi) \langle \mathbf{f}^h \rangle_{drag} \right]$$

where  $f(\phi)$  is the sedimentation hindrance function, but more general expressions involving a resistance tensor might be used. Furthermore, replacing  $n \langle \mathbf{f}^h \rangle_{drag}$  with the momentum equation for the particle phase (Equation (1.38a)) yields

$$\frac{\partial \phi}{\partial t} + \langle \mathbf{u} \rangle \cdot \nabla \phi = -\nabla \cdot \left[ \frac{2a^2}{9\eta} f(\phi) (n v_p \langle \mathbf{b}^{ext} \rangle^p + \nabla \cdot \Sigma^p) \right]. \quad (1.41)$$

Assuming that external forces such as gravity are negligible and that  $\Sigma^p$  has only normal contributions, Equation (1.41) can be written

$$\frac{\partial \phi}{\partial t} + \langle \mathbf{u} \rangle \cdot \nabla \phi = -\nabla \cdot \left[ \frac{2a^2}{9\eta} f(\phi) \nabla \cdot \Sigma_{\perp}^p \right]. \quad (1.42)$$

In Frank et al. (2003) it was suggested that,  $\Sigma_{\perp}^p$  can be decomposed into a contribution from thermodynamics

$$\Sigma_{t\perp}^p = -a(\phi) \mathbf{I} \quad (1.43)$$

where  $a(\phi)$  is the suspension stress at equilibrium, and another contribution from the hydrodynamic interactions

$$\Sigma_{h\perp}^p = -\eta \dot{\gamma} [\mathbf{b}^{-1}(\phi, Pe) + \mathbf{c}^{-1}(\phi)]^{-1} \quad (1.44)$$

which was designed by Frank et al. (2003) to reproduce the correct asymptotic regimes  $Pe \ll 1$  and  $Pe \gg 1$  based on the rheology determined analytically and numerically by Brady and Vicic (1995); Phung et al. (1996); Morris and Katyal (2002) for Brownian hard-spheres. The hydrodynamically-driven functions are

$$\mathbf{b}(\phi, Pe) = A\lambda^B Pe\phi \left(1 - \frac{\phi}{\phi_{max}}\right)^{-3}$$

$$\mathbf{c}(\phi) = \lambda^H \eta_n(\phi).$$

The parameters  $A$ ,  $\lambda^B$  and  $\lambda^H$  are parameters allowing the modelling of the normal stress differences. The normal stress viscosity for hard spheres  $\eta_n(\phi)$  is given by Morris and Boulay (1999)

$$\eta_n = 0.75 \left(\frac{\phi}{\phi_{max}}\right)^2 \left(1 - \frac{\phi}{\phi_{max}}\right)^{-2}. \quad (1.45)$$

In the works of Frank et al. (2003) and Semwogerere et al. (2007) the isotropic term  $a(\phi)$ , part of Equation (1.43), was termed “thermal stress contribution”. It was chosen as the osmotic pressure  $\Pi$  of a suspension of hard-spheres. Following this principle one can extend this thermal stress contribution to suspensions of “soft particles” (non-hard sphere) by means of the osmotic pressure. Further details on this approach will be included in Section 2 where ways to compute the equilibrium osmotic pressure will also be described.

### 1.2.2 Suspension momentum balance

In the suspension momentum balance Equation (1.38b), there are two stress tensors in need of closure relations,  $\Sigma^f$  and  $\Sigma^s$ . For the former, if the fluid phase is Newtonian then  $\Sigma^f$  is given by

$$\Sigma^f = -(1 - \phi)\langle p \rangle^f \mathbf{I} + 2\eta\langle \mathbf{e} \rangle \quad (1.46)$$

where  $(1 - \phi)\langle p \rangle^f \mathbf{I}$  has the role of a Lagrange multiplier to enforce incompressibility and  $\mathbf{e} = \frac{1}{2}(\nabla \mathbf{u} + \nabla \mathbf{u}^T)$  is the rate of strain tensor. In the latter expression  $\langle \mathbf{e} \rangle = (1 - \phi)\langle \mathbf{e} \rangle^f$  because particles are considered rigid.

In this work the solid phase stress ( $\Sigma^s$ ) is considered to have two contributions, one of hydrodynamic origin and one of thermodynamic origin. Following Morris and Boulay (1999) one can decompose its hydrodynamic part  $\Sigma_h^s$  into a shear and normal contribution, which writes

$$\Sigma_h^s = 2\eta_0\eta^s(\phi)\langle \mathbf{e} \rangle + \Sigma_{h\perp}^p \quad (1.47)$$

where  $\Sigma_{h\perp}^p$  is a tensor generating anisotropic normal stresses and given by (Equation (1.44)),  $\eta^s$  is the non-dimensional relative viscosity due to the particle phase,

$\eta_n$  is the normal component of the particulate viscosity and  $\dot{\gamma} = \sqrt{2\langle \mathbf{e} \rangle : \langle \mathbf{e} \rangle}$ . The thermodynamic part of the solid phase stress tensor ( $\Sigma_t^s$ ), as it was discussed for the particle transport equation, is considered to be isotropic and independent of shear. It can thus be considered that  $\Sigma_t^s \sim -\Pi \mathbf{I}$ , where  $\Pi$  is the equilibrium osmotic pressure. Nevertheless, since this term is isotropic, it does not affect the streamlines of the suspension flow and it can be neglected from the suspension momentum equation. Combining the above and neglecting external forces the suspension momentum equation reads

$$0 = -\nabla((1 - \phi)\langle p \rangle^f) + 2\nabla \cdot (\eta_0 \langle \mathbf{e} \rangle) + 2\nabla \cdot (\eta_0 \eta^s(\phi) \langle \mathbf{e} \rangle) + \nabla \cdot \Sigma_{h\perp}^p \quad (1.48)$$

A further advancement in the above equation can be given by combining the solid phase contribution to the shear stress,  $2\eta_0 \eta^s(\phi) \langle \mathbf{e} \rangle$ , with the contribution of the fluid to the shear stress,  $2\eta_0 \langle \mathbf{e} \rangle$ ,

$$0 = -\nabla((1 - \phi)\langle p \rangle^f) + 2\nabla \cdot (\eta_0(1 + \eta^s(\phi)) \langle \mathbf{e} \rangle) + \nabla \cdot \Sigma_{h\perp}^p \quad (1.49)$$

This last equation can be solved assuming that constitutive equations are given for the shear and normal viscosity. Their form were explicitly designed for hard spheres, neglecting shear-thinning or shear-thickening.  $\eta_n$  is given by (Equation (1.45)) and

$$1 + \eta^s(\phi) = 1 + 2.5\phi \left(1 - \frac{\phi}{\phi_{max}}\right)^{-1} + 0.1 \left(\frac{\phi}{\phi_{max}}\right)^2 \left(1 - \frac{\phi}{\phi_{max}}\right)^{-2} \quad (1.50)$$

### 1.3 Code validation case

The system of Eulerian equations (1.42)-(1.49) will be solved using the code JADIM developed in the Institut de Mecanique des Fluides de Toulouse (IMFT). It is a generic fluid dynamics code, solving the three-dimensional Navier Stokes equations. During this work, an additional functionality was added to the existing code to take into account a variable diffusion coefficient for the solution of the convection-diffusion equation (1.42) used for the transport of scalar quantities. For the discretization of the system of equations, the finite volume method on a structured mesh was used and for the time integration a hybrid Runge-Kutta/Crank-Nicholson scheme was employed, leading to a method of second order in both space and time.

The implementation of the scalar transport was validated against an analytical solution obtained by Mason and Weaver (1924) for a case of particle settling. In this

publication they compared a one-dimensional analytical solution of the convection-diffusion equation against experimental measurements of gamboge grains settling from Perrin (1910).

The experimental setup consists of a tube with a liquid of known viscosity  $\mu$ , where a known particle number  $n_0$  of size  $a$  is dispersed homogeneously. The next step is leave the system to evolve freely, which means that apart from the self-diffusion of the particles, the only external force acting on them is the gravity  $g$ . Observations can be made with different techniques that can quantify the concentration of particles that settle towards the bottom of the tube. The velocity of moving particles is called *terminal velocity* and can be calculated for a dilute suspension by Newton's second law, assuming that the particle Reynolds number is low enough for the Stokes drag law to be valid. Eventually, particle concentration will become higher at the bottom of the tube than on the surface. Concentration profiles for different times can be found solving the scalar transport equation

$$\frac{dn}{dt} = A \frac{\partial^2 n}{\partial x^2} - B \frac{\partial n}{\partial x}$$

where  $A = k_b T / (6\pi\mu a)$  is the diffusion coefficient and  $B = 2g\delta a^2 / (9\mu)$  is the Stokes velocity;  $k_b$  is the Boltzmann constant,  $\delta$  is defined as  $(\rho_p - \rho_f)$  and  $g$  the gravity constant. A solution can be found, given that the top and bottom surface have an impermeable boundary (no flux) and symmetry is considered for both sides. The no flux boundary condition for the scalar transport equation is

$$A \frac{\partial n}{\partial x} = Bn.$$

Using the substitutions  $lx = y$ ,  $\frac{A}{Bl} = a$ ,  $\frac{l}{B} = \beta$  and  $\beta t' = t$ , the above system of equations is reduced to

$$\frac{\partial n}{\partial t'} = a \frac{\partial^2 n}{\partial y^2} - \frac{\partial n}{\partial y} \tag{1.51}$$

$$a \frac{\partial n}{\partial y} = n, \quad y = 0, \quad y = 1. \tag{1.52}$$

The solution of the above system of equations considering an initial homogeneous particle concentration  $n_0$  is

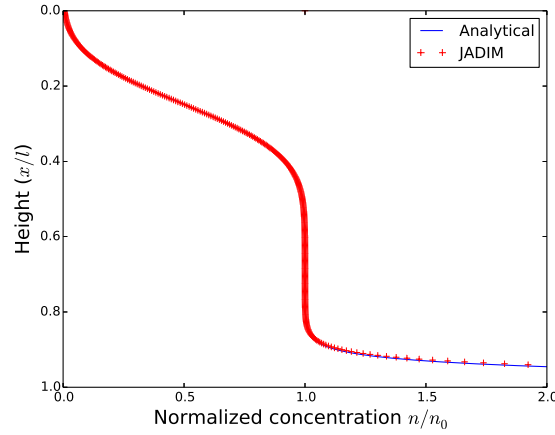


**Figure 1.3:** Number density of particles  $n$ , normalised by the initial number density  $n_0$  along the height  $l$  of the sedimentation tube

$$\frac{n}{n_0} = \frac{e^{y/a}}{a(e^{1/a} - 1)} + 16a^2\pi e^{(2y-t')/4a} \sum_{m=1}^{\infty} \frac{e^{-am^2\pi^2t'} m(1 \mp e^{-1/2a}) [\sin m\pi y + 2\pi m a \cos m\pi y]}{(1 + 4\pi^2 m^2 a^2)^2} \quad (1.53)$$

with upper sign holding for  $m$  even and the lower for  $m$  odd. In Figure 1.3 the numerical solution of the SBM obtained with JADIM and the analytical solution 1.53 are both plotted for a value of  $a = 0.025$  and show a very good agreement. Note however that no shear rate enters this problem, so that only the implementation of the normal thermodynamic stress is tested here. Other simulations based on the SBM are presented in the rest of this chapter.

#### 1.4 Discussion and Summary

In this section a modelling strategy was developed to simulate macroscopically suspensions containing interacting nano-particles. Using the volume averaging method (Anderson and Jackson (1967); Jackson (1997); Nott et al. (2011)) it was made possible to derive a system of equations that can be solved by a Computational Fluid Dynamics software. The system consists of three equations. The first two equations are the suspension incompressibility and momentum equations

$$0 = \nabla \cdot \langle \mathbf{u} \rangle \quad (1.54)$$

$$0 = -\nabla(1 - \phi)\langle p \rangle^f \mathbf{I} + 2\nabla \cdot (\eta_0(1 + \eta^s(\phi))\langle \mathbf{e} \rangle) + \nabla \cdot \Sigma_{\perp}^p \quad (1.55)$$

and the third one is the suspension-averaged particle transport equation

$$\frac{\partial \phi}{\partial t} + \langle \mathbf{u} \rangle \cdot \nabla \phi = -\nabla \cdot \frac{2a^2}{9\eta} f(\phi) \nabla \cdot \Sigma_{\perp}^p. \quad (1.56)$$

where  $\Sigma_{\perp}^p = -\left(\Pi \mathbf{I} + \eta \dot{\gamma} [\mathbf{b}^{-1}(\phi, Pe) + \mathbf{c}^{-1}(\phi)]^{-1}\right)$ .

Solution of this equation will give access to the suspension velocity field, the suspension pressure and more importantly the particle concentration. The right hand side of Equation (1.56) contains two terms, the equilibrium osmotic pressure  $\Pi$  related to the thermodynamic diffusion of particles, and a term related to the shear induced migration of particles. These two terms can have opposing effects; shear induced migration has the tendency to transport particles towards lower shear regions, while the osmotic pressure is a term which is related to the opposition of the particles to be concentrated. For example, in a channel flow the particles will start moving towards the center of the channel, where a low shear zone lies, creating a concentration gradient. On the other hand, entropic forces such as the osmotic pressure, have the tendency to oppose the creation of concentration gradients and will disperse them. Of course the actual weight of each one of these terms depends on the flow conditions, the particle size and the electrostatic charge of the particles. In order to evaluate the significance of each term for different flow conditions, the shearing flow of concentrated nano-particles will be presented in Section 2. Generally it is expected that for suspension flows with  $Pe \ll 1$  the osmotic pressure has more weight since the system is close to equilibrium, while in flows where  $Pe > 1$  the shear induced term is expected to be more relevant.

## 2 When do we have to include thermodynamic and hydrodynamic effects in continuous models of flowing colloidal suspensions?

As mentioned in the previous section, flowing suspensions contain particles that undergo both hydrodynamic and colloidal interactions. These interactions induce macroscopic mass fluxes that are modelled in the SBM. Hydrodynamic interactions give rise to shear-induced migration modelled with a normal stress tensor such as  $\Sigma_{h,\perp}^p$ , with particles moving from high shear zones to low shear zones. Colloidal interaction, and in particular electrostatic interactions, generate a diffusive flux from highly concentrated regions to low concentration regions modelled with the term involving the normal thermodynamic stress  $\Sigma_{t,\perp}^p \simeq -\Pi I$ . Both types of particle fluxes are rather delicate to model at the continuous level, although accounting for them is necessary to design efficiently large-scale systems.

The thermodynamic mass flux due to colloidal interactions is independent of the shear rate, while the migration flux due to hydrodynamic interactions is proportional either to the shear rate or to its gradients. The thermodynamic flux therefore dominates over shear-induced migration (SIM) at low shear rates, and vice versa. However, what “low” actually means in charge-stabilized colloidal suspensions has never been clearly assessed. It is nonetheless necessary to determine a priori if SIM models have to be implemented in continuous flow solvers. The aim of the article reproduced hereafter is precisely to establish and understand the flow diagram discriminating the “hydrodynamic” region (dominated SIM effects) from the “colloidal” region (dominated by electrostatic effects) in the  $(\phi, Pe, \kappa a, Zl_B/a)$  parameter space. These parameters are the volume fraction, the Péclet number, the scaled electrostatic interaction range, and the scaled colloidal surface charge, respectively.

To achieve this, we extend the suspension balance model (SBM) developed for Brownian hard spheres by Jeff Morris’ group Frank et al. (2003) to include electrostatic interactions as described in the previous section. In the article, we provide information on the different methods used to compute the osmotic pressure of the suspension as a function of the volume fractions and other physico-chemical parameters. We then perform simulations using this extended SBM in a channel flow to locate the boundary of colloidal and hydrodynamic flow regimes in the parameter space mentioned above. Finally, we propose a simple analytical model to predict this “phase” boundary and validate it against numerical results.

The main conclusions of this work are that (i) the usual Péclet number used to

discriminate these regimes for Brownian hard spheres is not relevant for (even moderately) charge-stabilized suspensions (ii) a rescaled Péclet number comparing viscous and thermodynamic (entropic and electrostatic) stress scales can be designed to build the flow diagram analytically and, (iii) the thermodynamic stress scale, here considered as the osmotic pressure of the bulk suspension, has to be modelled carefully to account for subtle electrostatic effects that can influence the flow regime, such as ion condensation.

It is now possible to turn back to the problem of surface coating with a paint made of nano-containers. Since the boehmite nano-particles need to remain separated to offer a good coverage and homogeneity, we must operate at a  $pH$  and an ionic strength such that they remain quite strongly charge-stabilized. At the same time, the drying of the paint is known to be stronger near edges so that a tangential flow can be created inside the drying suspension (this is responsible for the well-known “coffee ring effect”). The evaporation rate of water at room temperature is of the order of  $0.1 \text{ kg/h/m}^2$ , corresponding to an air-water interface velocity of the order of  $V_v = 30 \text{ nm/s}$ . The horizontal propagation of drying fronts leads to the existence of semi-dry zones next to liquid zones, the water being pumped by capillarity through the semi-dried zones. This induces horizontal velocities  $V_h$  in the drying film that are of the order of  $\alpha V_v$ , where  $\alpha$  is the ratio of the interfacial surface area of semi-dried zones to the surface area open to the flow between the liquid and semi-dried zone. This ratio can be of the order of  $10^5$  for semi-dried zones in the centimeter scale and a film thickness of the order of one micrometer. The horizontal velocity can therefore be as high as  $\text{mm/s}$ . The shear rate in the film would then be of the order of the  $1000 \text{ s}^{-1}$ . The size of the boehmite particles is however of the order of  $10 \text{ nm}$  so that the Péclet number is  $\sim 10^{-3}$ . As electrostatic interactions are important, the relevant number is the rescaled  $Pe^*$ , which is much smaller than  $Pe$ . In light of the results of this article, this very crude analysis shows that the drying of a film of nano-particles is always very far in the colloidal regime and shear-induced migration can be neglected. Therefore, in the rest of this thesis, focus will be put on the physico-chemical characterization of boehmite, with a view to predicting the equation of state  $\Pi(\phi)$  as accurately as possible, and at determining if these particles can indeed adsorb and desorb corrosion inhibitors.

# The continuous modeling of concentrated colloidal suspensions in shear flows

Y. Hallez, I Gergianakis, M. Meireles & P. Bacchin

January 18, 2016

## Abstract

Flows of concentrated colloidal suspensions may exhibit a rich set of behaviors due to both hydrodynamic and colloidal interactions between the particles. Colloidal flows are generally modeled with an effective Navier-Stokes equation and a mass balance for the solid phase involving a diffusion coefficient given by the generalized Stokes-Einstein relation. This picture corresponds to a near equilibrium regime in which entropic and colloidal forces dominate over hydrodynamic interactions, the latter being totally ignored. On the other hand, suspension flows far from equilibrium require the modeling of important hydrodynamic stresses responsible in particular for shear-induced migration, a phenomenon known to occur in some industrial processes involving colloids, such as ultrafiltration. The choice of the proper modeling ingredients requires the knowledge of the domains in parameter space in which colloidal or hydrodynamic effects are dominant. In this article, such a phase diagram is established for a channel flow of charge-stabilized colloids with a version of the suspension balance model including both colloidal and hydrodynamic effects at the continuous level. It is shown that the classical Péclet number is not sufficient to characterize the flow regime. The phase boundary between the colloidal and hydrodynamic regimes exhibits an original shape explained by the dependence of electrostatic interactions with the colloidal surface charge, and in particular by the phenomenon of ionic condensation. We also show that the phase diagram can be predicted based on the knowledge of a rescaled Péclet number comparing the hydrodynamic stress scale to the osmotic pressure of the suspension. The criterion determined here provides important guidelines for an efficient modeling of colloidal flows.

## 1 Introduction

Flows of colloidal suspensions are involved in a number of everyday life and industrial applications such as the spreading of paint, slurry transport in pipes, ceramic molding, coating, filtration or food and beverage processing. Being able to predict and control these flows is essential to optimize colloid-based engineering processes, for example with a view to reducing energy loss by viscous dissipation in pipe flows, controlling mixing and segregation in particle suspensions, or increasing mass or heat transfer phenomena in complex fluids. The characteristics of suspension flows depend on the hydrodynamic and colloidal interactions between particles, as well as on their Brownian motion.

The behavior of suspension flows of Brownian hard spheres is often described in two limits, either close to equilibrium or far from equilibrium. The extent of the departure from equilibrium is measured with the Péclet number  $Pe$ , which can be considered either as a ratio of diffusion and advection time scales, or as a ratio of viscous hydrodynamic and thermal stress scales. Near-equilibrium systems are characterized by  $Pe \ll 1$  and the far-from-equilibrium “pure hydrodynamic” limit corresponds to  $Pe \gg 1$ .

Due to the presence of solid particles in the fluid phase, suspension flows may differ from single-phase flows both qualitatively and quantitatively. The effect of the solid dispersed phase on the bulk suspension rheology is twofold: the existence of particles and of interactions between them increases the effective suspension viscosity and can generate potentially anisotropic normal stresses. For  $Pe \rightarrow 0$ , the normal stresses are nearly isotropic and dominated by the contribution of the classical osmotic pressure of the suspension  $\Pi$  defined at equilibrium. Being an isotropic stress, the osmotic pressure does not influence the streamlines of the suspension flow. For large Péclet numbers, normal stress differences appear and are commensurate with the

average normal stress. The normal stress differences influence the structure of curvilinear flows [18].

Apart from modifying the flow streamlines, the hydrodynamic and colloidal interactions determine mass transport phenomena by generating “shear-induced” and “thermodynamic” mass fluxes, respectively. The thermodynamic flux  $\mathbf{j}_{\text{th}}$  exists in response to an asymmetry of colloidal interactions around one point, which is translated into the existence of a gradient of osmotic pressure  $\Pi$  at this point, so that  $\mathbf{j}_{\text{th}} \propto -\nabla\Pi$ . If the chain rule is employed on this relation, the thermodynamic flux may be written  $\mathbf{j}_{\text{th}} = -D(\phi)\nabla\phi$ , where  $D(\phi)$  is the effective gradient diffusion coefficient given by the well known generalized Stokes-Einstein (GSE) relation. Note that this flux only requires the existence of colloidal interactions and a concentration gradient. It therefore exists at any shear rate. The shear-induced mass flux  $\mathbf{j}_{\text{s}}$  corresponds to the shear-induced migration (SIM) phenomenon[16]. It’s form can be either constructed from phenomenological arguments or from the suspension balance model, but in both cases its intensity is related to that of the shear rate  $\dot{\gamma}$  and of the gradient of shear rate[25, 22]. Hence this flux vanishes when the shear rate vanishes. From this discussion, we understand that  $\mathbf{j}_{\text{th}} \gg \mathbf{j}_{\text{s}}$  near equilibrium and that  $\mathbf{j}_{\text{s}} \gg \mathbf{j}_{\text{th}}$  sufficiently far from equilibrium.

This brief review of possible physical effects in suspension flows can help to shed some light on the various modeling strategies that have been previously adopted. Crossflow filtration is a process in which all these effects have been considered at some point. If the momentum balance equation of the suspension was generally considered as a (Navier-)Stokes equation with an effective suspension shear viscosity, considerable discussion was involved concerning the modeling of mass transport. It was recognized that considering only a Fickian mass flux with the Stokes-Einstein diffusion coefficient was not sufficient to reproduce available experimental results. Additional phenomena were considered to solve this problem, among them shear-induced migration and the thermodynamic flux described above. On one hand it was recognized that including the shear-induced migration flux  $\mathbf{j}_{\text{s}}$  in modeling attempts was necessary for typical micro-filtration conditions, i.e. for particles larger than, say,  $0.5\ \mu\text{m}$  and shear rates of the order of  $1000\ \text{s}^{-1}$ [39, 29, 4, 2]. On the other hand, considering only the thermodynamic flux  $\mathbf{j}_{\text{th}}$  in the mass transport equation led to an excel-

lent agreement with experimental measurements of bovine serum albumin (BSA) and lactoferrin transport in nano-filtration experiments.[6, 7]. These macromolecules have a radius of gyration of the order of  $3\ \text{nm}$ . From a theoretical point of view, nano- and micro-filtration are the same flow of a colloidal suspension, but with a Péclet number ranging between  $\sim 0$  in nano-filtration to  $O(10^2)$  or higher in micro-filtration. The published modeling strategies reported here thus perfectly illustrate the aforementioned idea that  $\mathbf{j}_{\text{th}}$  dominates other fluxes near equilibrium and that  $\mathbf{j}_{\text{s}}$  is the flux determining mass transport far from equilibrium.

If it is true that including both fluxes in a model of colloidal flow should always lead to correct solutions, it would be, to date, a somewhat uncontrolled model. Indeed, the closure relations for both fluxes are still not fully understood. The thermodynamic flux given by the GSE involves in particular a function depending on many-body hydrodynamic interactions between colloids whose form is often quite heuristic and which has a great influence on the diffusion coefficient[28]. It also requires the knowledge of the equation of state of the suspension depending on many-body colloidal interactions, the precise determination of which is still an active area of research. On the other hand, the most consistent definition of the shear-induced migration flux, based on the suspension balance model[22], involves the divergence of an hydrodynamic stress depending on many-body hydrodynamics and whose form is only known in asymptotic limits, even for hard spheres[12]. It is then of practical importance to determine a priori if a prescribed colloidal flow is “near” or “far” from equilibrium, so that the modeling efforts can be concentrated on the one and only relevant flux, if possible. This is the aim of the present work.

For Brownian hard spheres, these “colloidal” (near equilibrium) and “hydrodynamic” (far from equilibrium) regimes are usually characterized by  $Pe < 1$  and  $Pe > 1$ , respectively. Indeed, the suspension micro-structure (determining the rheology) is the result of a balance between the distorting hydrodynamic stress and the restoring thermal stress, the ratio of which precisely defines the Péclet number. It has already been shown that the thermal stresses keep the microstructure of a suspension of hard spheres almost isotropic up to  $Pe = 10$ [11]. In suspensions of “soft” particles (non-hard spheres), the forces helping to restore the micro-structure against the flow deforma-

tion are both of thermal and colloidal (here electrostatic) origin. The pertinent thermodynamic stress scale is therefore not the thermal scale, especially in concentrated suspensions, and the classical Péclet number is therefore not a relevant dimensionless group anymore as will be shown in this article. In this work, we will introduce a “dressed” Péclet number  $Pe^*$  as a ratio comparing the hydrodynamic and thermodynamic stress scales, the latter being provided by the equation of state of the suspension including both thermal and interaction-induced stresses. The aim of this article is to demonstrate that this number can be computed a priori and used to predict the transition from a colloidal near-equilibrium regime to a hydrodynamic far-from-equilibrium regime in a suspension flow containing charge-stabilized colloids.

To highlight how the flow regime can be anticipated, we will consider the flow of a charge-stabilized colloidal suspension between parallel plates. The model solved in order to predict the concentration and velocity profiles across the channel, accounting for both electrostatic and hydrodynamic effects, is presented in section 2. The numerical and analytical computation of a phase diagram identifying the colloidal and hydrodynamic domains in the parameter space will be presented in section 3. From these results, we will show that the colloidal and hydrodynamic regimes are determined by  $Pe^* \ll 1$  and  $Pe^* \gg 1$ , respectively. A discussion on the main hypotheses and on the conclusions of this work is presented in section 4.

## 2 Model

### 2.1 The Suspension Balance Model

We consider the fully developed flow between two flat plates. The direction of the flow is along the  $x$  axis and the direction orthogonal to the plates is the  $y$  axis. The volume-averaged momentum and mass conservation equations are written in the suspension balance model (SBM) formalism [22, 18], and more specifically an adaptation of the one developed by Frank and coworkers[12] for Brownian hard spheres. In the fully developed flow, the suspension velocity  $\mathbf{u}$  is perpendicular to the scalar gradient so the governing equations are

$$\nabla \cdot \boldsymbol{\Sigma} = \mathbf{0} \quad (1)$$

$$\nabla \cdot \mathbf{j} = 0 \quad (2)$$

where  $\boldsymbol{\Sigma}$  is the total bulk stress in the suspension,

$$\mathbf{j} = \phi(\mathbf{u}^p - \mathbf{u}) \quad (3)$$

is the particle migration flux relative to the bulk velocity, and  $\mathbf{u}^p$  is the particle phase average velocity. The suspension stress can be decomposed in

$$\boldsymbol{\Sigma} = -P\mathbf{I} + \eta\eta_s(\phi)\mathbf{e} + \boldsymbol{\Sigma}^s \quad (4)$$

where  $P$  is a pressure which can contain contributions from the fluid and solid phases but is in any case fully determined by the suspension incompressibility condition  $\nabla \cdot \mathbf{u} = 0$ ,  $\eta_s$  is the suspension relative shear viscosity modeled here as

$$\eta_s(\phi) = 1 + 2.5\phi(1 - \bar{\phi})^{-1} + 0.1\bar{\phi}^2(1 - \bar{\phi})^{-2} \quad (5)$$

and depending on the particle volume fraction  $\phi$  and the maximum volume fraction  $\phi_m$  through  $\bar{\phi} = \phi/\phi_m$ ,  $\mathbf{e}$  is the average rate of strain tensor, and  $\boldsymbol{\Sigma}^s$  is the contribution of the solid phase to the bulk stress[3]. In the unidirectional flow considered here, only the projection of (1) in the  $x$  direction is necessary and there is no contribution from the particle stress to the suspension momentum balance. It reads

$$-\partial_x P + \partial_y(\eta\eta_s(\phi)\partial_y u) = 0. \quad (6)$$

This equation can be integrated once to yield, with  $\dot{\gamma} \equiv \partial_y u$  and  $\partial_y u|_{y=0} = 0$ ,

$$\eta\eta_s(\phi)\dot{\gamma} = y\partial_x P \quad (7)$$

The solid phase flux  $\mathbf{j}$  is determined with the SBM. The particle phase momentum conservation equation reads

$$\rho\langle \mathbf{f}_d \rangle + \nabla \cdot \boldsymbol{\Sigma}^p = 0 \quad (8)$$

where  $\rho$  is the number density of particles,  $\rho\langle \mathbf{f}_d \rangle$  is the average drag experienced by the particles, and  $\boldsymbol{\Sigma}^p$  is the particle phase stress[23]. The drag force is given as a function of the slip velocity between the solid and bulk phases as

$$\rho\langle \mathbf{f}_d \rangle = -\frac{9\eta}{2a^2}f^{-1}(\phi)\phi(\mathbf{u}^p - \mathbf{u}), \quad (9)$$

where  $f(\phi)$  is the sedimentation hindrance function. Combining (3), (8), and (9) leads to

$$\mathbf{j} = \frac{2a^2}{9\eta}f(\phi)\nabla \cdot \boldsymbol{\Sigma}^p. \quad (10)$$

In the present unidirectional flow, the mass conservation equation (2) then reduces to

$$\partial_y \left[ \frac{2a^2}{9\eta}f(\phi)\partial_y \Sigma_{yy}^p \right] = 0 \quad (11)$$

The term between the brackets is constant and equal to zero due to the symmetry around the  $y = 0$  plane. The mass conservation equation is then simply  $\partial_y \Sigma_{yy}^p = 0$ , or  $\Sigma_{yy}^p = \Sigma_{yy}^p|_{y=0}$ . A closure relation for the particle phase stress is required to make further progress. We write this stress as the sum of a thermodynamic part corresponding the suspension stress at equilibrium, i.e. the osmotic pressure  $\Pi$ , and a hydrodynamic part designed by Frank and coworkers to reproduce the correct asymptotic regimes at  $Pe \ll 1$  and  $Pe \gg 1$ [12]

$$\Sigma_{yy}^p = -\Pi - \eta\dot{\gamma} [b^{-1}(\phi, Pe) + c^{-1}(\phi)]^{-1}, \quad (12)$$

where

$$b(\phi, Pe) = A\lambda_2^B Pe\phi(1-\bar{\phi})^{-3}, \quad (13)$$

$$c(\phi) = \lambda_2^H \eta_n(\phi), \quad (14)$$

and here we choose  $A = 0.4$ ,  $\lambda_2^H = 0.75$ ,  $\lambda_2^B = 1.8$ ,  $\phi_m = 0.64$ , and

$$\eta_n(\phi) = 0.75\bar{\phi}^2(1-\bar{\phi})^{-2}, \quad (15)$$

in line with the modeling proposed by Frank et al.[12], based on the rheology determined analytically and numerically by Brady & Vicic[8], Phung et.al[26], and Morris & Katyal[19] for Brownian hard spheres. When equation (12) is used in (10), the first and second terms lead to the thermodynamic and shear-induced fluxes mentioned in the introduction,  $\mathbf{j}_{th}$  and  $\mathbf{j}_s$  respectively.

Let us note immediately that the form of the shear viscosity (5) and of the hydrodynamic contribution in (12) were explicitly designed for hard spheres, neglecting shear-thinning since volume fractions will remain moderate[12, 36]. However, in this work we use it even for charge-stabilized suspensions. This modeling is therefore expected to be satisfactory for low surface charges but may be inaccurate for high surface charges. It is known that the shear viscosity depends strongly on electrostatic interactions in particular through the secondary electro-viscous effect[30]. Increasing the interaction range tends to strongly increase the shear viscosity and the shear-thinning behavior of charge stabilized suspensions at moderate  $Pe$  numbers (see e.g. [21] for recent computations). Although many rheological measurements of the shear viscosity of charge-stabilized suspensions have been published, and although it is possible to fit these measurements with phenomenological models[17], a general analytical viscosity model depending in the physico-chemical parameters (surface charge, interaction range) of

the suspension is still elusive even if some results have been obtained in certain asymptotic limits and for electrostatic pair interactions with specific forms[30]. To our knowledge, there are also to day no analytical models of the hydrodynamic normal stresses in the presence of colloidal interactions. For the sake of simplicity, we therefore use the original modeling of hydrodynamic effects of Frank and coworkers for Brownian hard spheres. However, as will become clear at the end of this article, the main conclusions drawn are actually linked to the specific behavior of the osmotic pressure in (12) and are therefore not believed to depend strongly on the precise form of the hydrodynamic stresses.

In using the form (12) for  $\Sigma_{yy}^p$ , we make one additional assumption worth underlining. We assume that the anisotropic microstructure generated by the flow does not induce a significant perturbation to the thermodynamic part of the stress. This hypothesis is certainly true for low shear rates but its validity for larger shear rates depends on the type, range, and strength of physico-chemical interactions considered. Comments will be made on this issue in section 4 in light of the results of this work, but in short, it is a justified hypothesis here.

## 2.2 The Equation Of State

The function  $\Pi$  in (12) is the equilibrium equation of state (EOS) of the colloidal suspension. It was computed with different approaches briefly summarized here. For uncharged hard spheres, the EOS is very well modeled by [9, 38, 27, 31]

$$\Pi_{HS} = \begin{cases} \rho kT \frac{1+\phi+\phi^2-\phi^3}{(1-\phi)^3} & \text{for } \phi \leq 0.5 \\ \rho kT \frac{1.85}{\phi_m - \phi} & \text{for } \phi > 0.5 \end{cases} \quad (16)$$

When the colloids are charged, they attract counter-ions near their surfaces, leading to electrostatic interactions due to both the electric field and the pressure exerted by the ions on the surfaces of the colloids. The full, precise computation of these interactions from first principles is still difficult in a general case (non-additivity of pair-potentials, ion specificity, electrostatic coupling effects, etc) but satisfactory approaches have been developed especially for the case of 1:1 electrolytes. In this context, the electrostatic coupling between ions and the surfaces is weak, so that they can be treated as uncorrelated. If the ions are not too concentrated (say below  $0.1M$ ), their finite size can also be neglected. This picture corresponds to

the Poisson-Boltzmann theory. It is still a non-linear theory in general. A further simplification is to consider the colloids weakly charged and diluted so that the electrostatic potential is lower than  $kT/e$  ( $e$  is the electron charge) everywhere. This is the Debye-Hückel theory. In this context, a pair of spherical colloids in an infinite empty medium experiences an interaction potential following the Yukawa form

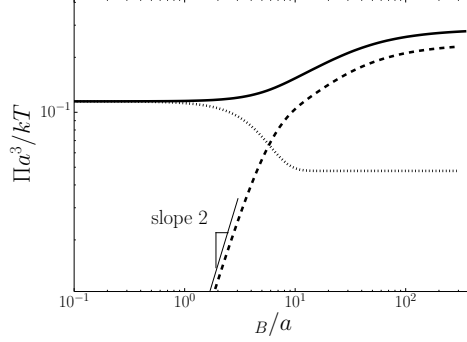
$$\beta u = Z^2 l_B \left[ \frac{e^{\kappa a}}{1 + \kappa a} \right]^2 \frac{e^{-\kappa r}}{r}, \quad (17)$$

where  $\beta = 1/kT$ ,  $Z$  is the net number of charges on one colloid,  $l_B = e^2/4\pi\epsilon kT$  is the Bjerrum length,  $\epsilon$  is the liquid dielectric permittivity,  $\kappa = \sqrt{8\pi l_B n_0}$  is the inverse of the Debye length, and  $n_0$  is the ion number density in a very large ion reservoir that would be in thermodynamic equilibrium with the suspension. If the interaction potentials are considered additive, the classical integral equations theories can be employed to compute the radial distribution function  $g(r)$  of a dispersion, and from it the equation of state  $\Pi = \rho kT + \Pi_{\text{contact}} + \Pi_{\text{ES}}$ , where  $\Pi_{\text{contact}} = \rho kT 4\phi g(2a)$  is the pressure contribution due to contacts and

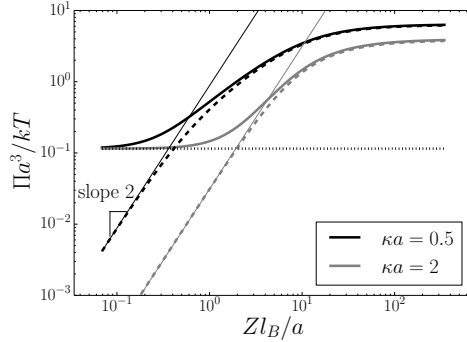
$$\Pi_{\text{ES}} = -\frac{\rho^2}{6} \int r g(r) u'(r) dr \quad (18)$$

is the pressure contribution due to electrostatic interactions. In this article, the Ornstein-Zernike equation will be used with a Rogers-Young closure known to provide accurate results for hard-sphere-Yukawa potentials. If the colloidal surface charge is too high for the Debye-Hückel theory to be valid, the interaction potential can still be written in the form (17) but with effective parameters  $Z_{\text{eff}}$  and  $\kappa_{\text{eff}}$ . When this renormalization procedure is necessary, we employ the method detailed by Trizac et. al[33]. The integral equations theory used with a renormalization approach is valid if the typical surface to surface distance between colloids  $d$  is larger than the Debye length,  $\kappa d > O(1)$ [5]. This method is used for the simulations of systems with short-ranged interactions,  $\kappa a = 10$  in this work (see figure 1a).

If the double layers significantly overlap (at low salt contents or high volume fraction), the electrostatic forces are not pairwise additive anymore. Hopefully, it is the conditions in which the cell model is quite precise[13]: the colloids in the suspension feel strong interactions from several neighbors, which tend to create a solid-like structure in the dispersion with every colloid



(a) Pressure calculation for  $\kappa a = 10$ . Both contributions stem from the equilibrium microstructure predicted with the OZ-RY theory.



(b) Pressure calculation for  $\kappa a = 0.5$  and  $2$ . The electrostatic contribution is given by the cell model. The entropic and contact contributions are taken as  $\Pi_{\text{HS}}$ , given by (16). Thin lines: analytical approximation  $\Pi_{\text{ES}} = \alpha(Zl_B/a)^2$  with  $\alpha$  given by (27).

Figure 1: Calculation of the osmotic pressure  $\Pi$  for a volume fraction  $\phi = 0.2$ . Thick continuous lines: full pressure  $\Pi$ ; Dashed lines: electrostatic contribution  $\Pi_{\text{ES}}$ ; Dotted lines: entropic and contact contributions  $\rho kT + \Pi_{\text{contact}}$ .

in an electro-neutral cell. We suppose for simplicity these cells are spherical with the colloid at their center. The one-dimensional non-linear Poisson-Boltzmann equation can be solved numerically in such a cell to get the electrostatic potential field and the ion distribution around one colloid. The electrostatic contribution to the osmotic pressure  $\Pi_{\text{ES}}$  is simply related to the total ion density at the boundary of the cell  $n(R)$  by

$$\Pi_{\text{ES}} = n(R)kT - 2n_0kT. \quad (19)$$

More details about the cell model can be found in Refs. [37, 1, 15, 33]. For intermediate and long-range interactions, i.e.  $\kappa a = 2$  and  $\kappa a = 0.5$  in the present work,  $\Pi_{\text{ES}}$  will be computed with the cell model. The entropic and contact contributions will be approximated by  $\Pi_{\text{HS}}$ , which is not true in general since the electrostatic interactions may perturb the radial distribution at contact from to its value for hard spheres, as evidenced on figure 1a for  $\kappa a = 10$ . The osmotic pressure however boils down to  $\Pi_{\text{HS}}$  for vanishing surface charges and is dominated by  $\Pi_{\text{ES}}$  for large surface charges and long range interactions, as illustrated on figure 1b. The approximation  $\rho kT + \Pi_{\text{contact}} \simeq \Pi_{\text{HS}}$  is thus only expected to perturb the pressure value slightly in the intermediate charge regime.

### 2.3 Numerical Implementation

With the knowledge of the equation of state for a prescribed set of physico-chemical conditions, the final set of equations to be solved for given hydrodynamic conditions is

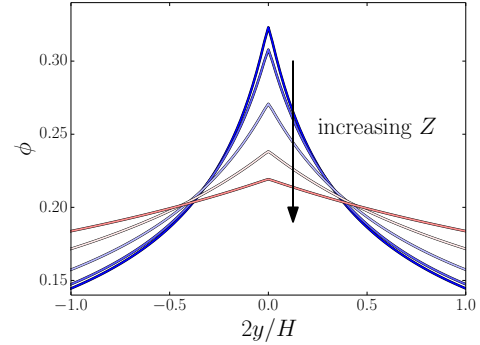
$$\eta \eta_s(\phi) \dot{\gamma} = y \partial_x P \quad (20)$$

$$\eta \dot{\gamma} [b^{-1} + c^{-1}]^{-1} = \Pi|_{y=0} - \Pi(\phi). \quad (21)$$

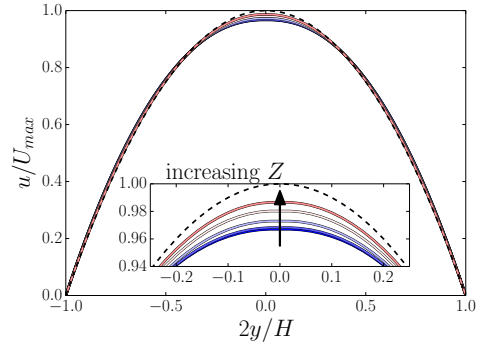
The group  $\eta \dot{\gamma}$  can be expressed as a function of  $\phi$  only thanks to relation (20). Once its occurrences in (21) have all been replaced, the latter equation reduces to a non-linear algebraic equation for the volume fraction profile  $\phi(y)$ . This equation is resolved numerically on a 1D grid with standard root finding algorithms available in Python-SciPy. Once the volume fraction profile is known, the shear rate profile is given by (20) and the velocity profile is obtained by integrating numerically  $\dot{\gamma} = \partial_y u$ . During the numerical resolution, we also impose the constraint

$$\frac{1}{H} \int_{-H/2}^{H/2} \phi dy = \phi_b, \quad (22)$$

where  $\phi_b$  a prescribed bulk volume fraction.



(a) Volume fraction



(b) Suspension velocity scaled by the maximum velocity  $U_{\text{max}}$  of a parabolic flow (dashed line) with the same flow rate.

Figure 2: Volume fraction and suspension velocity profiles for increasing surface charge densities  $\sigma = 0, 0.010, 0.025, 0.050, 0.100 e/nm^2$  at  $Pe_B = 50$ ,  $\kappa a = 2$ , and  $a = 7.5 nm$ .

In the next section, an example of such a computation is presented to highlight the main features of charge-stabilized colloidal flows. Results of many such simulations are then presented and discussed to show how the flow regime can be predicted.

## 3 Results

### 3.1 The channel flow of charge-stabilized colloids

Typical volume fraction and velocity profiles obtained in the fully developed channel flow are reported in figure 2 for  $Pe_B = 50$  and  $\kappa a = 2$ , and for increasing surface charge densities  $\sigma = Ze/4\pi a^2$ . The most spiked curve ( $\sigma = 0$ ) corre-

sponds to the classical flow of a suspension of Brownian hard spheres. The volume fraction profile is fully established when shear-induced migration is balanced by Brownian motion and collisions at any point [12, 32]. The suspension velocity profile is slightly more blunted than the classical channel flow profile due to the shear rheology imposed by relation (5).

When increasing the surface charge density, the inter-particle repulsions increase and add their contribution to the transverse thermodynamic flux already containing effects of Brownian motion and collisions. Shear induced migration is therefore balanced by a thermodynamic flux of particles increasing with the surface charge density. This is the reason of the flattening of the volume fraction profile observed on figure 2a with the increase of the surface charge. Naturally, since a high surface charge tends to restore a uniform concentration profile, it also tends to restore a uniform viscosity and a parabolic flow profile as depicted on figure 2b.

As shown in the example of figure 2, it is possible to suppress shear-induced migration by increasing the strength of thermodynamic repulsive interactions. The shear-induced migration flux scales as  $\dot{\gamma}a^2$  [16], while colloidal interactions are independent of the shear rate at first order. The appearance of non-homogeneous concentration profiles due to SIM is thus only - but always - expected for high shear rates. Nonetheless, the shear rate values required to observe SIM in strongly stabilized suspensions, or even for dispersion of small uncharged colloids, might be impossible to attain in practice. Indeed, the concentration inhomogeneity observed on figure 2a for the highest surface charge density is quite weak despite a shear rate of the order of  $10^7 s^{-1}$ . The physico-chemical parameters employed are on the other hand quite realistic and could correspond to moderately charged Ludox HS40 spheres. This certainly explains why a part of the literature on the continuous modeling of colloidal flows only considers the effective viscosity in the (Navier-)Stokes equation and an effective diffusion coefficient given by the GSE to account for colloidal interactions, neglecting any transverse migration of hydrodynamic origin [6, 7, 28]. Shear induced migration is however known to occur in some processes involving colloidal suspensions such as crossflow ultra-filtration [39, 29, 2, 35]. One important question for colloidal engineering is then: What are the physico-chemical and hydrodynamic conditions required to observe significant effects of either colloidal interactions or shear-induced mi-

gration? The answer to this question dictates whether efforts have to be made concerning the design of a closure relation for  $\dot{\mathbf{j}}_{th}$  or for  $\dot{\mathbf{j}}_s$  (or both). For Brownian suspensions without interactions, the scale of the stress restoring the equilibrium microstructure is of entropic origin, leading to a critical shear rate to observe SIM given by Péclet number of order unity. For colloidal suspensions dominated by strong hydrodynamics and electrostatics, the restoring stress scale rather depends on the strength and range of electrostatic interactions. The boundary between flows exhibiting SIM and simpler flows therefore lies in a phase space with axes, say,  $(Pe, Zl_B/a, \kappa a)$ . The first and second axes can be seen as dimensionless shear rate and colloidal charge, respectively. The reference scale is given by entropy in both cases. The last axis is relative to the range of interactions. Equivalent axes can be defined by combination of these ones.

### 3.2 The phase diagram

We now turn to the determination of the phase diagram discriminating the colloidal and hydrodynamic regions in the  $(Pe, Zl_B/a, \kappa a)$  space. This diagram will be obtained first numerically by solving the model described in section (2) for various hydrodynamic and physico-chemical parameters. It will then be obtained theoretically from arguments developed in this section. This will enable us to shed some light in particular on the peculiar asymptotic behavior of the curve separating the colloidal and hydrodynamic regimes for charge-stabilized suspensions.

The colloidal radius was set to  $a = 7.5 nm$ . For each couple  $(Zl_B/a, \kappa a)$  determining colloidal interactions, the system (20)-(21) is solved recursively for various  $Pe$  numbers in order to determine the critical Péclet number  $Pe_c$  such that  $max(\phi)/\phi_b = 1.1$ . This is an arbitrary condition separating the ‘‘colloidal’’ regime with negligible SIM and an almost uniform volume fraction profile ( $max(\phi)/\phi_b < 1.1$ ) and the ‘‘hydrodynamic’’ regime characterized by significant volume fraction gradients ( $max(\phi)/\phi_b > 1.1$ ) due to shear-induced migration. The resulting critical points are represented as symbols in the  $(Pe, Zl_B/a)$  plane shown on figure 3 for  $\kappa a = 0.5, 2, \text{ and } 10$ . In aqueous systems, the lower  $\kappa a$  value is typical of long-range interactions in semi-deionized water and the intermediate and large values are quite standard for colloids with a size ranging from  $10 nm$  to  $1 \mu m$ , depending on the salt concentration. The range of surface charge density explored corresponds

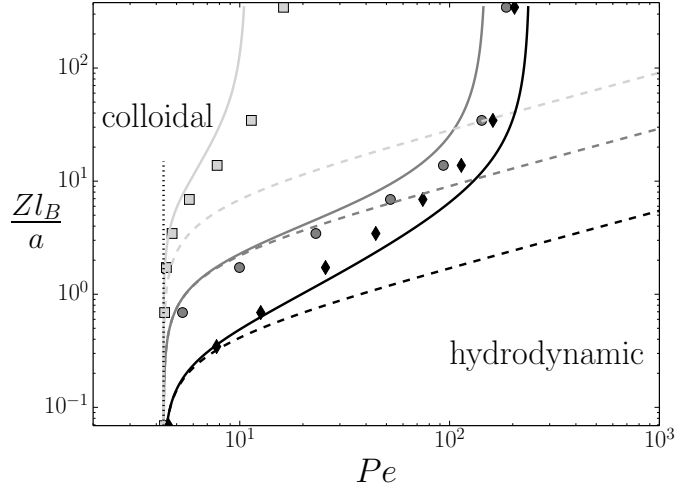


Figure 3: Phase diagram identifying the colloidal and hydrodynamic domains in the parameter space  $(Pe, Zl_B/a, \kappa a)$ . The colloidal domain is characterized by strong colloidal repulsions preventing shear-induced migration. In the hydrodynamic domain, flows exhibit noticeable shear-induced migration despite the diffusive effect of colloidal interaction. Symbols: boundary computed numerically with the suspension balance model described in section 2. Continuous lines: boundary given by relation (24); Dashed lines: boundary given by relation (26); Black symbols and lines:  $\kappa a = 0.5$ ; Gray symbols and lines:  $\kappa a = 2$ ; Light gray symbols and lines:  $\kappa a = 10$ .

to what would be observable for silica particles, depending on the  $pH$ . The lowest surface charge density does not affect the dynamics of the colloids, and is representative of a suspension near the iso-electric point. The highest charge considered corresponds to a surface charge density of  $5 e/nm^2$ , which is somewhat unrealistically high, but is reported to highlight an asymptotic limit to be described later. The second to last surface charge corresponds to a surface charge density of  $0.5 e/nm^2$ , which is classically observed for fully charged silica particles in water[24, 14].

The diagram represented on figure 3 shows common features for the three interaction ranges investigated. For all interaction ranges, an S-shaped boundary delimits a colloidal regime at low shear rates and/or high surface charges and an hydrodynamic regime at high shear rates and/or low surface charges. Moreover, all the S-shaped boundaries also exhibit vertical asymptotes in the low charge and high charge regimes. The asymptote in the low charge regime is unique but the location of the asymptote in the high charge regime depends on the interaction range. Interestingly, the existence of a colloidal regime with no significant evidence of SIM can be observed up to  $Pe \sim O(100)$  for high sur-

face charges and long-range interactions. It provides support, if it was ever required, to the idea that for charge-stabilized suspensions the Péclet number is not relevant anymore to assess if mass transport is dominated by hydrodynamic or thermodynamic effects.

Since the boundary in the phase diagram separates regions with dominating thermodynamic effects and dominating hydrodynamic effects, it is tempting to try to define it as the location in the parameter space where thermodynamic and hydrodynamic stress scales are equal. This yields the following equation for the separation curve

$$\eta\eta_n(\phi_b)\dot{\gamma} = c\Pi(\phi_b, \kappa a, Zl_B/a) \quad (23)$$

where  $c$  should be an  $O(1)$  constant. Multiplication of this relation by the entropic stress scale  $6\pi a^3/kT$  leads to

$$Pe = c \frac{\tilde{\Pi}(\phi_b, \kappa a, Zl_B/a)}{\eta_n(\phi_b)} \quad (24)$$

where  $\tilde{\Pi} = \Pi 6\pi a^3/kT$  is a dimensionless osmotic pressure. Using relation (15) for  $\eta_n$  and the equations of state determined as described in section 2 we predict from (24) the boundaries represented as continuous lines on figure

3. The constant  $c$  was found to be 0.31 for the bulk volume fraction used in this work by matching the curves with the numerical results at  $Z = 0$ . More comments about this value will be given later. As shown on figure 3, relation (24) provides a quite good estimate of the S-shaped boundary for all the interaction ranges and charges investigated. Interestingly, this relation only requires the knowledge of the normal viscosity and of the equation of state of the colloidal suspension. The latter can be determined numerically as in the present work or experimentally from osmotic compression, or light or neutron scattering measurements. One of the main practical conclusions of this work is therefore that obtaining a diagram as the one of figure 3 is quite accessible using relation (24) with classical measurements or numerical models of EOSs for a given colloidal suspension, and that it can be done in order to design a flow model as adapted as possible to anticipated flow conditions.

Regardless of the practical point of building diagrams as the one presented on figure 3, the form of the S-shaped boundaries is of interest and may seem counter-intuitive at first glance. In order to understand this form, it is convenient to recall that the osmotic pressure can be decomposed as  $\Pi = \rho kT + \Pi_{\text{contact}} + \Pi_{\text{ES}}$ , where  $\Pi_{\text{contact}}$  arises from collisions between colloids and is related to the pair distribution function at contact, while  $\Pi_{\text{ES}}$  is the contribution of electrostatic interactions here, and more generally to any type of interaction at a distance.

At vanishing surface charge density,  $\Pi_{\text{contact}} \gg \Pi_{\text{ES}}$  and the osmotic pressure is  $\Pi(\phi) = \Pi_{\text{HS}}(\phi) + \epsilon(\phi, \kappa a, Zl_B/a)$  where  $\epsilon$  is small compared to the other terms and vanishes with  $Z$ . The boundary equation (24) thus becomes independent of  $Z$  and  $\kappa a$  in this limit, leading to the vertical asymptote observed on figure 3 and determined by

$$Pe = c \frac{\tilde{\Pi}_{\text{HS}}(\phi)}{\eta_n(\phi)}. \quad (25)$$

For non-zero but still moderate surface charges, the colloidal interactions may be strong enough to alter significantly the osmotic pressure. For the purely repulsive system considered here, the osmotic pressure increases monotonically with the surface charge. The critical shear rate or Péclet number necessary to observe hydrodynamic effects must therefore also increase monotonically with  $Z$ . This explains the positive and finite slope of the S-shaped boundaries in the intermediate charge regime. A crude at-

tempt at predicting the boundary is possible in the weak charge regime. Both the form of the pair potential (17) and the analytical solution of the cell model in the Debye-Hückel limit suggest an electrostatic contribution to the osmotic pressure  $\Pi_{\text{ES}}$  scaling as  $Z^2$ , and this is verified on figure 1. The thermodynamic stress then has the form  $\Sigma^{th} \sim \Sigma_{\text{col}}^{th} + \alpha(Zl_B/a)^2$ , where  $\Sigma_{\text{col}}^{th} = \rho kT + \Pi_{\text{contact}}$  and  $\alpha$  is a constant commented later. The location of the separation between the colloidal and hydrodynamic regimes is then expected to be given by

$$Pe = c \frac{\tilde{\Sigma}_{\text{col}}^{th} + \tilde{\alpha} \left(\frac{Zl_B}{a}\right)^2}{\eta_n}, \quad (26)$$

where  $\tilde{\alpha} = \alpha 6\pi a^3/kT$ . This equation is represented with dotted lines on figure 3, assuming  $\Sigma_{\text{col}}^{th} \simeq \Pi_{\text{HS}}$ . At vanishing surface charge  $Z$ , we recover relation (25) valid for hard spheres. For  $\kappa a = 0.5$  and 2, the theoretical prediction from the linearized cell model was employed for  $\alpha$

$$\frac{\alpha}{2n_0 kT} = 2(\kappa a)^2 \left[ (\kappa R + 1)(1 - \kappa a)e^{\kappa(a-R)} + (\kappa R - 1)(1 + \kappa a)e^{-\kappa(a-R)} \right]^{-2} \quad (27)$$

where  $R = a\phi^{-1/3}$  is the radius of the cell. For  $\kappa a = 10$ , the value of  $\alpha$  was measured on the numerical data presented on figure 1a in the low charge regime. Note that the model (26)-(27) requires linearizing the PB equation, which is valid at high  $\kappa a$  and low charges, and a solid-like structure to employ the cell model, which is valid at low  $\kappa a$  and high charges. This why it works best at intermediate  $\kappa a$  and  $Zl_B/a$  values on figure 3, and this is also why it is rather useless in practice.

The deficiency of model (26)-(27) has however the merit to show that even when it gives satisfactory results as in the  $\kappa a = 2$  case for intermediate charges, it can definitely not capture the vertical asymptote at high surface charge. Indeed, any modeling of the electrostatic contribution to the osmotic pressure as a power law of  $Z$  would generate inclined asymptotes as the dashed curves of figure 3. The vertical asymptotes obtained numerically are signatures of the thermodynamic stress becoming independent of  $Z$  at high surface charge. The analytical model (24) contains this feature thanks to the modeling of the osmotic pressure detailed in section 2.2. The reason for the saturation of the pressure at high surface charge is the phenomenon of ionic condensation[5]: when the surface charge is increased towards very high values

( $Zl_B/a > O(10 - 100)$ ), counter-ions are more and more attracted in a small region near the surface of the colloids in a manner such that any new charge added to the surface of the colloid is neutralized by a new “condensed” counter-ion. As a consequence, we can define an effective colloid encompassing the real colloid and the condensed ionic region, and attribute to it an effective charge  $Z_{\text{eff}}$ . At low surface charges, there is no condensation such that  $Z_{\text{eff}} \simeq Z$ . At high surface charges the effective charge saturates and reaches a finite value  $Z_{\text{eff}}^{\text{sat}}(\phi, \kappa a)$ [34]. As a consequence, the electrostatic contribution to the osmotic pressure also saturates to an asymptotic value  $\Pi_{ES}^{\text{sat}}$  depending only on  $\phi$  and  $\kappa a$ , as illustrated on figure 1. Since electrostatic interactions become independent of the bare charge  $Z$ , so does the radial distribution function and the collision contribution also saturates towards a value  $\Pi_{HS}^{\text{sat}}(\phi, \kappa a)$ . The thermodynamic stress scale is then  $\Sigma^{\text{sat}}(\phi, \kappa a) = \Pi_{\text{col}}^{\text{sat}} + \Pi_{ES}^{\text{sat}}$ . The equation of the boundary in the phase diagram (24) then becomes

$$Pe_c = c \frac{\tilde{\Sigma}^{\text{sat}}(\phi, \kappa a)}{\eta_n(\phi)}. \quad (28)$$

It is a vertical asymptote in the  $(Pe, Zl_B/a)$  plane since it does not depend on  $Z$  anymore, but its position still depends on the interaction range  $\kappa a$ , as observed in figure 3. It is important to emphasize at this point that a modeling of the equation of state based on pair potentials with a classical DLVO or Yukawa form ignoring ion condensation effects would not permit to recover the S-shaped boundary on the flow diagram 3. It would only yield boundaries similar to the dashed lines.

Instead of defining a complex boundary in the  $(Pe, Zl_B/a)$  plane, relation (23) also suggests the definition of a “dressed” Péclet number

$$Pe^* = \frac{\eta_n \dot{\gamma}}{\Pi} \quad (29)$$

equal to an  $O(1)$  constant at the transition between the colloidal and hydrodynamic regimes, independently of the separate values of the shear rate, colloidal interaction range and surface charge. The location of the flow regime boundaries determined numerically with the SBM and represented on figure 3 in the  $(Pe, Zl_B/a)$  plane are recast on figure 4 in the  $(Pe^*, Zl_B/a)$  plane. As expected, they collapse on a single line with equation  $Pe^* = Pe_c^*$ , where  $Pe_c^*$  is the (constant) critical dressed Péclet number at the transition between the colloidal and hydrodynamic regimes. In the hard sphere limit, we have determined previously  $Pe_c^* \equiv c = 0.31$  for the bulk

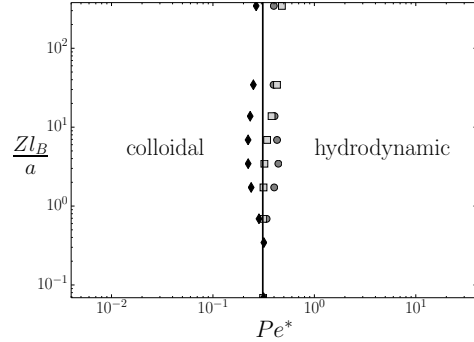


Figure 4: Phase diagram identifying the colloidal and hydrodynamic domains in the parameter space  $(Pe^*, Zl_B/a, \kappa a)$ . The flow regime boundary is found at  $Pe^* \simeq 0.33$  (for  $\phi_b = 0.2$  here). The  $Pe^*$  axis extends over four decades to show the good collapse of the data, keeping in mind that the range of  $Pe^*$  accessible in real systems is typically from 0 at equilibrium to  $O(10^4)$  for strongly sheared suspensions of micrometer-sized particles.

volume fraction  $\phi_b = 0.2$  used in this work. The numerical determination of  $Pe_c^*$  for any surface charge and from the SBM results presented on figure 4 leads to  $Pe_c^* = 0.33$  on average, in perfect agreement with the hard-sphere value. The standard deviation is only 0.07 for the full extent of interaction ranges and surface charge investigated in this article, although as mentioned before they correspond to the full range of realistic values in aqueous suspensions. The idea that the transition between colloidal and hydrodynamic regimes occurs at a constant  $Pe^*$  is therefore quite robust. Besides, the deviations of the numerical values obtained with the SBM from the average value of  $Pe_c^*$  show no monotonic or systematic dependence on  $\kappa a$  or  $Zl_B/a$ . This is also a confirmation the general relevance of this number.

To conclude, besides plotting a flow diagram with relation (24) it is also possible to compute the value of the rescaled Péclet number  $Pe^*$  with relation (29) for prescribed hydrodynamic and physico-chemical condition and compare it to unity to determine a priori if the flow is in the colloidal or hydrodynamic regime.

## 4 Discussion

In this article, we presented a modeling strategy aimed at simulating flows of charge-stabilized colloidal suspensions. The main conclusions were that (i) the Péclet number is not a relevant dimensionless group to characterize the departure from equilibrium in a suspension stabilized by significant electrostatic interactions; (ii) it is possible to define a more relevant rescaled Péclet number as the ratio of viscous and thermodynamic stress scales; (iii) the thermodynamic stress scale, here considered as the osmotic pressure at equilibrium, has to be modeled carefully to account for subtle physico-chemical effects which can influence the flow regime, such as ion condensation. In this section, we propose a few comments to discuss the general validity of these conclusions and the limits of the numerical modeling approach.

### 4.1 Comments on the model

The first critical point concerning the computation of the channel flow with the SBM is probably related to the form of equation (12). One of the main assumptions here is that the thermodynamic component of the total stress is isotropic and equal to the osmotic pressure at equilibrium. It is a quite reasonable premise near-equilibrium but it may be wrong at high shear rates. Even though simulations have been conducted at  $Pe$  numbers as high as  $O(100)$ , it should now be clear that only  $Pe^*$  is relevant to measure the distance to equilibrium in charge-stabilized suspensions, and that by design the present simulations are all at  $Pe^* \sim 1$  (0.33 on average to be more precise). It would be tempting to use the SBM as formulated in this article for higher shear rates. However, in this case the flow would make the microstructure of the suspension significantly anisotropic. Since the osmotic pressure of the suspension derives from its microstructure, we could expect deviations between the non-equilibrium thermodynamic component of the suspension stress and the equilibrium osmotic pressure. Besides, the anisotropy would suggest the use of a thermodynamic stress tensor instead of a unique pressure. To date, we know no analytical model of the thermodynamic stress tensor in a flow of charged stabilized colloids at  $Pe^* > 1$ , and as a function of  $Pe$ ,  $\kappa a$  and  $Zl_B/a$ . This issue is a cornerstone for the improvement of the continuous modeling of colloidal flows, and it ought to receive attention in future rheological studies.

The second issue of the model also concerns the form of the thermodynamic stress in (12). Assuming one considers a flow at  $Pe^* < 1$  as in the present work, so that a “simple” equilibrium osmotic pressure can represent reliably the thermodynamic stress tensor, the equations of state calculated here are only approximations of the real ones although we took care to use renormalization, the OZ theory, and the cell model in the range of parameters in which they should work best. The most detailed computations of the osmotic pressure at equilibrium require including both colloids and ions in a Molecular Dynamics (MD) or Monte Carlo (MC) simulation box and wait a few hours or days for statistics to converge. Generating such data in view of a use for flow modeling is however unimaginable to date. Indeed, even simple flows might involve variations of colloid concentration, ion concentration, and even  $pH$  making the parameters  $\phi$ ,  $\kappa a$ , and  $Zl_B/a$  non-uniform in space and time. Establishing the full dependence of the EOSs in this parameter space would require thousands of such simulations. This illustrates the need for fast and efficient means to compute equations of state of charge-stabilized suspensions with simple models like the ones employed in this article. The development of fast models going beyond the PB theory, like the modified PB theory, density functional theory, or self-consistent field theory, is still a subject of research. In spite of the above-mentioned reserves about the precise form of the equations of state employed here, let us insist on the fact that the EOSs used during the simulations and for the analysis of section 3 were the same, so that the simulations and the conclusions drawn in this work are self-consistent. In particular, the important idea that ionic condensation and effective charge saturation has to be accounted for is robust and would be obtained with any fully detailed thermodynamic model.

### 4.2 Comments on the main results

The re-definition of the Péclet number as  $Pe^* = \eta\eta_n\dot{\gamma}/\Pi$  for colloidal suspensions is one of the main conclusions of this work. Although other rescalings have been proposed in the literature for more or less similar purposes, the present definition has some interesting advantages worth underlying.

Brady & Vicic [8] proposed a Péclet number defined as  $\bar{Pe} = \dot{\gamma}a^2/D_0^s(\phi)$  in a scaling theory aimed at modeling the stresses in Brownian concentrated hard sphere suspensions at low  $Pe$ . It consists in replacing the Stokes-Einstein

diffusivity  $D_0$  (valid in the dilute limit) in the classical  $Pe$  by the short time self-diffusivity  $D_0^s$  in concentrated suspensions. The  $Pe^*$  defined here consists in replacing the thermodynamic stress  $kT/a^3$  (valid in the dilute limit) by the full osmotic pressure relevant for “electrostatically concentrated” suspensions. The parallel however stops here since the  $\bar{Pe}$  of Brady & Vucic is a microscopic Péclet number aimed at comparing time scales in a sheared homogeneous suspension. The present Péclet number is macroscopic in the sense that it aims at comparing the macroscopic thermodynamic and shear-induced fluxes.

To compare macroscopic fluxes, it might be tempting to define an effective  $Pe$  by comparing the thermodynamic diffusive time scale  $a^2/D_\nabla$ , where the diffusion coefficient is given by the GSE, and some hydrodynamic time scale associated to shear-induced migration, typically  $\dot{\gamma}^{-1}$ . The rescaled Péclet number would be  $\dot{\gamma}a^2/D_\nabla$ , by analogy with the usual Péclet number  $\dot{\gamma}a^2/D_0$ . This is, once again, inappropriate since  $D_\nabla$  contains the hydrodynamic function  $f(\phi)$ , while in the present steady-state channel flow there is no need to introduce it in the final model (20)-(21). The explanation of this apparent paradox is as follows. The Péclet number is a ratio comparing the strength of hydrodynamic and diffusion phenomena. It usually compares a solute *advection* flux  $\mathbf{j}_a = \mathbf{u}\phi$  and a diffusion flux in a mass transport equation. In the present flow, and in all colloidal flows with a moderate slip velocity between the solid and fluid phases but significant shear, the mass flux of hydrodynamic origin is not the advection flux. It is the shear-induced migration flux  $\mathbf{j}_s$  computed from equations (3) and (12). This flux contains the same hydrodynamic function  $f(\phi)$  as the thermodynamic flux, so that comparing their scales leads to  $Pe^*$ , independently of the hydrodynamic hindrance function.

Some works about charge-stabilized colloidal flows also introduce the number  $A = Fa/kT$  comparing the inter-particle (here electrostatic) force scale  $F$  to the Brownian force scale  $kT/a$ [30, 20]. The ratio  $Pe/A$  compares hydrodynamic forces to thermodynamic forces in a manner similar to our  $Pe^*$  comparing hydrodynamic and thermodynamic bulk stresses. There is however a difficulty in computing the force scale  $F$  since it varies between 0 and  $\infty$  depending on the distance between two colloids, if we assume it derives from a Yukawa potential (17). The correct force scale depends on some typical interaction distance  $L$ , which is a priori unknown

unless the microstructure is computed. On the other hand, we have access directly and with a good precision to the osmotic pressure in electrostatically concentrated suspensions with the cell model, independently of the knowledge of the microstructure of the suspension. Therefore, even if  $Pe^*$  and  $Pe/A$  are theoretically equivalent, it is often much easier to compute  $Pe^*$  than to compute  $Pe/A$ .

Finally, let us note the similarity between the present  $Pe^* = \eta\eta_n\dot{\gamma}/\Pi$  and the dimensionless shear rate introduced by Fagan & Zukoski  $\eta\dot{\gamma}/G$ , where  $G$  is the elastic modulus of the suspension[10]. These authors remarked the collapse of flow curves obtained for charged silica particles in water when plotted as a function of this ratio, invoking as an explanation the strong role of electrostatic forces and of the microstructure in determining  $G$ . This argument is similar to the one developed here, with the distinction that  $\Pi$  is a normal stress response to the normal compression due to shear-induced migration, while  $G$  is a response to a tangential strain.

## 5 Conclusion

Different approaches concerning the continuous modeling of colloidal flows exist. They differ on the treatment of the mass conservation equation. Some researchers interested by suspensions of macromolecules or small colloids only considered a thermodynamic mass flux given as a Fickian flux with a diffusion coefficient obtained from the generalized Stokes-Einstein relation to account for inter-particle colloidal interactions. Other researchers concerned by the modeling of large colloids in flows with large shear rates considered only a shear-induced mass flux due to hydrodynamic interactions between particles. In a general flow, both ingredients are a priori necessary, but it can be anticipated that the thermodynamic and shear-induced fluxes dominate at small and high shear rates, respectively. It is therefore of practical interest to determine a priori if both types of fluxes have to be implemented in a flow solver. The central questions driving the developments of this article was: can we predict with simple tools if colloidal and hydrodynamic effects are to be expected for prescribed physico-chemical and hydrodynamic conditions?

To answer this question, we considered the fully-developed channel flow problem for charge-stabilized colloidal suspensions by adapting the suspension balance model (SBM) of Frank and

coworkers[12]. In this approach, both thermodynamic and hydrodynamic fluxes are modeled. Simulations at various interaction ranges, interaction strengths and hydrodynamic conditions permitted to draw a phase diagram in the  $(Pe, Zl_B/a, \kappa a)$  space showing regions dominated by colloidal or hydrodynamic effects. The boundary between these domains was found to exhibit a non-intuitive shape, which we could model successfully with a simple stress balance. The main conclusions of this work were deduced from this diagram: (i) the Péclet number alone is not sufficient to characterize the flow regime; (ii) a more relevant rescaled Péclet number  $Pe^*$  can be defined as the ratio of a viscous stress scale  $\eta\eta_n\dot{\gamma}$  and thermodynamic stress scale  $\Pi$  to identify the phase boundary as  $Pe^* \sim 1$ ; (iii) the thermodynamic stress scale involved in this number, here considered as the osmotic pressure at equilibrium, has to be modeled carefully to account for subtle physico-chemical effects which can influence the flow regime, such as ion condensation.

The SBM strategy employed here is believed to be robust in the present simulations with  $Pe^* \sim 1$ . It would however require significant improvements to model colloidal flows at  $Pe^* > 1$ . In these conditions, the thermodynamic stress might not be isotropic anymore and should depend on the microstructure imposed by the shear flow while the hydrodynamic stresses will also depend on colloidal interactions. Determining the suspension stress tensor as a function of the volume fraction, shear rate, and range and strength of interactions is a key to make further progress on the modeling of concentrated charge-stabilized suspension flows, in particular for non-pairwise additive colloidal interactions. It should now be possible with detailed simulations coupling hydrodynamics and electrostatics at the particle scale.

## References

- [1] S. Alexander, P. M. Chaikin, P. Grant, G. J. Morales, P. Pincus, and D. Hone. Charge renormalization, osmotic pressure, and bulk modulus of colloidal crystals: Theory. *The Journal of Chemical Physics*, 80(11):5776–5781, 1984.
- [2] P. Bacchin, P. Aimar, and V. Sanchez. Model for colloidal fouling of membranes. *AIChE Journal*, 41(2):368–376, 1995.
- [3] G. K. Batchelor. The stress system in a suspension of force-free particles. *Journal of Fluid Mechanics*, 41:545–570, 4 1970.
- [4] Georges Belfort, Robert H. Davis, and Andrew L. Zydney. The behavior of suspensions and macromolecular solutions in crossflow microfiltration. *Journal of Membrane Science*, 96(1):1–58, 1994.
- [5] Luc Belloni. Ionic condensation and charge renormalization in colloidal suspensions. *Colloids and Surfaces A: Physicochemical and Engineering Aspects*, 140:227–243, 1998.
- [6] W. Richard Bowen and Paul M. Williams. Prediction of the rate of cross-flow ultrafiltration of colloids with concentration-dependent diffusion coefficient and viscosity — theory and experiment. *Chemical Engineering Science*, 56(10):3083–3099, 2001.
- [7] W. Richard Bowen and Paul M. Williams. Quantitative predictive modelling of ultrafiltration processes: Colloidal science approaches. *Advances in Colloid and Interface Science*, 134–135(0):3–14, 2007. Surface forces: wetting phenomena, membrane separation, rheology. Topical issue in honour of Victor Starov.
- [8] John F Brady and Michael Vicic. Normal stresses in colloidal dispersions. *Journal of Rheology (1978-present)*, 39(3):545–566, 1995.
- [9] Norman F. Carnahan and Kenneth E. Starling. Equation of State for Nonattracting Rigid Spheres. *The Journal of Chemical Physics*, 51(2):635–636, 1969.
- [10] M. E. Fagan and C. F. Zukoski. The rheology of charge stabilized silica suspensions. *Journal of Rheology*, 41(2):373–397, 1997.
- [11] David R. Foss and John F. Brady. Structure, diffusion and rheology of Brownian suspensions by Stokesian Dynamics simulation. *Journal of Fluid Mechanics*, 407:167–200, 3 2000.
- [12] Martin Frank, Douglas Anderson, Eric R. Weeks, and Jeffrey F. Morris. Particle migration in pressure-driven flow of a Brownian suspension. *Journal of Fluid Mechanics*, 493:363–378, 10 2003.

- [13] Yannick Hallez, Joseph Diatta, and Martine Meireles. Quantitative Assessment of the Accuracy of the Poisson–Boltzmann Cell Model for Salty Suspensions. *Langmuir*, 30(23):6721–6729, 2014. PMID: 24834492.
- [14] Sarah Hocine, Remco Hartkamp, Bertrand Siboulet, Magali Duvail, Benoit Coasne, Pierre Turq, and Jean-Francois Dufrêche. How Ion Condensation Occurs at a Charged Surface: a Molecular Dynamics Investigation of the Stern Layer for Water-silica Interfaces. *The Journal of Physical Chemistry C*, 2015.
- [15] C. Holm, P. Kékicheff, and R. Podgornik. *Electrostatic Effects in Soft Matter and Biophysics*. NATO Science Series, 2000.
- [16] David Leighton and Andreas Acrivos. The shear-induced migration of particles in concentrated suspensions. *Journal of Fluid Mechanics*, 181:415–439, 1987.
- [17] Jan Mewis and Norman J Wagner. *Colloidal suspension rheology*. Cambridge University Press, 2012.
- [18] Jeffrey F. Morris and Fabienne Boulay. Curvilinear flows of noncolloidal suspensions: The role of normal stresses. *Journal of Rheology (1978-present)*, 43(5):1213–1237, 1999.
- [19] Jeffrey F. Morris and Bhavana Katyal. Microstructure from simulated Brownian suspension flows at large shear rate. *Physics of Fluids*, 14(6):1920–1937, 2002.
- [20] Jeffrey F. Morris. A review of microstructure in concentrated suspensions and its implications for rheology and bulk flow. *Rheologica Acta*, 48(8):909–923, 2009.
- [21] Ehssan Nazockdast and Jeffrey F. Morris. Effect of repulsive interactions on structure and rheology of sheared colloidal dispersions. *Soft Matter*, 8(15):4223–4234, March 2012.
- [22] Prabhu R Nott and John F Brady. Pressure-driven flow of suspensions: simulation and theory. *Journal of Fluid Mechanics*, 275(1):157–199, 1994.
- [23] Prabhu R. Nott, Elisabeth Guazzelli, and Olivier Pouliquen. The suspension balance model revisited. *Physics of Fluids (1994-present)*, 23(4):–, 2011.
- [24] J Persello. Surface and interface structure of silicas. *Surfactant Science Series*, pages 297–342, 2000.
- [25] Ronald J. Phillips, Robert C. Armstrong, Robert A. Brown, Alan L. Graham, and James R. Abbott. A constitutive equation for concentrated suspensions that accounts for shear induced particle migration. *Physics of Fluids A: Fluid Dynamics (1989-1993)*, 4(1):30–40, 1992.
- [26] Thanh N. Phung, John F. Brady, and Georges Bossis. Stokesian Dynamics simulation of Brownian suspensions. *Journal of Fluid Mechanics*, 313:181–207, 4 1996.
- [27] P. N Pusey and W. van Megen. Properties of concentrated suspensions of slightly soft colloidal spheres. *Complex and Supramolecular Fluids*, pages 673–98, 1987.
- [28] Rafael Roa, Emiliy K. Zholkovskiy, and Gerhard Nagele. Ultrafiltration modeling of non-ionic microgels. *Soft Matter*, 11:4106–4122, 2015.
- [29] Cecily A. Romero and Robert H. Davis. Global model of crossflow microfiltration based on hydrodynamic particle diffusion. *Journal of Membrane Science*, 39(2):157–185, 1988.
- [30] William B. Russel. The rheology of suspensions of charged rigid spheres. *Journal of Fluid Mechanics*, 85:209–232, 3 1978.
- [31] W.R. Russel, D.A. Saville, and W.R. Schowalter. *Colloidal dispersions*. Cambridge University Press, 1999.
- [32] DENIS SEMWOGERERE, JEFFREY F. MORRIS, and ERIC R. WEEKS. Development of particle migration in pressure-driven flow of a Brownian suspension. *Journal of Fluid Mechanics*, 581:437–451, 6 2007.
- [33] E. Trizac, L. Bocquet, M. Aubouy, and H. H. von Grünberg. Alexander’s Prescription for Colloidal Charge Renormalization. *Langmuir*, 19(9):4027–4033, 2003.
- [34] Emmanuel Trizac, Miguel Aubouy, and Lydéric Bocquet. Analytical estimation of effective charges at saturation in Poisson-Boltzmann cell models. *Journal of Physics: Condensed Matter*, 15(1):S291, 2003.

- 
- [35] H. M. Vollebregt, R. G. M. van der Sman, and R. M. Boom. Suspension flow modelling in particle migration and microfiltration. *Soft Matter*, 6(24):6052, 2010.
- [36] Norman J Wagner and John F Brady. Shear thickening in colloidal dispersions. *Physics Today*, 62(10):27–32, 2009.
- [37] Hakan Wennerstrom, Bo Jonsson, and Per Linse. The cell model for polyelectrolyte systems. Exact statistical mechanical relations, Monte Carlo simulations, and the Poisson–Boltzmann approximation. *The Journal of Chemical Physics*, 76(9):4665–4670, 1982.
- [38] Leslie V Woodcock. Glass Transition In The Hard-Sphere Model And Kauzmann’s Paradox. *Annals of the New York Academy of Sciences*, 371(1):274–298, 1981.
- [39] Andrew L. Zydney and Colton Clark K. A concentration polarization model for the filtrate flux in cross-flow microfiltration of particulate suspensions. *Chemical Engineering Communications*, 47(1-3):1–21, 1986.

### 3 Suspension drying in a micro-evaporator

A micro-evaporator is a device used for concentrating substances like colloidal dispersions. It is a micro-channel, possibly of rectangular cross-section, with one face covered with a polymer (or membrane) that allows water to pass through, which creates a flow inside the channel. A container filled with the dispersion is connected to one of the ends of the channel. Once the channel is filled with suspension, the solvent is evaporated (or drained) through the membrane. During the draining of the solvent, particles are transported by the flow towards the end of the channel and they start concentrating. The volume of solvent evaporated is replenished by the solution in the connected reservoir. In this work the micro-evaporator of Salmon and Leng (2010); Merlin et al. (2012) was used as a reference and it is depicted in Figure 1.4. The typical dimensions for this type of device are  $h = 5 - 30 \mu m$ ,  $L_0 = 0.5 - 10 mm$  and  $w = 20 - 100 \mu m$ . Typical observed evaporation velocities are in the range of  $u_e = 10 - 50 nm/s$ . Considering the very large aspect ratio  $L_0/h = 100 \sim 1000$ , evaporation creates a flow with a horizontal velocity much higher than the evaporation rate itself since it is magnified by this aspect ratio. The principal advantage of

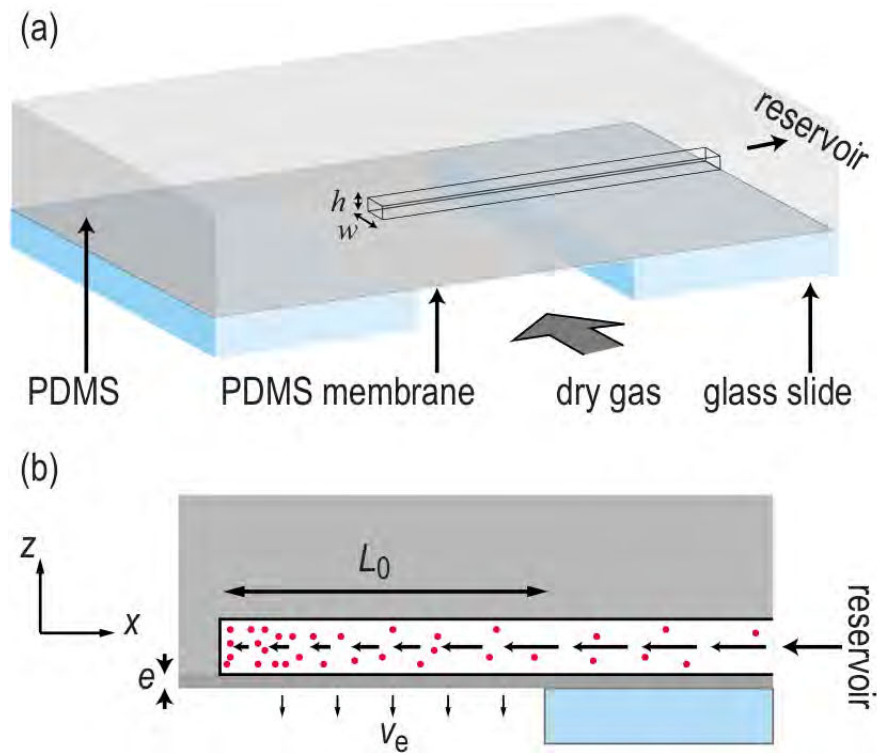


**Figure 1.4:** Microevaporator design from Salmon and Leng (2010); Merlin et al. (2012).

using such a device to study suspension drying, or the concentration of a suspension, is the controlled conditions under which drying is effectuated. In terms of simulation, the advantage of such a device is first of all the simplicity of the implementation of the drying interface. The geometry is a simple rectangle without a moving interface, as would be the case for drying droplets experiments. Consequently, a greater focus can be given on the physics of the flow of the suspension driven by evaporation and how it can impact the homogeneity of the drying film.

In the domain of thin film drying Routh and Russel (1998); Routh and Zimmerman (2004) categorized homogeneity of films obtained after drying in terms of a macroscopic Peclet number  $Pe_y = HV_e/D_0$ , where  $H$  is the height of the film,  $V_e$  is the evaporation velocity and  $D_0$  is the Stokes-Einstein diffusion. When  $Pe_y \ll 1$  diffusion is strong and uniform particle profiles are expected along the thickness of the film. On the other hand, when  $Pe_y \gg 1$ , evaporation is more important and large concentration differences between the surface and the bottom of the film are expected, a phenomenon called skinning or skin formation. In the paper of Merlin et al. (2012) they use another Peclet number not based on the evaporation rate and the thickness of the film, but on the velocity at the inlet of the channel ( $v_0$ ) and the length of the evaporating zone ( $L_0$ ),  $Pe_x = v_0L_0/D_0$ . It can be demonstrated that both approaches are related by

$$Pe_y = Pe_x \left( \frac{h}{L_0} \right)^2. \quad (1.57)$$

Using the geometrical and physical restriction of the device, it is interesting to explore the possible  $Pe_y$  that this system can attain. Considering a channel height ranging between  $h = 0.01 \text{ mm}$  and  $0.1 \text{ mm}$ , which is close to the range reported by Merlin et al. ( $h = 0.005 - 0.03 \text{ mm}$ ), and the evaporation rate takes the values reported in the introduction,  $10 - 50 \text{ nm/s}$ , then for particles of radius  $R = 250 \text{ nm}$ , the values of  $Pe_y$  lie between 0.1 to 5. Consequently, according to Routh and Zimmerman (2004) both horizontal drying fronts and skin formation can be observed in the channels. Note that the formation of a skin with a normal in the  $y$  direction is determined by  $Pe_y$ , but that  $Pe_x$  is the best suited dimensionless number to predict the propagation of a horizontal front in the  $x$  direction.

The *particle* Peclet number is more appropriate to discuss interactions at the particle scale. It is defined as  $Pe_p = R^2\dot{\gamma}/D_0$ , where  $\dot{\gamma}$  is a characteristic shear rate of the suspension. In the general case, the shear rate can be calculated from  $\dot{\gamma} = \sqrt{2\langle e \rangle : \langle e \rangle}$ , where  $\langle e \rangle$  is the rate of strain. In a simple shear the shear rate can be written as  $\dot{\gamma} = du_x/dy$ , where  $u_x$  is the  $x$ -component of the velocity. Assum-

ing that the flow inside the microevaporator is similar to a Couette flow, at least at the inlet, the velocity gradient can be calculated from an analytical expression of the velocity. Since a Couette flow is unidirectional there is only one component of the velocity vector  $u_x$ , and its value, for the steady state case, can be given by

$$u_x = \frac{6}{H^3} Q_{in} (Hy - y^2) \quad (1.58)$$

where  $H$  is the height of the channel,  $Q_{in} = \int_0^H u_x(y) dy = \langle u_x \rangle H$  is the flow rate in the channel. In the case of the microevaporator, the flow in the inlet is created due to evaporation in the evaporating zone, so  $Q_{in} = Q_{ev}$  needs to hold true, where  $Q_{ev}$  is the flow rate on the evaporating surface and is given by  $Q_{ev} = V_{ev}L$ . Replacing in the above equation and differentiating along the  $y$  direction

$$\dot{\gamma} = \frac{du_x}{dy} = \frac{6}{H^3} v_{ev} L (H - 2y) \quad (1.59)$$

Since the shear rate in this case is a linear function of height, the maximum absolute values will be on the top and bottom of the channel. Using the equation for particle Peclet number from above, the particle radius  $R = 250 \text{ nm}$  and the shear rate calculated from Equation (1.59) the maximum values of  $Pe_p$  are presented in Figure 1.5. The particle Peclet is ranging between  $10^{-5} \sim 10^{-2}$ . Since the values are small compared to unity some significant simplifications can be made to the system of equations based on the study of the channel flow in Section 2. This will be discussed in the next section.

In a first time, the system of equations will be presented for the transport of colloids inside a microevaporator, as well as the constitutive equations needed for their closure. A 1-D and a 2-D solution of the flow of hard spheres inside the microevaporator assuming constant viscosity will be given. This results will be compared with the results given by Merlin et al. (2012) for a 1-D case. In a second time the same system of hard spheres will be tested, this time by taking into account a variable viscosity model, for different Peclet number. Lastly, the same microevaporator will be tested with electrostatically charged particles for the same conditions.

### 3.1 Numerical implementation

The flow of the suspension inside the channel as well as the particle transport can be described by the system of equations detailed in Section 1. The first two equations are the suspension incompressibility and momentum equations

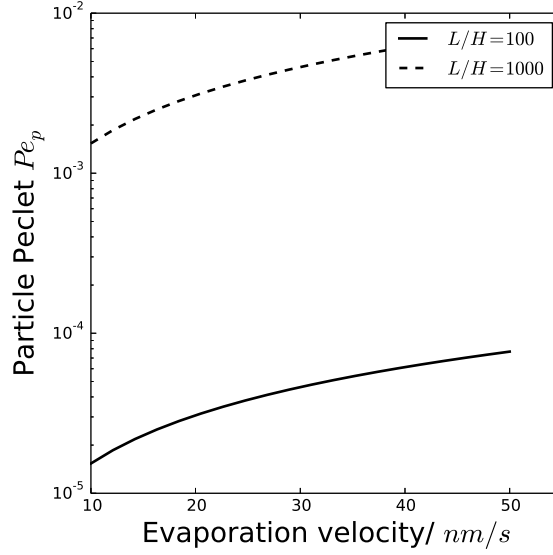


**Figure 1.5:** Particle Peclet number  $Pe_p$  as a function of the evaporation rate for two different aspect ratios ( $L_0/h$ ). The evaporation rates, as well as, all the parameters for the calculation of the Peclet number were found in Merlin et al. (2012).

$$0 = \nabla \cdot \langle \mathbf{u} \rangle$$

$$0 = -\nabla[(1 - \phi)\langle p \rangle^f] + 2\nabla \cdot (\eta_0(1 + \eta^s(\phi))\langle \mathbf{e} \rangle) + \nabla \cdot \Sigma_{\perp}^p$$

and the third one is the averaged particle transport equation

$$\frac{\partial \phi}{\partial t} + \langle \mathbf{u} \rangle \cdot \nabla \phi = -\nabla \cdot \left[ \frac{2a^2}{9\eta} f(\phi) \nabla \cdot \Sigma_{\perp}^p \right].$$

In the previous sections, we considered the closure relation

$$\Sigma_{\perp}^p = -\Pi \mathbf{I} - \eta \dot{\gamma} [\mathbf{b}^{-1}(\phi, Pe) + \mathbf{c}^{-1}(\phi)]^{-1}$$

Some very important simplifications can be realized in this system of equations, rising from the fact that the particle Peclet number in the microchannel is very low  $Pe_p \ll 1$ . Based on the results presented in Section 2, when in the case of a channel flow the particle Peclet number is well below 1 then hydrodynamic interactions that give rise to shear induced migration can be neglected even for the case of hard-spheres. Considering the above, the equations are simplified to

$$0 = \nabla \cdot \langle \mathbf{u} \rangle \quad (1.60)$$

$$0 = -\nabla[(1 - \phi)\langle p \rangle^f] + 2\nabla \cdot (\eta_0(1 + \eta^s(\phi))\langle \mathbf{e} \rangle) \quad (1.61)$$

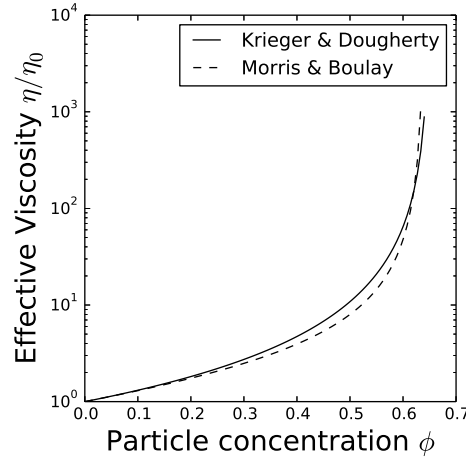


**Figure 1.6:** Effective viscosity  $\eta/\eta_0$  as a function of particle volume fraction. The solid line corresponds to the phenomenological viscosity of Krieger and Dougherty (1959). The dashed line is the expression used by Morris and Boulay (1999)

where the equilibrium osmotic term has been omitted since in this work it is considered isotropic and thus has no effect on the flow. The particle transport equation becomes

$$\frac{\partial \phi}{\partial t} + \langle \mathbf{u} \rangle \cdot \nabla \phi = \nabla \cdot \left[ \frac{2a^2}{9\eta} f(\phi) \nabla \Pi \right] \quad (1.62)$$

where only the osmotic pressure term is now relevant. If constitutive equations are given for the suspension viscosity and the equilibrium osmotic pressure then the above system can be solved.

In the simulations presented hereafter, the viscosity is either considered constant or variable but it does not take into account shear-thinning or shear-thickening as it may be expected for systems of very high concentration and charged nano-particles. We will use the phenomenological model of Krieger and Dougherty (1959). Even though it is simple compared to more elaborate models, for example from Morris and Boulay (1999), the choice of one viscosity model or the other does not affect significantly the results. In Figure 1.6 the viscosity is plotted as a function of particle concentration from the equation

$$\frac{\eta}{\eta_0} = \left( 1 - \frac{\phi}{\phi_{cp}} \right)^{-[\eta]\phi_{cp}} \quad (1.63)$$

where  $\phi_{cp}$  is the concentration in close packing,  $[\eta]$  is the intrinsic viscosity which takes the value 2.5 for spheres.

The particle transport equation Equation (1.62) can be written

$$\begin{aligned}\partial_t \phi + \langle \mathbf{u} \rangle \nabla \phi &= \nabla \cdot \left( D_0 f(\phi) \beta V_p \frac{d\Pi}{d\phi} \nabla \phi \right) \\ &= \nabla \cdot (D(\phi) \nabla \phi)\end{aligned}\quad (1.64)$$

where  $D_0 = kT/(6\pi\eta R)$  is the Stokes-Einstein diffusion coefficient,  $\beta = 1/kT$  and  $V_p$  is the volume of the particle. Constitutive equations  $\Pi(\phi)$  and  $f(\phi)$  are needed for the closure of the particle transport equation.

The osmotic pressure for hard-spheres is given by an expression derived by Peppin et al. (2006) that is asymptotic close to the random close-packing of hard-spheres  $\phi_{cp} = 0.64$ . This expression is valid over the entire concentration range

$$\frac{\Pi V_p}{kT} = \phi \frac{1 + a_1 \phi + a_2 \phi^2 + a_3 \phi^3 + a_4 \phi^4}{1 - \phi/\phi_{cp}} \quad (1.65)$$

where  $a_1 = 4 - 1/\phi_{cp}$ ,  $a_2 = 10 - 4/\phi_{cp}$ ,  $a_3 = 18 - 10/\phi_{cp}$  and  $a_4 = 1.85/\phi_{cp}^5$ . The osmotic pressure for the charged particles was calculated as presented in Section 2.

Concerning the hindrance factor  $f(\phi)$ , initially in order to compare the results obtained in this work with the results of Merlin et al. (2012) the hindrance factor will be given from

$$f(\phi) = (1 - \phi)^{6.55}. \quad (1.66)$$

After the comparison, for the rest of the work the value of  $f(\phi)$  will be given by a hindrance factor discussed in Lecampion and Garagash (2014) where they compared simulation and experimental data with different closures, finally suggesting

$$f(\phi) = (1 - \phi)^{5.1}. \quad (1.67)$$

In Figure 1.7a the osmotic pressure  $\Pi V_p/kT$  of three different types of particles is presented as a function of the particle concentration  $\phi$ . The solid black line corresponds to the hard-sphere osmotic pressure as calculated from Equation (1.65), while the dashed and dash-dot lines correspond to particles with surface charges  $\sigma_0 = 0.025 e/nm^2$  and  $\sigma_0 = 0.050 e/nm^2$  respectively. There is a clear difference in the osmotic pressure for the different kinds of particles, with the surface charge increasing it considerably. Even for particle concentrations below  $\phi = 0.1$  the value of the osmotic pressure for the most charged particles is at least 2 times higher than the one for the hard-spheres. Let us underline that a charge density of  $0.05 e/nm^2$  is actually rather low compared to what can be encountered for mineral oxides or polymers like DNA. An important remark has to be noted here for the values of the

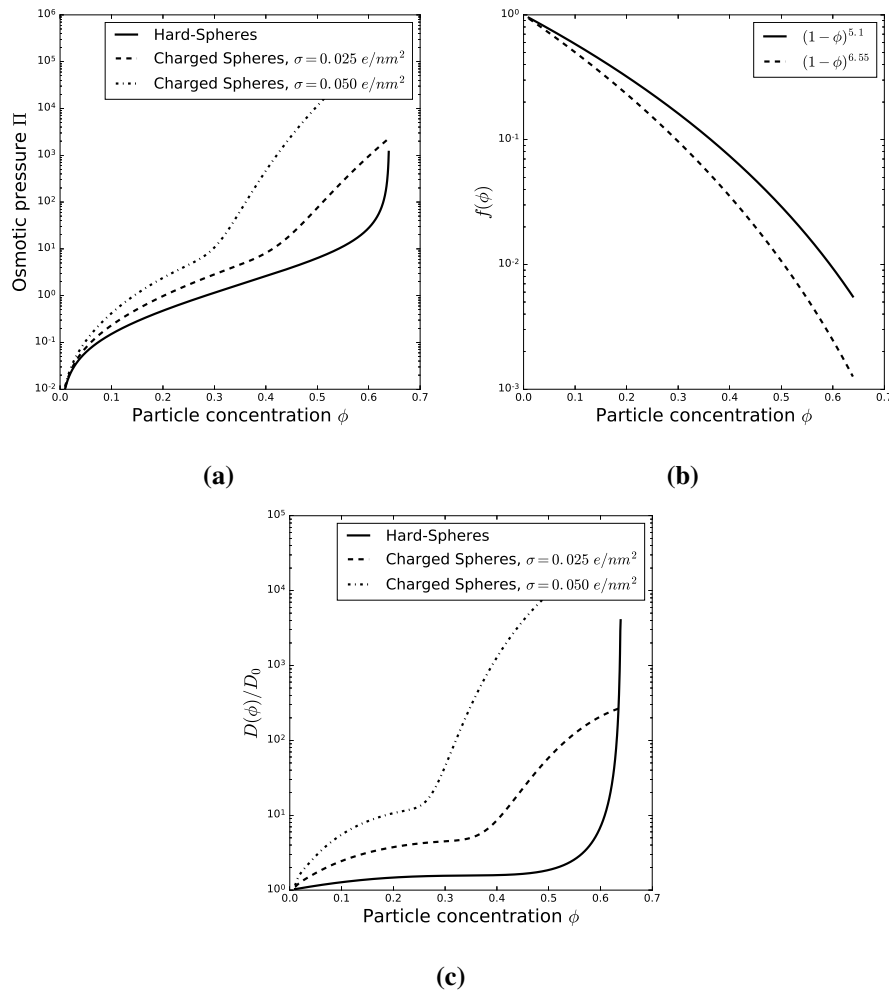


**Figure 1.7:** (a) Osmotic pressure  $\Pi$  of hard spheres and electrostatically charged spheres as a function of particle concentration  $\phi$ , b) Hindrance factor  $f(\phi)$  as a function of particle concentration and (c) The effective diffusion  $D(\phi)/D_0$ , where  $D(\phi) = D_0 f(\phi) \beta V_p d\Pi/d\phi$ .

osmotic pressure of the charged particles, for particle concentration  $\phi > 0.3$ . The sudden slope change is related to the polynomial fit extrapolating the simulated values and not to the actual values of the osmotic pressure. Because of lack of time the osmotic pressure of charged particles was calculated only up to a concentration of 0.3. However, this will not affect the conclusion to be made. In Figure 1.7b the two different expressions of the hindrance factor used in this work are plotted. In Figure 1.7c the diffusion coefficient  $D(\phi)/D_0$  is plotted for the three different types of particles used here. The diffusion coefficient for the hard spheres seems to stay almost unaffected until a particle concentration of  $\phi \sim 0.5$  is reached. For the other two systems even at particle concentration of  $\phi \sim 0.1$  they reach a diffusivity as high

as the one of a hard-sphere system near close packing. The fact that the diffusivity reaches so elevated values means that a very high advection flux (or evaporation rate) must be applied in order for these systems to concentrate. This might not be possible with a microevaporator.

## 3.2 Simulation of drying

### 3.2.1 Comparison between 2-D and 1-D approach

Since the approach used here is based on the full resolution of the transport equations using a generic CFD software, the results obtained are multi dimensional. As a first step of validation and reference a comparison will be realized with the numerical results of Merlin et al. (2012) in a one dimensional case. To my knowledge there are no experimental results concerning the profile of particle concentration perpendicular to the film in a microevaporator. In the numerical solution of Merlin et al. (2012) they considered that drying perpendicular to the channel is homogeneous following a theoretical background set by Schindler and Ajdari (2009). It is important at this point to mention that viscosity in this simulation is kept constant and the simulation time is non-dimensional defined as  $t = hT/v_e$

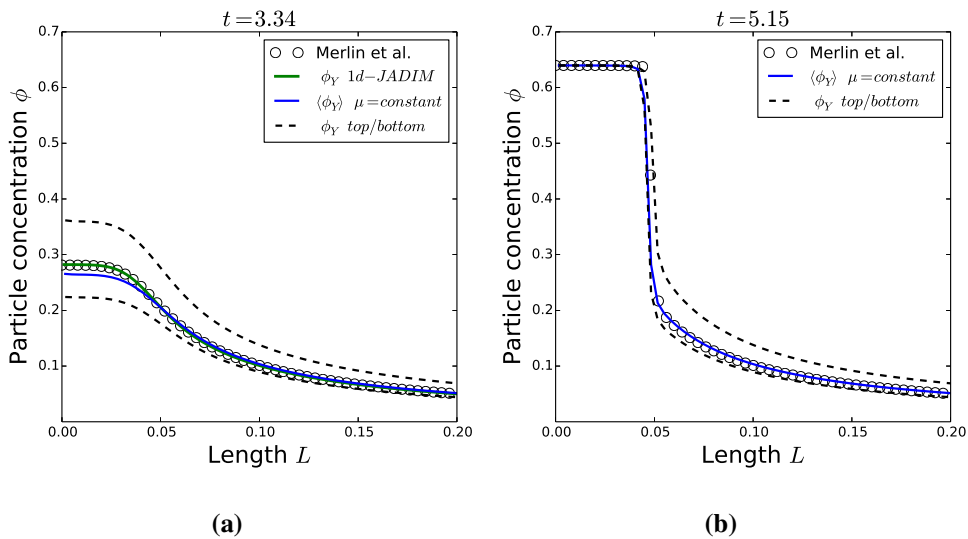


**Figure 1.8:** Comparison of 1-D results from Merlin et al. (2012) with pseudo 1-D results obtained with our CFD code, and 2-D concentration profiles with constant viscosity along the microchannel for two different times (a)  $t = 3.34$  and (b)  $t = 5.15$ .  $\langle\phi_Y\rangle$  represents the average concentration, the average being performed in the cross-section of the micro-channel. The top (resp. bottom) dashed line corresponds to the concentration at the top (resp. bottom) of the channel.

In Figure 1.8, different concentration profiles are plotted along the channel for times  $t = 3.34$  and  $t = 5.15$ . The concentration profiles from Merlin et al. (2012) is represented with empty circle ( $\circ$ ) markers the green line ( $-$ ) is obtained from the pseudo-1D results produced with the CFD code JADIM. The left side of the graphs corresponds to the closed end of the microevaporator while the right side corresponds to a distance  $L = 0.2$  upstream of the end of the channel. Once evaporation is initiated the particles are convected towards the end of the channel and a concentration gradient is starting to form. At a certain time the particles will reach a critical concentration where the diffusion will balance the convective flux and no further increase will be noted. This concentration for the case of hard spheres is near the close packing concentration of  $\phi = 0.64$ . In Figure 1.8, for  $t = 5.15$ , it is clear that the particle concentration has reached its maximum possible value, creating a sharp front that propagates towards the entrance of the channel. The pseudo-1D case obtained with JADIM, assuming a one-dimensional linear transport velocity in the channel, gives results identical to the ones of Merlin et al.. This validates the numerical implementation of the model.

In the same Figure 1.8, the blue line ( $-$ ) corresponds to the cross-section-averaged concentration profile when a 2-D solution is obtained as shown in Figure 1.9. The upper (resp. lower) dashed line ( $--$ ) corresponds to the concentration profile at the top (resp. bottom) of the channel. In the case of a 2-D flow, the average concentration  $\langle \phi_Y \rangle$  is similar to the one obtained with the solution of the 1-D model. What is important though is that the concentrations at the top and bottom of the channel given by the dashed lines are considerably different, at least for  $t < 5.15$ . This implies that there is a significant 2-D flow, even for conditions for which it was considered that concentration variations in the  $y$  direction could be omitted. It can thus be expected that for more complex geometries this approach is indispensable.

Nevertheless these differences seem to vanish for longer times,  $t = 5.15$ . When the concentrated particles reach close packing, the diffusive flux is very high and a homogeneous, close-packed front is propagating towards the channel entrance. In this case, the 1-D and 2-D approaches yield the same result. In Figure 1.9 a time lapse of the particle concentration is shown in a sequence of contours. As already mentioned, particle accumulation is not homogeneous. The highest concentration is in the upper left corner, and it remains high until it reaches  $\phi \sim 0.64$  which is the close packing concentration. At this point, the diffusion coefficient increases dramatically. Particles then diffuse towards the bottom to create a solid front which

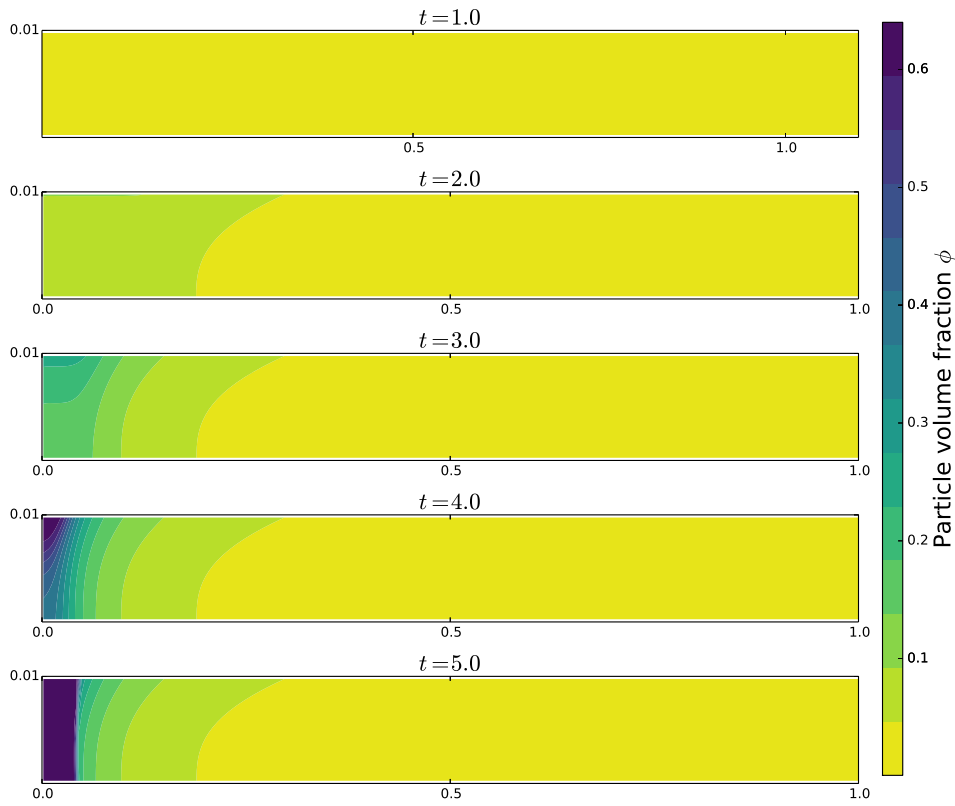


**Figure 1.9:** Particle concentration  $\phi$  contours for five different times from top to bottom  $t = 1, 2, 3, 4, 5$ . The suspension enters from the right side of the channels and the evaporation occurs from the top.

propagates towards the inlet.

It should be noted that in this first study the viscosity was kept constant which is far from true for the range of concentration that was involved here. In cases where particle concentration is not expected to reach important values, viscosity can be considered constant, which is important since the only coupling between the Navier-Stokes equation and the mass transport equation is precisely through the shear viscosity. Therefore, for a constant viscosity the momentum equation can be solved only one time and its solution (the average velocity field of the suspension) can be used for every subsequent time despite the motion of colloids and the evolution of the concentration field. This property might be counter-intuitive since we usually think in terms of “fluid velocity”  $\langle u \rangle^f$  or “solid phase velocity”  $\langle u \rangle^s$ , and since these velocities indeed depend on the concentration field and on time. Because of the incompressibility of the suspension, if particles move locally in one direction, the fluid has to move in the other direction to occupy their former volume. The local volume fluxes of solid

and liquid are therefore equal in magnitude and opposite in sign. This makes the suspension velocity  $\langle u \rangle = \phi \langle u \rangle^s + (1 - \phi) \langle u \rangle^f$  independent of these motions if they do not alter the constitutive relations.

### 3.2.2 Effect of viscosity in the solution

In the previous subsection the viscosity of the suspension was considered constant, which is not the case for colloidal suspensions. The suspension momentum equation depends on the viscosity, a function of particle concentration. Therefore variations in volume fraction provoke variations in viscosity, and it may have important effects on the suspension flow field. Using the same geometry as previously, two cases of

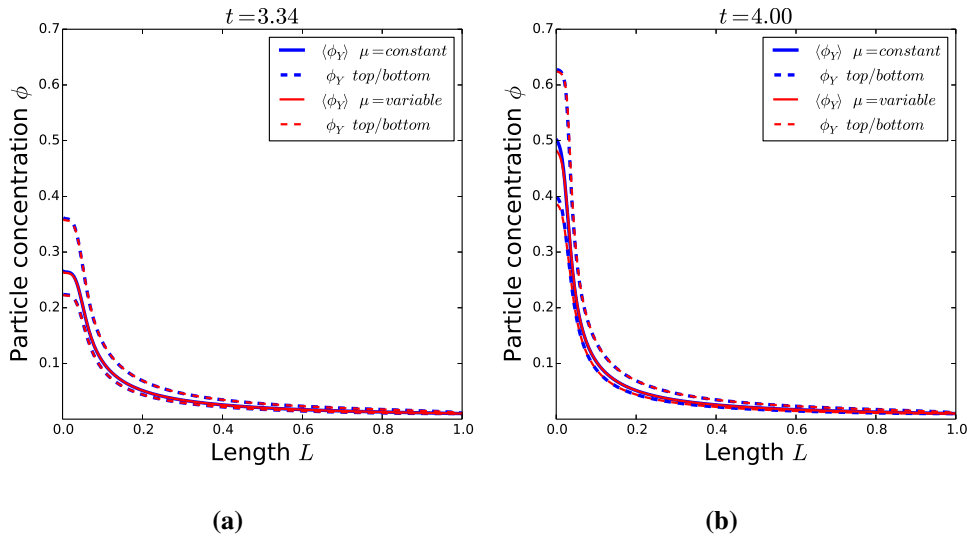


**Figure 1.10:** Comparison of the concentration profiles between two cases: constant viscosity (blue line) and varying viscosity according to Krieger’s formula (red line). Two different times are presented (a)  $t = 3.34$  (b)  $t = 4.00$ . Solid lines represent the cross-section-averaged concentration. The top (resp. bottom) dashed lines correspond to the particle concentration in the top (resp. bottom) of the channel.

drying in a microevaporator were simulated. In the first one the viscosity of the suspension was considered constant while in the second one it varied following the phenomenological equation of Krieger and Dougherty (1959). In Figure 1.10 the average particle concentration  $\langle \phi_Y \rangle$  is represented with the solid lines, and the top and bottom concentration profiles are plotted with the dashed lines. The blue line corresponds to results obtained using a constant viscosity and the red line to the variable viscosity case. As previously the particles are transported towards the end of the channel where they start concentrating until the maximum volume fraction value

of 0.64 is reached. For time  $t = 3.34$  the results seem to superimpose exactly one over the other.

For time  $t = 4.00$  the results are almost indistinguishable with a very small difference at the very end the channel. In the case of the variable viscosity the average concentration is lower than in the case of constant viscosity. This result suggests that the dependence of the viscosity on the particle concentration is not of great importance in the simulation of drying in a microevaporator under conditions of low Peclet. To confirm this idea, another simulation was ran for a system with a higher Peclet ( $Pe_y = 10$ ). By increasing the evaporation rate in the microevaporator, the

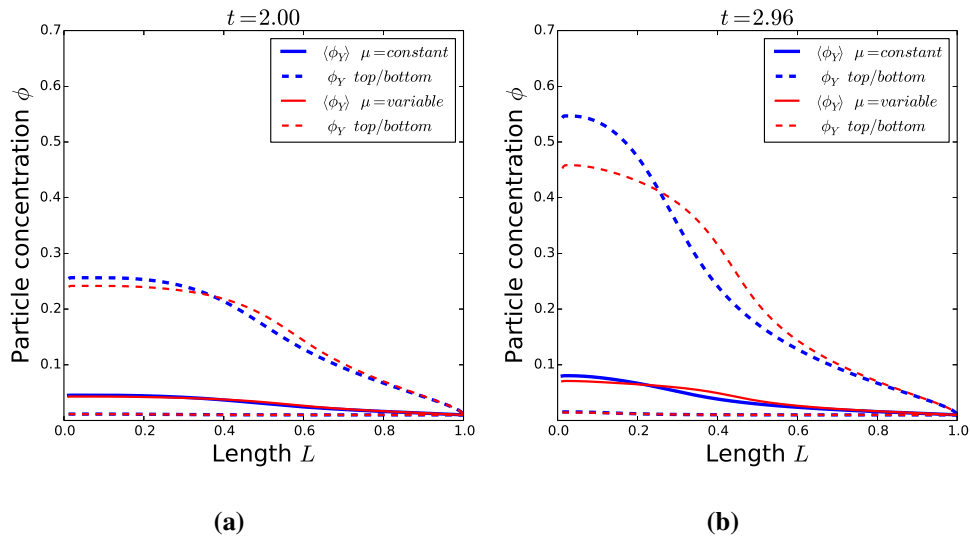


**Figure 1.11:** Comparison of concentration profiles along the  $x$ -axis. Blue lines correspond to constant viscosity cases and red lines to variable viscosity cases. Two different times are presented (a)  $t = 2.00$  (b)  $t = 2.96$ .

Peclet number increases. The profiles of particle concentration are presented in Figure 1.11, again with the solid lines representing the cross-section-averaged concentrations  $\langle \phi_Y \rangle$  and the dashed lines the concentrations at the top and bottom of the channel. The blue color corresponds to constant viscosity and the red color to variable viscosity. This system shows a significantly different behavior from the previous one at  $Pe_y = 1$ . What can be initially observed is that the concentration at the top of the microevaporator is much higher than in the rest of the channel for both times. For  $t = 2.00$  the concentration at the top is at least 4 times higher than the calculated average and  $\sim 20$  times higher than the one at the bottom of the channel.

The same tendency continues for longer times (see  $t = 2.96$  in Figure 1.11) with the gap between the concentration at the top of the channel and the average value get-

ting larger. This extreme difference in concentration between the top and the bottom of the channel has been reported as skin formation by many authors considering the drying of thin films (references in Routh (2013)). It is considered to be an important drying inhomogeneity. Furthermore, in the condition of high Peclet the variable viscosity has a significant effect not only in the absolute values of the concentration but as well on the distribution of this concentration along the  $x$ -axis.

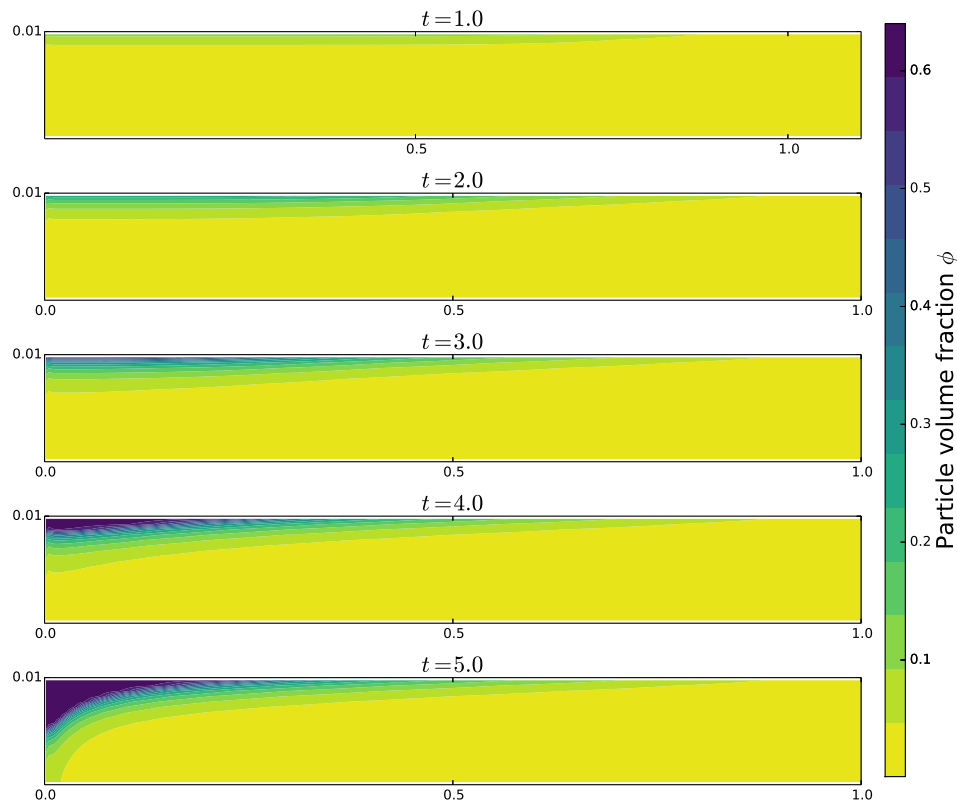


**Figure 1.12:** Particle concentration  $\phi$  contours for five different times from top to bottom  $t = 1, 2, 3, 4, 5$ . In this figure,  $Pe_y = 10$  and the viscosity was held constant.

Unfortunately, access to longer times was only possible in the case of constant viscosity. For a variable viscosity, the time step used in the present numerical scheme needed to decrease with increasing viscosity, until a prohibitive point ( $dt = 10^{-7}$ ) was reached. Future uses of the SBM in JADIM would benefit from the implementation of a fully implicit and stable temporal scheme to prevent this issue. Nevertheless, some general tendencies of the suspension flow in a microchannel will be shown in Figure 1.12, where the particle concentration contours are presented for the case of constant viscosity at different times  $t = 1.0, 2.0, 3.0, 4.0, 5.0$ . As already discussed the particles are transported towards the surface of the channel and they continue to

accumulate until close-packing is reached. As it was shown in Figure 1.11 and now visualized in Figure 1.12 the bottom of channel has a very low concentration of particles, while the skinning zone at the top of the channel is very thin. It seems that close packing is initially reached at the top left corner of the channel and starts propagating towards the inlet in a diagonal way.

The above results indicate that the variations of viscosity due to particle concentration gradients are not affecting the suspension flow for  $Pe_y = 1$ . On the other hand for higher Péclet numbers a significant influence can be observed. For cases of very low Péclet where the deposition of particles is almost perpendicular to the flow there should not be any effect of the viscosity on the suspension flow.

### 3.2.3 Comparison of cases with different Péclet numbers

In this section a comparison will be demonstrated between three simulation cases with different Péclet numbers  $Pe_y = 0.1, 1, 10$ . The results presented concern the shape of particle concentration profiles that can be obtained by varying the Peclet number, and the influence of the viscosity on the suspensions streamlines.

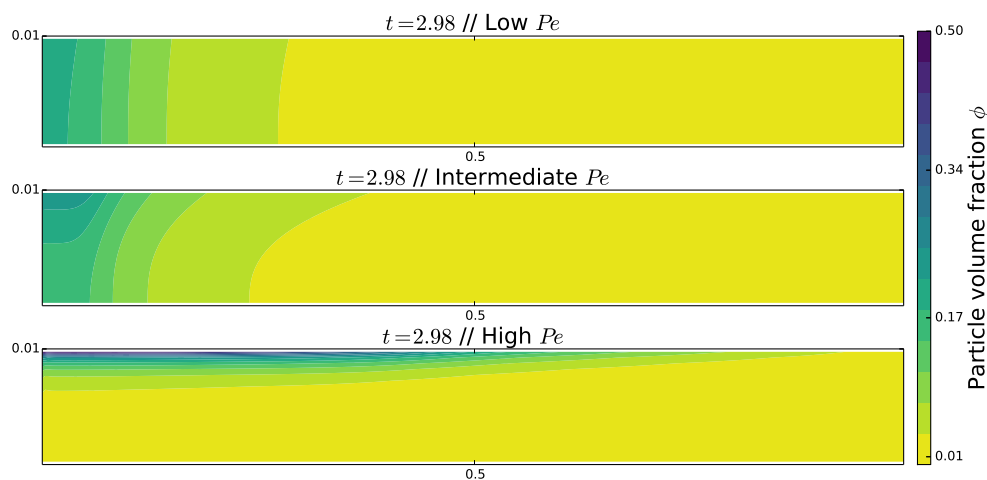


**Figure 1.13:** Comparison of the concentration contours for three different Péclet numbers (*Top*)  $Pe_y = 0.1$ , (*Middle*)  $Pe_y = 1$  and (*Bottom*)  $Pe_y = 10$  for the same simulation time  $t = 2.98$

In Figure 1.13 the particle concentration contours are shown for the three evaporation rates. At the top of the figure is the case of low evaporation rate ( $Pe_y = 0.1$ ). Since the diffusion of the particles is more significant now, particles are transported at the end of the channel creating an homogeneous deposit perpendicular to the main flow direction. It propagates towards the entrance (horizontal drying front). Since the

convective flux created by evaporation is not significantly higher than the diffusive mass flux, it is expected that once the particle diffusivity becomes more important due to particle concentration, the propagating front might not have the concentration of closed packed particles. This a typical example found in literature as horizontal drying front Routh (2013) where  $Pe_y \ll 1$ .

As was already discussed, for Péclet values  $Pe = 1$  the concentration of particles is initially inhomogeneous in the direction perpendicularly to the flow, but as soon as the close packing concentration is reached ( $\phi \sim 0.64$ ) at the top of the channel the high diffusivity of the particles makes them diffuse to the bottom. A steep front is created, and it subsequently propagates towards the entrance of the channel. This kind of drying is also reported as horizontal drying front but the front propagation behavior is obtained for high particle concentrations.

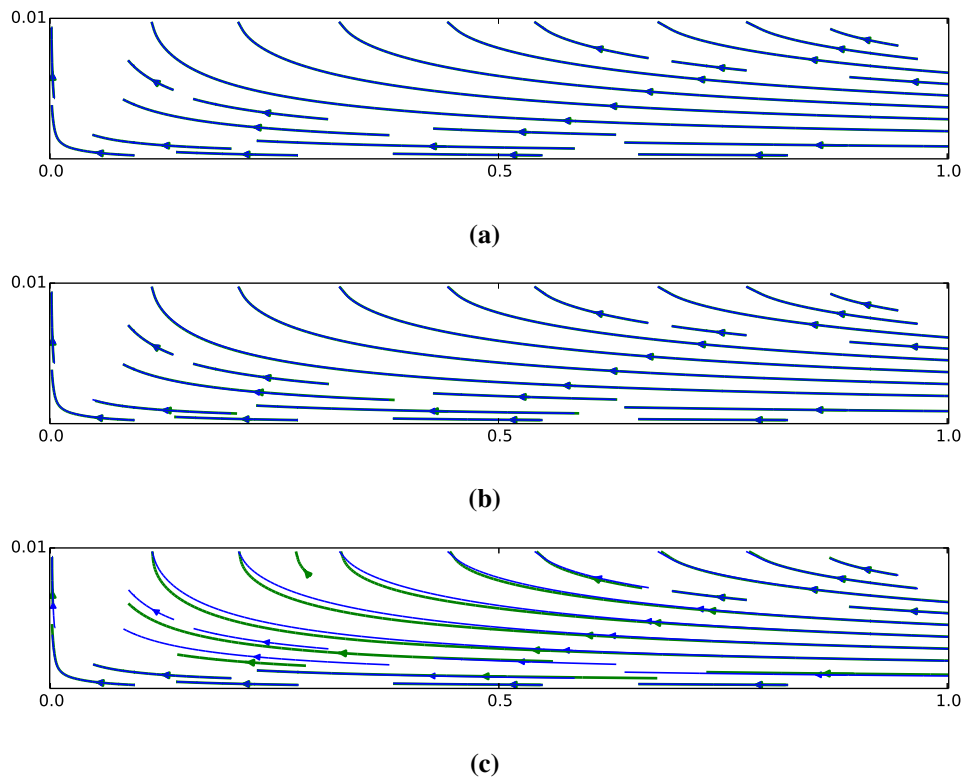


**Figure 1.14:** Comparison of streamlines between simulations where the viscosity was constant (*blue* streamlines) and simulations where viscosity was given by Krieger's formula (*green* streamlines). Three different Péclet numbers are presented (a)  $Pe_y = 0.1$ , (b)  $Pe_y = 1$  and (c)  $Pe_y = 10$ .

For high Péclet values ( $Pe > 1$ ) another type of drying was identified, the skinning or skin formation. In this case, because of the high evaporation rate the particles

are transported directly at the top of the channel creating a region of very high particle concentration that leads to skin creation.

In Figure 1.14 the suspension streamlines are plotted for the three Péclet values discussed above ( $Pe = 0.1$ ,  $Pe = 1$  and  $Pe = 10$ ). The blue lines are the cases for which viscosity is constant and the green lines correspond to simulations with variable viscosity. For  $Pe = 0.1$  and  $Pe = 1$  it can be stated that the variable viscosity does not modify the streamlines. On the other hand, for  $Pe = 10$  there is a clear influence of the viscosity. Streamlines close to the evaporation zone, and especially in the region where the particle concentration is high, tend to become more perpendicular to the flow. The fact that streamlines are more sensitive to viscosity variations at high  $Pe$  numbers is linked to the volume fraction field structure: at high  $Pe$  the skin at the top of the channel induces a high viscosity zone at this position. In order to minimize viscous dissipation, it is expected that the streamlines penetrate into this thin zone in a perpendicular manner. This is what is observed in Figure 1.14.

### 3.2.4 Comparison of cases with different particle charges

After the evaluation of many possible situations such as different evaporation rates and the variation of the viscosity as a function of the particle concentration, it is interesting to realize a final test case which is more relevant with the application in this work, the simulation of electrostatically charged nano-particles. As in the case of hard spheres, the quantity used to model the collective diffusive behavior of the particles was the equilibrium osmotic pressure  $\Pi$ . A detailed description on how to calculate it was given in Section 2. The plot of the osmotic pressure as function of the particle concentration was given in Figure 1.7. A significant increase in the absolute value of the osmotic pressure is noted, even for nano-particles with a small charge ( $0.025 e/nm^2$ ). This increases considerably the value of the generalized Stokes-Einstein diffusion coefficient. It may be anticipated that since the diffusion coefficient of the particle transport equation is increased, colloids will be deposited following the horizontal drying front picture.

In Figure 1.15 the particle concentration contours are plotted for three different charges. The first corresponds to particles with zero charge (hard spheres), the second one to a small surface charge of  $0.025 e/nm^2$  and the third one to a moderate charge of  $0.050 e/nm^2$ . The Péclet number for all the cases was the same and equal to  $Pe_y = 1$ .

In the case of hard spheres, as was already discussed, the highest particle concentration occurs at the top left corner of the channel. Once the diffusion becomes

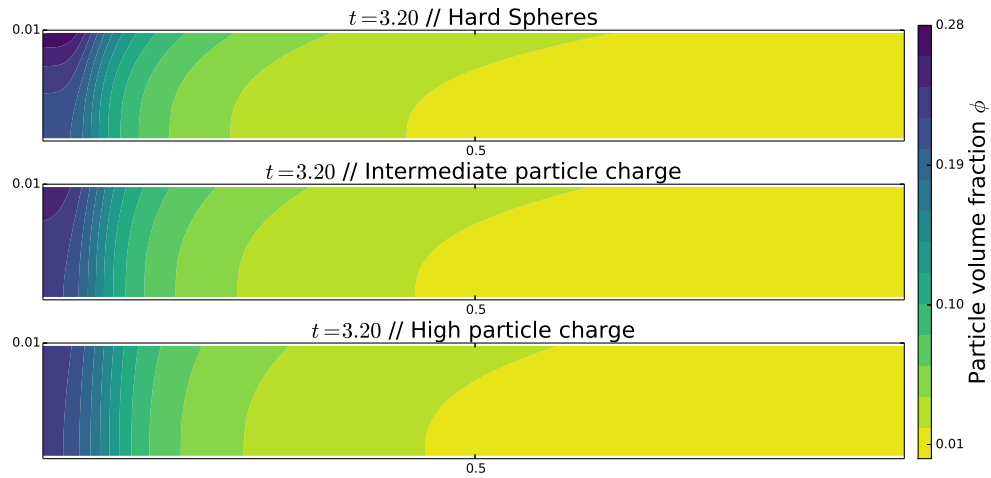


**Figure 1.15:** Comparison of the concentration contours for particles with different surface charges. (*Top*) Hard-Spheres, (*Middle*) Surface charge  $\sigma_0 = 0.025 e/nm^2$  and (*Bottom*) Surface charge  $\sigma_0 = 0.050 e/nm^2$ . The initial macroscopic Péclet is  $Pe_y = 1$  for all cases and the simulation time is  $t = 2.98$ .

important, near close-packing, particles diffuse towards the bottom of the channel. For the cases of charged particles, particle concentration seems to be homogeneous in the direction perpendicular to the main flow even for time  $t = 3.20$  where particles are far from reaching a close-packed state ( $\phi \sim 0.2$ ). The diffusion coefficient is so high that particles can diffuse back against the main flow in the  $x$  direction and propagate towards the entrance of the channel. Simulations were stopped before the the boundary condition defined there could influence the solution. In any case no significant behavior change is expected for longer times since the diffusion of the particle phase is only increasing with the concentration of the particles.

This is an interesting outcome if related with a real experiment. Assuming that three suspensions with the characteristics detailed above are dried under similar conditions, the one containing the hard-spheres may reach at some point close packing creating a dense solid phase since the particles do not interact strongly except for high concentrations. On the other hand, for the charged particles, the evaporation rate may not create enough flow to overcome the strong interactions between particles that gives rise to an important osmotic pressure. Thus, after reaching a point where the convective flux is equalized with the diffusional one, particles will not concentrate anymore. This concentration may be well below  $\phi \sim 0.6$  as shown in the simulation of the micro-evaporator in Figure 1.15. Consequently, the dried suspension will either have an increased porosity or a high water content.

Even though this systems seem trivial to simulate since the high diffusivity of the

particles masks the convective flux which mostly creates the inhomogeneities, one has to take into account that the surface charge can change depending on the composition of the solution containing the particles. It is known that the charge of the particles is influenced by the  $pH$  of the solution as well as the salt concentration. This means that for the same type of nano-particles, simply changing the composition of the solution containing them can lead to different behaviors during drying; from horizontal drying fronts to skin formation. Moreover, in cases where a strong convective flux is expected, electrolyte ions can be transported as well, creating regions inside the domain with different ionic strengths and thus different interaction ranges. Hence, for practical implementations, knowing the equation of state  $\Pi(\phi)$  is not sufficient. We must be able to model the variations of the osmotic pressure with  $\phi$ , the Debye length, and the surface charge density.

### 3.3 Summary and Conclusions

In this section, a modeling strategy was presented for the simulation of the drying of colloidal suspensions. The case of a micro-evaporator was used as an example because of the controlled conditions under which drying is effectuated. In terms of simulation, the advantage of such a device is first of all the simplicity of the implementation of the drying interface. The geometry is a simple rectangle without a moving interface.

In a first time the closure of the equations was given with the constitutive equations for the viscosity and the osmotic pressure. It was stated that, because the particle Péclet number is well below one ( $Pe_p = 10^{-5} \sim 10^{-2}$ ), the effect of hydrodynamic interactions between particles can be neglected. Thus terms related with the shear-induced migration and with the normal stress differences were omitted. The equations of motion of the suspension are then

$$0 = \nabla \cdot \langle \mathbf{u} \rangle \quad (1.68)$$

$$0 = -\nabla[(1 - \phi)\langle p \rangle^f] + 2\nabla \cdot (\eta_0(1 + \eta^s(\phi))\langle \mathbf{e} \rangle). \quad (1.69)$$

The particle transport equation becomes

$$\frac{\partial \phi}{\partial t} + \langle \mathbf{u} \rangle \cdot \nabla \phi = \nabla \cdot \left[ \frac{2a^2}{9\eta} f(\phi) \nabla \Pi \right]. \quad (1.70)$$

The solution of these equations was realized with the CFD code JADIM (IMFT). The modifications of this code to include a varying diffusion coefficient and a varying

viscosity were validated in a first time against a 1-D numerical solution of Merlin et al. (2012). After the validation, an evaluation of the necessity for a 2-D solution was performed. The results from the 1-D model were compared with the results of the 2-D model averaged over the channel cross-section. Even for simple geometries there is a significant 2-D flow inside the micro-evaporator. This leads to the conclusion that for complex geometries the full resolution of the flow and the particle transport is a necessity. On the other hand, for simple flows with a macroscopic Péclet number  $Pe_y \leq 1$ , one dimensional approaches are sufficient.

The viscosity was considered constant during this initial study of multi-dimensional effects. This is a very strong approximation for suspensions with particle concentrations  $\phi > 0.2$ . Hence, in a second time the dependence of the film homogeneity was examined by using a viscosity relation depending on the particle concentration. Again it was demonstrated that, in the present flow, the viscosity has a minor role for Péclet values  $Pe_y \leq 1$ . On the other hand for  $Pe_y > 1$  the very inhomogeneous concentration field generates high and low viscosity zones affecting significantly both the streamlines of the suspension and the transport of the particles.

Comparing the simulation results for three different Péclet regimes,  $Pe_y = 0.1, 1, 10$ , two deposition scenarios were identified. For  $Pe_y = 0.1$  the suspension dries in a way reported in the literature as a horizontal drying front. The concentration field is homogeneous in the cross-section of the channel and after reaching a maximum concentration a concentration front propagates upstream towards the entrance of the channel. The maximum value of the volume fraction obtained depends on the Péclet number. Hence for the case of  $Pe_y = 1$  this propagating front attains a concentration equal to the close packing one  $\phi \sim 0.64$ . The other deposition scenario was observed for Péclet  $Pe_y = 10$ . In this case the particles are transported directly towards the surface of the channel, thus creating a dense layer with concentrations close to 0.64. This scenario is reported in literature as skinning or skin creation, with many detrimental consequences in the drying process as it is possible to inhibit evaporation or to lead to film buckling or cracking.

Lastly, a comparison between hard-spheres and charged nano-particles was performed. It was demonstrated that for  $Pe_y = 1$  all suspensions are drying following the horizontal front propagation mechanism. This was somewhat expected from the fact that this mechanism is observed for  $Pe < 1$  for hard spheres, and that the relevant Péclet number for charged particles is  $PeD_0/D(\phi)$ , where  $D_0/D(\phi) \ll 1$ .

The results of Section 2 indicate that for the problem of a drying film, subtle hydrodynamic effects such as shear-induced migration can be neglected. Following

the rigorous derivation of the suspension balance model, we then conclude that the suspension can be modeled as an effective fluid with a viscosity depending on the volume fraction (at least) and that the standard Stokes-Einstein diffusion coefficient has to be replaced by the generalized Stokes-Einstein coefficient. The fact that simulations performed for charged particles led to results significantly different from those obtained for hard spheres indicates a very strong role of non-hydrodynamic interactions in the transport processes involved in a drying film. This is why it is of prime importance to characterize carefully the suspensions of boehmite particles considered as nano-container candidates. This is the aim of the next chapter.

---

## 4 References

- Anderson, T. B. and Jackson, R. (1967). Fluid Mechanical Description of Fluidized Beds. Equations of Motion. *Industrial and Engineering Chemistry Fundamentals*, 6(4):527–539.
- Brady, J. F. and Vicic, M. (1995). Normal stresses in colloidal dispersions. *Journal of Rheology*, 39(3):545–566.
- Clausen, J. R. (2013). Using the suspension balance model in a finite-element flow solver. *Computers & Fluids*, 87:67–78.
- Dbouk, T., Lemaire, E., Lobry, L., and Moukalled, F. (2013). Shear-induced particle migration: Predictions from experimental evaluation of the particle stress tensor. *Journal of Non-Newtonian Fluid Mechanics*, 198:78–95.
- Drew, D. A. (1983). Mathematical Modeling of Two-Phase Flow. *Annual Review of Fluid Mechanics*, 15(1):261–291.
- Frank, M., Anderson, D., Weeks, E. R., and Morris, J. F. (2003). Particle migration in pressure-driven flow of a Brownian suspension. *Journal of Fluid Mechanics*, 493:363–378.
- Jackson, R. (1997). Locally averaged equations of motion for a mixture of identical spherical particles and a Newtonian fluid. *Chemical Engineering Science*, 52(15):2457–2469.
- Krieger, I. M. and Dougherty, T. J. (1959). A Mechanism for Non-Newtonian Flow in Suspensions of Rigid Spheres. *Transactions of The Society of Rheology (1957-1977)*, 3(1):137–152.
- Lecampion, B. and Garagash, D. I. (2014). Confined flow of suspensions modelled by a frictional rheology. *Journal of Fluid Mechanics*, 759:197–235.
- Leighton, D. and Acrivos, A. (1987). The shear-induced migration of particles in concentrated suspensions. *Journal of Fluid Mechanics*, 181:415–439.
- Lhuillier, D. (2009). Migration of rigid particles in non-Brownian viscous suspensions. *Physics of Fluids*, 21(2):023302.
- Mason, M. and Weaver, W. (1924). The Settling of Small Particles in a Fluid. *Physical Review*, 23(3):412–426.

- Merlin, A., Salmon, J.-B., and Leng, J. (2012). Microfluidic-assisted growth of colloidal crystals. *Soft Matter*, 8(13):3526–3537.
- Miller, R. M., Singh, J. P., and Morris, J. F. (2009). Suspension flow modeling for general geometries. *Chemical Engineering Science*, 64(22):4597–4610.
- Morris, J. F. and Boulay, F. (1999). Curvilinear flows of noncolloidal suspensions: The role of normal stresses. *Journal of Rheology*, 43(5):1213–1237.
- Morris, J. F. and Katyal, B. (2002). Microstructure from simulated Brownian suspension flows at large shear rate. *Physics of Fluids*, 14(6):1920–1937.
- Nott, P. R. and Brady, J. F. (1994). Pressure-driven flow of suspensions: simulation and theory. *Journal of Fluid Mechanics*, 275:157–199.
- Nott, P. R., Guazzelli, E., and Pouliquen, O. (2011). The suspension balance model revisited. *Physics of Fluids*, 23(4):043304.
- Peppin, S. S. L., Elliott, J. a. W., and Worster, M. G. (2006). Solidification of colloidal suspensions. *Journal of Fluid Mechanics*, 554:147–166.
- Perrin, J. (1910). *Brownian movement and molecular reality*. London : Taylor and Francis.
- Phillips, R. J., Armstrong, R. C., Brown, R. A., Graham, A. L., and Abbott, J. R. (1992). A constitutive equation for concentrated suspensions that accounts for shear induced particle migration. *Physics of Fluids A*, 4(1):30–40.
- Phung, T. N., Brady, J. F., and Bossis, G. (1996). Stokesian Dynamics simulation of Brownian suspensions. *Journal of Fluid Mechanics*, 313:181–207.
- Prosperetti, A. and Tryggvason, G. (2009). *Computational Methods for Multiphase Flow*. Cambridge University Press.
- Routh, A. F. (2013). Drying of thin colloidal films. *Reports on Progress in Physics*, 76(4):046603.
- Routh, A. F. and Russel, W. B. (1998). Horizontal drying fronts during solvent evaporation from latex films. *AIChE Journal*, 44(9):2088–2098.
- Routh, A. F. and Zimmerman, W. B. (2004). Distribution of particles during solvent evaporation from films. *Chemical Engineering Science*, 59(14):2961–2968.

- 
- Salmon, J.-B. and Leng, J. (2010). Application of microevaporators to dynamic exploration of the phase diagram. *Journal of Applied Physics*, 107(8):084905.
- Schindler, M. and Ajdari, A. (2009). Modeling phase behavior for quantifying micro-pervaporation experiments. *The European Physical Journal E*, 28(1):27–45.
- Semwogerere, D., Morris, J. F., and Weeks, E. R. (2007). Development of particle migration in pressure-driven flow of a Brownian suspension. *Journal of Fluid Mechanics*, 581:437–451.



Let there be nano-containers

2



---

## 1 How are they made and what do they look like?

In the previous chapter we demonstrated that the flow of a colloidal suspension is highly dependent on the non-hydrodynamic particle-particle interactions; so much that it masked the hydrodynamic interactions between particles. A correct account of the interactions is therefore needed and for this reason the following part is consecrated to the interactions between particles in electrolyte solutions. As explained in the introduction, one of the problematics in this thesis is to model the transport of nano-containers in order to create homogeneous thin films for protection against corrosion.

Nano-containers, as the word suggests, are nano structures that have the ability to contain or enclose a material of interest. In the domain of anti-corrosion coatings, the materials of interest are corrosion inhibitors. An important function of these containers is the ability to release the contained material when triggered from their local environment. The reason for such an approach is to create a new family of active coatings that can self-repair when the coating is damaged.

Recent developments in surface and coating science propose two different concepts for the fabrication of active, self-healing surfaces (Shchukin and Möhwald (2007)). Either the fabrication of active composite-layered systems in which the passive coating matrix is alternated with layers bearing an active coating component (e.g., inhibitor, lubricant) (see Figure 2.1a) or the integration of nano-scale containers (carriers) loaded with the active components into existing coatings (see Figure 2.1b). Even though the first approach seems to be easier in application it suffers from an important shortcoming, the spontaneous leakage of the corrosion inhibitor to the environment due to ageing. The main idea of the second approach is to load the corrosion inhibitor into nano-containers with a permeable shell and then disperse them into the coating volume. The advantage of such a system is the homogeneous distribution of the nano-containers and most importantly that the inhibitors are confined until triggered from the environment.

A third approach developed by Zheludkevich et al. (2005a,b) and later used by Jaubert (2012) in his thesis, is based on the physisorption of the corrosion inhibitor on nano-particles. It is an electrochemical approach where an electrolyte (the corrosion inhibitor) is adsorbed on the charged surface of a particle by means of electrostatic interactions. As long as the interactions are strong enough the ions stay adsorbed. The trigger for the release of the inhibitors could be the  $pH$  change when corrosion starts. This is shown schematically in Figure 2.2. It is thus suggested that  $pH$  variations can change the electrostatic interactions, with an immediate effect being the release

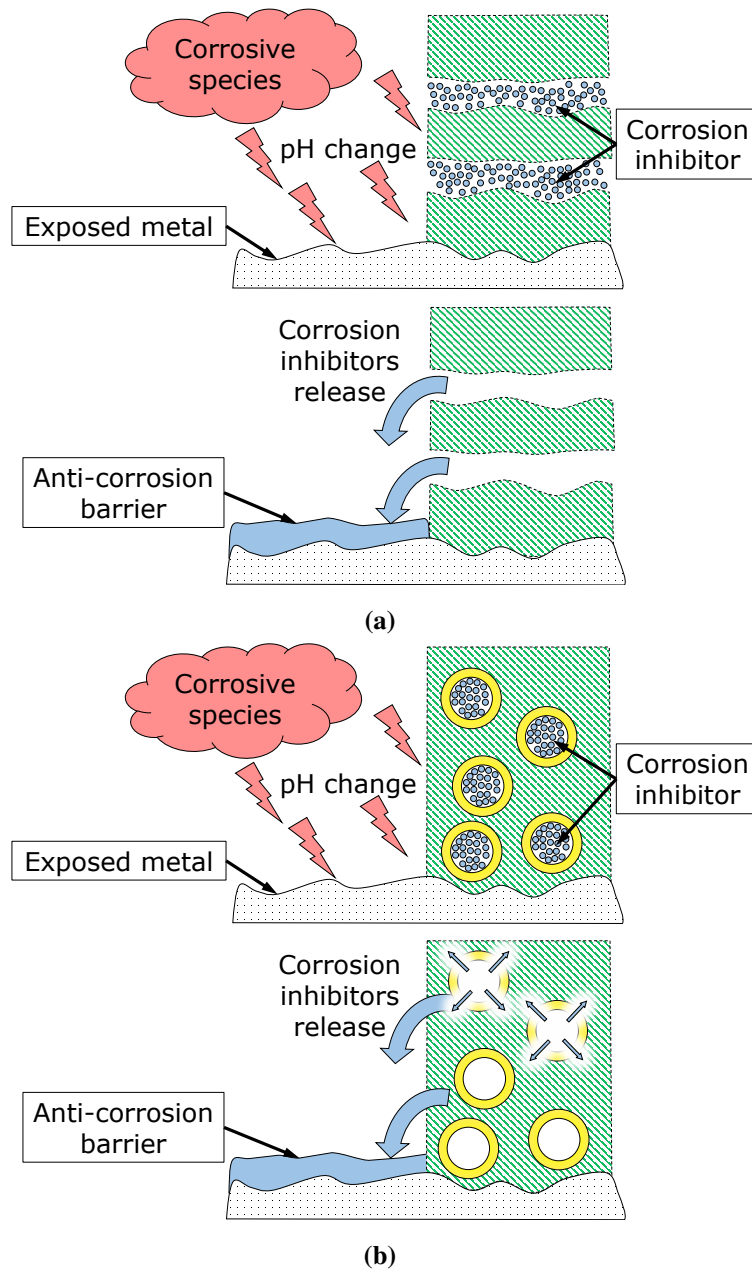


**Figure 2.1:** (a) Layer-by-Layer nano-containers approach, where the coating contains passive layers alternated with layers loaded with the active component, (b) Active component is encapsulated in a carrier shell (container) that possesses controlled permeability properties

of the inhibitors.

Since the concept of this type of nano-containers is to "bind" the corrosion inhibitor on the surface, it is natural to think that high container surface area leads to high capacity. This narrows down the possible container-candidates to container-

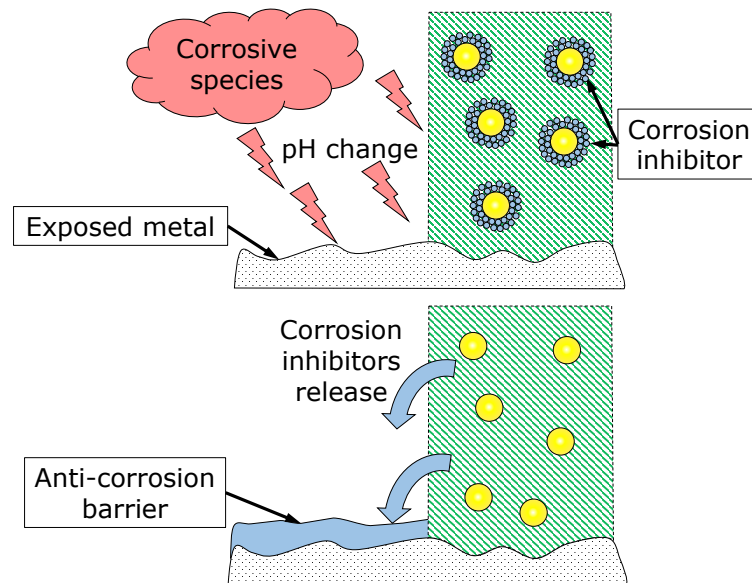


**Figure 2.2:** Nano-containers in this work, where the active component is physisorbed or adsorbed on the surface of the nano-particles

particles in the colloidal scale (nano-particles). Furthermore, for reasons of chemical compatibility with the substrate, which is important in corrosion studies (Tavandashti and Sanjabi (2010)), the choice is further narrowed down to aluminum nano-particles.

This section is consecrated to the creation of the actual container. Firstly, the nano particle synthesis will be briefly presented but with no further insights on the mechanisms that lead to the specific nano-particles since it is a topic discussed elsewhere (Zakharchenya (1996); Jaubert (2012)). Secondly, the different phases that co-exist (particles and liquid matrix) will be characterised separately. The interaction between the two will be considered in Section 2. To close this section, some insights will be given concerning the molecular structure of the nano-particles and how it could affect their behaviour when they are in contact with an electrolyte.

### 1.1 Nano-container development

Alumina or aluminum hydroxides can exist in nature in different crystalline structures. Alumina are usually termed the anhydrous aluminum oxides such as  $\text{Al}_2\text{O}_3$  and can have different types of crystal structures named for example  $\alpha$  or  $\gamma$ . Among the aluminum hydroxides there is the trihydroxide ( $\text{Al}(\text{OH})_3$ ) gibbsite and bayerite or the monohydroxide ( $\text{AlOOH}$ ) boehmite, which is relevant here.

There are many different synthesis protocols for the preparation of nano-particles (Jaubert (2012)). The protocol chosen in this work allows for the synthesis of nano-

particles that are already suspended in a liquid, without passing in a powder state which may be problematic for an industrial application. Furthermore, no particle washing and centrifugation is needed for the incorporation into the polymer matrix coating. This last feature, though, needs to be evaluated, since the suspending liquid contains all the by-products of the synthesis that may influence the performance of the nano-containers.

### 1.1.1 Particle synthesis

The particles were synthesized following a protocol initially developed by Yoldas (1973, 1975) for the creation of amorphous alumina and which has been used since in numerous studies (Pierre and Uhlmann (1987); Gieselmann and Anderson (1989); Yoon et al. (2002); Alphonse and Courty (2005); Bleta et al. (2011)). It is based on the hydrolysis of an aluminum alkoxide  $\text{Al}(\text{OR})_n$ , where OR is the alkoxy group with R being the alkyl chain. The precursor used is the Aluminum-tri-Sec-Butoxide (**ASB**)<sup>1</sup> (CID: 16685157) with a purity of 97%. The water used is of ultra-pure quality with a resistivity of  $18.2 \text{ M}\Omega \text{ cm}$ ; the concentration of the nitric acid ( $\text{HNO}_3$ ) was 68%<sup>2</sup>.

Initially an amount of ASB is put into a thermostated glass beaker under slow agitation with a magnetic stirrer in ambient temperature for about 15 minutes. Then, an excess quantity of water (100 mole of water for each mole of ASB) at  $\sim 85^\circ \text{C}$  is added, and stirred vigorously for 1 hour. During this time, hot water ( $\sim 85^\circ \text{C}$ ) is circulated into the thermostated beaker to keep the temperature stable. Then,  $\text{HNO}_3$  is added in a drop-wise manner so that a molar ratio of 0.07  $\text{HNO}_3$  to  $\text{Al}^{3+}$  is achieved. Lastly, the beaker is closed to prevent evaporation and left under stirring for 24 hours. At the end, the solution recovered is almost transparent and stable for weeks with a  $pH$  value of  $\sim 4 - 4.5$ . Following this protocol leads to the creation of a stable suspension of Boehmite nano-particles ( $\text{AlOOH}$ , Aluminum oxyhydroxyde) dispersed in a "mostly" aqueous matrix. An approximate concentration of the solids (particles, salt) in the suspension,  $\sim 38 \text{ gr L}^{-1}$ , was measured by weighing the solids after drying a known volume of suspension at  $150^\circ \text{C}$ . At this point there is no other information concerning the composition of the matrix, so a further refinement of the concentration will follow.

---

<sup>1</sup>SIGMA-Aldrich

<sup>2</sup>VWR

### 1.1.2 Physical characteristics of the particles

Information about the physical characteristics of particles, such as size and specific surface are important in a first step towards verifying that the synthesis was reproduced correctly. More importantly, the correct account for the shape and size of the particles is essential in understanding particle interactions and the specific surface of the particles gives an indication of the surface available for adsorption.

The two techniques used to define the shape of the particles and measure their size are the Dynamic Light Scattering (**DLS**), with details given in Malvern (2014), and cryo-Transmission Electron Microscopy (**cryo-TEM**).

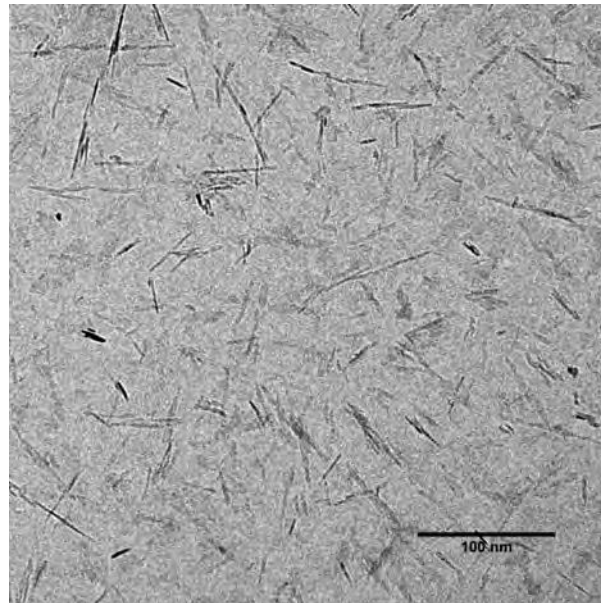
DLS<sup>3</sup> is used to determine the hydrodynamic size of the particles, as well as to provide a qualitative quality control of the suspension after its synthesis. The hydrodynamic size measurement with this technique lacks the information of shape of the particles since it assumes that all objects are spherical. Furthermore, if the objects are spherical but not mono-disperse, the polydispersity can only be retrieved using somewhat uncontrolled post-processing. In the case of non-spherical, poly-disperse particles, the above remarks indicate that we only have access to an average value which includes all possible orientations of particles during measurement, and depends on the geometry of the object.

The sample preparation is very simple since the particles are already suspended in a solvent, and it suffices to find the required concentration for robust and reproducible results. The concentration will depend upon the relative refractive index (between particles and solvent) and the particle size. The larger the particle size, the more scattered light it produces and hence the lower the concentration that can be measured. In addition a high particle refractive index will also lead to a high level of scattering. Furthermore, the theory used in dynamic light scattering is generally valid in the case of the free diffusion of particles, meaning that there should be minimal influence of the motion of particles between them. Finally, the correct concentration is chosen by experimentally testing different concentrations and seeing the effects in the repeatability of the size measurement and the polydispersity index. The latter needs to be  $< 0.7$  since algorithms used for its determination may not yield correct results.

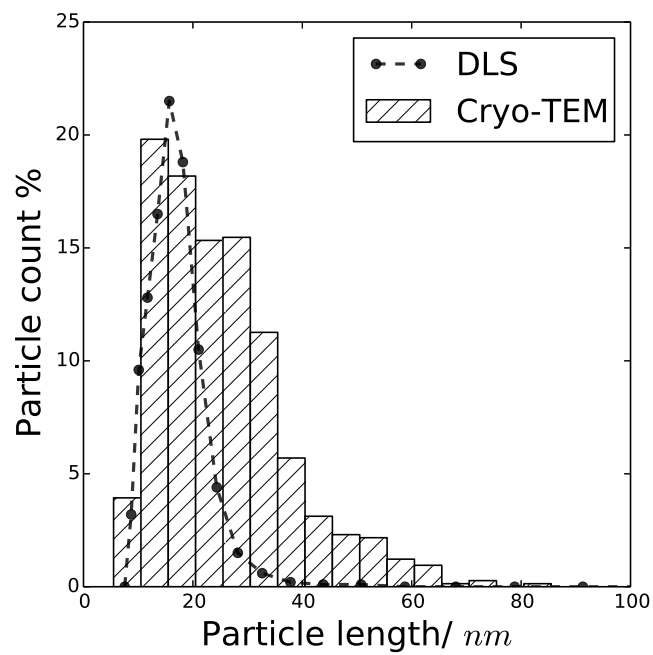
When the stock solution was used, particle size was varying and the polydispersity index had its maximum value ( $\sim 1$ ). By diluting with ultra-pure water to reach a concentration of  $0.38 \text{ gr } L^{-1}$  or a volume fraction  $\phi \sim 0.01\%$ , particle size measurement was reproducible with a low polydispersity index .

---

<sup>3</sup>Malvern Zetasizer ZS90, fixed scattering angle of  $90^\circ$



(a)



(b)

**Figure 2.3:** (a) Cryo-TEM image of boehmite nano-particles, (b) Particle size distribution measured by DLS and cryo-TEM, and represented in particle count percentage as a function of particle size.

Usually, with the electron microscopy techniques the sample preparation for particles already suspended is simple; it consists of simply dipping the sample holder (grid) into the solution and letting it dry. The problem with this technique is that during the solvent evaporation particles approach each other, create aggregates and essentially modify the observations. In cryo-TEM instead of drying the suspension onto the grid, it is quickly frozen with liquid nitrogen. This immobilizes the initially well dispersed particles in a disperse state.

Cryo-TEM<sup>4</sup> can be more quantitative compared to DLS since it gives access to the true form of particles and their absolute size, while being suspended in solution. The particle size can be accessed by post-treatment of the microscope images where particles are counted one-by-one or, if they are easily distinguished, automatically by the software. This method however, incorporates an error that can influence the results. Measuring a length on a two dimensional image can represent the real length only if the object measured is parallel with the field of observation or if the positioning angle is known. This is not the case in cryo-TEM measurements as the particles are “frozen” inside their matrix and can have different orientations.

In Figure 2.3a a cryo-TEM image of boehmite nano-particles is presented, where it can be clearly stated that particles are very anisotropic with a shape that resembles a rod, cylinder, or a needle. In some cases particles seem to create small aggregates with other particles oriented in the same direction, creating small platelets observed from other researchers as well (Bleta et al. (2011); Alphonse and Courty (2005)). With the use of an image post-processing software (ImageJ) a number of images were treated to measure the particle distribution. After averaging over  $\sim 750$  particles, the size distribution obtained for the length of the particles is plotted in Figure 2.3b represented by the hatched bars. The average length of the particles is  $\sim 20$  nm with a width in the order of few nanometers. The asymmetrical attribute of the particles is highly sought since elongated objects like needles or thin flat plates, have a higher surface area compared with spheres with an equal volume fraction; consequently they are expected to have a higher adsorption capacity. Moreover, this difference in the dimensions of the particles is important because it can be used as a criterion for the choice of theoretical models. For example particle interaction theories mainly exist for spheres or cylinders.

Superposed in Figure 2.3b is the size distribution given by DLS. Even though this technique is most probably not adapted for this kind of particle, it seems to predict correctly some average particle size when compared with cryo-TEM. This is very

---

<sup>4</sup>Jeol JEM-2100

useful for the quality control of new batches of synthesized particles, as well as for the study of the stability of the suspension.

The accessible surface area of the particles is usually measured by a specific surface measurement technique. Even though there are a number of techniques, the most abundantly used is the BET (Brunauer–Emmett–Teller). This technique is based on the adsorption of an inert gas (Nitrogen,  $N_2$ ) on the surface of a dried solid phase as a function of the boiling temperature of the gas and the atmospheric pressure. Hence, the specific surface that is measured depends on the gas used, since the radius of gas molecules will have access to different parts of the particles. Furthermore, the measurement is realised in vacuum conditions and not in a liquid which would be of more interest here since the corrosion inhibitor adsorption is realised in a liquid medium. The BET specific surface was measured using a surface area analyser<sup>5</sup> by physical gas adsorption. Using the BET (Brunauer–Emmett–Teller) theory one has access to the BET surface, which in this case is in the order of  $\sim 280 \text{ m}^2 \text{ gr}^{-1}$ . This result is in accordance with BET surface measurements for the same particles (Alphonse and Courty (2005); Jaubert (2012)) and comparable with the values reported in Chiche et al. (2011) for plate-like boehmite particles ( $200 - 350 \text{ m}^2 \text{ gr}^{-1}$ ). In Shchukin and Möhwald (2007) it is briefly reported that aluminum oxyhydroxide nano-containers should have a specific surface of at least  $100 \text{ gr}^2 \text{ L}^{-1}$  but with no further justification. The specific surface measured by BET can not be used as an absolute criterion though to decide if a surface is a good or a bad adsorbent. Since adsorption of ions depends on the porosity of the solid, the accessibility of the surface area to the specific ion and the size of the ion, a surface can present very high adsorption of nitrogen compared with another but when a bigger ion is used it may result in the same specific surface.

Furthermore, one can compare this measured surface with the mean particle surface using the average size of the particles above and the density of boehmite taken as  $3.07 \text{ gr cm}^{-3}$  (Belounis (2015)). For  $1 \text{ gr}$  of boehmite the surface area is calculated at  $360 \text{ m}^2$ . The fact that the specific surface and the mean surface are in the same order of magnitude may suggest that the particles have no or negligible porosity. If this is the case, then the specific surface will mostly depend on the molecule used to determine the specific area.

#### *Freeze-dried powder preparation*

The measurement of specific surface is effectuated on a dried, solid medium but here the particles are already suspended in a liquid matrix. That means drying step is

---

<sup>5</sup>ASAP 2010



**Figure 2.4:** Very fine powder of boehmite nano-particles after freeze-drying

needed to bring the solution in a powder form. After some tests of simply drying a sample on a heated plate, it was found that this method is not adapted and produces big chunks of solid that need breaking in order to be usable. Furthermore, because of aggregation one can naturally question what effect there would be in the measurement of the specific surface. Because of the aforementioned, another drying process was chosen, named freeze-drying or lyophilisation. It is based in the principle of sublimation where the frozen solvent sublimates directly into vapour. Therefore, after freezing a certain amount of the suspension in liquid nitrogen, it is placed under vacuum for at least 3 days. The result is a very fine powder that can be used for the measurement of the specific surface.

### 1.1.3 Matrix composition

As discussed in the introduction, charged particles interact strongly with their environment. Changes in  $pH$  and salt concentration have an immediate effect on the properties and adsorption performance of the interface. Therefore, it is of great interest to analyse the composition of the background solution and elucidate the impact it could have on the adsorption performance.

The solution contains the by-products of the synthesis; an alcohol (2-butanol, Gieselmann and Anderson (1989)), nitrate ions ( $\text{NO}_3^-$ ) coming from the addition of nitric acid and an important quantity of aluminum ions ( $\text{Al}^{3+}$ ). The aluminum ions are expected to exist because they were not consumed for the formation of particles during the synthesis or from a partial dissolution of the particles to reach equilibrium.

The concentration of  $\text{Al}^{3+}$  was measured by means of Inductively Coupled Plasma - Optical Emission Spectrometry (**ICP-OES**<sup>6</sup>), a technique usually used for the detection of traces of metals. It is based on the emission of characteristic wavelengths from thermally excited electrons, after the atomization of a molecule. The sample is nebulised and then passed through a plasma torch, usually created by Argon, which breaks the molecules down to atoms. The continuous association and dissociation of electrons around atoms produce characteristic wavelengths that are detected by a CCD camera.

To isolate  $\text{Al}^{3+}$  ions in order to quantify their concentration, a known volume of stock suspension was dialysed against ultra-pure water for a week (see Appendix 4). The dialysis membrane<sup>7</sup> will restrict the particles inside the dialysis sack, but ions will be diffused over the entire container containing ultra-pure water. As expected, since a fixed amount of ions now occupies a bigger volume, the ion concentration is much lower than in the stock suspension. This is not a problem because all volumes can be recovered and analysed by ICP-OES calibrated with  $\text{Al}(\text{NO}_3)_3$ .

The concentration of  $\text{Al}^{3+}$  is found to be  $C_{\text{Al}^{3+}} \sim 0.02 \text{ mol L}^{-1}$ . In the literature there is only one study (Gieselmann and Anderson (1989)) to my knowledge that reports on the  $\text{Al}^{3+}$  ions in the suspension using the same synthesis protocol. The value ( $0.002 \text{ mol L}^{-1}$ ) is significantly lower than the one in this work. The possible reasons for this difference could lie first of all in the different techniques used for the measurement; in their study Gieselmann and Anderson measured the conductivity of the suspension and then compared against a calibration curve of conductivity made with known quantities of  $\text{Al}(\text{NO}_3)_3$ . Another possible reason could lie in the selection of dialysis membrane with a cut-off size that is not sufficient to stop very small particles ( $< 5 \text{ nm}$ ) passing through the membrane. Lastly, another source of error could lie in the gradual dissolution of  $\text{Al}^{3+}$  from the particles surface during dialysis. In Franks and Gan (2007) they report that in alumina solid phases, when immersed in water, the solution concentration of  $\text{Al}(\text{III})_{\text{aq}}$  will increase slowly with time until the solubility limit is reached.

An estimation of the nitrate ions ( $\text{NO}_3^-$ ) in solution can be easily given since the only source is the nitric acid added during synthesis which is a known quantity. In the synthesis example (given in Section 1.1.1),  $474 \mu\text{L}$  of  $\text{HNO}_3$  was added, which corresponds to a concentration of  $\text{NO}_3^-$  of  $0.035 \text{ mol L}^{-1}$ .

<sup>6</sup>Perkin Elmer 8300

<sup>7</sup>Spectra/Por, 12-14 *kD*

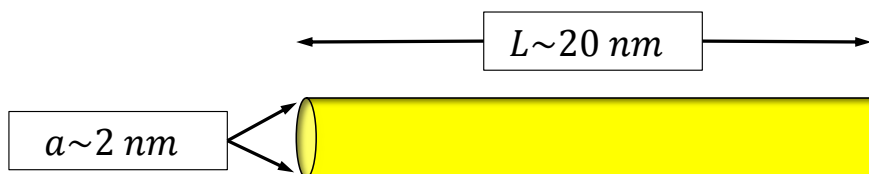


**Figure 2.5:** Coarse-grained particle model used for modelling

## 1.2 Discussion and Summary

In this section, important answers were provided concerning the synthesis of the nano-particles (nano-containers), their physical characteristics and the matrix that surrounds them.

It was shown that the protocol used for the synthesis yields a transparent, stable suspension (no sedimentation) of rod-shaped particles. The solids (particles and salt) were measured  $38 \text{ gr } L^{-1}$ , but since the principal components of the matrix are now known ( $Al^{3+}$ ,  $NO_3^-$ ), the particle concentration can be calculated  $36 \text{ gr } L^{-1}$ . The dimensions of the particles are more or less homogeneous considering they are the product of a bulk synthesis. Their average length is  $L \sim 20 \text{ nm}$  and their width ( $W$ ) is a few nanometers. High asymmetry of the particles can be considered as an important feature of the nano-particles since very thin and elongated surfaces offer a very high surface area compared with the volume they occupy.

Based on the physical characteristics of the particles, a coarse-grained particle model can be proposed (see Figure 2.5) which will be used in the next section concerning the stability of the suspension. Their high anisotropy ( $L \sim 5 W$ ) and resemblance with a cylindrical body leads to the decision of a cylindrical particle model.

The specific surface of a powder of boehmite nano-particles was measured by nitrogen adsorption at  $280 \text{ m}^2 \text{ gr}^{-1}$ , which is well above the  $100 \text{ m}^2 \text{ gr}^{-1}$  criterion argued in Shchukin and Möhwald (2007) even though somewhat arbitrary.

Concerning the composition of the surrounding matrix, it was found to contain a significant amount of ions. These ions are the synthesis "by-products" and they can influence significantly the properties of the suspension. More precisely, aluminum ions ( $Al^{3+}$ ) were discovered with a concentration of  $C_{Al^{3+}} \sim 0.02 \text{ mol } L^{-1}$  that most probably were not consumed during the synthesis or were the product of partial nano-particle dissolution. Furthermore, there is a high concentration of nitrate ions ( $C_{NO_3^-} \sim 0.035 \text{ mol } L^{-1}$ ) because of the peptization step with nitric acid.

The interface between aluminum oxides and water is important in a wide num-

ber of applications (Franks and Gan (2007)). An important parameter that influences the outcome or performance of these applications lies in the interactions of the aluminum surfaces with other species such as ions, polymers or surfactants. In some applications, for example in this work, the interaction with the surface is of direct interest since the purpose is to adsorb and desorb ions on the surface. The adsorption of a solution species to a solid surface is mainly influenced by the charge on both the surface and solution species, and by non-electrostatic interactions.

Boehmite ( $\text{AlOOH}$ ), as the composition suggests, is an aluminum oxide hydroxide. A clean surface of metal oxides, such as boehmite, in vacuum is composed of unsatisfied bonds of metal and oxygen atoms. Once in contact with water or air humidity, the surface reacts with the water and produces hydroxyl groups. Thus, the reactive functional group is the hydroxyl ion ( $\text{OH}^-$ ) which is coordinated in various ways with aluminum cations (Franks and Gan (2007)). Furthermore, in the case of a non-ideal surface that contains crystal lattice defects, unsatisfied bonds with hydroxyls can create a charge imbalance. In order for the surface to achieve electro-neutrality, ions or molecules are adsorbed in the empty or incomplete sites (Sposito (1995); Franks and Gan (2007)). This process is shown schematically in Figure 2.6; subfigure (a) shows the aluminum-vacuum interface with the unsatisfied bonds that lead to negative and positive charge sites. In subfigure (b) the aluminum surface comes into contact with water and a reaction between the surface sites and water molecules gives rise to surface hydroxyl groups ( $\text{Me}-\text{OH}$ )

In the case of particles the main contribution of charge is from the edges and corners (in an atomic level) because the crystal structure there is truncated. Thus the surface contains a larger number of unsatisfied bonds in comparison with the main body of the particle. When immersed in an electrolyte solution, the  $pH$  of the solution determines the charge and the potential of the surface, by the adsorption of  $\text{H}^+$  and  $\text{OH}^-$  as well as salt ions. Because of this property of adsorbing or releasing protons these metal oxides surfaces are generally called *amphoteric* (Hunter (2001)) and the  $\text{H}^+$  and  $\text{OH}^-$  are called *potential-determining ions (pdi)*. This process can be written in a reaction form where  $\text{M}$  is referred to the metal oxide surface. The difference in concentration of  $\text{H}^+$  and  $\text{OH}^-$  on the oxide surface is what determines the overall charge of the particles. The  $pH$  for which there is no difference in the number of positive and negative surface charges is defined as the *point of zero charge (pzc)*. As an example, in many aluminum hydroxides or alumina powders when  $pH < pH_{pzc}$  the surfaces are positively charged because the concentration of  $\text{H}^+$  is higher than that of  $\text{OH}^-$ , and negatively charged for  $pH > pH_{pzc}$  (Karamalidis and

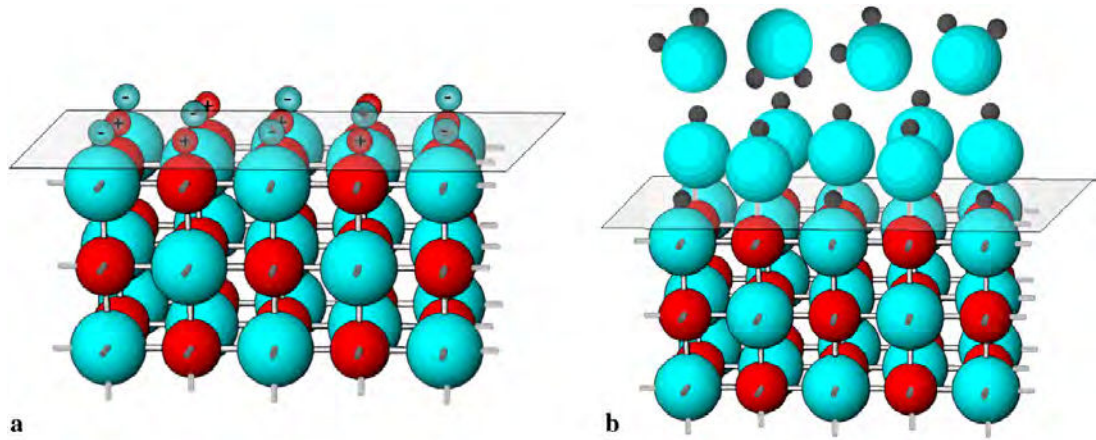
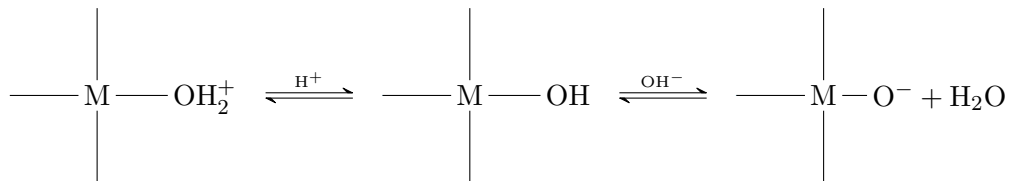


**Figure 2.6:** Schematic representation of the surface of metal oxides from Franks and Gan (2007). The blue spheres represent oxygen, the red spheres a metal cation and the small grey spheres represent hydrogen. (a) When an aluminum surface is in vacuum, an equal number of positive and negative sites exist due to unsatisfied bonds of atoms. (b) When the surface comes in contact with water or air humidity, water reacts with the surface to form surface hydroxyl groups (Me-OH).

Dzombak (2011); Franks and Gan (2007) and references inside).



Because of this imbalance of charge on the surface, nano-particles are expected to carry a net charge (either positive or negative) and because of this charge, other charged species in the solution will react correspondingly. This interaction will be the subject of Section 2.

## 2 Do they stay suspended?

When particles, of a very small size (colloids), are dispersed in a liquid medium they will be undergoing continuous movement (Brownian motion) and they will collide. These collisions can lead to permanent associations between them if no mechanism exists to prevent this. In the case of charged particles it is the electrostatic effects that can play this role of prevention. If the permanent association, or aggregation, is prevented then the suspension is considered stable and these suspensions are called electro-statically stabilized. The height of the preventive electrostatic barrier is determined by the charge of the particles, the concentration of electrolyte ions in the suspension as well as their valency. Consequently, the stability of the suspension depends on phenomena happening on the interface between the solid particles and the liquid matrix.

When a charged surface comes into contact with an electrolyte, the solid-liquid interface is surrounded by ions with the opposite charge (counter-ions) in a way that far from the particle, the system of particle-ions appears to be electrically neutral. Because the particles and the counter-ions have a different charge sign, they are electro-statically attracted. The strength of the attraction depends on the distance, the particle charge, as well as the charge of the ions (or valency). The main concept is shown schematically in Figure 2.7, where the counter-ions form a kind of “cloud”. The first “layers” of counter-ions close to the charged surface are electro-statically “bound” on the particle surface, forming what is called a dense ionic layer (ionic condensation see Belloni (1998)), and the rest form a continuously decreasing concentration until the bulk concentration of counter-ions is reached. This structure of diffuse electric charge around the particle is called the *Diffuse Electrical Layer*. The layer that lies right after the charged surface and contains ions that “touch” the surface is called the *Stern Layer*. Combined, the Diffuse Electrical Layer and the Stern Layer form the *Electrical Double Layer (EDL)* which has been a subject of research for well over a century (Hunter (2001)). This description is quite simplistic and represents only a part of the phenomena that happen inside the electrical double layer. For example, ions have a finite volume and a hydration layer, and this volume will probably be of importance when the particle-ion separation is comparable with the ion size. Furthermore, salt ions can affect the surface charge of the particle, which implies that the surface charge is not independent of the salt ion concentration near the surface.

If it is assumed that the electrolyte ions do not have a finite size, that ion-ion correlations are omitted and that the solvent has a uniform dielectric permittivity, the

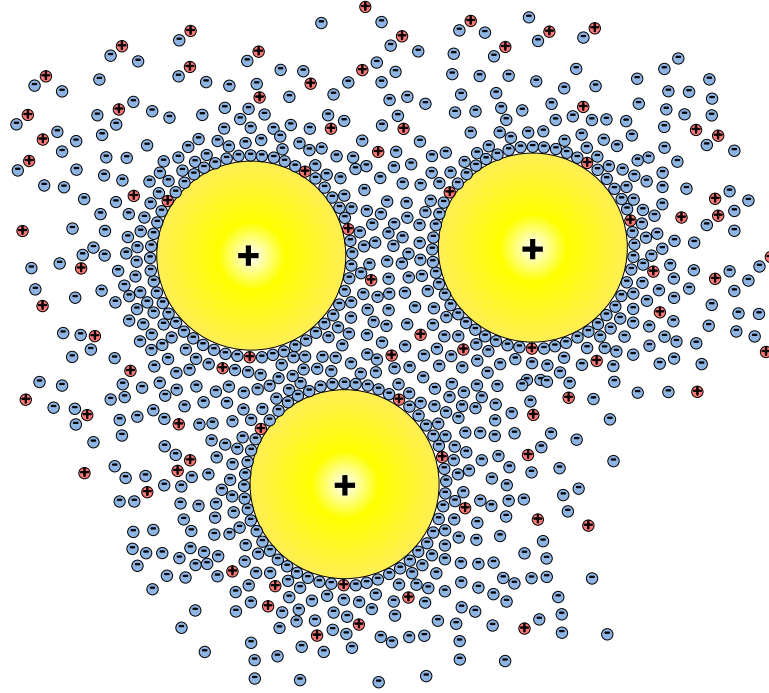


**Figure 2.7:** Schematic representation of an Electrical Double Layer developed around a spherical, positively charged particle. Counter-ions are accumulated around the particle to form what is called a diffuse layer.

Poisson-Boltzmann theory gives quite satisfactory results, mostly in cases of particles that are suspended in a 1 : 1 electrolyte. The Poisson-Boltzmann equation can describe the electrostatic interactions between charged surfaces (Russel et al. (1992); Hunter (2001); Trefalt et al. (2013)). It is a non-linear differential equation for the electric potential field  $\psi$  inside an electrolyte solution. For a solution in equilibrium with a reservoir of ions at density  $n_{ib}$  the full expression writes

$$\nabla^2 \psi(\mathbf{r}) = -\frac{1}{\epsilon_r \epsilon_0} \sum_i z_i e n_{ib} \exp \left[ -\frac{z_i e \psi(\mathbf{r})}{kT} \right]. \quad (2.1)$$

where  $\epsilon_r$  is the relative permittivity of the electrolyte solution,  $\epsilon_0$  is the vacuum permittivity and  $z_i$  is the valence of the ionic species  $i$ . If the potential  $\psi$  is considered low ( $|z_i e \psi / kT| \ll 1$ ), then the Poisson-Boltzmann equation can be rewritten as

$$\nabla^2 \tilde{\psi}(\mathbf{r}) = \kappa^2 \tilde{\psi}(\mathbf{r}) \quad (2.2)$$

where  $\tilde{\psi} = \psi e/kT$  and  $\kappa$

$$\kappa = \left( \frac{1}{\epsilon_r \epsilon_0 kT} \sum_i z_i^2 e^2 n_{ib} \right)^{1/2}. \quad (2.3)$$

This is the linearised form of the Poisson-Boltzmann equation (Debye-Hückel approximation) which holds true for low surface potentials. The inverse of  $\kappa$  is the Debye length ( $\kappa^{-1}$  or  $\lambda_D$ ) which corresponds to the thickness of the double layer. Depending on the boundary conditions used for the solution of the Poisson-Boltzmann equation, one can obtain for example the electrostatic potential at a distance  $r$  from an isolated surface or calculate the electrostatic potential of interaction of two approaching charged surfaces (Ohshima (2006)).

This section will be mainly focused on the electrostatic interactions between particles and ions, as well as between particles. The reason for this study is to further understand the behaviour of boehmite nanoparticles when they come in contact with an electrolyte which in this case is the corrosion inhibitor ( $\text{Ce}(\text{NO}_3)_3$ ). It is known that when a important quantity of an electrolyte is mixed with a suspension containing colloids it can de-stabilize it. Since the nano-containers need to be incorporated in a coating matrix (based on polymers) their properties and behaviour should be first of all predictable and secondly not affect their polymeric matrix. For the above reasons, the stability of the suspension will be evaluated in terms of electrostatic repulsion by measuring the charge on the particles in conditions of relatively low salt concentration. The limits of stability will be evaluated by measuring the hydrodynamic size of particles as a function of added salt. Finally, some theoretical insights will be given about the possible reasons and ways that particles aggregate when  $\text{Ce}(\text{NO}_3)_3$  is used as an added electrolyte by means of the DLVO theory.

## 2.1 Electrokinetic testing of stability

### 2.1.1 Evaluation of interface-solution properties from electrophoretic velocity

Electrophoresis refers to the movement of a charged particle suspended in an electrolyte solution, under the influence of an electric field (Delgado et al. (2007)). The velocity with which the particles move is called *electrophoretic velocity*, and when divided by the magnitude of the electric field applied, gives rise to the *electrophoretic mobility* ( $m^2V^{-1}s^{-1}$ ). During the displacement of particles, the electrical double layer composed by the electrolyte ions can deform. The magnitude of deformation is related to the strength of the attraction of the ions by the particle; for example the

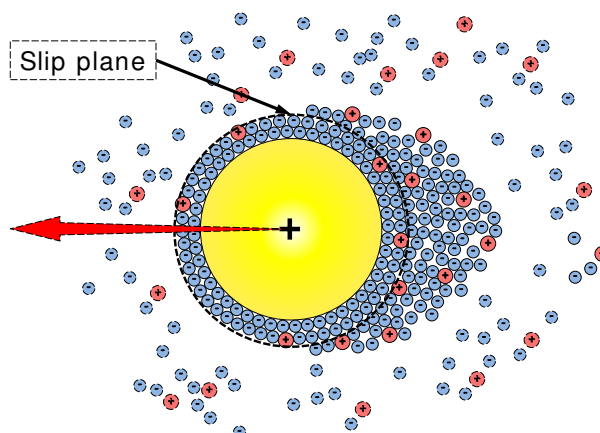


Figure 2.8: The slip plane

ions located very close to the charged surface will be attracted strongly leaving almost no room for displacement, meaning that they are bound to the surface as far as hydrodynamics are concerned. It has been postulated that there exists a plane at a certain distance from the surface, after which, ions are no more hydro-dynamically immobile. This plane is named *slip plane* and the potential in this plane is identified as the *zeta potential* or  $\zeta$ .

The electrophoretic mobility of the particles was measured with an electrophoretic light scattering apparatus<sup>8</sup> based on the Laser Doppler effect. Under the assumption that particles do not interact between them, one can translate this mobility in the  $\zeta$ . As in the case of the samples used to measure the size by dynamic light scattering, the stock suspension is too concentrated ( $38 \text{ gr L}^{-1}$  or in terms of volume fraction  $\phi \sim 1\%$ ) to be used for this kind of measurement. For this reason it was diluted against ultra-pure water, reaching a volume fraction of  $\phi = 0.01\%$  with a  $pH \sim 4.5$ . Then the solution was put in the zeta potential capillary cell<sup>9</sup> with attention not to leave any bubbles inside that could compromise the measurement. The experiment was repeated three times and every time the sample renewed. The measured value of electrophoretic mobility in each experiment was the average of at least 10 measurements. The electrophoretic mobility of the diluted suspension is  $\mu = 4.8 \cdot 10^{-8} \text{ m}^2\text{V}^{-1}\text{s}^{-1}$  with a relative error of  $\sim 1\%$ . This result is in accordance with Buining et al. (1994) who measured the electrophoretic mobility in a similar system of boehmite nano-particles.

In the case of cylindrical particles the electrophoretic mobility depends on the ori-

<sup>8</sup>Malvern Zetasizer ZS90

<sup>9</sup>Malvern DTS1070

entation of the particles with respect to the applied electric field. Hence, for cylinders that are oriented parallel with the electric field the relation between electrophoretic mobility  $\mu$  and  $\zeta$  potential, which is the potential at the slipping plane, is given by the equation of Smoluchowski for dilute suspensions with  $\kappa a \gg 1$

$$\mu_{\parallel} = \frac{\epsilon_0 \epsilon_r \zeta}{\eta_s} \quad (2.4)$$

where  $\epsilon_0$  is the permittivity in vacuum,  $\epsilon_r$  is the relative permittivity of the solvent (mostly water) and  $\eta_s$  is the viscosity of the suspension.  $\kappa$  is the inverse of the Debye length  $\kappa^{-1}$  which was defined in Equation (2.3). For a 1 : 1 electrolyte solution the Debye length

$$\kappa^{-1} = \sqrt{\frac{\epsilon_0 \epsilon_r k_B T}{2e^2 N_A I}} \quad (2.5)$$

where  $e$  is the elementary charge and  $I$  is the ionic strength defined as

$$I = \frac{1}{2} \sum_i z_i^2 c_i \quad (2.6)$$

where  $z_i$  is the charge number and  $c_i$  is the molar concentration of ions in a dilute suspension. On the other hand when the cylinder is oriented perpendicular to the electric field then  $\zeta$  also depends on the value of  $\kappa a$ , where  $a$  is the particle radius (Ohshima (2006)). For particles with a low  $\zeta$  potential, the electrophoretic mobility is given by

$$\mu_{\perp} = \frac{\epsilon_0 \epsilon_r \zeta}{\eta_s} f(\kappa a) \quad (2.7)$$

where  $f(\kappa a)$  is an expression given in Ohshima (2006) that is bound between 1/2 and 1 for cases of  $\kappa a \rightarrow 0$  and  $\kappa a \rightarrow \infty$  correspondingly. Combining Equations (2.4) and (2.7), the average electrophoretic mobility is given by  $\mu_{av} = \mu_{\parallel}/3 + 2\mu_{\perp}/3$ . For the limiting case of  $\kappa a \rightarrow \infty$  the average electrophoretic mobility yields Equation (2.4). On the other hand for  $\kappa a \rightarrow 0$  the  $\zeta$  calculated from the electrophoretic mobility will be higher by a factor of 6/4. At this point a decision was made to use Smoluchowski expression, corresponding to  $\kappa a \gg 1$  (Equation (2.4)) based on the following arguments.

Even if the exact composition of the solution matrix is not accessible, the concentration of  $\text{Al}^{3+}$  was determined in Section 1.1.3 at  $0.02 \text{ mol L}^{-1}$ . Making an approximation that all the anions in the solution are monovalent, the concentration needed to neutralize  $\text{Al}^{3+}$  is three times  $C_{\text{Al}^{3+}}$ , thus  $C_{\text{anions}} \sim 0.06 \text{ mol L}^{-1}$ . Since

Author		$\mu$ ( $10^{-8} m^2V^{-1}s^{-1}$ )	$\zeta$ mV	IEP	PZC
Buining et al. (1994)	AlOOH	4.1	75	9.8	8.6
Wood et al. (1990)	AlOOH	-	60	9.1	8.6
Ramsay et al. (1978)	AlOOH	4	-	8-9	
de Lint et al. (2003)	$\gamma$ -Al <sub>2</sub> O <sub>3</sub>		60	8.3	8.3
Sprycha (1989)	$\gamma$ -Al <sub>2</sub> O <sub>3</sub>		60	8.1	8.1

**Table 2.1:** Electro-kinetic data for boehmite ( $\gamma$ -alumina) found in literature

the sample was diluted 100 times to perform electrophoretic experiments, a hundred-fold decrease of the concentration of ions is expected, thus  $0.0006 \text{ mol L}^{-1}$ . Taking this estimated ion concentration and  $z = 1$  for the valency of counter-ions, yields a Debye length of  $\kappa^{-1} \sim 8 \text{ nm}$ . For the particles that are oriented parallel to the electric field,  $a$  is their length ( $20 \text{ nm}$ ) and the product  $\kappa a$  is equal to 2.5. This value even though it is not much greater than 1, is nevertheless the minimum value that it can take. When the particles are oriented perpendicular to the electric field, then  $a$  is their radius ( $2 \text{ nm}$ ) and the product  $\kappa a$  is equal to 0.2. This value is smaller than 1, and thus the Smoluchowski approximation is not valid. But, as it was shown above for the limit  $\kappa a \rightarrow 0$ ,  $\zeta$  is expected to be 6/4 times of the value of  $\zeta$  calculated for  $\kappa a \rightarrow \infty$ . Consequently, the  $\zeta$  calculated in the approximation  $\kappa a \gg 1$  (Equation (2.4)) here will be at least the minimum value it can have.

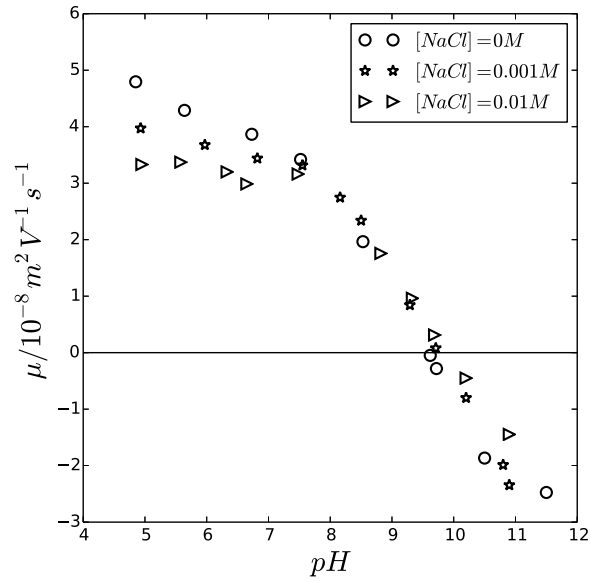
Under the aforementioned assumptions, a value of  $\zeta \simeq 60 \text{ mV}$  is obtained. This value is in accordance with the  $\zeta$  of boehmite particles found in literature and reported in Table 2.1. It is worthwhile emphasizing that suspensions with a  $\zeta$  potential larger than  $30 \text{ mV}$  are considered stable.

The iso-electric point is the value of  $pH$  for which the measured  $\zeta$  equals zero; differently said the value of  $pH$  or  $pH_{IEP}$  for which the potential at the slipping plane is zero. Usually the iso-electric point is a parameter related with the stability of a suspension since it is the  $pH$  value where particles are not electro-statically stabilized any more.

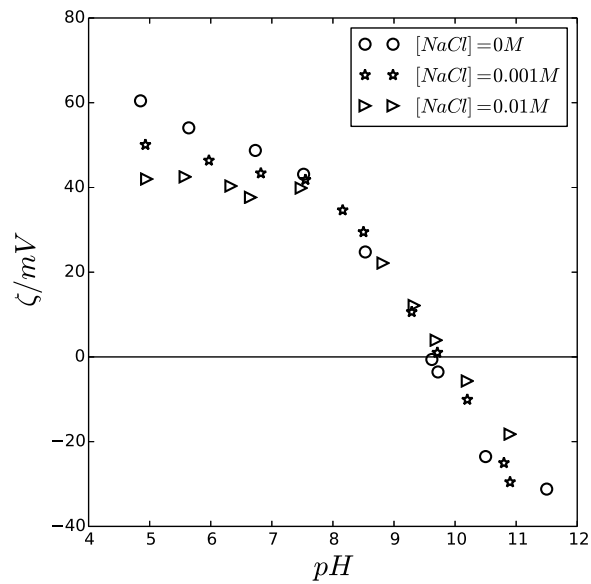
The iso-electric point was determined experimentally by measuring the  $\zeta$  in a range of different  $pH$ s. The experiments were realised in the same capillary cell<sup>10</sup> as previously, by connecting it with an automated titrator<sup>11</sup>. Since the technique used here is the same as in the measurement of  $\zeta$ , the sample preparation is based on the same principle. Three samples were prepared at a given particle concentration, with

<sup>10</sup>Malvern DTS1070

<sup>11</sup>Malvern MPT-2



(a)



(b)

**Figure 2.9:** (a) Electrophoretic mobility and (b)  $\zeta$  of boehmite suspension as a function of  $pH$ , obtained by addition of  $NaOH$  of  $0.5M$ . Added salt concentrations  $\circ = 0 M$ ,  $\star = 0.001 M$ ,  $\triangleright = 0.01 M$

the addition of NaCl in different concentrations (0 M, 0.001 M, 0.01 M). The titrating solution was NaOH at 0.5 M and the final added volume was negligible to keep the same particle concentration until the end of the measurement. After each injection of the titrant, the solution was stirred vigorously for several minutes until  $pH$  stabilization. For each value of  $pH$  three repetitions were executed and before each measurement the sample was changed. The resulting mobility of each repetition is the average of ten measurements with a standard deviation of  $\sim 5\%$ .

The values presented in Figure 2.9a are the electrophoretic mobilities of three different suspensions in a range of  $pH$  between 4.5 – 11. The difference between the suspensions lies in the concentration of the added NaCl. It can be clearly stated that the electrophoretic mobility depends on the added salt concentration for  $pH$  values below 7.5. The suspension containing the higher salt concentration has the lower electrophoretic mobility. After  $pH = 7.5$  the curves superpose and cross the zero mobility axis at a value of 9.5. After  $pH = 9.5$  the electrophoretic mobility takes negative values which is an indication of charge inversion of the particles.

In Figure 2.9b the  $\zeta$  potential is presented based on the values of the electrophoretic mobilities from above. Like before, the Smoluchowski approximation (Equation (2.4)) is used but this time this choice is more justified. The addition of NaOH to change the  $pH$  and the added salt concentration have as an effect to increase the ionic strength in the suspensions and thus further decrease the Debye length. For an added salt concentration of 0.01 M,  $\zeta$  has a value of 40 mV. If the same trend follows, further addition of salt will possibly decrease  $\zeta$  under 30 mV which is often the limit to discriminate a stable from a non stable suspension. It could be noticed that increasing salt concentration does not seem to affect the value of the iso-electric point at least within the experimental accuracy, which occurs at  $\sim pH_{IEP} = 9.5$ . This is an indication that the counterion that screens the electric potential is monovalent.

Both,  $\zeta$ -potential and the IEP, were found to be in accordance with the literature (see Table 2.1). Even though the data presented in the table are not exclusively for  $\gamma$ -AlOOH, but also for  $\gamma$ -Al<sub>2</sub>O<sub>3</sub>, it is considered that their interfacial properties are not very far. Furthermore, in the review of Franks and Gan (2007), it is argued that alumina powders have an IEP between 8 and 10 irrespective of their crystal phase. An important implication of the  $\zeta$  is to model particle-particle interactions which will be the topic of the next section.

### 2.1.2 Repulsive electrical potential between rod-like particles

The motivation to investigate the particle-particle interactions, rise from the fact that the corrosion inhibitor that will be used to charge the nano containers, come in the form of salt, and salt can screen the repulsions between particles. One should note that the salt of interest is *Cerium Nitrate*,  $\text{Ce}(\text{NO}_3)_3$ , which is a multivalent, asymmetric electrolyte  $z : 1$ . However, since the nano-particles are charged positively, it is the monovalent anion that screens the electrical potential around the colloids and affects the stability of the system. So from an anion point of view the results are obtained in conditions of a 1:1 electrolyte. In a very recent paper by Cao et al. (2015), a study of colloidal particles in an electrolyte solution is presented, where the co-ion is multivalent and the counter-ion is monovalent and they reported that Poisson-Boltzmann theory is expected to be valid.

When two or more charged particles approach one another, close enough that ions lying in the electrical double layer of one particle sense the ions lying in the EDL of the other, they tend to oppose further approach. The theory that treats particle-particle interactions and explains at least partially the phenomenon of aggregation of particles, is referred to as *DLVO* (named after Derjaguin, Landau, Verwey and Overbeek). DLVO is based on the assumption that the potential energy of interaction between two charged surfaces can be decomposed in two potential energies of different source. An electrostatic  $V_R$  that has a repulsive character for same-charged surfaces, and an attractive  $V_A$  that arises from the van der Waals force (see Figure 2.11). The total potential energy of interaction  $V_T$  is then

$$V_T = V_R + V_A. \quad (2.8)$$

The electrostatic potential energy per square meter of the repulsive force between two similar flat surfaces can be evaluated from the osmotic pressure difference  $\bar{p}$  between the bulk solution and midway between the surfaces (Russel et al. (1992); Hunter (2001))

$$V_R = - \int_{\infty}^D \bar{p} dD \quad (2.9)$$

where  $D$  is the separation from the surfaces. Using the fact that at the mid-plane between the plates  $(d\psi/dx)_{\psi=\psi_m} = 0$ , then  $\bar{p}$  can be defined as

$$\bar{p} = 2n_b kT \left[ \cosh \left( \frac{ze\psi_m}{kT} \right) - 1 \right] \quad (2.10)$$

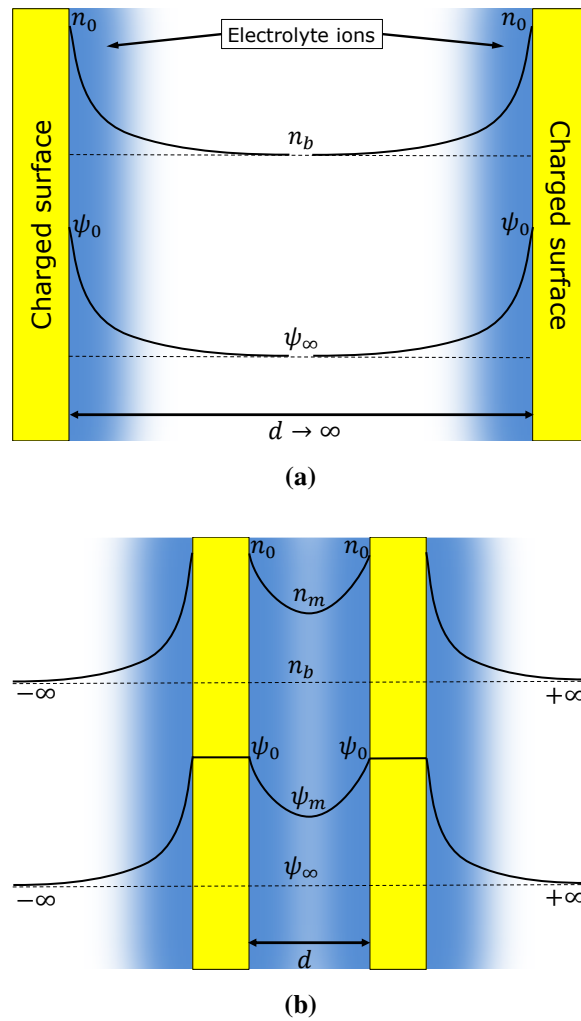


**Figure 2.10:** Electrostatic interaction between two charged flat plates in an electrolyte solution. The counter-ion concentration  $n$  and electrostatic potential  $\psi$  are shown schematically for the case of large (a) and small separation (b) separation between the plates.

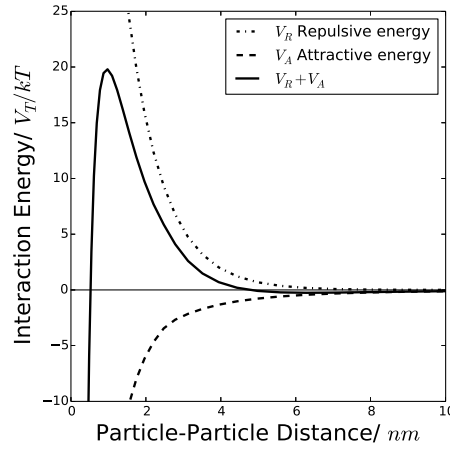


**Figure 2.11:** Schematic representation of the interaction potential  $V_T$  between two surfaces as a function of the separation distance between them. In DLVO theory,  $V_T$  is considered the sum of a repulsive electrostatic potential  $V_R$  and a potential arising from the van der Waals interaction  $V_A$

where  $\psi_m$  is the potential in the mid-plane (see Figure 2.10b). The last expression is derived by integrating once the Poisson-Boltzmann equation (Equation (2.1)) written for the case of a symmetrical  $z : z$  electrolyte

$$\epsilon_r \epsilon_0 \nabla^2 \psi = 2ezn_b \sinh\left(\frac{ez\psi}{kT}\right). \quad (2.11)$$

To calculate the potential  $V_R$  as a function of the separation  $D$ , Equations (2.9) and (2.10) need to be solved. Unfortunately,  $\psi_m$  is needed as a function of the separation distance but this is only possible for some limiting cases even for this simple case of flat surfaces.

The Poisson-Boltzmann equation can be solved either analytically or numerically; the analytical solutions are usually restricted to plate-like surfaces for arbitrary potential, or in the case of low surface potential for spherical and cylindrical particles. In the case of approaching particles that have curved boundaries, the repulsive force occurs not only from the osmotic pressure but also from electric stresses. A variety of approximations exist, that provide ways to calculate the interaction between curved surfaces. In the work of Sparnaay (1959), the Derjaguin approximation was used to calculate the repulsive potential energy of cylindrical particles using the linearised form (Debye-Hückel approximation) of the Poisson-Boltzmann equation (Equation (2.2)). The use of these two approximations impose some limitations.

The Derjaguin approximation can be used in cases where  $\kappa a > 1$  (Russel et al. (1992); Verwey et al. (1999)); this is most probably the case for the suspension of this study. It was shown (Section 2.1.1) that the minimum values of  $\kappa a$  would be  $\kappa a \sim 0.2$ , when  $a = 2 \text{ nm}$  (particle radius), and  $\kappa a \sim 2.5$ , when  $a = 20 \text{ nm}$  (particle length). However for salt concentrations above  $0.01 \text{ M}$  then the minimum value of  $\kappa a$  will be for both cases above 1.

The next approximation lies in the use of the linearised form of the Poisson-Boltzmann equation, which is true for cases of low surface potential ( $|z_i e \psi / kT| \ll 1$  or  $\psi \sim 26 \text{ mV}$  for  $25^\circ \text{ C}$ ). Here the surface potential is unknown; what is known is the  $\zeta$  as estimated previously. It is expected that since  $\zeta$  is measured on a plane at a certain distance from the particle surface, the actual surface will have a higher value of potential. Nonetheless, if it is assumed that the ions that lie between the particle surface and the slip plane are strongly bound and they stay attached even when other particles approach very close, then one can say that these ions are part of the particle and the potential on this “new surface” is  $\zeta$ . This is a very strong assumption, but the only other alternative would be to solve numerically the non-linear Poisson-Boltzmann equation for cylinders using the true surface potential which is also unknown. In Figure 2.9b the value of  $\zeta$  is ranging between  $60 \text{ mV}$ , for dilute suspensions with no salt added, down to  $40 \text{ mV}$  for a dilute suspension with  $0.01 \text{ mol L}^{-1}$  of NaCl. Since it was observed that particles do not aggregate for salt concentration up to  $0.01 \text{ mol L}^{-1}$ , the domain of interest for aggregation would be for salt concentrations over  $0.01 \text{ mol L}^{-1}$ ; hence the value of  $\zeta \sim 40 \text{ mV}$  can be used.

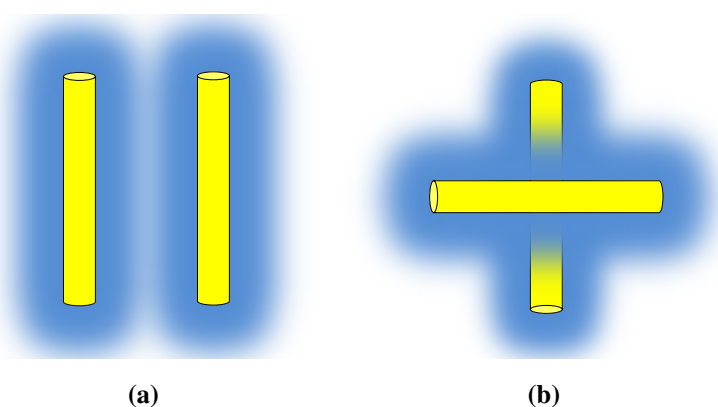


**Figure 2.12:** Two interacting cylinders in parallel orientation (a) and in crossed orientation (b).

Since the discussion in this subsection does not have as a purpose a quantitative

comparison between theory and experiment the above approximations and considerations are acceptable. Qualitatively the behaviour will remain the same and only the absolute values will change.

Equations (2.12) and (2.13) give the repulsive potential for cylinders that interact in the first case when they have parallel orientation (Figure 2.12a) and in the other case when they are crossed (Figure 2.12b):

$$V_R^p = 64\pi^{\frac{1}{2}}n_b kT \gamma^2 L \frac{(\kappa a)^{\frac{1}{2}}}{\kappa^2} \exp(-\kappa D) \quad (2.12)$$

$$V_R^c = 128\pi n_b kT \gamma^2 L \frac{a}{\kappa^2} \exp(-\kappa D) \quad (2.13)$$

where  $\gamma = \tanh(e\zeta/4kT)$ ,  $L$  and  $a$  is the length and radius of the cylinder, and  $D$  the surface-surface distance.

The expressions for the attractive potential obtained by Sparnaay (1959); Buining et al. (1994) will be used, again for the case of parallel  $V_A^p$  and crossed cylinders  $V_A^c$

$$V_A^p = -\frac{3\pi}{8} A \frac{L}{a} a^5 U_5 \quad (2.14)$$

where  $A$  is the Hamaker constant and  $U_5$  is a complex function of the radius  $a$  and the distance between the cylinder axes  $R$  and can be expressed in terms of *Appell's* hypergeometric function  $F_4\left(\frac{5}{2}; \frac{5}{2}; 2, 2; \frac{a^2}{R^2}, \frac{a^2}{R^2}\right)$  (Sparnaay (1959); Bouwkamp (1947)). For the case of crossed cylinders  $V_A^c$  is given by

$$V_A^c = -\frac{A}{3} \left[ \frac{1 - \frac{1}{2}k^2}{1 - k^2} \mathbf{E}(k) - \mathbf{K}(k) \right] \quad (2.15)$$

where  $k = 2a/R$  and  $\mathbf{E}$  and  $\mathbf{K}$  are the complete elliptic integrals of the first and second order respectively.

In Figure 2.13 the interaction potential is plotted against the separation distance between cylinders since the form of the nano-particles have a similar shape. The cylinders can be oriented in two different ways; one way is to interact being parallel to each other and the other way in a crossed configuration as discussed by Sparnaay (1959). Using Equations (2.12) and (2.14) for the parallel configuration and Equations (2.13) and (2.15) for the crossed configuration, two different interaction potential are derived. The parameters used, were either measured previously or were given in Buining et al. (1994) and are presented in Table 2.2. Before commenting on the figure, it should be underlined that even though the model equations are valid for large  $\kappa a$ , Sparnaay argues that they are expected to be somewhat valid for  $\kappa a > 1/2$ .

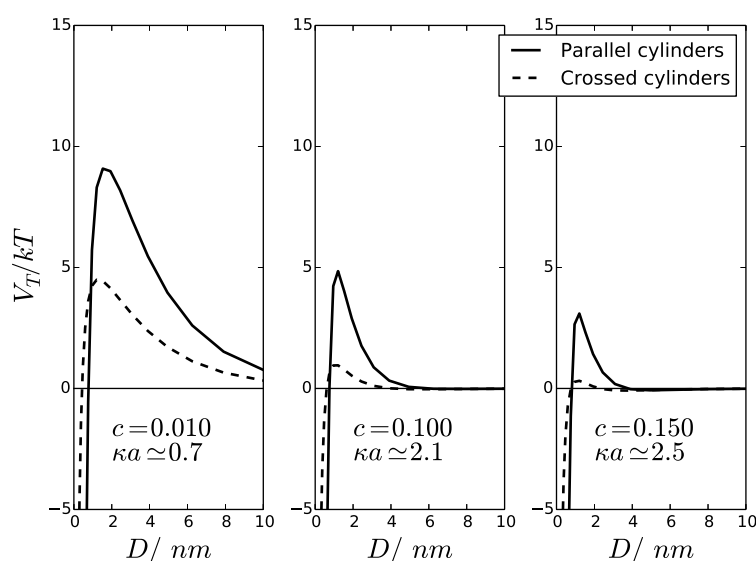


**Figure 2.13:** Calculation of the DLVO interaction potential  $V_T$  for a pair of cylinders that have a parallel or crossed configuration in three different electrolyte concentrations  $c$ . (Left)  $c = 0.01$ , (Middle)  $c = 0.1$ , (Right)  $c = 0.15$ . The electrostatic potential of the surface  $\psi$  is considered to be equal to  $\zeta = 40$  mV, as measured by electrophoresis. Hamaker constant  $A = 6.7 \cdot 10^{-20}$  from Buining et al. (1994), Length and radius as measured from cryo-TEM  $L_{av} = 20$  nm and  $a_{av}$  respectively

Furthermore, the value of potential  $\psi$  used for the calculation, is the  $\zeta$  which seems to be relevant for the separation distance between the particles.

In the left part of Figure 2.13, the interaction potential for an electrolyte concentration ( $c$ ) of 0.01 M shows a potential barrier at 9 kT for the parallel cylinders and a maximum of 4.4 kT for the crossed particles. In the middle snapshot of Figure 2.13 the increase of the electrolyte concentration has an immediate effect on the barrier, decreasing for both configuration. This is an indication that aggregation in suspension of colloidal cylinders will probably initiate from the particles that are not parallel

	$\gamma$ -AlOOH
$L_{av}/nm$	20
$a_{av}/nm$	2
$A/m^2kg s^{-2}$	$6.7 \cdot 10^{-20}$
$\zeta/mV$	40

**Table 2.2:** Parameters used for the calculation of the potential of interaction

since they present a low repulsive barrier. For the last case the electrolyte concentration is further increased to  $c = 0.15$ , and it can be noticed that the barrier for the crossed particles has almost completely vanished, as for the parallel configuration it still has a repulsive barrier that is probably not enough for the particles to repel each other.

## 2.2 Experimental investigation of destabilizing conditions

A common technique to study aggregation, from an experimental point of view, is by means of dynamic light scattering (Holthoff et al. (1996); Elimelech et al. (2013); Cao et al. (2015)). The essence of this technique lies on the measurement of the average particle size (or aggregate size in case of aggregation) as a function of time for different electrolyte concentrations. What is expected is that for very low salt concentration the size remains the same, but with further increase a noticeable size increase is observed. Since salt counter-ions accumulate around the charged particle, they screen the electrostatic potential and consequently the repulsive barrier between particles. For low salt concentration the rate of size increase depends on the screening of the potential barrier and thus on salt concentration. When a rapid increase of the average size is noticed and further increase of added salt concentration does not change the rate of size increase, aggregation has changed regime from slow coagulation to rapid (Holthoff et al. (1996)). The concentration of salt for which slow coagulation gives way to fast coagulation is defined as the critical coagulation concentration (*CCC*).

As already mentioned, the salt of interest ( $Ce(NO_3)_3$ ) is multivalent and asymmetric, at least in terms of its chemical formula. Instead of directly testing a complicated electrolyte, it would be of interest to test a monovalent, symmetrical one for which the behaviour is more or less expected. In this study it was decided to keep the same cation and change the anion to a monovalent, leading to the choice of  $NaNO_3$ .

Particles were put in contact with the electrolyte by mixing equal volumes of the suspension and the salt solutions in different concentrations. The particle concentrations tested was ranging between  $C_{NP} = 1.9 - 38 \text{ gr } L^{-1}$  or in terms of volume fraction  $\phi = 0.04\% - 1\%$ ; the salt concentration was ranging from  $C_{salt} = 0.001$  to  $0.1 \text{ mol } L^{-1}$ . The reason for following a 1-1 volume mixing is to avoid the use of electrolyte solutions with high concentration, since when added in the suspension, they can locally create small aggregate or crystals. After mixing for some seconds with a magnetic stirrer, a sample was removed with a micro-pipette and inserted in the measurement cell<sup>12</sup>. After each measurement a new cell was used.

<sup>12</sup>Malvern 12mm Square Polystyrene Cuvettes (DTS0012)

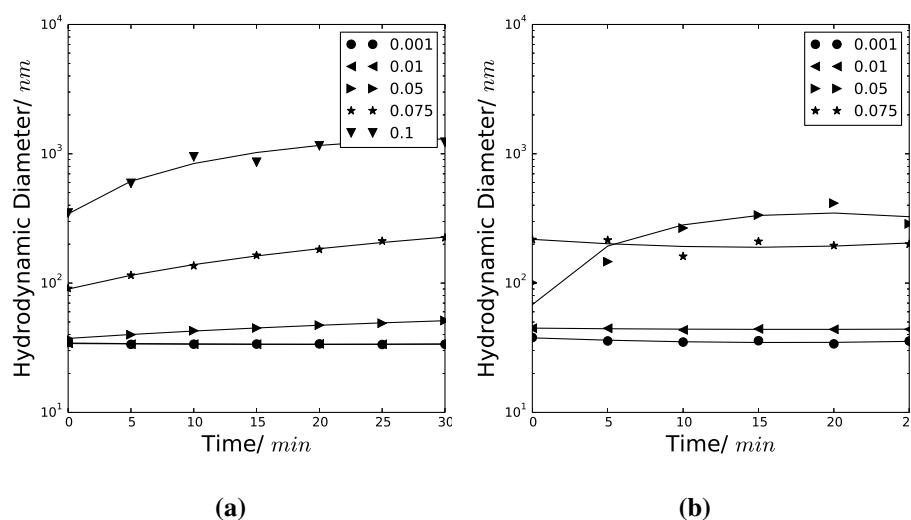


**Figure 2.14:** DLS measurement of hydrodynamic radius of aggregates as a function of time with increasing  $\text{NaNO}_3$  concentration ( $\text{mol L}^{-1}$ ). (a) particle concentration  $1.9 \text{ gr L}^{-1}$ , (b) particle concentration  $19 \text{ gr L}^{-1}$

In Figure 2.14, the hydrodynamic diameter of the aggregates is presented as a function of time, for two different particle concentrations when put in contact with salt solutions of  $\text{NaNO}_3$  in different concentrations (0.001, 0.01, 0.05, 0.075, 0.1). The salt concentration corresponds to the added salt in the solution and not the total concentration. In Figure 2.14a the particle concentration is  $1.9 \text{ gr L}^{-1}$  ( $\phi = 0.04\%$ ) and it is clear that aggregation initiates for a salt concentration of  $0.05 \text{ mol L}^{-1}$ . Increasing salt concentration to  $0.075 \text{ mol L}^{-1}$  the suspension has already formed aggregates before starting the measurement. This is the indication of very fast aggregation. In Figure 2.14b, the hydrodynamic diameter of the aggregates are presented as a function of time, for a suspension with particle concentration  $38 \text{ gr L}^{-1}$  ( $\phi = 0.1\%$ ). In this case, for an added salt concentration of  $0.05 \text{ mol L}^{-1}$  the aggregates increase their average hydrodynamic size much faster than in the dilute suspension case. Furthermore, for an added salt concentration of  $0.075 \text{ mol L}^{-1}$  the hydrodynamic diameter seems to stay stable, because the test sample was gelified. It can thus be considered that  $CCC$  lies below  $0.075 \text{ mol L}^{-1}$  of added  $\text{NaNO}_3$  and more close to  $0.04 \text{ mol L}^{-1}$ . This result is in agreement with other publications; Gieselmann and Anderson (1989) reports a value of 0.06 for the same boehmite nano-particles and  $\text{KNO}_3$  and Buining et al. (1994) a value above 0.05 for rod-shaped, boehmite nano-particles made with a different protocol.

Even though the  $CCC$  is not expected to depend on the particle concentration for

dilute suspensions, in this case the matrix of the suspension already contains an important concentration of ions, as seen in Section 1.1.3. This means that for every dilution of the particles, the ion concentration of the matrix is also diluted. It is expected that for higher dilutions, the  $CCC$  measured will be higher since the salt concentration noted on the figures is the added salt concentration. Another issue of working in high salt concentrations with concentrated suspensions, is the almost instant gelification of the suspension at higher particle concentration which incapacitates the measurement by DLS. This kind of behaviour can be seen in Figure 2.14b where for an added salt concentration of  $0.075 \text{ mol L}^{-1}$  the suspension is already gelified. Following the same experimental procedure for  $\text{Ce}(\text{NO}_3)_3$ , similar results were obtained.

Combining the results for the entire range of particle and salt concentrations, a working phase diagram for  $\text{Ce}(\text{NO}_3)_3$  can be created. Since the exact composition of the matrix in terms of salt concentration is not known, in Figure 2.15a the different phases obtained are presented as a function of the added  $\text{Ce}(\text{NO}_3)_3$ . The first information from this diagram is that three different zones can be noted. The green circles corresponds to low salt concentration (bottom of the graph) and represent suspensions that are stable for a period of at least one day. Above the green circles, lay the blue circles where unstable suspensions were produced. The instabilities were manifested differently depending on the particle concentration. For low particle concentrations ( $C_{NP} < 18 \text{ gr L}^{-1}$ ) the solutions became translucent because of aggregation and in the course of one day the particulate phase was completely sedimented. For high particle concentrations ( $C_{NP} > 18 \text{ gr L}^{-1}$ ) the suspensions became translucent again but instead of sedimenting, it was slowly gelified in the course of one day. Finally the red circles corresponds to cases where instant gellification was observed. Between the different zones, the orange stripes signify the phase transition from one phase to the other. The lower orange stripe, between the green and blue circles, corresponds to a zone where the  $CCC$  should lay. Even though more precise measurements were not possible to determine the exact critical concentration of coagulation, from the plot it is suggested that it should be between  $0.02$  and  $0.04 \text{ mol L}^{-1}$  of added salt.

Normally, the phase diagrams should be designed with the total salt concentration in solution and not only the added salt concentration. In the present system, only a part of the constituents are known. Nevertheless, progress can be made by considering that the quantity of  $\text{NO}_3^-$  is known (added  $\text{HNO}_3$  during synthesis) and that the density of charged sites of boehmite is  $0.7 \text{ e nm}^{-2}$  as measured by Buining et al. (1994) for boehmite particles using a similar synthesis. Multiplying the den-

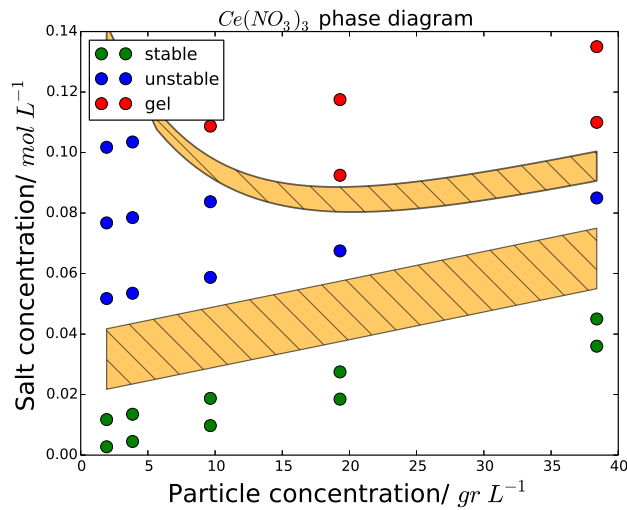
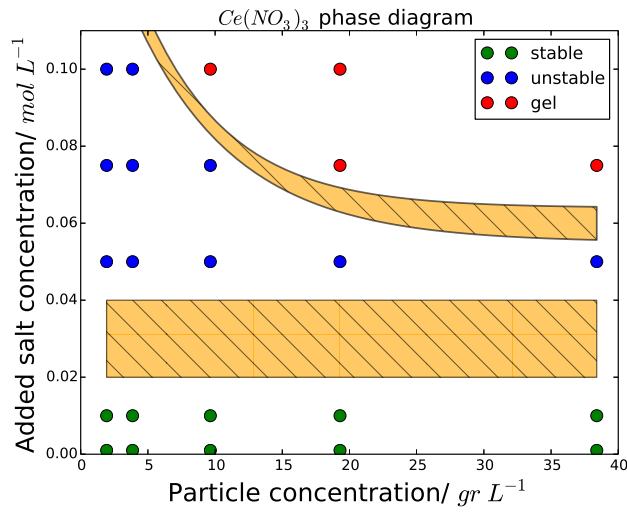


**Figure 2.15:** Phase diagram of boehmite nano-particles and  $Ce(NO_3)_3$  where the orange stripes signify transition between the phases. (a) Different phases as a function of added  $Ce(NO_3)_3$  and particle concentration, and (b) Different phases as a function of total salt in solution and particle concentration

sity of charged sites with the specific surface measured previously  $S_{BET}$ , with the concentration of particles, and dividing by the Avogadro number, yields

$$0.7 \cdot 10^{18} \frac{e}{m^2} \cdot 283 \frac{m^2}{gr} \cdot 38 \frac{gr}{L} \cdot \frac{1}{N_A} = 1.25 \cdot 10^{-2} \frac{mol}{L} \text{ of } e \quad (2.16)$$

which is the amount of positive sites in one liter of nano-particles. In order for the suspension to be electro-neutral, mobilizing an equal quantity of anions is required, thus  $1.25 \cdot 10^{-2} \text{ mol L}^{-1}$  of  $\text{NO}_3^-$ . Up to here the calculation does not contain any approximation. However, for the  $\text{NO}_3^-$  left from this calculation, two extreme cases can be assumed to achieve the solution electroneutrality. In the first case it can be assumed that the free Aluminum ions in the solution have formed complexes of the type  $\text{Al}(\text{XXX})^+$  with other constituents of the solution, thus acting as monovalent ions and needing only one anion to be electroneutral. Subtracting  $1.25 \cdot 10^{-2} \text{ mol L}^{-1}$  from the initial concentration of nitrates in the stock solution,  $0.035 \text{ mol L}^{-1}$  returns  $0.0225 \text{ mol L}^{-1}$ . This means that  $0.0225 \text{ mol L}^{-1}$  of this complex is needed, a value close to the concentration of the Aluminum free in the solution measured experimentally ( $0.02 \text{ mol L}^{-1}$ ) in Section 1. In the second case it can be assumed that the aluminum in the solution has its ionic form  $\text{Al}^{3+}$  and thus it needs three  $\text{NO}_3^-$  to be electroneutral. Based on that,  $0.0075 \text{ mol L}^{-1}$  of  $\text{Al}^{3+}$  can be related with the  $0.0225 \text{ mol L}^{-1}$  of  $\text{NO}_3^-$ . Aluminum ions that are not related with the nitrates may be related with other ions existing in the suspension.

Following the first hypothesis, the phase diagram is re-drawn in Figure 2.15b but this time taking into account the total salt concentration of the solution. For a particle concentration equal to the one of the synthesis,  $38 \text{ gr L}^{-1}$ , the initial salt concentration is  $0.035 \text{ mol L}^{-1}$ . On the other hand, for the lowest particle concentration the initial salt concentration is  $0.00175 \text{ mol L}^{-1}$ , since it is diluted 20 times. This difference of the initial concentrations skews the phase diagram, and the *CCC* seems to depend on the particle concentration. For low particle concentrations the *CCC* is between  $0.02$  and  $0.04 \text{ mol L}^{-1}$ , while for high particle concentrations lies between  $0.04$  and  $0.06 \text{ mol L}^{-1}$ .

The fact that the measured *CCC* between two salts ( $\text{NaNO}_3$  and  $\text{Ce}(\text{NO}_3)_3$ ) is the same is very interesting. Assuming that salts decompose completely when dispersed and that the salt co-ions do not interact with the particles, one should expect the destabilization to occur for the same concentration of counter-ions of the two salts. In this case, for the same concentration  $c$  of added salt,  $\text{NaNO}_3$  would give  $c \text{ mol L}^{-1}$  of  $\text{NO}_3^-$  while  $\text{Ce}(\text{NO}_3)_3$  would give  $3c \text{ mol L}^{-1}$  of  $\text{NO}_3^-$ . This is somewhat contradicting with what was measured experimentally above, since it was found that the *CCC* occurs at the same concentration of added salt for both salts.

To my knowledge there are not many studies concerned with the aggregation of particles caused by asymmetrical electrolytes with multivalent co-ions. Cao et al. (2015) argue in their publication that the aggregation of colloidal particles in the

presence of multivalent co-ions, follows the *inverse Schulze-Hardy* rule

$$CCC \propto \frac{1}{z} \quad (2.17)$$

where  $z$  is the valence of the co-ion. It means that the  $CCC$  of our system in the presence of  $\text{Ce}(\text{NO}_3)_3$  should be  $\simeq 3$  times lower than when  $\text{NaNO}_3$  was used. Considering that the  $CCC$  for  $\text{NaNO}_3$  occurs between  $0.02$  and  $0.04 \text{ mol L}^{-1}$ , then the  $CCC$  for  $\text{Ce}(\text{NO}_3)_3$  should occur between  $0.0067$  and  $0.013 \text{ mol L}^{-1}$ . On the contrary, results show that for this concentration there is no change in the aggregates size.

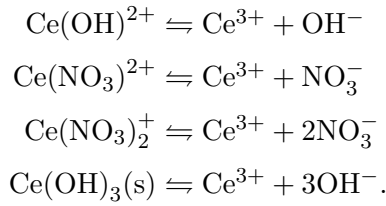
This is an unexpected outcome. One possible explanation could be that  $\text{Ce}(\text{NO}_3)_3$  does not completely dissociates when dispersed in water, thus releasing less nitrate ions in the suspension. Differently put, when  $\text{Ce}(\text{NO}_3)_3$  is dispersed in water it will not only be split in  $\text{Ce}^{3+}$  and  $\text{NO}_3^-$ ; it will give way to a number of complexes for example  $\text{Ce}(\text{NO}_3)_2^+$ ,  $\text{Ce}(\text{NO}_3)_2^{2+}$ . The number and the composition of complexes will depend on many factors, one of them being the salt concentration. Nelson and Irish (1973) and Fratiello et al. (1992) studied the complexation of Cerium nitrate in aqueous solvent mixtures. Both argue that Cerium-nitrato complexes are mostly found in the form of  $\text{Ce}(\text{NO}_3)_2^+$  and  $\text{Ce}(\text{NO}_3)_2^{2+}$  with less chances to create higher order complexes. If this holds true for the solutions considered here, it means that there are less  $\text{NO}_3^-$  available free in solution and for this reason the inverse Schulze-Hardy rule can not work. This result led us to perform a speciation analysis for Cerium Nitrate in different concentrations and  $pH$  values.

### 2.2.1 Speciation analysis

Speciation of an element refers to the distribution of this element between defined chemical species in a system (Templeton et al. (2000)). There are several publications working on the speciation of Cerium nitrate or generally in nitrates of lanthanides, and a number of different species in aqueous solutions are reported. Nelson and Irish (1973) and Fratiello et al. (1992) studied the complexation of Cerium nitrate in aqueous solvent mixtures and both argue that Cerium-nitrato complexes are mostly found in the form of  $\text{Ce}(\text{NO}_3)_2^+$  and  $\text{Ce}(\text{NO}_3)_2^{2+}$  with less chances to create higher order complexes. Oikawa et al. (2011) studied the lanthanide nitrate species in solution and reported that the following species were observed  $(\text{Ln}(\text{OH})(\text{H}_2\text{O})_j)^{2+}$ ,  $(\text{Ln}(\text{OH})_2(\text{H}_2\text{O})_k)^+$ ,  $(\text{Ln}(\text{NO}_3)(\text{OH})(\text{H}_2\text{O})_l)^+$  and  $(\text{Ln}(\text{NO}_3)_2(\text{H}_2\text{O})_m)^+$  (where  $j, k, l, m$  is the number of bound  $\text{H}_2\text{O}$ ). Consequently, there seems to be an agreement that Cerium Nitrate when dispersed in water does not only decompose in  $\text{Ce}^{3+}$  and

$\text{NO}_3^-$ , but a number of chemical species. Therefore if nitrate ions are complexed with Cerium ions, it means that there are less nitrates free to adsorb on the surface. This is in accordance with what was discussed for the stability of the suspension.

Assuming that Cerium can form a complex with  $\text{OH}^-$ , two complexes with  $\text{NO}_3^-$  and a precipitate phase with  $\text{OH}^-$ , the complexation can be written in a reaction form as



The reaction constants that correspond to the above reaction are

$$\begin{aligned}\text{with } pK_1 = 4.6, \text{ i.e. } K_1 &= \frac{[\text{Ce}^{3+}][\text{OH}^-]}{[\text{Ce}(\text{OH})^{2+}]} = 10^{-4.6} \simeq 2.5 \cdot 10^{-5} \\ \text{with } pK_2 = 1.04, \text{ i.e. } K_2 &= \frac{[\text{Ce}^{3+}][\text{NO}_3^-]}{[\text{Ce}(\text{NO}_3)^{2+}]} = 10^{-1.04} \simeq 0.0912 \\ \text{with } pK_3 = 1.51, \text{ i.e. } K_3 &= \frac{[\text{Ce}^{3+}][\text{NO}_3^-]^2}{[\text{Ce}(\text{NO}_3)_2^+]} = 10^{-1.51} \simeq 0.0309 \\ \text{with } pK_4 = 19.82, \text{ i.e. } K_4 &= \frac{[\text{Ce}^{3+}][\text{OH}^-]^3}{[\text{Ce}(\text{OH})_3]} = 10^{-19.82} \simeq 1.5 \cdot 10^{-20}.\end{aligned}$$

Initially the simplest hypothesis is used, that the activity is constant. Solving the system of equations returned the fraction of each species concentration as a function of the  $pH$  as presented in Figure 2.16 for four different concentrations of  $\text{Ce}(\text{NO}_3)^{2+}$  in solution,  $C_{\text{Ce}} = 0.001, 0.01, 0.1, 0.3 \text{ mol L}^{-1}$ . For low salt concentration (Figures 2.16a and 2.16b) it is predicted that Cerium is mainly in its ionic form of  $\text{Ce}^{3+}$  and the other species take a very small fraction of the overall concentration. However, as the salt concentration increases it is clear that  $\text{Ce}^{3+}$  is not any more the prevailing species. For  $C_{\text{Ce}} = 0.1 \text{ mol L}^{-1}$  it is predicted that the species with the highest concentration is  $\text{Ce}(\text{NO}_3)^{2+}$ . Further increase of the salt concentration decreases even more the concentration of  $\text{Ce}^{3+}$  and now the prevailing species is  $\text{Ce}(\text{NO}_3)_2^+$ . These results suggest that for salt concentrations that are relevant to this work, the principal cation free in solution might not be  $\text{Ce}^{3+}$  and even if it is, its concentration is much lower than the stoichiometric one. Consequently, in terms of anions in the solution, a much lower concentration of  $\text{NO}_3^-$  are expected to be free in solution.

To verify that this result is not the outcome of a false implementation of the equations, or of the assumption of the activity coefficient to equal the concentration, a

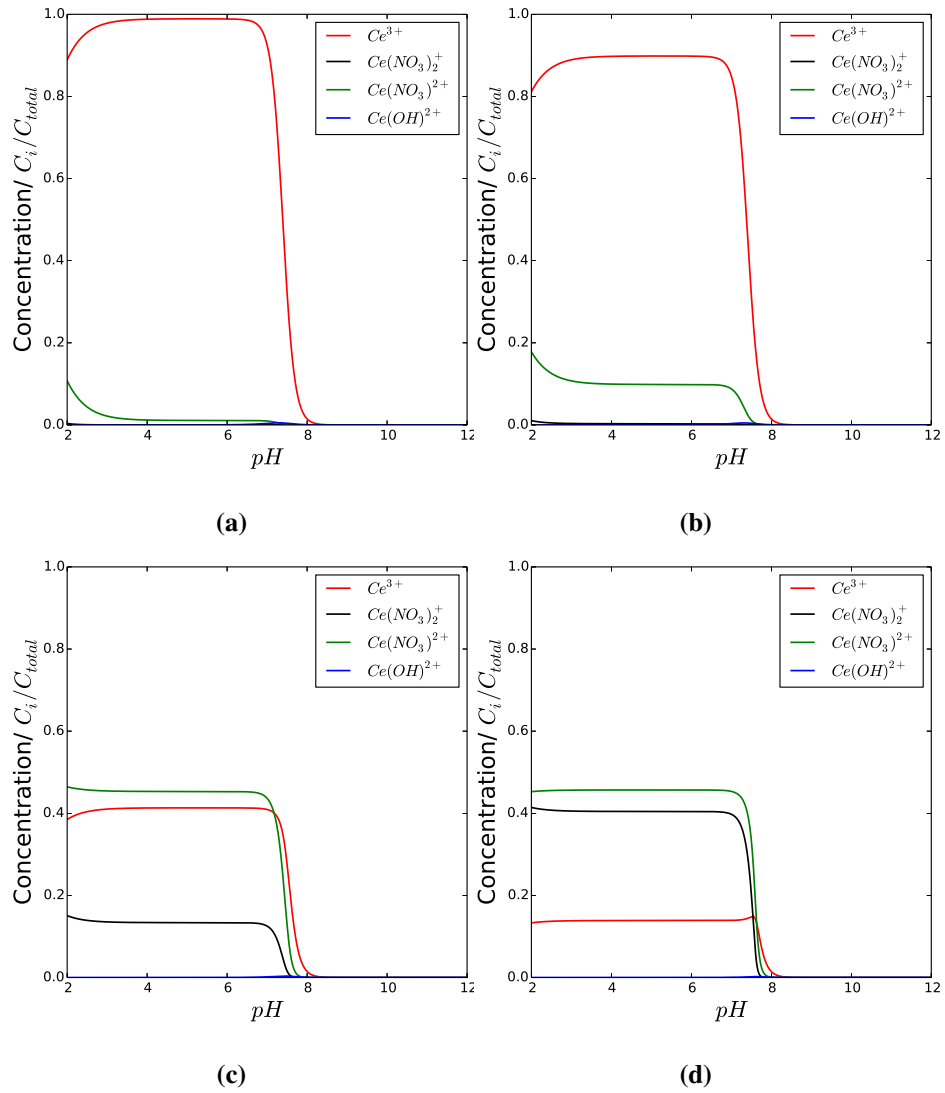


**Figure 2.16:** Partial concentration of species in solution as a function of the solution pH for different concentrations of  $Ce(NO_3)_3$  assuming that the activity coefficient equals the concentration. (a)  $C_{Ce} = 0.001 \text{ mol L}^{-1}$ , (b)  $C_{Ce} = 0.01 \text{ mol L}^{-1}$ , (c)  $C_{Ce} = 0.1 \text{ mol L}^{-1}$  and (d)  $C_{Ce} = 0.3 \text{ mol L}^{-1}$

chemical equilibrium software was used (MINTEQ). The important difference using this software instead of the one above, is the inclusion of an activity coefficient correction given by the equation of Davies

$$-\log\gamma = 0.5z_1z_2 \left( \frac{\sqrt{I}}{1 + \sqrt{I}} - 0.3I \right) \quad (2.18)$$

where  $\gamma$  is the activity coefficient,  $z_1$  and  $z_2$  are the charges of the dissociated electrolyte ions and  $I$  is the ionic strength. Eventhough, Davies formula might not be applicable for Cerium Nitrate and other models might offer higher precision, for the purpose of this qualitative discussion is sufficient and a much better approximation than to consider  $\gamma$  as constant.

The results of speciation using MINTEQ are presented in Figure 2.17. For low salt concentration (Figures 2.17a and 2.17b) the results are almost identical with the previous ones. For salt concentration  $C_{Ce} = 0.1 \text{ mol L}^{-1}$  (Figure 2.17a) it is predicted that  $\text{Ce}^{3+}$  is still the prevailing species in the solution, but a significant contribution is given by  $\text{Ce}(\text{NO}_3)^{2+}$  and  $\text{Ce}(\text{NO}_3)_2^+$ . Further increase of salt concentration (Figure 2.17d) decreases significantly the concentration of free  $\text{Ce}^{3+}$ , and the species with the highest concentration is  $\text{Ce}(\text{NO}_3)_2^+$ . These results eventhough significantly different for what was shown previously for high salt concentrations, they equally suggest that in high salt concentration the nitrates free in solution are less than the ones expected in a completely disassociated salt.

Relating these results with the observations from aggregation, then the fact that the inverse Schulze-Hardy rule is not strictly followed for the case of Cerium Nitrate is very possible as it is shown qualitatively that the nitrate ions, which are responsible for aggregating the suspension, for high salt concentrations are not completely dissociated from the Cerium and thus their bulk concentration is less than the expected one.

## 2.2.2 Aggregation of cylinders and CCC

The potential of interaction between particles calculated in Section 2.1.2, can be used to explain and predict the stability behaviour of suspensions. The potential barrier, discussed previously, depends not only on the charge of the particles but also on the counter-ion concentration. Thus it is possible to modify the magnitude of this barrier (particle-particle repulsions) as well as the extent of the double layer, by changing the electrolyte concentration of the suspension. In the case where the repulsions are not sufficient enough to repel the particles, particles will approach each other by the

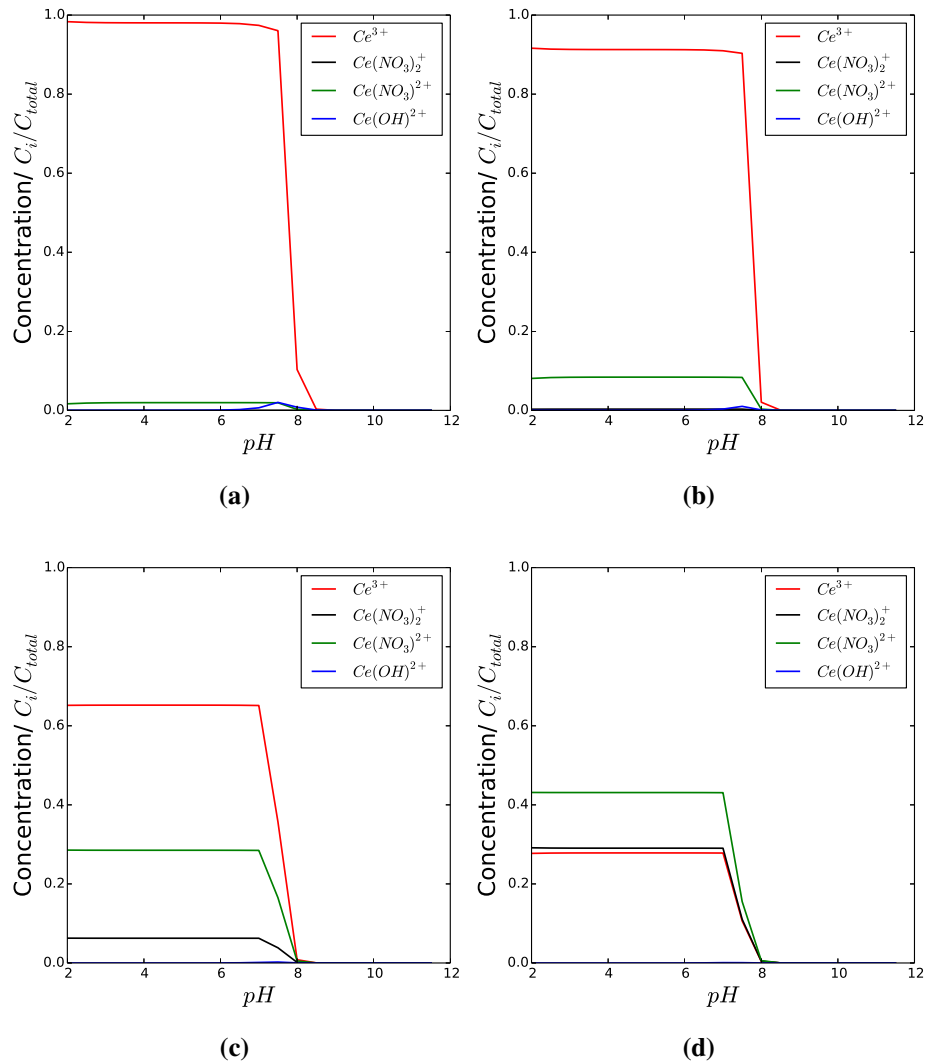


**Figure 2.17:** Partial concentration of species in solution as a function of the solution  $pH$  for different concentrations of  $Ce(NO_3)_3$  using MINTEQ. (a)  $C_{Ce} = 0.001 \text{ mol L}^{-1}$ , (b)  $C_{Ce} = 0.01 \text{ mol L}^{-1}$ , (c)  $C_{Ce} = 0.1 \text{ mol L}^{-1}$  and (d)  $C_{Ce} = 0.3 \text{ mol L}^{-1}$

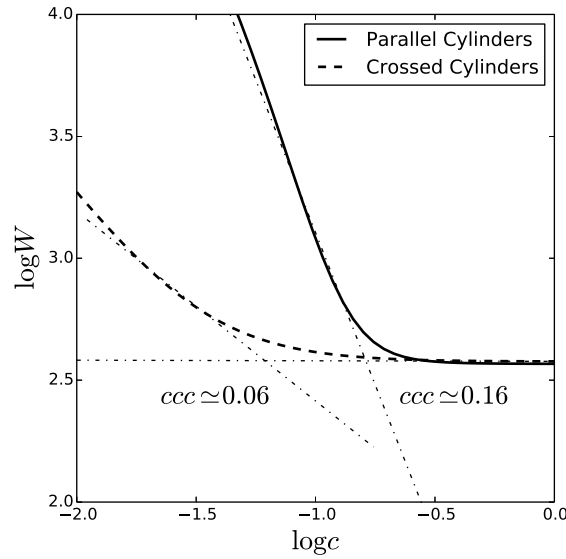


**Figure 2.18:** Calculated stability ratio  $W$  as a function of electrolyte concentration  $c$  for the two different configurations (parallel and crossed). The constants used are the same as in Figure 2.13.

attractive van der Waals potential and create aggregates. In terms of potential energy, a suspension is considered stable when the barrier height is at the order of  $20kT$ . The higher the energy potential, the less chance have the particles to surmount the barrier. Since only a fraction of collisions are effective, one can define the *collision efficiency*,  $\alpha$ , the reciprocal of which is known as the *stability ratio*  $W$ . Elimelech et al. (2013) refers to Fuchs (1934) for the treatment of the stability ratio on a theoretical basis which leads to define  $W$  as

$$W = 2a \int_0^{\infty} \frac{\exp(V_T/kT)}{\left(\frac{D}{a} + 2\right)^2} dD \quad (2.19)$$

where  $V_T$  is the interaction potential defined before,  $D$  is the particle separation and  $a$  is the particle radius assuming that particles are spherical. When,  $W$ , is plotted against the concentration,  $c$ , of a symmetric electrolyte  $z : z$  in log-log form, it is possible to determine the *CCC* of the suspension by identifying the breaking point of the curve (Cao et al. (2015)).

In Figure 2.18 the stability ratio  $W$  was calculated as a function of the electrolyte concentration  $c$  for the two different particle orientations (parallel and crossed). The breaking point of the curves was defined by tracing two tangents of the curves and define the *CCC* at their point of intersection. For the case of parallel particle orienta-

tion the  $CCC$  predicted is at  $1.6 \text{ mol L}^{-1}$ , while for the crossed particle orientation the  $CCC$  was at the order of  $0.06 \text{ mol L}^{-1}$ . Hence, it can be expected that in a real system, aggregation will start from particles that are oriented in a cross configuration or close to it. Furthermore, the value of  $CCC$  predicted by this model is in a very good agreement with the range of values of  $CCC$  suggested by the experiment.

### 2.3 Discussion and Summary

This section was focused on the interactions between particles and ions, and particles between them, to obtain a more clear picture of the impact a salt, such as  $\text{Ce}(\text{NO}_3)_3$ , can have on a suspension. Furthermore, in terms of the application as nano-containers, some limiting conditions had to be found for which they could be incorporated in the coating matrix without affecting it. All the measurements on this section were realised in a suspension that was not purified from the by-products of the synthesis. Thus, the quantities of electrolytes added in the suspension refer to the added quantities and not the total of the suspension. For measurements where significant dilution had to be made, the added concentration is close to the total one. But for experiments realised on the stock solution, or slightly diluted, the difference is important.

In a first time the interface between particles and ions was studied by measuring the electrophoretic mobility of the particles in different salt concentrations. It was shown that boehmite nano-particles are positively charged with a  $\zeta$  of  $60 \text{ mV}$ . For suspensions with a  $\zeta$  of more than  $30 \text{ mV}$  is an indication of a stability, which was already suggested in the Section 1 since sedimentation of the suspension was not observed for several months after the synthesis.  $\zeta$  was measured for different added salt concentrations ( $0 - 0.01 \text{ mol L}^{-1}$ ) and  $pH$  conditions, to observe if there is a significant impact of these parameters on the charge of the particles. The salt used in this study was  $\text{NaCl}$  and the  $pH$  was modified using  $\text{NaOH}$ . Adding salt in the suspension decreases the value of  $\zeta$  from  $\sim 60 \text{ mV}$  to about  $40 \text{ mV}$  for  $pH$  values between 5 and 7. For  $7 < pH < 10$   $\zeta$  seems to be unaffected by salt and only depends from the  $pH$ . Addition of  $\text{NaOH}$  increases  $pH$ , which leads to a gradual decrease of  $\zeta$ , finally reaching a null value for a  $pH = 9.5$ . This  $pH$  value is the iso-electric point and the addition of  $\text{NaCl}$  does not affect its absolute value. From the above, one can conclude that for salt concentrations up to  $0.01 \text{ mol L}^{-1}$  and a  $pH$  value close to the one of the synthesis ( $pH \sim 4.5$ ), the suspension remains stable. This is an important information that can act as a basis to define the limitations of the suspensions in terms of salt concentration.

Based on the measurement of the  $\zeta$ , and the coarse grained particle model from Section 1, the interaction potential between two cylindrical particles was studied using the DLVO theory. Two configurations of interaction were considered, one parallel and one crossed. It was demonstrated that the potential of interaction between crossed particles is much lower than the parallel particles. For a salt concentration of  $0.01 \text{ mol L}^{-1}$  both configurations produce a repulsive barrier that is sufficient to repel the particle. Further increase of salt concentration ( $0.1 \text{ mol L}^{-1}$ ), decreases significantly the interaction potential for both configurations, almost diminishing it for the case of crossed particles. This is an indication that aggregation of particles will most probably start from particles that have a crossed configuration.

To verify the validity of the above predictions, an experimental study of aggregation was realised by means of Dynamic Light Scattering. A series of samples containing different concentrations of boehmite nano-particles ( $1.9 - 38 \text{ gr L}^{-1}$  or  $\phi = 0.04\% - 1\%$ ) and salt ( $0.001 - 0.1 \text{ mol L}^{-1}$ ) were tested. Initially, instead of testing stability with  $\text{Ce}(\text{NO}_3)_3$ , tests were realised with  $\text{NaNO}_3$  which is a simpler salt, to see if there is a significant effect of the cation. However, due to experimental difficulties having to do with the instant aggregation or even gelification of the sample for certain concentration of salts, only qualitative observations could be made. It was observed that for both salts, aggregation initiates at a salt concentration of  $0.05 \text{ mol L}^{-1}$ , while further increase of the concentration leads either to aggregation, for suspensions with low particle concentration, or to instant gelification, for suspensions with high particle concentration. Due to these difficulties, the value of critical concentration of coagulation was not precisely defined, but certainly lies between  $0.02 - 0.05 \text{ mol L}^{-1}$  of added salt, between  $0.02 - 0.07 \text{ mol L}^{-1}$  for the total salt concentration in the suspension. The most important result obtained from this experiment was that both salt yields similar results for the same added salt concentration. As it was discussed, this behaviour was somewhat unexpected; assuming complete dissociation of the salts when dispersed in water, then for  $x \text{ mol L}^{-1}$  of  $\text{NaNO}_3$  there are  $x \text{ mol L}^{-1}$  of  $\text{NO}_3^-$  dispersed. On the other hand, for  $x \text{ mol L}^{-1}$  of  $\text{Ce}(\text{NO}_3)_3$  there are  $3x \text{ mol L}^{-1}$  of  $\text{NO}_3^-$ . Considering now that the main mechanisms of destabilization is the screening of the particle repulsion due to  $\text{NO}_3^-$  attracted from the particles, then for the case of the Cerium Nitrate the *CCC* should have laid three times lower than the *CCC* for the Sodium Nitrate. The explanation given for this interesting behaviour, was based on the speciation of Cerium Nitrate which led in the implementation of speciation study of  $\text{Ce}(\text{NO}_3)_3$ .

When  $\text{Ce}(\text{NO}_3)_3$  is dispersed in an aqueous solvent, several species are formed.

The type of species depends on the concentration of salt added. The possible species that may be formed found in literature are  $\text{Ce}(\text{NO}_3)^{2+}$ ,  $\text{Ce}(\text{NO}_3)_2^+$ ,  $\text{Ce}(\text{OH})^{2+}$  and a precipitated phase  $\text{Ce}(\text{OH})_3$ . Using reaction constants found in literature and a homemade code it was found that for salt concentrations relevant to ones that aggregation was studied, the concentration of the aforementioned species increases significantly. This means that there are less free  $\text{NO}_3^-$  ions in the solution than the stoichiometry suggests. In light of these findings a more precise modelling of speciation was realised using a chemical equilibrium software. Even if the results are less accentuated than previously, there still is a significant increase of  $\text{Ce}(\text{NO}_3)^{2+}$  and  $\text{Ce}(\text{NO}_3)_2^+$  in the solution. Making the link with the aggregation results, it means that when  $\text{Ce}(\text{NO}_3)_3$  is dispersed in significant quantities, is not expected to dissolve completely, consequently releasing less than  $3x \text{ mol } L^{-1}$  of  $\text{NO}_3^-$ .

Using the interaction potential calculated from before, the *CCC* can be calculated theoretically, again for particles that are either parallel or in crossed configuration. The predicted *CCC* for parallel particles was estimated at  $0.16 \text{ mol } L^{-1}$ , while for the crossed configuration it was estimated  $0.06 \text{ mol } L^{-1}$ . This value is very close to the range of *CCC* that was measured experimentally and it is suggested again that aggregation is most probably initiated from particles that are not parallel between them.

To conclude, as already mentioned in the introduction, the nano-particles (or nano-containers) need to be stable in order to be incorporated in the polymeric coating matrix. Hence, if Cerium Nitrate concentration is limited below  $C_{Ce} < 2 \cdot 10^{-2} \text{ mol } L^{-1}$ , it was shown that the suspension behaviour is not affected. Taking this concentration as the upper limit of added Cerium Nitrate, in Section 3 a study of the adsorption capabilities of boehmite nano-particles, and thus their potential as nano-containers, will be realised.

### 3 Are they actually nano-containers?

A container in general, needs first of all to contain the largest amount possible of the material of interest, and in a second time it needs to be able to release this material when needed. Hence, to answer the question posed in the title the subsequent questions have to be answered first. The first is "*Can boehmite nano-particles "contain", or rather adsorb, Cerium?*". If the answer is positive then the next question arises naturally, "*How much can they contain?*" and the last one but equally important "*Can they desorb or not?*".

The answer to the first question was implicitly discussed in Sections 1 and 2 of this chapter. In Section 1 it was discussed that boehmite nano-particles can carry a net charge (positive or negative) that occur from the difference in the concentration of positive and negative sites of its surface. Then, in Section 2, it was demonstrated that for a  $pH = 4.5$  they carry a positive charge and its absolute value depends on the salt concentration of the solution they are suspended. This dependence was justified by the formation of the Electrostatic Double Layer that screens the electrostatic potential of the particle. What was maybe not that clear is that inside the Electrostatic Double Layer co-ions can also exist, although in much a lower concentration compared to counter-ions because of the electrostatic repulsions of the similarly charged particle. It should also be expected that, the higher the valency of the co-ion is, the more intensive the repulsions will be, hence the lower the co-ions concentration around the particles will be. The possible reasons of the existence of co-ions in the Electrostatic Double Layer could be attributed either to entropic forces, or to a feeble attractive potential created from a portion of the surface charges that carry an oppositely signed charge. If somehow the term "adsorption" is broadened to take into account not only ions that are rigidly bound on the surface, but the ions that can remain related to the surface even at a certain distance, then the answer to the first question is "*Yes, boehmite nano-particles can adsorb Cerium*".

Before continuing to answer the next questions there is a number of limitations that need to be discussed and will help understand the approach followed in the experiments. The first limitation has to do with the  $pH$  for which adsorption has to be made. Because of the amphoteric property of boehmite surfaces to change their net charge polarity as a function of  $pH$ , a seemingly easy solution to adsorb more Cerium would be to reverse the charge of the particles by increasing the  $pH$  to a value larger than the iso-electric point. That way Cerium becomes the counter-ion and thus it is expected to be adsorbed in much higher concentrations. Unfortunately, this can not be the case here for a number of reasons. First, the polymeric matrix where the nano-

containers will be incorporated was optimized for a  $pH$  value between 4 – 6, thus significantly changing the  $pH$  of the suspension would mean developing a new matrix. A second problem would be the destabilization of the suspension when changing the  $pH$  from 4.5 to over 9.5 which is the iso-electric point; since this  $pH$  denotes the complete screening of the electrostatic barrier between particles, an aggregated phase may be created that can have a completely different macroscopic behaviour and could heavily affect the incorporation of the nano-containers in the polymeric matrix. Thus the first restriction is to adsorb in the “natural”  $pH$  of the synthesis,  $\sim 4.5$

The second limitation is imposed by the use of these nano-containers in an industrial application, where post-treatment of a suspension such as freeze-drying or dialysis are avoided for security reasons (nano-powder) and cost increase. Hence the stock solution had to be used with the very charged surrounding solution in terms of aluminum and nitrate ions (see Section 1).

Finally, adsorption experiments should be realised in a particle concentration that is similar to the one used when the nano-containers are mixed with the polymeric matrix to create the coating solution,  $C_{np} \sim 19 \text{ gr } L^{-1}$  (Jaubert (2012)).

At this point, it should be pointed out that because of the high concentration of aluminum and nitrate ions ( $C_{Al^{3+}} \sim 0.02 \text{ mol } L^{-1}$  and  $C_{NO_3^-} \sim 0.0035 \text{ mol } L^{-1}$ ) the adsorption performance of Cerium can be altered due to a competitive adsorption mechanism.

After having set the objectives of this section and the imposed limitations, in a first time the experimental protocol used to study the adsorption of Cerium on boehmite nano-particles will be described. Afterwards, the adsorption results will be presented and an answer to the second question will be given, concerning the capacity of nano-containers. Lastly, some further insights into the adsorption and desorption mechanism of Cerium will be given, using a surface complexation model.

### 3.1 Experimental study of adsorption

Adsorption was investigated by means of batch experiments. A volume of boehmite suspension, at a concentration of  $38 \text{ gr } L^{-1}$ , was mixed with  $Ce(NO_3)_3$ <sup>13</sup> in different concentrations in a 1:1 volume ratio. After continuous stirring for 24 h (for determination of contact time see Appendix 6) in a closed vial at room temperature ( $20 \sim 25^\circ C$ ), the mixture was recovered and the particles were removed from the system either by filtration or centrifugation. The remaining solution, contained the Cerium that was not adsorbed by the particles and it was quantified either by ICP-

<sup>13</sup>purity 99%, SIGMA-ALDRICH

Graph symbol	Boehmite type	Dialysis	Separation method	Cerium detection
★	Synthesised	No	Filtration	ICP-OES
●	Commercial	Yes	Centrifugation	Xylenol UV-Vis

**Table 2.3:** Summary table of adsorption experiments

OES, for low Cerium concentration, or by UV-Vis, for high Cerium concentration. A more detailed description of the exact protocols used, is given in Appendix 5. The quantity adsorbed was calculated by

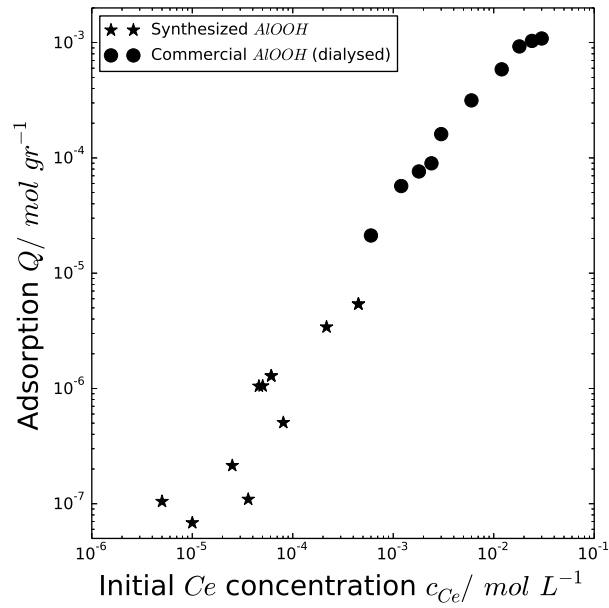
$$Q = \frac{C_{ini} - C_{final}}{C_{np}} \quad (2.20)$$

where  $C_{ini}$  is the initial concentration of Cerium put in the mixture in  $mol L^{-1}$ ,  $C_{final}$  is the concentration of Cerium recovered in the solution after the particles were removed and  $C_{np}$  is the concentration of nano-particles in the solution in  $gr L^{-1}$ .

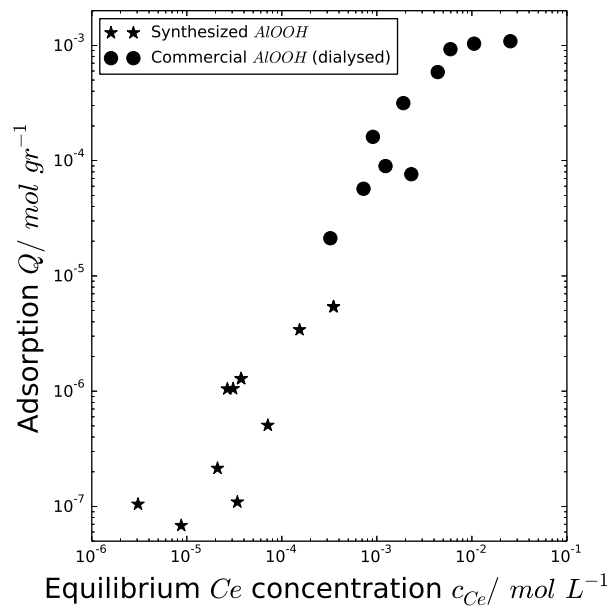
Initially, because of the requirements discussed in the introduction, synthesized nano-particles were used. However, because of the small yield of the synthesis in terms of suspension volume ( $\sim 250 mL$ ), the synthesis time and the need for a high particle concentration in each experiment, it was later decided to use a commercial boehmite powder<sup>14</sup>. The commercial nano-particles were chosen in order to have similar hydrodynamic size ( $\sim 25 nm$ ) and specific surface ( $260 m^2 gr^{-1}$ ) as the synthesized ones. When dispersed in ultrapure water the mixture exhibited a  $pH$  of 4.5 because it is already acidified in powder form. In Figure 2.19 the adsorption  $Q$  of Cerium is plotted against the initial  $Ce(NO_3)_3$  concentration (Figure 2.19a) and the Cerium concentration at equilibrium,  $C_{final}$  (Figure 2.19b). The star markers (★) correspond to adsorption experiments realized on synthesized nano-particles, while the circle markers (●) correspond to adsorption experiments on the commercial nanoparticles. The conditions and the techniques used for the experiments are summarised in Table 2.3.

The first thing to notice in Figure 2.19a is a steady, almost linear in log-log, increase of Cerium adsorption for a very broad range of added Cerium in the solution ( $10^{-5}$  to  $10^{-2} mol L^{-1}$ ). In the initial study with the synthesised nano-particles for a low concentration of Cerium ( $c_{Ce} < 10^{-3}$ ), no saturation of the adsorption was noticed. It was thus suggested to extend the range of added Cerium to higher concentrations ( $c_{Ce} > 10^{-3}$ ), using a commercial powder of boehmite nano-particles.

<sup>14</sup>DISPERAL®P2, Sasol Tech



(a)



(b)

**Figure 2.19:** Adsorption  $Q$  in  $\text{mol}$  of Cerium per  $\text{gr}$  of nano-particles as a function of (a) the initial Cerium concentration and (b) the concentration of Cerium at equilibrium. The star markers ( $\star$ ) correspond to adsorption experiments realized on synthesized nano-particles. The circle markers ( $\bullet$ ) correspond to adsorption experiments on the commercial nanoparticles.

However, the protocol developed for the detection of Cerium in these concentrations, necessitated the removal of aluminum ions that existed in the solution by dialysis. Hence the second information to be observed, is the slightly higher adsorption measured of the dialysed suspension corresponding to circle marks (●). Meaning, that a fitting straight line that passes through the experimental point of the commercial nano-particles is slightly deplacé over a similar fitting line passing through the points of the synthesised nano-particles. This increase is most probably related with the removal of the ions from the commercial suspension.

In the introduction it was suggested that because of the initial high concentration of ions ( $\text{Al}^{3+}$  and  $\text{NO}_3^-$ ) there could be an inhibitive or competitive behaviour on the adsorption of Cerium in order to take its place in the Electrostatic Double Layer. Seemingly this could be the case here. By means of dialysis an excess of ions was removed from the solution and thus of the Electrostatic Double Layer, allowing that way more Cerium to be adsorbed. On the other hand, this could simply be an artifact from the fact that the suspension is different, and thus  $\text{Al}^{3+}$  and  $\text{NO}_3^-$  have no effect in the adsorption of Cerium.

Finally, it looks as if the last points ( $c_{Ce} > 10^{-2} \text{ mol L}^{-1}$ ) are reaching saturation in terms of adsorption and probably form a plateau. Eventhough, the fluctuations of the values are too significant to conclude if this is the beginning of a plateau or not, the value of the critical concentration of coagulation ( $CCC = 0.02 - 0.04 \text{ mol L}^{-1}$ ) measured in Section 2.2 seem to reinforce this hypothesis. The  $CCC$  is a salt concentration where most of the electrostatic forces are screened, which also means that no further ions would stay attached with the particles and thus no further adsorption. Unfortunately, no other experimental data were found in literature concerning similar cases. Usually adsorption studies are limited to concentration of adsorbates much lower than the concentration of Cerium in this study.

From the above results, one can safely conclude that boehmite nano-particles can act as a container for Cerium. The  $pH$  restriction at a value of  $\sim 4.5$  and the positive charge of the nano-particles, initially created a doubt about the feasibility of adsorbing Cerium on the surface of boehmite. Nevertheless, it was shown that Cerium is adsorbed through a very wide range of concentrations reaching close to the critical concentration of coagulation of the suspensions ( $0.02 - 0.04 \text{ mol L}^{-1}$ ).

To gain a greater insight on the mechanism of adsorption, usually adsorption results are fitted with adsorption isotherms such as Freundlich, Langmuir or BET. These models are principally used for systems where the exact composition of the adsorbent is not known or it is very inhomogeneous and the description of adsorption in each

different phase makes almost impossible the use of a more insightful approach. In this almost “ideal” system it would be almost a shame not to use a more elaborate model to explain the results.

### 3.2 How is Cerium adsorbed?

Understanding Cerium adsorption in a more profound way is a key factor in this type of nano-containers since the whole concept is based on the interaction between the salt ions and the nano-particles surface. If for example in the future a different matrix, that does not restrict the  $pH$  range, is developed, then a predictive model of the adsorption behaviour would be very useful. Furthermore and most importantly, this knowledge will allow us to predict the release or desorption of Cerium when triggered.

#### 3.2.1 Surface complexation modeling

Among the models that exist for metal oxides the one developed by Yates et al. (1974); Davis and Leckie (1978); Davis et al. (1978); Davis and Leckie (1980) attempts to treat in a complete way the charging phenomena and there is a large body of literature around it. Their theory was developed with the postulation by Yates et al. that the surface charges are distributed on the surface in a discrete way and that the electrolyte anions are mainly distributed in two ways; 1) on the solid-liquid interface, ion-charge pairs are formed with oppositely charged surface groups and 2) ions form a diffuse layer to balance the remaining surface charged to achieve electro-neutrality. They named their model the “site-binding model”; it considers that the EDL is separated by three planes ( $0-$ ,  $\beta-$ ,  $d-$ ) as it can be seen in Figure 2.20, that is why it is also called the “Triple Layer Model”.

The first plane ( $0-$ ), also called Stern plane, is defined on a surface very close to the real metal surface, wherein the adsorbed potential determining ions ( $H_3O^+$ ,  $OH^-$ ) and water molecules lie. On this plane, a charge  $\sigma_0$  and potential  $\psi_0$  can be defined, which are respectively the true charge and potential of the particle since these ions are strongly attached to the surface and in a very small (atomic) distance.

The next plane ( $\beta-$ ), also called inner Helmholtz plane (**IHP**), is the external boundary of a region occupied by strongly bound counter- and co- ions; therein a charge  $\sigma_\beta$  and potential  $\psi_\beta$  can be defined. As explained in Levine and Smith (1971); Yates et al. (1974), the plane  $\beta-$  is an abstract plane where a mean electrostatic potential  $\psi_\beta$  can be defined to replace the “micro-potential” (local potential created by ion interaction) that exists locally.

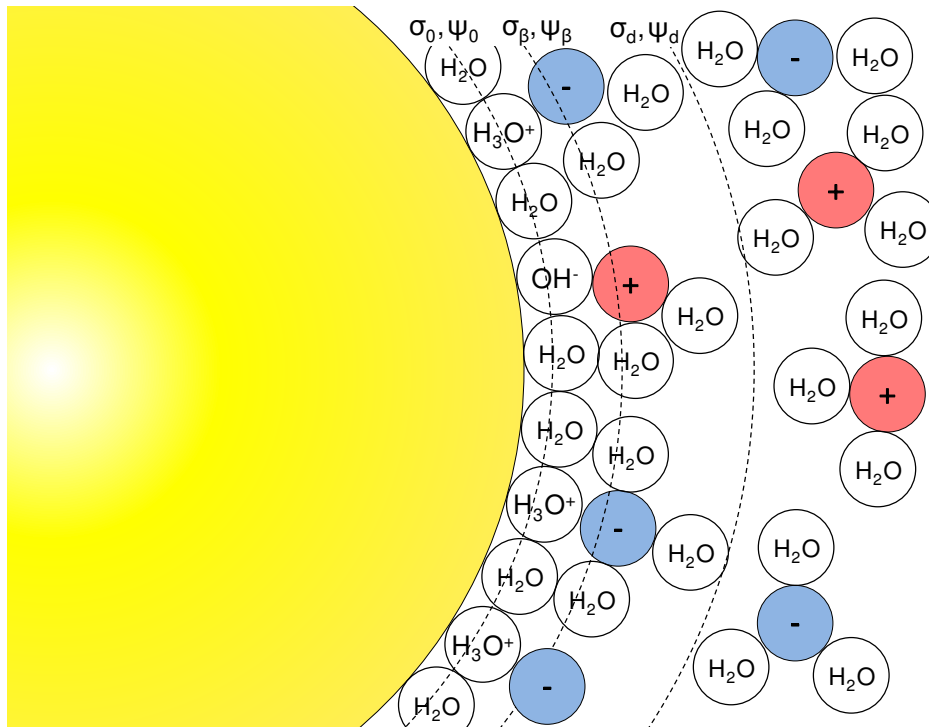


**Figure 2.20:** Schematic representation of an oxide-water interface showing possible locations for molecules to bind. The first layer, starting from the surface, defines plane 0– where the potential determining ions are adsorbed along with a hydration layer. The plane  $\beta$ – comprises of co- and counter-ions that are strongly adsorbed on the particle surface. Lastly, plane  $d$ – defines the start of the diffuse layer where no specific adsorption of ion takes place.

Lastly, plane ( $d$ –), also called outer Helmholtz plane, is where the diffusive electrostatic layer starts. Ions that lie beyond this plane compose an ion shell that is not tightly attached to the particle, since each ion interact mainly by electrostatic forces that depend on the distance. It means that the physical characteristics (size, shape) of this shell depends for example on the phoretic movement of the particles, the electrostatic forces etc. Correspondingly, the charge on the plane is  $\sigma_d$  and the potential  $\psi_d$ .

The above description implies that ions distinctively lie on restricted and different planes, which probably is a poor approximation. As discussed by Yates et al. it is implied that the potential determining ions are adsorbed in one plane (0–) and the salt ions in a second plane ( $\beta$ –) and after plane ( $d$ –) ions form the diffusive electrostatic layer.

Based on the concept of the Triple Layer model, the association and dissociation of the ions on a surface can be described as equations of chemical reactions, and it is

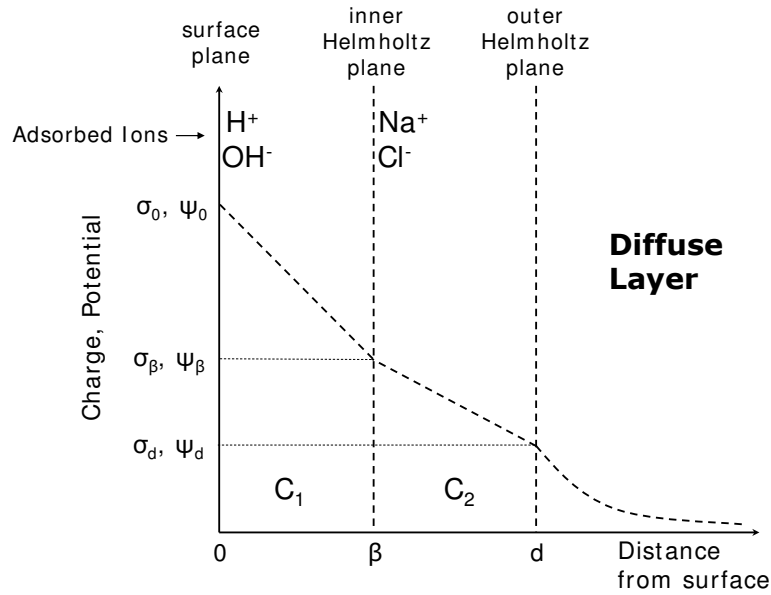
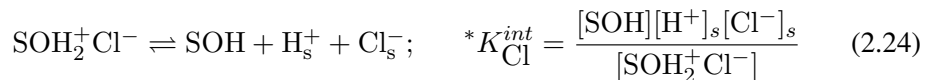


**Figure 2.21:** A quantitative representation of the charge and potential distribution at an idealized oxide-water interface as a function of distance from the surface.

detailed in James and Parks (1982). The first set of equations consider the reaction on the surface, denoted as  $S$ , where the hydroxyl groups either receive or release a proton



where the subscript  $[-]_s$  refers to a concentration of an ion on the surface  $S$ . In a similar manner of the ion pair formation of the potential determining ions, salt ions can be assumed to be binded through ion pairing. Below an example is given for NaCl



Some clarification is needed for the ions with the subscript  $s$ . In the first set of equations, the protons involved ( $\text{H}_s^+$ ) are assumed to lie in the surface plane (0–);

similarly in the second set, the salt ions ( $\text{Na}_s^+$ ,  $\text{Cl}_s^-$ ) are assumed to lie in the plane  $\beta^-$ . Unfortunately, these quantities can not be measured experimentally on the surface. Usually the concentration of ions is known in the bulk, thus one can assume the concentration in the surface plane using Boltzmann's equation for the ion distribution from the surface to the bulk

$$[\text{Ion}]_s = [\text{Ion}]_b \exp(-ze\psi_i/kT) \quad (2.25)$$

where  $z$  is the valency of the ion,  $\psi_i$  is the electrical potential experienced from the ion on surface  $i$  and  $b$  refers to a point in the solution where  $\psi = 0$ . As already mentioned  $\psi_i$  can take values as  $\psi_0, \psi_\beta$  and  $\psi_d$ . For simplicity from here on  $\psi_i^* = ze\psi_i/kT$ . Combining the above with Equation (2.21) and Equation (2.23) the reaction constants become

$$K_{a1}^{int} = \frac{[\text{SOH}][\text{H}^+]_b}{[\text{SOH}_2^+]_b} \exp(-\psi_0^*) \quad (2.26)$$

$$K_{a2}^{int} = \frac{[\text{SO}^-][\text{H}^+]_b}{[\text{SOH}]_b} \exp(-\psi_0^*) \quad (2.27)$$

and

$$*K_{\text{Na}}^{int} = \frac{[\text{SO}^- \text{Na}^+][\text{H}^+]_b}{[\text{SOH}][\text{Na}^+]_b} \exp(-\psi_0^* + \psi_\beta^*) \quad (2.28)$$

$$*K_{\text{Cl}}^{int} = \frac{[\text{SOH}][\text{H}^+]_b [\text{Cl}^-]_b}{[\text{SOH}_2^+ \text{Cl}^-]_b} \exp(-\psi_0^* + \psi_\beta^*) \quad (2.29)$$

where the term  $\exp(-\psi_0^* + \psi_\beta^*)$  expresses the assumption put forward by Yates et al. that salt ions can only be bound in the mean plane  $\beta^-$ . The number of surface sites available per unit area,  $N_s$ , the surface density of titratable charge,  $\sigma_0$  and the amount of charge loss because of the adsorbed ions  $\sigma_\beta$  are given by

$$N_s = N_A ([\text{SOH}] + [\text{SOH}_2^+] + [\text{SO}^-] + [\text{SOH}_2^+ \text{Cl}^-] + [\text{SO}^- \text{Na}^+]) \quad (2.30)$$

$$\sigma_0 = eN_A ([\text{SOH}_2^+] - [\text{SO}^-] + [\text{SOH}_2^+ \text{Cl}^-] - [\text{SO}^- \text{Na}^+]) \quad (2.31)$$

$$\sigma_\beta = eN_A ([\text{SO}^- \text{Na}^+] - [\text{SOH}_2^+ \text{Cl}^-]) \quad (2.32)$$

$$\sigma_d = -\frac{4000N_A e c}{\kappa} \sinh(z\psi_d^*/2) \quad (2.33)$$

where  $N_A$  is the Avogadro number,  $e$  is the elementary charge and  $c = [\text{Na}^+]_b = [\text{Cl}^-]_b$ . Since electro-neutrality needs to be maintained

$$\sigma_0 + \sigma_\beta + \sigma_d = 0 \quad (2.34)$$

It is assumed that in the region between the planes 0–,  $\beta$ – and  $d$ – the capacitances are constant and they relate the charge density to the potential gradient

$$\psi_0 - \psi_\beta = \frac{\sigma_0}{C_1} \quad (2.35)$$

$$\psi_d - \psi_\beta = \frac{\sigma_d}{C_2} \quad (2.36)$$

where  $C_1$  and  $C_2$  are the integral capacitances of the inner (from plane 0– to  $\beta$ –) and outer (from  $\beta$ – to  $d$ –) regions of the inner EDL.

Once values for the fixed parameters ( $N_s$ ,  $K_{a1}^{int}$ ,  $K_{a2}^{int}$ ,  $*K_{\text{Na}}^{int}$ ,  $*K_{\text{Cl}}^{int}$ ,  $C_1$  and  $C_2$ ) are defined, provided that

$$pH_{pzc} = \frac{pK_{a1}^{int} + pK_{a2}^{int}}{2} \quad (2.37)$$

then one can solve for the charge  $\sigma_i$  and potential  $\psi_i$  in different planes. The system of equations can be solved using a generalised chemical equilibrium software (*Visual MINTEQ*, *MINEQL*, *PHREEQC*). The most common procedures for the estimation of the constants are double graphical extrapolation and optimization with a computer software (James and Parks (1982); Hunter (2001)). Amongst the six variables above ( $\sigma_0$ ,  $\psi_0$ ,  $\sigma_\beta$ ,  $\psi_\beta$ ,  $\sigma_d$ ,  $\psi_d$ ), the only one that can be measured experimentally with some certainty is  $\sigma_0$ , using potentiometric titration. In many cases,  $\psi_d$  is assimilated with the electro-kinetic or zeta potential  $\zeta$  which probably is a poor approximation.

In most of the references contained above, surface complexation studies were realised in very low concentrations in terms of particles and ions, and the salts used were symmetrical and monovalent. There are very few studies in the literature where more complex systems in terms of electrolyte composition and concentration are studied. Furthermore, phenomena that take place in bulk systems, such as dissolution of solid phases and chemical speciation of the electrolytes were not taken into account. In Section 2.2.1 it was demonstrated that Cerium Nitrate solutions can compose different chemical species as a function of its bulk concentration. Thus, in the case of our system if a more complete understanding is needed, association/dissociation constants need to be found for each of the species that exist in the system.

### 3.2.2 Adsorption of a monovalent cation

In the next few lines, a modelling example of adsorption will be given, of a system of charged boehmite surface in contact with a 1 : 1 electrolyte (NaCl) and will be compared quantitatively with the experimental results presented previously. The purpose of such demonstration is first of all to provide a proof of concept of the nano-containers, meaning their adsorption/desorption capability. In a second time, to evaluate if a similar approach applied for an asymmetric electrolyte, like Cerium nitrate ( $\text{Ce}(\text{NO}_3)_3$ ), can exist and what are the difficulties.

Author	Electrolyte	$pK_{a1}^{int}$	$pK_{a2}^{int}$	$pK_{anion}^{int}$	$pK_{cation}^{int}$
Wood et al. (1990)	$\text{KNO}_3$	6.3	11.9	7.5	9.7
Huang and Stumm (1973)	NaCl	5.2	11.8	7.9	9.2
This work	NaCl	6.9	12.1	7.5	9.7

**Table 2.4:** Electro-kinetic data for boehmite ( $\gamma$ -alumina) found in literature

The parameters used in the model were found in literature, mainly from the works of Wood et al. (1990); Huang and Stumm (1973) who studied the electro-chemistry of the boehmite-water interface for solutions that contain different amounts of 1 : 1 electrolytes. The reaction constants for the salt ions were kept the same, while the constants for the proton capture/release were modified to satisfy Equation (2.37), having assumed that  $pH_{iep} = pH_{pzc}$ .

In Figure 2.22 the experimental results of adsorption are presented (marker points), together with the adsorption results obtained numerically using the Triple Layer Model presented above (dashed and solid lines). In terms of the model, the adsorption is given by the evaluation of the term  $[\text{SO}^-\text{Na}^+]$  (Equation (2.23)) divided by the concentration of particles. The dashed line correspond to an evaluation using the parameters in Table 2.4, while the solid lines are a heuristic attempt to approach the experimental results by changing the reaction constant of the cation. Despite the fact that the “guessed” value may not have any physical meaning or may be completely wrong, it is evident that the correct account of the chemistry or physics could greatly influence the outcome. Changing the association of the cation to a value of  $pK_{cation} = 5$ , fits the adsorption results almost perfectly. A correct account of the chemistry in the case of Cerium Nitrate would be first of all the inclusion of the chemical species formed when Cerium Nitrate is dispersed in water as discussed in Section 2.2.1. Consequently, if all the different species formed have a possibility

to be adsorbed, in the case of the Triple Layer Model the association/dissociation constant with the boehmite surface needs to be evaluated for each one of them.

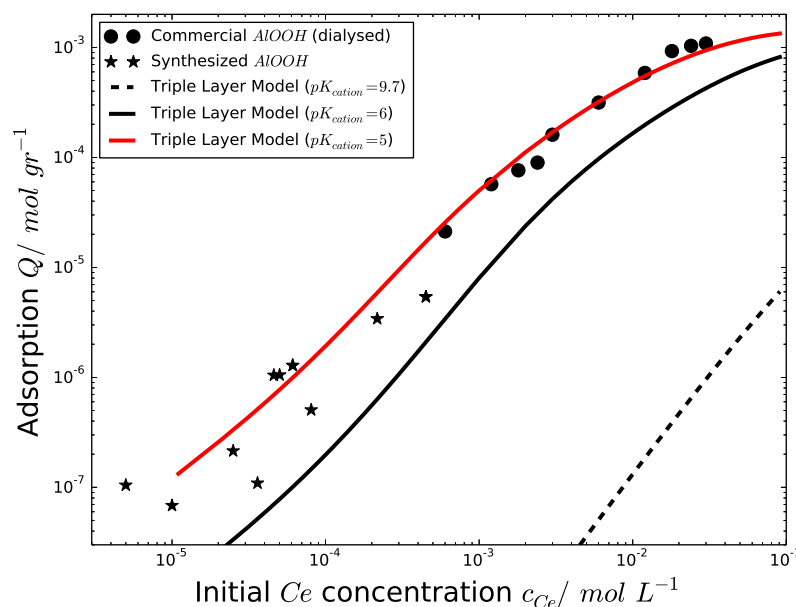


**Figure 2.22:** Adsorption  $Q$  as a function of the initial Cerium concentration. The dashed line is the prediction of adsorption of the Triple Layer Model using the constants in Table 2.4. The solid lines is the prediction of adsorption of the Triple Layer Model by changing the association/dissociation constant to fit the results.

In the Triple Layer Model, salt ions are considered adsorbed only if they are associated in the inner Helmholtz plane. No prediction of adsorption is made for ions that lie after the outer Helmholtz plane. In reality since there is no such distinction of planes and the distribution of ions is continuous from the surface out the bulk, it is most probable that ions will be bound on the particles even if they lie after the hypothetical outer Helmholtz plane. It is thus expected that models such as the one used here, underestimate the prediction of adsorption in cases of high concentration of adsorbates.

Lastly, it is interesting to see if desorption of Cerium from the surface can be predicted by changing the  $pH$  of the solution. If the initial concentration of Cerium in the solution is  $10^{-3} \text{ mol L}^{-1}$ , the particle concentration  $1 \text{ gr L}^{-1}$  and the  $pH = 5$ , then in Figure 2.23a it is predicted that  $\sim 4 \cdot 10^{-5} \text{ mol L}^{-1}$  of Cerium is adsorbed on the surface. If the  $pH$  of the solution is increased, as it is happening for aluminum alloys where corrosion has initiated, this model predicts an increase of the adsorption and in the same time a decrease of the aqueous concentration of the cation in bulk

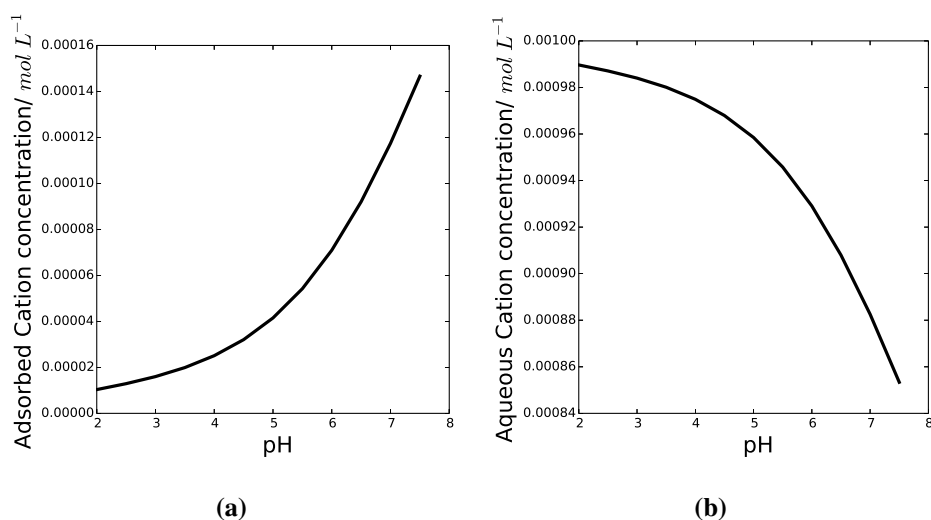


**Figure 2.23:** (a) Concentration of adsorbed cation as a function of  $pH$ , (b) Concentration of cations in the bulk.

(Figure 2.23b). Thus the expected mechanism of desorption by the nano-containers by  $pH$  triggering, is not plausible in the case of aluminum alloys corrosion, since an increase of the  $pH$  is expected. Nevertheless, a secondary desorption effect can be outlined. The nano-containers solution that is mixed with the polymer matrix, contains also a quantity of Cerium that was not adsorbed. When the coating is damaged, the Cerium that is free in the coating volume will be “consumed” first. Decreasing the concentration of Cerium in the bulk will most probably have as an effect, the desorption of Cerium from the particles surface due to equilibrium change. Concluding, eventhough the expected mechanism of desorption based on  $pH$  triggering is not expected to take effect, a gradual desorption of Cerium is expected due to the change of equilibrium with the bulk concentration.

### 3.3 Summary

In this section three different questions were answered in order to evaluate the possibility of using nano-particles as containers. The first one was “*Can boehmite nano-particles adsorb Cerium?*”. With a positive answer given implicitly in the introduction of the section the second question was “*How much can they adsorb?*”.

To answer this question, an adsorption experiment was realized in systems that are concentrated in terms of particles, as well as salt. The protocol consisted of first putting the particles in volume by mixing equal volumes, then separate the particle

from the solutions, measure the concentration of Cerium in equilibrium and finally evaluate the quantity adsorbed by  $Q = (C_{ini} - C_{final})/C_{np}$ .

In terms of adsorption performance, boehmite nano-particles demonstrated a continuous capability of adsorbing as Cerium in the solution was increased. Even at very high salt concentrations, approaching the *CCC*, nano-particles were still able to adsorb Cerium. As an indicative value, in a solution of 1 L, with a Cerium concentration of  $10^{-2}$  mol and 13 gr of boehmite nano-particles, it is predicted that  $6.5 \cdot 10^{-3}$  mol of Cerium will be adsorbed which is  $\sim 65\%$  of the initial concentration.

To have a better understanding of the mechanism involved, adsorption was studied by means of the Triple Layer Model. Even though a full approach of the model including chemical speciation of Cerium Nitrate was not realized, the results obtained for a case of a monovalent symmetric electrolyte with a modified association/dissociation constant seem to be in accordance with the experimental results.

Lastly, by using the Triple Layer model it was demonstrated that changing the *pH* of the surrounding solution can act as a trigger to release adsorbed Cerium, but not in the case of aluminum alloys where an increase of *pH* is expected. The increase of *pH* is predicted to increase adsorption for the case of boehmite nano-particles. However, due to the existence of Cerium in the bulk of the coating which will be firstly "consumed", the change of equilibrium will most probably lead to a long-term desorption of Cerium. In conclusion, the answer to the last question, "*Can they desorb or not?*", is yes but not for the expected reason. Thus, the choice of boehmite particles as nano-containers is feasible, but there are probably other better suited systems.

## 4 References

- Alphonse, P. and Courty, M. (2005). Surface and porosity of nanocrystalline boehmite xerogels. *Journal of Colloid and Interface Science*, 290(1):208–219.
- Belloni, L. (1998). Ionic condensation and charge renormalization in colloidal suspensions. *Colloids and Surfaces A: Physicochemical and Engineering Aspects*, 140(1–3):227–243.
- Belounis, F. (2015). *Structuration par voie colloïdale de nanopoudres de boehmite à partir de systèmes mixtes organique/inorganique*. Phd thesis, Université de Limoges.
- Bleta, R., Jaubert, O., Gressier, M., and Menu, M.-J. (2011). Rheological behaviour and spectroscopic investigations of cerium-modified AlO(OH) colloidal suspensions. *Journal of Colloid and Interface Science*, 363(2):557–565.
- Bouwkamp, C. J. (1947). A study of Bessel functions in connection with the problem of two mutually attracting circular disks. *Proceedings of the Section of Sciences of the Koninklijke Nederlandse Akademie van Wetenschappen*, 50:1071–1083.
- Buining, P. A., Philipse, A. P., and Lekkerkerker, H. N. W. (1994). Phase Behavior of Aqueous Dispersions of Colloidal Boehmite Rods. *Langmuir*, 10(7):2106–2114.
- Cao, T., Szilagyi, I., Oncsik, T., Borkovec, M., and Trefalt, G. (2015). Aggregation of Colloidal Particles in the Presence of Multivalent Co-Ions: The Inverse Schulze–Hardy Rule. *Langmuir*, 31(24):6610–6614.
- Chiche, D., Chanéac, C., Revel, R., and Jolivet, J.-P. (2011). Use of polyols as particle size and shape controllers: application to boehmite synthesis from sol–gel routes. *Physical Chemistry Chemical Physics*, 13(13):6241–6248.
- Davis, J. A., James, R. O., and Leckie, J. O. (1978). Surface ionization and complexation at the oxide/water interface: I. Computation of electrical double layer properties in simple electrolytes. *Journal of Colloid and Interface Science*, 63(3):480–499.
- Davis, J. A. and Leckie, J. O. (1978). Surface ionization and complexation at the oxide/water interface II. Surface properties of amorphous iron oxyhydroxide and adsorption of metal ions. *Journal of Colloid and Interface Science*, 67(1):90–107.

- 
- Davis, J. A. and Leckie, J. O. (1980). Surface ionization and complexation at the oxide/water interface. 3. Adsorption of anions. *Journal of Colloid and Interface Science*, 74(1):32–43.
- de Lint, W. B. S., Benes, N. E., Lyklema, J., Bouwmeester, H. J. M., van der Linde, A. J., and Wessling, M. (2003). Ion Adsorption Parameters Determined from Zeta Potential and Titration Data for a  $\gamma$ -Alumina Nanofiltration Membrane. *Langmuir*, 19(14):5861–5868.
- Delgado, A. V., González-Caballero, F., Hunter, R. J., Koopal, L. K., and Lyklema, J. (2007). Measurement and interpretation of electrokinetic phenomena. *Journal of Colloid and Interface Science*, 309(2):194–224.
- Elimelech, M., Gregory, J., and Jia, X. (2013). *Particle Deposition and Aggregation: Measurement, Modelling and Simulation*. Butterworth-Heinemann.
- Franks, G. V. and Gan, Y. (2007). Charging Behavior at the Alumina–Water Interface and Implications for Ceramic Processing. *Journal of the American Ceramic Society*, 90(11):3373–3388.
- Fratiello, A., Kubo-Anderson, V., Azimi, S., Marinez, E., Matejka, D., Perrigan, R., and Yao, B. (1992). A direct nitrogen-15 NMR study of cerium(III)-nitrate complexes in aqueous solvent mixtures. *Journal of Solution Chemistry*, 21(7):651–666.
- Fuchs, N. (1934). Über die Stabilität und Aufladung der Aerosole. *Z. Physik*, 89(11–12):736–743.
- Gieselmann, M. J. and Anderson, M. A. (1989). Effect of Ionic Strength on Boehmite Hydrogel Formation. *Journal of the American Ceramic Society*, 72(6):980–985.
- Holthoff, H., Egelhaaf, S. U., Borkovec, M., Schurtenberger, P., and Sticher, H. (1996). Coagulation Rate Measurements of Colloidal Particles by Simultaneous Static and Dynamic Light Scattering. *Langmuir*, 12(23):5541–5549.
- Huang, C.-P. and Stumm, W. (1973). Specific adsorption of cations on hydrous  $\gamma$ -Al<sub>2</sub>O<sub>3</sub>. *Journal of Colloid and Interface Science*, 43(2):409–420.
- Hunter, R. J. (2001). *Foundations of Colloid Science*. Oxford University Press, Oxford ; New York, 2 edition edition.

- James, R. O. and Parks, G. A. (1982). Characterization of Aqueous Colloids by Their Electrical Double-Layer and Intrinsic Surface Chemical Properties. In Matijević, E., editor, *Surface and Colloid Science*, number 12 in *Surface and Colloid Science*, pages 119–216. Springer US.
- Jaubert, O. (2012). *Revêtements hybrides multifonctionnels élaborés par voie sol-gel pour la protection d'alliages d'aluminium pour l'aéronautique*. PhD thesis, Université Toulouse III - Paul Sabatier.
- Karamalidis, A. K. and Dzombak, D. A. (2011). *Surface Complexation Modeling: Gibbsite*. John Wiley & Sons.
- Levine, S. and Smith, A. L. (1971). Theory of the differential capacity of the oxide/aqueous electrolyte interface. *Discussions of the Faraday Society*, 52(0):290–301.
- Malvern (2014). *Dynamic Light Scattering: An Introduction in 30 Minutes*. Technical note.
- Nelson, D. L. and Irish, D. E. (1973). Interactions in lanthanide systems. Part 2.—Raman study of aqueous cerium(III) nitrate. *Journal of the Chemical Society, Faraday Transactions 1*, 69(0):156–160.
- Ohshima, H. (2006). *Theory of Colloid and Interfacial Electric Phenomena*. Academic Press.
- Oikawa, T., Urabe, T., Kawano, S.-i., and Tanaka, M. (2011). Basic Study of Lanthanide Nitrate Species in Solution by Electrospray Ionization Mass Spectrometry. *Journal Solution Chemistry*, 40(6):1094–1107.
- Pierre, A. C. and Uhlmann, D. R. (1987). Gelation of Aluminum Hydroxide Sols. *Journal of the American Ceramic Society*, 70(1):28–32.
- Ramsay, J. D. F., Daish, S. R., and Wright, C. J. (1978). Structure and stability of concentrated boehmite sols. *Faraday Discussions of the Chemical Society*, 65(0):65–75.
- Russel, W. B., Saville, D. A., and Schowalter, W. R. (1992). *Colloidal Dispersions*. Cambridge University Press.
- Shchukin, D. and Möhwald, H. (2007). Self-Repairing Coatings Containing Active Nanoreservoirs. *Small*, 3(6):926–943.

- Sparnaay, M. J. (1959). The interaction between two cylinder shaped colloidal particles. *Recueil des Travaux Chimiques des Pays-Bas*, 78(9):680–709.
- Sposito, G. (1995). *The Environmental Chemistry of Aluminum, Second Edition*. CRC Press.
- Sprycha, R. (1989). Electrical double layer at alumina/electrolyte interface: I. Surface charge and zeta potential. *Journal of Colloid and Interface Science*, 127(1):1–11.
- Tavandashti, N. P. and Sanjabi, S. (2010). Corrosion study of hybrid sol–gel coatings containing boehmite nanoparticles loaded with cerium nitrate corrosion inhibitor. *Progress in Organic Coatings*, 69(4):384–391.
- Templeton, D. M., Ariese, F., Cornelis, R., Danielsson, L.-G., Muntau, H., van Leeuwen, H. P., and Lobinski, R. (2000). Guidelines for terms related to chemical speciation and fractionation of elements. Definitions, structural aspects, and methodological approaches (IUPAC Recommendations 2000). *Pure and Applied Chemistry*, 72(8).
- Trefalt, G., Szilagyi, I., and Borkovec, M. (2013). Poisson–Boltzmann description of interaction forces and aggregation rates involving charged colloidal particles in asymmetric electrolytes. *Journal of Colloid and Interface Science*, 406:111–120.
- Verwey, E. J. W., Overbeek, J. T. G., and Overbeek, J. T. G. (1999). *Theory of the Stability of Lyophobic Colloids*. Courier Corporation.
- Wood, R., Fornasiero, D., and Ralston, J. (1990). Electrochemistry of the boehmite–water interface. *Colloids and Surfaces*, 51:389–403.
- Yates, D. E., Levine, S., and Healy, T. W. (1974). Site-binding model of the electrical double layer at the oxide/water interface. *Journal of the Chemical Society, Faraday Transactions 1*, 70(0):1807–1818.
- Yoldas, B. E. (1973). Hydrolysis of aluminium alkoxides and bayerite conversion. *Journal of Applied Chemistry*, 23(11):803–809.
- Yoldas, B. E. (1975). Alumina gels that form porous transparent  $\text{Al}_2\text{O}_3$ . *Journal of Materials Science*, 10(11):1856–1860.
- Yoon, S.-j., Helmke, P. A., Amonette, J. E., and Bleam, W. F. (2002). X-ray Absorption and Magnetic Studies of Trivalent Lanthanide Ions Sorbed on Pristine and Phosphate-Modified Boehmite Surfaces. *Langmuir*, 18(26):10128–10136.

- Zakharchenya, R. I. (1996). Influence of peptization on the properties of alumina produced from boehmite sols. *Journal of Sol-Gel Science and Technology*, 6(2):179–186.
- Zheludkevich, M. L., Salvado, I. M., and Ferreira, M. G. S. (2005a). Sol–gel coatings for corrosion protection of metals. *Journal of Materials Chemistry*, 15(48):5099–5111.
- Zheludkevich, M. L., Serra, R., Montemor, M. F., Yasakau, K. A., Salvado, I. M. M., and Ferreira, M. G. S. (2005b). Nanostructured sol–gel coatings doped with cerium nitrate as pre-treatments for AA2024-T3: Corrosion protection performance. *Electrochimica Acta*, 51(2):208–217.

# General conclusions and perspectives

## Conclusions and Perspectives

This work was realized in the framework of project ECOREV, a project mainly focused on the development of new surface treatment techniques without chromium for the aircraft industry. The motivation emerged from the European regulation REACH to ban chromium VI, since it is considered Carcinogenic, Mutagenic or toxic for Reproduction. Currently, a possible strategy to replace chromium for surface treatment is to build a barrier coating inside which nano-containers functionalized with a corrosion inhibitor (Cerium) are incorporated. This coating is obtained thanks to a sol-gel transition. Boehmite nano-particles were considered as candidates for the role of nano-containers in this work. Even though some promising results have been obtained, a clear understanding of the function as well as of the limitations of this type of nano-containers was missing. Thus, a correct account of the mechanisms of adsorption and desorption of the corrosion inhibitor on the nano-particles was needed. Furthermore, it has been shown that significant particle transport can occur during the evaporation of a thin film, giving rise to different deposit structures. Actually, the final morphology of the deposit, and therefore its homogeneity, will depend on several parameters such as the evaporation rate and the interactions between particles.

In order to obtain efficient anti-corrosion coatings, it is imperative to assure that the nano-containers are homogeneously dispersed inside the coating matrix after the deposition. To this end, a macroscopic model for the transport of interacting nano-particles in an electrolyte solution was developed. After a rigorous derivation of the average transport equations, two quantities are seen to affect particle transport. The first one is the hydrodynamic contribution to the particle stress tensor, related to hydrodynamic interactions between particles. It is responsible in particular of shear induced migration. The second important quantity is the thermodynamic contribution to this tensor, related with non-hydrodynamic particle-particle interactions. It is considered isotropic and given by the equilibrium osmotic pressure of the suspension here. In some flows, such as a channel flow, these terms can have opposing effects. Shear induced migration has the tendency to transport particles towards low-shear regions, which is the center of the channel, while the osmotic pressure is a term related with the opposition of the particles to be concentrated and to create concentration gradients. Depending on the flow conditions, the particle size, the electrolyte composition and the electric charge of the particles, the relative weight of hydrodynamic and thermodynamic stresses changes. Generally it is expected that for suspension flows with a particle Péclet number  $Pe_p \ll 1$  the osmotic pressure has more weight since the system is close to equilibrium, while in flows where  $Pe_p > 1$  the shear-

---

induced migration mechanism is more relevant. Using a channel flow as a test case, it was demonstrated that the usual definition of the Péclet number is not relevant for charge-stabilized suspensions. A more relevant Péclet number was defined as the ratio of viscous and thermodynamic stress scales for the case of interacting nano-particles. Based on this definition, a flow phase diagram was constructed where a clear discrimination of the purely hydrodynamic and purely thermodynamic regimes was possible. These results indicated that for the problem of a drying film, subtle hydrodynamic effects such as shear-induced migration can be neglected. This progress simplifies significantly the system of equations. Based on this result, the simulation of the drying of a suspension of nano-particles with different charges has been realized in the geometry of a micro-evaporator. It is suggested that for simple geometries and a macroscopically defined Péclet number  $Pe_y \leq 1$ , a one dimensional approach is sufficient. If there is a significant two or three dimensional flow, then the full resolution of the equations is needed. Furthermore, the inclusion of a variable viscosity model seems to be relevant only for  $Pe_y > 1$  in this flow. Indeed, in this case the strong flow generates an inhomogeneity of the deposited film, leading to zones with significantly different viscosities. Comparing the simulation results for three different Péclet regimes,  $Pe_y = 0.1, 1, 10$ , two deposition scenarios were identified. For  $Pe_y = 0.1$  the suspension dries in a way reported in the literature as a horizontal drying front. The concentration profile is homogeneous in the direction perpendicular to the flow, and after reaching a maximum concentration this front propagates upstream, towards the entrance of the channel. The maximum value of the volume fraction depends on the Péclet number. For the case of  $Pe_y = 1$ , this propagating front presents a concentration equal to the close packing concentration  $\phi \sim 0.64$ , while for  $Pe_y = 0.1$  the maximum concentration is inferior. The other deposition scenario was observed for Péclet  $Pe_y = 10$ , where the particles were directly transported towards the surface of the channel, creating a dense pack with concentrations close to the close packing one. This scenario is reported in literature as skinning or skin creation with many consequences in the drying process, as it is possible to inhibit evaporation or lead to film cracking. Lastly, by comparing results at  $Pe_y = 1$  for suspensions of hard-spheres and charged particles, it was demonstrated that all the suspensions dry following the horizontal front propagation mechanism. Considering that the different particle interactions led to significantly different simulation results, there was a definite motivation to study these interactions in the system of boehmite nano-particles, our candidate in the design of nano-containers.

The second aim of this work was therefore to create the system of boehmite nano-

containers, and to study their stability and their adsorption capability in a range of cerium nitrate concentration. To this end, after synthesizing the particles, a detailed description of their physical characteristics was given. Even though some concerns existed initially about the actual shape and size of the particles, it was finally demonstrated that boehmite particles created with the specific protocol used in this study have the form of needles. This was an important outcome since elongated objects tend to have a high specific surface area, which is important for nano-containers. Using the nano-particles in the synthesis solvent was a restriction put forward by the industrial partner of the project. Therefore, the composition of this solvent needed to be characterized. It was shown that a large concentration of aluminum and nitrate ions exist in the solvent at the end of the synthesis. These ions need to be taken into account for the subsequent studies. In particular, we were interested by the description of the interface between the particles and the solvent, as it affects the stability and adsorption capability of the suspension. After testing the stability of the suspension in a range of concentration of cerium nitrate to define some limiting concentrations, it was observed that the cerium nitrate displayed a critical concentration of coagulation similar, or close to, to the one of sodium nitrate. This result was not expected since the stoichiometry of cerium nitrate suggests a concentration of nitrates, which is relevant for the stability of the positively charged particles, three times higher than the one of sodium nitrate. This unexpected result, led to the implementation of a speciation study of cerium nitrate. The results showed that for high salt concentrations, the species present in the solution change, decreasing the total amount of free nitrates in the solution. Lastly, after the upper limit of salt concentration was specified to ensure colloidal stability, bulk adsorption experiments of cerium were realized. They indicated an important capacity of boehmite particles to capture cerium species for a very large range of concentration. Using a surface complexation model fitted to the experimental results, the feasibility of the concept of  $pH$  triggered release of cerium from nano-containers was demonstrated: the trigger is a decrease of the  $pH$  of the solution. However, corrosion studies on aluminum alloys have shown an increase of the  $pH$  of solutions when corrosion appears. This suggests that the  $pH$  effect in this type of nano-containers dispersion is exactly opposite to what is desired. Nevertheless, a secondary mechanism of desorption was proposed. Since the functionalized nano-containers are mixed together with the barrier coating, the quantity of cerium that was not adsorbed will remain in the coating volume. In case of coating damage this “free” cerium will be first consumed to protect the surface. The equilibrium change between the concentrated cerium on the particle surface and the depleted cerium in

---

the bulk forces adsorbed cerium to desorb. Thus, the choice of boehmite particles as nano-containers might be possible, but there are probably other systems better suited to a use as nano-containers.

In the light on these results, in the next few lines, some suggestions will be given that may solve issues confronted in this work or give some new perspectives for research.

Even if the subject of speciation only came up late in this project, making an extended literature review impossible, only a limited number of publications was found relating surface complexation and adsorption on aluminum oxide particles. Very low concentrations of electrolytes were generally considered in these studies, thus greatly simplifying the speciation analysis. Usually, the electrolytes are completely dissolved to their constituents in the very low concentration limit. Thus a more precise modelling of speciation and how it is related to adsorption seems mandatory for studies of adsorption in high electrolyte concentration. Some experimental techniques that have been used to identify the mechanism of ion adsorption on charged surfaces are Time Resolved Laser Fluorescence Spectroscopy (TRLFS) and Extended X-ray Absorption Fine Structure (EXAFS).

Concerning the concept of “nano-container”, a different approach can be proposed, using also the counter-intuitive concept of adsorbing a positively charged corrosion inhibitor inside the volume of a positively charged hollow sphere. When these spheres are suspended in an electrolyte solution, the co-ions are strongly repelled outside and away from the particles at low volume fraction, similarly to what is observed for full spheres. On the other hand, when these vesicles are concentrated, the electrostatic potential inside the particles is lower than the one outside them, thus forcing the migration and caging of the co-ions inside the hollow spheres. Actually, the film drying process used to form the coating is precisely a concentration process that would trigger this migration of Cerium inside the particles. In case of a damage on the coating, some particles would be exposed to an aqueous environment free of other particles, i.e. a local “dilution” process, authorizing the automatic release of Cerium.

Concerning the numerical simulations, the shear viscosity model used in this work was designed for hard-spheres. However, shear viscosity is known to depend strongly on electrostatic interactions, demonstrating a strong increase with the particle charge, as well as a shear-thinning behavior for particle concentrations over 30%. Although many rheological measurements have been realized on charged colloidal particles, to my knowledge no general analytical models for the dependence of the

viscosity with physico-chemical parameters exist. Additionally, strong hypotheses have been invoked concerning the normal stresses. The thermodynamic stress was assumed to be given by its equilibrium value, the osmotic pressure, which might not be correct in flowing suspensions due to the micro-structure distortion. The uncertainty on the results associated with this hypothesis is not controlled yet. Finally, electrostatic interactions also perturb the microstructure, and thus the hydrodynamic part of the normal stresses. Once again, to date, there are no analytical models for these normal stresses as a function of the shear rate and physico-chemical parameters. Obtaining such knowledge would greatly improve the modelling of flowing colloidal suspensions.

Lastly, an implementation of electrolyte transport in the Suspension Balance Model formulation can be envisaged. This advance would allow the relation of the osmotic pressure term used to model particle interactions with the electrolyte concentration. This improvement may have a significant impact on drying simulations since the ion bulk concentration varies in space and time in such processes.

# Appendix

A large, white, serif capital letter 'A' is centered within a dark gray rectangular box. The letter is bold and has a classic, slightly ornate design with a horizontal bar and a small serif at the top.

## 1 Proof of relation (1.19)

$$\langle \nabla_{\mathbf{y}} \cdot \mathbf{u} \rangle = \int \chi g \nabla_{\mathbf{y}} \cdot \mathbf{u} \, dV + \int (1 - \chi) g \nabla_{\mathbf{y}} \cdot \mathbf{u} \, dV. \quad (\text{A.1})$$

Both parts of the right hand side of the equation can be re-written

$$\int \chi g \nabla_{\mathbf{y}} \cdot \mathbf{u} \, dV = \int \nabla_{\mathbf{y}} \cdot (\chi g \mathbf{u}) \, dV - \int g \mathbf{u} \cdot \nabla_{\mathbf{y}} \chi \, dV - \int \chi \mathbf{u} \cdot \nabla_{\mathbf{y}} g \, dV \quad (\text{A.2})$$

using the identity

$$\nabla \cdot (\psi \mathbf{A}) = \mathbf{A} \cdot \nabla \psi + \psi (\nabla \cdot \mathbf{A}) \quad (\text{A.3})$$

where  $\psi$  is a scalar quantity and  $\mathbf{A}$  is a tensor. Using the divergence theorem for the first member of the equation reduces to a surface integral bounding volume  $V$ . Provided that the distance between the volume boundaries and  $\mathbf{x}$  is large it reduces to zero (remember that  $\lim_{|\mathbf{r}| \rightarrow \infty} g(\mathbf{r}) = 0$ ). Replacing  $D\chi/Dt \equiv \partial\chi/\partial t + \mathbf{u} \cdot \nabla_{\mathbf{y}} \chi = 0$  in the second part it reduce to  $\partial\phi/\partial t$ . The last part can be re-written as  $\nabla \cdot (\phi \langle \mathbf{u} \rangle^s)$ , having used  $\nabla_{\mathbf{x}} g = -\nabla_{\mathbf{y}} g$  and taking into account that inside the integral  $g$  was the only term depending on  $\mathbf{x}$ . Combining the above yields

$$\frac{\partial\phi}{\partial t} + \nabla \cdot (\phi \langle \mathbf{u} \rangle^s) = 0. \quad (\text{A.4})$$

The same transformations exist for the second part of the right hand side of eq. (A.1) replacing where  $\chi$  with  $(1 - \chi)$  that yields

$$\frac{\partial(1 - \chi)}{\partial t} + \nabla \cdot [(1 - \chi) \langle \mathbf{u} \rangle^f] = 0. \quad (\text{A.5})$$

Summing the above equation and using  $\langle \xi \rangle = \phi \langle \xi \rangle^s + (1 - \phi) \langle \xi \rangle^f$  yields the mass balance of the suspension

$$\nabla \cdot \langle \mathbf{u} \rangle = 0 \quad (\text{A.6})$$

## 2 Proof of relation (1.21)

$$\langle \nabla_{\mathbf{y}} \cdot \boldsymbol{\sigma} \rangle = \int \chi g \nabla_{\mathbf{y}} \cdot \boldsymbol{\sigma} dV + \int (1 - \chi) g \nabla_{\mathbf{y}} \cdot \boldsymbol{\sigma} dV + \int g \mathbf{b} dV. \quad (\text{A.7})$$

Both parts of the right hand side of the equation can be re-written

$$\int \chi g \nabla_{\mathbf{y}} \cdot \boldsymbol{\sigma} dV = \int \nabla_{\mathbf{y}} \cdot (\chi g \boldsymbol{\sigma}) dV - \int g \boldsymbol{\sigma} \cdot \nabla_{\mathbf{y}} \chi dV - \int \chi \boldsymbol{\sigma} \cdot \nabla_{\mathbf{y}} g dV \quad (\text{A.8})$$

using the identity

$$\nabla \cdot (\psi \mathbf{A}) = \mathbf{A} \cdot \nabla \psi + \psi (\nabla \cdot \mathbf{A}) \quad (\text{A.9})$$

where  $\psi$  is a scalar quantity and  $\mathbf{A}$  is a tensor. Using the divergence theorem for the first member of the equation reduces to a surface integral bounding volume  $V$ . Provided that the distance between the volume boundaries and  $\mathbf{x}$  is large it reduces to zero (remember that  $\lim_{|\mathbf{r}| \rightarrow \infty} g(\mathbf{r}) = 0$ ). The third part can be re-written as  $\nabla \cdot [\phi \langle \mathbf{u} \rangle^s]$ , having used  $\nabla_{\mathbf{x}} g = -\nabla_{\mathbf{y}} g$  and taking into account that inside the integral  $g$  was the only term depending on  $\mathbf{x}$ . Replacing  $\nabla_{\mathbf{y}} \chi = -\mathbf{n} \delta(\mathbf{y} - \mathbf{y}_s)$  in the second part

$$\int g \boldsymbol{\sigma} \cdot \nabla_{\mathbf{y}} \chi dV = - \int g \boldsymbol{\sigma} \cdot \mathbf{n} \delta(\mathbf{y} - \mathbf{y}_s) dV. \quad (\text{A.10})$$

Correspondingly for the fluid phase stress

$$\int g \boldsymbol{\sigma} \cdot \nabla_{\mathbf{y}} (1 - \chi) dV = \int g \boldsymbol{\sigma} \cdot \mathbf{n} \delta(\mathbf{y} - \mathbf{y}_s) dV. \quad (\text{A.11})$$

where attention has been made for the direction of vector  $\mathbf{n}$  which is defined facing outwards of the particle. Combination of the above leads to the expression of the suspension average stress

$$\nabla \cdot [(1 - \phi) \langle \boldsymbol{\sigma} \rangle^f] + \nabla \cdot [\phi \langle \boldsymbol{\sigma} \rangle^s] + \langle \mathbf{b} \rangle = 0. \quad (\text{A.12})$$

### 3 Proof of relation (1.25)

Taking advantage of the fact that particles are considered rigid allows the reformulation of the solid stress  $\phi\langle\boldsymbol{\sigma}\rangle^s$  in terms of the surface traction on particles. First, the averaging function  $g$  has to be developed in a Taylor series about the particle  $i$  center  $\mathbf{y}_i$

$$g(\mathbf{x}, \mathbf{y}) = g(\mathbf{x}, \mathbf{y}_i) + \mathbf{y}' \cdot \nabla_{\mathbf{y}} g(\mathbf{x}, \mathbf{y}_i)|_{\mathbf{y}_i} + \frac{1}{2!} \mathbf{y}' \mathbf{y}' : \nabla_{\mathbf{y}} \nabla_{\mathbf{y}} g(\mathbf{x}, \mathbf{y}_i)|_{\mathbf{y}_i} + \dots \quad (\text{A.13})$$

where  $\mathbf{y}_i \equiv \mathbf{y} - \mathbf{y}_i$  and  $g(\mathbf{x}, \mathbf{y}_i)$  is the averaging function in the center of the particle  $i$ . Using the expansion and  $\nabla_{\mathbf{x}} g = -\nabla_{\mathbf{y}} g$ , solid stress can be written

$$\phi\langle\boldsymbol{\sigma}\rangle^s = \sum_i g_i \int_{V_i} \boldsymbol{\sigma} dV - \nabla \cdot \sum_i g_i \int_{V_i} \mathbf{y}' \boldsymbol{\sigma} dV + \dots \quad (\text{A.14})$$

where  $g_i = g(\mathbf{x}, \mathbf{y}_i)$ . Each term of the equation can be re-written using a formula used by Batchelor (1970),  $\boldsymbol{\sigma} = [\nabla_{\mathbf{y}} \cdot (\boldsymbol{\sigma} \mathbf{y}')]^T - \mathbf{y}' \nabla_{\mathbf{y}} \cdot \boldsymbol{\sigma}$ . Using the divergence theorem for the first and substituting  $\nabla_{\mathbf{y}} \cdot \boldsymbol{\sigma} = \mathbf{b}$ , which holds true in every point in the suspension, then the first term can be re-written

$$\sum_i g_i \int_{V_i} \boldsymbol{\sigma} dV = \sum_i g_i \int_{V_i} \mathbf{y}' \mathbf{n} \cdot \boldsymbol{\sigma} dS + \sum_i g_i \int_{V_i} \mathbf{y}' \mathbf{b}. \quad (\text{A.15})$$

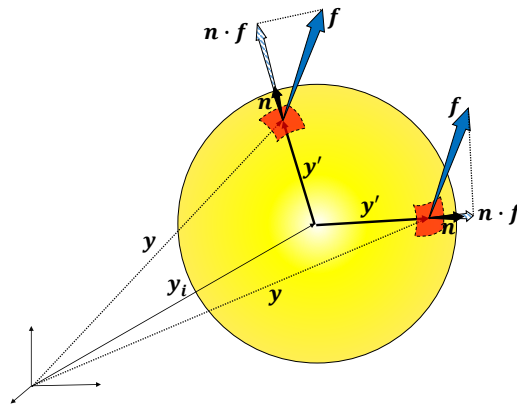


**Figure A.1:** Traction  $\mathbf{n} \cdot \boldsymbol{\sigma}$  on the particle surface

This transformation exists for every term in equation... as proven by Nott et al. (2011), and finally transforms the equation to

$$\begin{aligned} \phi\langle\boldsymbol{\sigma}\rangle^s &= n\langle\mathbf{S}\rangle^p - \frac{1}{2}\nabla \cdot n\langle\mathbf{Q}\rangle^p + \dots \\ &+ \sum_p g_i \int_{V_p} \mathbf{y}'\mathbf{b} \, dV - \frac{1}{2}\nabla \cdot \sum_p g_i \int_{V_p} \mathbf{y}'\mathbf{y}'\mathbf{b} \, dV + \dots \end{aligned} \quad (\text{A.16})$$

where  $\mathbf{S}$  is the first moment of surface traction and  $\mathbf{Q}$  is the second moment of surface traction on the surface. The first and the second moment of traction are defined starting from the force exerted on the particle  $\mathbf{f}$

$$\begin{aligned} \mathbf{f} &= \int_{S_p} \mathbf{n} \cdot \boldsymbol{\sigma} \, dS \\ \mathbf{S} &= \int_{S_p} \mathbf{y}'\mathbf{f} \, dS \\ \mathbf{Q} &= \int_{S_p} \mathbf{y}'\mathbf{y}'\mathbf{f} \, dS. \end{aligned}$$

## 4 Dialysis procedure

Dialysis is a procedure used for the separation of small molecules and ions from a colloidal suspension. The suspension is restricted in on side of a semi-permeable membrane, while on the other side a washing solution is used, in this case ultrapure water. The membrane pore size should be small enough to restrict the particles in their compartment but large enough to permit smaller molecules and ions to freely move between the compartments.

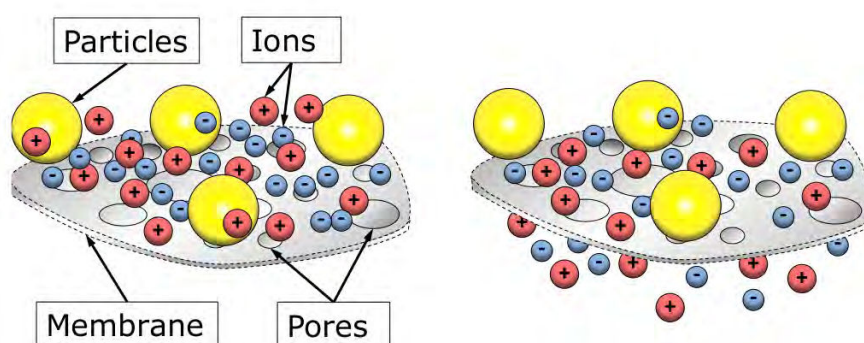


**Figure A.2:** Dialysis concept (*left*) at time  $t_0$  (*right*) at equilibrium

Ions and small molecules are expected to pass through the membrane as a consequence of a concentration difference, implying a purely diffusive process, a phenomenon termed *osmosis*. The actual driving force of the flow of the solutes is the difference in the chemical potential between the compartments. Finally the system can reach equilibrium if the chemical potential is equal in both compartments.

The dialysis concept is presented in Figure. A known volume of stock suspension, as prepared in Section 1.1.1, is inserted in a dialysis sack, with attention not to include air, and then closed tightly with the appropriate closures. Attention has to be made not to fill the sack to the fullest, to allow the expansion of the sack because of the inflow of water. After filling a beaker with a known volume of ultrapure water, the filled sack is dipped inside. The chemical potential of ultrapure water is higher in the outer compartment, which creates an inflow of water inside the sack by osmosis, diluting the suspension. In the same time the ions and small molecules inside the sack, are diffused in the outer compartment. One can have an indication of whether the system reached equilibrium by measuring the conductivity of the outer compartment. Normally the first and second day of dialysis there is a rapid increase of conductivity due to the increase of ion concentration and equilibrium is reached after five days.

## 5 Adsorption protocol

### *Synthesized nano-particles*

All adsorption tests were realised with the addition of an aqueous solution of Cerium Nitrate at a certain concentration, with a suspension of particles in stock concentration  $38 \text{ gr L}^{-1}$  at equal volumes. After continuous stirring at room temperature for a certain period (to be determined in results) in a closed vial, the mixture was recovered and filtered through an ultrafiltration membrane<sup>1</sup> so that the particle phase is retained. After a sufficient volume (10 mL) of permeate was recovered it was analysed by ICP-OES to determine the quantity of Cerium that was not adsorbed.

For the calibration of ICP-OES, a stock suspension of nano-particles (No Cerium nitrate added) was filtered as before, to recover the matrix. In this matrix, a known quantity of Cerium Nitrate was added in different concentrations and the solutions were used as the calibration standards. The reason for using the matrix as the background solution for the standards was to remove possible interferences from the matrix itself.

Unfortunately, because of our ICP-OES limitation the samples and calibration standards had to be purified by traces of alcohol. This means that the 2-butanol had to be removed from the suspension. Consequently, before the adsorption experiments, the suspension was first freeze-dried. After recovering the powder, it was re-dispersed in ultrapure water in the same initial concentration of  $38 \text{ gr L}^{-1}$ . To confirm that there were no aggregates inside the solution, the hydrodynamic size was measured in each batch by Dynamic Light Scattering.

Eventhough ICP-OES is the appropriate technique to detect traces of elements, the results were far from satisfactory; experiments were in most cases not repeatable, in other cases the concentration of Cerium detected was higher than concentration initially mixed. The most probable source for these errors lies in the sample preparation (freeze-drying, filtration) and the preparation of the calibration standards.

### *Commercial nano-particles*

As before, adsorption tests were realised by mixing equal volumes of aqueous solutions of Cerium Nitrate at certain concentrations with a suspension of the commercial particles at  $26 \text{ gr L}^{-1}$ . After continuous stirring for 24 h in a closed vial, a volume of an aqueous solution of Sodium Nitrate at  $0.15 \text{ mol L}^{-1}$  was added to induce aggregation of the particles and separate the particles by centrifugation. The concentration

<sup>1</sup>weight cut-off of the 25 kD, equivalent pore size of 5 – 10 nm

of Sodium nitrate after mixing was  $0.1 \text{ mol L}^{-1}$ . If no salt was added, the mixture could not be separated by centrifugation due to high repulsive forces between particles. After centrifugation the supernatant was recovered and mixed with an equal volume of an aqueous solution that contained the reactive agent (Xylenol-Orange<sup>2</sup>) at a concentration of  $1.3 \cdot 10^{-3} \text{ mol L}^{-3}$ . The adsorption on each sample was measured with a UV/Vis spectrophotometer.

The suspension of nano-particles was prepared by dispersing 26 gr of powder in 1 L of ultrapure water and let it under stirring for 24 h. Because this powder contains already Nitric acid, no further addition of chemical was needed for the powder to completely disperse. The suspension obtained was stable with a  $pH = 4.5$ . To verify that no particle aggregates existed, the hydrodynamic size of the particles was measured by means of Dynamic Light Scattering and a single particle population was reported around 25 nm which conforms with the details of the producer.

Initially the calibration standards were prepared to reproduce the composition of supernatant after centrifugation, assuming that it would contain Cerium, Sodium and Nitrates at a  $pH = 4.5$ . Two different calibration sets were used; one for Cerium concentration between  $6 \cdot 10^{-4} \text{ mol L}^{-1}$  to  $2.4 \cdot 10^{-3} \text{ mol L}^{-1}$  and a second one for concentration  $6 \cdot 10^{-3} \text{ mol L}^{-1}$  to  $2.4 \cdot 10^{-2} \text{ mol L}^{-1}$ . In a detailed study from Tonosaki and Otomo (1962) it was found that Cerium creates a 1 : 1 complex with Xylenol-Orange, giving a linear response of light absorbance with Cerium concentration only for a certain extent of the range of Cerium and for a Xylenol-Orange concentration below  $2 \cdot 10^{-3} \text{ mol L}^{-1}$ . Consequently, for Cerium concentrations in solution higher than the optimal concentration of Xylenol-Orange, a dilution of the supernatant had to be made. But by diluting the supernatant the matrix is also diluted and this has a significant influence in the absorption response. For the first set of calibration standards that corresponds to the lower Cerium concentration, in an aqueous solution of Xylenol-Orange at  $1.3 \cdot 10^{-3} \text{ mol L}^{-3}$ , Sodium nitrate was added to reach a concentration of  $0.1 \text{ mol L}^{-1}$  and the  $pH$  was set at 4.5 with the addition of Nitric Acid. For the second set of standards, in the aqueous solution of Xylenol-Orange at  $1.3 \cdot 10^{-3} \text{ mol L}^{-3}$ , Sodium nitrate was added to reach a concentration of  $0.01 \text{ mol L}^{-1}$  and the  $pH$  was set at 4.5 with the addition of Nitric Acid. This concentration of Sodium corresponds to a ten-fold dilution of the supernatant. The next step was to add a volume of an aqueous solution of Cerium Nitrate in different concentrations from  $6 \cdot 10^{-4} \text{ mol L}^{-1}$  to  $2.4 \cdot 10^{-3} \text{ mol L}^{-1}$  and measure the absorbance. In Figure A.3 the absorbance of a number of different samples is

<sup>2</sup>SIGMA-ALDRICH

demonstrated and clear peaks absorbance of the the complexe Xylenol-Cerium can be distinguished at  $\sim 575 \text{ nm}$ .

Unfortunately, and this is where this protocol had to be further developed, the coloring reactive does not react only with Cerium ions but with other multivalent metal ions in general. When the supernatant after centrifugation was mixed with the Xylenol solution, absorbance measurements were saturated in the same value for all the concentrations of Cerium. In the suspension made from the commercial powder, as is the case for the synthesized suspension, there is a high concentration of Aluminum ions that “consume” the reactive. Because of this all the absorbances measured for different concentrations of Cerium were saturated in the same value thus providing no discrimination between the values. Furthermore, this problem seems to arise only for multivalent cations, since the addition of Sodium did not create any problems.

The only solution that seemed feasible at that moment was to remove aluminum ions by dialysis. The suspension was first dialysed (protocol see Appendix 4) for three days against ultrapure water. Furthermore, because dialysis can not always yield the exact same results, the calibration standards had to be prepared in the matrix of the dialysed suspension to avoid errors that rise from aluminum ions that were not completely removed. The matrix of the dialysed suspension was recovered by aggregating the particles with Sodium Nitrate as described previously and then centrifugating. Thus, each adsorption experiment should be matched with its calibration standards. Unfortunately, that very important detail was only realised when it was too late to restart the experiments. Therefore, the results of three calibration standards were averaged and produced a mean calibration curve presented in Figure A.4

The left graph corresponds to the initial concentrations of Cerium Nitrate that did not exceed the concentration of the reactive and thus did not need dilution. On the right graph correspond to concentration of Cerium Nitrate that exceeds the reactivities concentration of  $1.3 \text{ mol L}^{-1}$  and needed to be diluted. Each set of markers ( $\Delta$ ,  $\circ$ ,  $\square$ ) in the graphs correspond to a different set of calibration standards under the same conditions. The solid black line is the averaged calibration curve that will be used.

The red zone that surrounds each line is the standard deviation of the prediction  $s_x$  which reads

$$s_x = \frac{s_e}{a} \sqrt{\left( \frac{1}{n} + \frac{1}{m} + \frac{(\bar{y}_i - \bar{y})^2}{a^2 \sum_{i=1}^n (x_i - \bar{x})^2} \right)} \quad (\text{A.17})$$

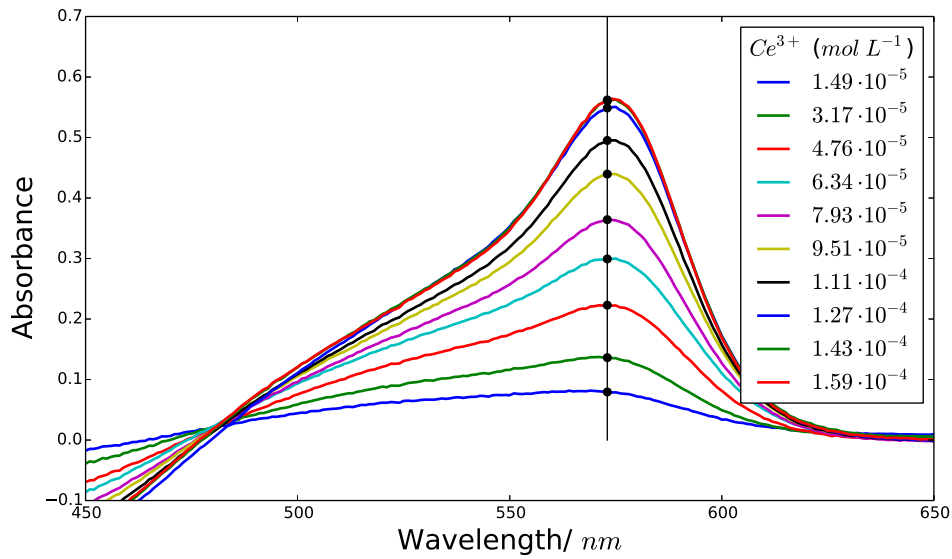


**Figure A.3:** Absorbance of the Xylenol-Cerium complex for different concentrations of Cerium. A clear absorption peak appears at 575 nm

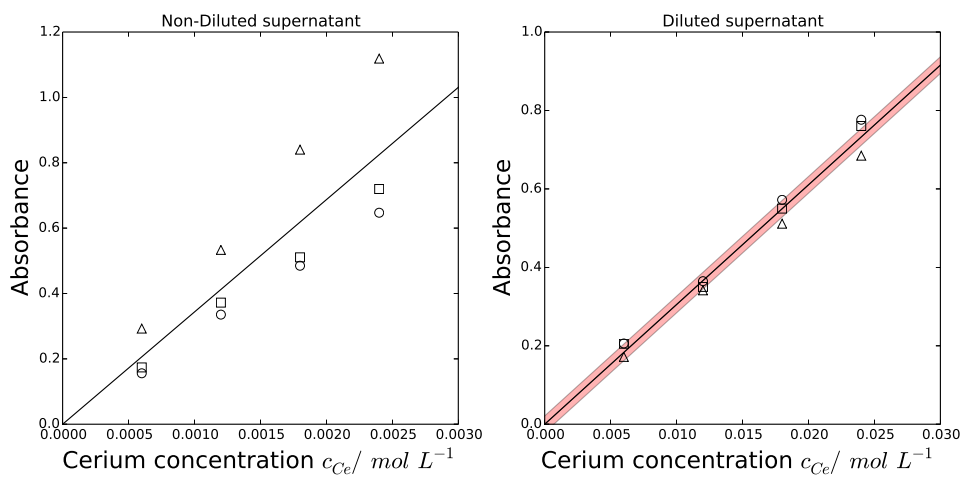


**Figure A.4:** Calibration curves of the second protocol for the non-dilute (left) and dilute supernatant (right). Red zones correspond to standard deviation of prediction.

---

where  $s_e$  is the residual standard deviation,  $a$  is the slope of the linear fit on the calibration data,  $m$  is the number of repetitions of the measurement,  $n$  is the number of calibration points,  $\bar{y}_i$  is the average of the  $m$  repeated measurements,  $\bar{y}$  is the average of all the values in the calibration standard,  $x_i$  is the value on the  $x$ -axis and  $\bar{x}$  is the average value of all the different  $x_i$ . The residual standard deviation is defined as (cite the book of feinberg)

$$s_e = \sqrt{\frac{\sum_{i=1}^n (y_i - \hat{y}_i)^2}{n - 2}} \quad (\text{A.18})$$

where  $y_i$  is the observed value of  $y$  for a given value of  $x_i$  and  $\hat{y}_i$  is the predicted value of  $y$  using the slope ( $a$ ) and the intercept  $b$  from the linear fit ( $\hat{y} = ax + b$ ).



---

Nonetheless, in other studies of adsorption of lanthanides on alumina (Shiao and Meyer (1981); Shiao et al. (1981); Rabung et al. (2000)) equilibration time ranged from 1 up to 7 days. In lack of more convincing experimental results, the contact time between nano-particles and cerium nitrate was set to 1 day.

## 7 References

- Batchelor, G. K. (1970). The stress system in a suspension of force-free particles. *Journal of Fluid Mechanics*, 41(03):545–570.
- Debnath, S. and Ghosh, U. C. (2008). Kinetics, isotherm and thermodynamics for Cr(III) and Cr(VI) adsorption from aqueous solutions by crystalline hydrous titanium oxide. *The Journal of Chemical Thermodynamics*, 40(1):67–77.
- Granados-Correa, F. and Jiménez-Becerril, J. (2009). Chromium (VI) adsorption on boehmite. *Journal of Hazardous Materials*, 162(2–3):1178–1184.
- Nott, P. R., Guazzelli, E., and Pouliquen, O. (2011). The suspension balance model revisited. *Physics of Fluids (1994-present)*, 23(4):043304.
- Rabung, T., Stumpf, T., Geckeis, H., Klenze, R., and Kim, J. I. (2000). Sorption of Am(III) and Eu(III) onto  $\gamma$ -alumina: experiment and modelling. *Radiochimica Acta International journal for chemical aspects of nuclear science and technology*, 88(9-11/2000):711.
- Shiao, S.-Y., Egozy, Y., and Meyer, R. E. (1981). Adsorption of Cs(I), Sr(II), Eu(III), Co(II) and Cd(II) by Al<sub>2</sub>O<sub>3</sub>. *Journal of Inorganic and Nuclear Chemistry*, 43(12):3309–3315.
- Shiao, S.-Y. and Meyer, R. (1981). Adsorption of inorganic ions on alumina from salt solutions: Correlations of distribution coefficients with uptake of salt. *Journal of Inorganic and Nuclear Chemistry*, 43(12):3301–3307.
- Tonosaki, K. and Otomo, M. (1962). Spectrophotometric Determination of Cerium(III) and Some Rare Earths with Xylenol Orange. *Bulletin of the Chemical Society of Japan*, 35(10):1683–1686.

## Implementation of anti-corrosion nano-containers in the processes of surface treatment

The use of hexavalent Chromium as a corrosion inhibitor in protective coatings of metal parts will soon be prohibited because this element is considered carcinogenic and mutagenic. One of the strategies suggested to overcome this problem is the incorporation of nano-containers containing corrosion inhibitors, other than Chromium, inside a coating matrix. The nano-containers approach used in this work is based on the physisorption of the corrosion inhibitor on charged nano-particles. It is an electrochemical approach where a salt, the corrosion inhibitor, is adsorbed on the surface of the charged nano-particles. After the incorporation of the charged nano-containers in the coating matrix and the deposition of the film on the substrate, the final morphology and therefore the homogeneity of the film will depend on several parameters such as the evaporation rate and the interactions between particles. Consequently, one has to insure that the nano-containers are homogeneously dispersed inside the coating matrix after the deposition, or be able to predict where inhomogeneities will develop. Hence, the first aim of this work is to develop a modeling strategy to study the flow of suspensions containing interacting nano-particles in electrolyte solutions. The interactions taken into account here are of hydrodynamic, thermal, and electrostatic origin and it is argued that in the application of film drying of nano-particles the interactions relevant are those of thermal and electrostatic origin only. Based on this idea, the simulation of the drying of a suspension with nano-particles of different charges has been realized in a micro-evaporator. Considering that particle interactions are influenced by the charge and the electrolyte concentration of the suspension, there is a clear motivation to study these interactions in a synthesized system of nano-particles, candidate in the design of nano-containers. Therefore, the second aim of this work is to synthesize boehmite nano-containers, study their stability in a range of corrosion inhibitor concentration, and finally qualify them as candidates for the application of anti-corrosion coatings.

*Keywords: colloidal suspensions, flow modeling, film drying, Cerium, Boehmite, nano-containers, adsorption*

---

## Mise en oeuvre de nano-réservoirs anti-corrosion dans des procédés de traitement de surface

L'utilisation de chrome hexavalent comme inhibiteur de corrosion dans les revêtements protecteurs de pièces métalliques sera bientôt interdit car cet élément est considéré comme cancérigène et mutagène. L'une des stratégies proposées pour remédier à ce problème est l'incorporation de nano-réservoirs contenant des inhibiteurs de corrosion, autres que le chrome, dans une matrice de revêtement. L'approche utilisée dans ce travail est basée sur la physisorption de l'inhibiteur de corrosion sur des nano-particules chargées. C'est une approche électrochimique où un sel, l'inhibiteur de corrosion, est adsorbé sur la surface des nano-particules chargées. Après l'incorporation de nano-réservoirs chargés dans la matrice de revêtement et le dépôt du film sur le substrat, la morphologie finale, et donc l'homogénéité, du film dépend de plusieurs paramètres tels que la vitesse d'évaporation du film et les interactions entre particules. Par conséquent, il faut s'assurer que les nano-réservoirs sont dispersés de manière homogène à l'intérieur du revêtement ou être en mesure de prédire où les inhomogénéités vont se développer. Ainsi, le premier objectif de ce travail est de développer une stratégie de modélisation pour étudier l'écoulement de suspensions contenant des nano-particules dans des solutions électrolytiques. Les interactions prises en compte ici sont d'origine hydrodynamique, thermique et électrostatique. Nous montrons que dans le cas du séchage d'un film contenant des nano-particules, les interactions pertinentes sont celles d'origine thermique et électrostatique seulement. Sur la base de ce résultat, l'exemple d'un micro-évaporateur est présenté dans lequel des expériences numériques du séchage d'une suspension de nano-particules avec différentes charges de surface ont été réalisées. Sachant que les interactions entre particules sont influencées surtout par la charge et la concentration de l'électrolyte dans la suspension, il existe une réelle motivation pour étudier ces interactions dans les systèmes de nano-particules synthétisées en vue de la conception de nano-réservoirs. Par conséquent, le deuxième objectif de ce travail est de synthétiser des nano-réservoirs de boehmite, d'étudier leur stabilité dans une gamme de concentration d'inhibiteur de corrosion, et finalement de valider ce type de nano-réservoirs pour des applications de revêtements anti-corrosion.

*Mots clés: suspensions colloïdales, modélisation de l'écoulement, séchage de films minces, Cérium, Boehmite, nano-reservoirs, adsorption*